



University  
of Glasgow

Sperling, Justin Ryan (2019) *Plasmonic nanostructures for molecular sensing and colour filtering*. PhD thesis.

<https://theses.gla.ac.uk/72464/>

Copyright and moral rights for this work are retained by the author

A copy can be downloaded for personal non-commercial research or study, without prior permission or charge

This work cannot be reproduced or quoted extensively from without first obtaining permission in writing from the author

The content must not be changed in any way or sold commercially in any format or medium without the formal permission of the author

When referring to this work, full bibliographic details including the author, title, awarding institution and date of the thesis must be given

Enlighten: Theses

<https://theses.gla.ac.uk/>  
[research-enlighten@glasgow.ac.uk](mailto:research-enlighten@glasgow.ac.uk)

# Plasmonic Nanostructures for Molecular Sensing and Colour Filtering

Justin Ryan Sperling

December 2018

A Thesis Submitted to the

Division of Biomedical Engineering

School of Engineering

University of Glasgow

In Fulfilment of the Requirements for

The Degree of Doctor of Philosophy (Ph.D.)

## Abstract

Plasmonic nanoarrays offer a number of advantages over other technologies when it comes to optical sensing and colour filtering—namely their full tunability across the visible spectrum, high sensitivity to local refractive index changes, relative stability, and ultra-high resolution. For optical sensors, as their use progresses towards portable devices capable of rapid and highly-specific sensing, reduction in complexity, device size, and data acquisition time is key; and for optical colour filtering and encoding, the desire for long-term-stability and ultra-high resolution is key. One way to achieve the aforementioned goals in both fields is through the development of optical devices capable of producing two signals/displays within one region. This thesis explores the fabrication and characterisation of such devices for applications in molecular sensing and colour display technologies.

First, a proof-of-concept device consisting of two nanoplasmonic arrays arranged in a multilayer configuration is explored. This device is demonstrated capable of self-correcting for drift by simultaneously obtaining both sensing and reference signals from a single measurement without complex optics or multiple sensing regions. This design holds promise for point-of-care diagnostics, where data acquisition occurs over extended periods of time and measurement stability due to the external environment may be problematic.

Next, another method of arranging two plasmonic nanoarrays is examined. These devices consist of superimposed aluminium and gold nanoarrays with modified surface chemistries resulting in a bimetallic device which produces two distinct resonance peaks for each sensing region. When combined, the signals from the different arrays are demonstrated capable of discriminating between organic solvents and between whiskies using trained pattern recognition. As each element in the bimetallic optical tongue produces two partially-selective measurements (rather than the one measurement capable with comparable devices), the proposed sensor is capable of halving device size and data-acquisition time. This advance in miniaturisation and multiplexed readout would be highly useful in areas that rely on assays for determining if a mixture is within tolerance, such as the medical, food & drug, and security industries.

Then, a new approach to high-density image encoding is demonstrated using full-colour, dual-state nano-pixels, doubling the amount of information that can be stored in a unit area. The smallest readable ‘unit’ using a standard optical microscope relates to 370 nm x 370

*Abstract*

nm. As a result, dual-state nano-pixels may prove significant for long-term, high-resolution optical image encoding, and counterfeit-prevention measures.

Finally, a combination of plasmonic sensing with the dual-state capabilities of the nano-pixel design presented is investigated. The dual-state capabilities of the nano-pixel design will allow trapping of biomolecules with one arm while simultaneously, yet independently, sensing with the other. While only preliminary work is covered, once successfully developed, such devices will aid the understanding of proteins and thus benefit the fields of biology, chemistry, medicine, and pharmacy. Additionally, they will allow for the testing and creation of new disease screenings and drug therapies.

## Table of Contents

Abstract.....	1
Table of Contents.....	3
List of Tables .....	7
List of Figures.....	7
Acknowledgements.....	10
Author's Declaration .....	11
Chapter 1: Introduction and Theory .....	12
1.1 Introduction.....	12
1.2 Plasmonics .....	12
1.2.1 Derivation of the Dielectric Function of Metals.....	12
1.2.1.1 Maxwell's Equations .....	12
1.2.1.2 Plasmon Resonance and the Plasma Model.....	14
1.2.1.3 Dielectric Function of Metals .....	15
1.2.2 Propagating and Localised Plasmon Resonance.....	16
1.2.2.1 Surface Plasmon Resonance (SPR) .....	16
1.2.2.2 Localised Surface Plasmon Resonance (LSPR) .....	18
1.2.3 Appropriate Metals .....	22
1.2.4 Types of Nano-Plasmonic Structures .....	22
1.2.4.1 Nanoparticle Array (NPA).....	23
1.2.4.2 Nano-Aperture Array (NAA) and Extraordinary Transmission (EOT) of Light.....	23
1.3 Applications of Plasmonics .....	25
1.3.1 Plasmonic Sensors .....	25
1.3.2 Coloured Image Displays .....	26
1.4 Research Work Described Herein .....	27
1.4.1 Development of a Novel LSPR Self-Referencing Sensor .....	27
1.4.2 Development of a Novel Bimetallic Optical Sensor Array .....	27
1.4.3 Development of Dual-State Pixels for High-Density Optical Encoding .....	28
1.5 References.....	28
Chapter 2: Materials and Methods.....	34
2.1 Introduction.....	34
2.2 Materials .....	34
2.3 Simulation Techniques .....	35
2.3.1 Finite-Difference Time-Domain (FDTD) Simulations.....	35
2.3.2 Lumerical FDTD .....	36
2.4 Fabrication Tools.....	37

*Table of Contents*

2.4.1 Electron-Beam (E-Beam) Lithography.....	37
2.4.2 Electron-Beam Metal Evaporation .....	40
2.4.3 Plasma Enhanced Chemical Vapour Deposition (PECVD) of SiO <sub>2</sub> .....	40
2.4.4 Inductively Coupled Plasmon Chemical Vapour Deposition (ICP-CVD) of SiN <sub>x</sub> .....	41
2.4.5 Reactive-Ion Etching (RIE) of Aluminium .....	41
2.5 Fabrication Processes.....	42
2.5.1 Design Software.....	42
2.5.2 Device Cleaning.....	42
2.5.3 Metal Structure Fabrication .....	42
2.5.4 Silicon Nitride Micro-Region Fabrication.....	45
2.5.5 HSQ Micro-Region Fabrication .....	46
2.5.6 Nano-Aperture Fabrication.....	47
2.5.7 Surface Modifications.....	49
2.6 Characterisation Tools and Techniques .....	49
2.6.1 Atomic Force Microscopy (AFM).....	49
2.6.2 Ellipsometry.....	50
2.6.3 Scanning Electron Microscopy (SEM).....	50
2.6.4 Spectrophotometry.....	51
2.7 Data Analysis Techniques .....	53
2.7.1 Transmission Trough Determination.....	53
2.7.2 Principal Component Analysis (PCA) and Linear Discriminant Analysis (LDA) .....	54
2.7.3 CIE XYZ Spectra.....	55
2.8 Conclusion .....	55
2.9 References.....	56
Chapter 3: Multilayered Nanoplasmonic Arrays for Self-Referenced Biosensing .....	58
3.1 Introduction.....	58
3.2 Materials .....	60
3.3 Methods .....	60
3.3.1 Fabrication of Multilayered Sensor .....	60
3.3.2 Experimental Setup.....	60
3.3.3 Peak Analysis.....	61
3.3.4 Sensor Calibration .....	61
3.3.5 Device Functionalisation .....	61
3.3.6 Biological Sensing .....	62
3.3.7 FDTD Simulations.....	62
3.3.7.1 Optimisation Simulations .....	62
3.3.7.2 Full Device Simulation .....	63

*Table of Contents*

3.3.8 Surface Planarisation .....	64
3.3.9 Nitride Characteristics .....	64
3.4 Results and Discussion .....	65
3.4.1 Design and Fabrication of Multilayer Sensor .....	65
3.4.1.1 FDTD Determination of Minimum Nitride Thickness .....	65
3.4.1.2 FDTD Determination of Minimum Distance Between Nanoarray Layers..	67
3.4.1.3 Determination of Minimum HSQ Thickness .....	69
3.4.1.4 Consistency of Nitride Deposition.....	72
3.4.2 Multilayer Sensor Calibration.....	73
3.4.3 Multilayer Device for Real-Time RI Sensing.....	76
3.4.4 Multilayer Device for Real-Time Biosensing.....	78
3.4.5 Full Device FDTD Simulation.....	79
3.5 Conclusion and Future Work.....	82
3.6 References.....	82
Chapter 4: Bimetallic Nano-Plasmonics for the Optical Tasting of Whisky.....	86
4.1 Introduction.....	86
4.2 Materials .....	88
4.3 Methods .....	88
4.3.1 Simulations of Designs .....	88
4.3.2 Fabrication of Nanostructures.....	88
4.3.3 Surface Chemistry Modifications .....	88
4.3.4 Solution Preparation .....	90
4.3.5 Experimental Setup and Data Collection.....	90
4.3.6 Data Analysis.....	91
4.4 Results and Discussion .....	92
4.4.1 Design and Fabrication of Bimetallic Nano-Square Sensors .....	92
4.4.1.1 Determination of Periodicity .....	92
4.4.1.2 Fabrication and Alignment .....	93
4.4.1.3 Effect of Al-Au Nanostructure Distance for Bimetallic Array.....	94
4.4.1.4 Transmission Response of Bimetallic Array .....	96
4.4.1.5 Analysis of Surface Chemistries.....	96
4.4.2 Organic Solvent Differentiation .....	98
4.4.3 Whisky Differentiation .....	103
4.4.3.1 Monometallic Sensor Array v. Bimetallic Sensor Array.....	103
4.4.3.2 Analysis of 10 Bimetallic Sensor Arrays.....	109
4.5 Conclusion and Future Work.....	113
4.6 References.....	113
Chapter 5: Plasmonic Nano-Apertures as Dual-State, Nanopixels for High-Density Micro-Image Encoding .....	118

*Table of Contents*

5.1 Introduction.....	118
5.2 Materials .....	119
5.3 Methods .....	119
5.3.1 Fabrication of Nano-Aperture Arrays.....	119
5.3.2 Optical Image Capturing.....	119
5.3.3 Optical Transmission Spectra .....	120
5.3.4 Angled Measurements .....	120
5.3.5 FDTD Simulations.....	120
5.4 Results and Discussion .....	120
5.4.1 FDTD Simulations of Nano-Pixel Design.....	120
5.4.2 Fabricated Nano-Pixels.....	123
5.4.3 Analysis of the Nano-Pixel Colour Palette Spectrum.....	125
5.4.4 Nano-Pixels for Dual-Image Printing and Encoding.....	127
5.4.5 Angle-Dependence of Nano-Pixel.....	131
5.5 Conclusion and Future Work.....	134
5.6 References.....	135
Chapter 6: Preliminary Work: Dual-State SIBA/FRET Trap for the Study of Individual Proteins .....	139
6.1 Introduction.....	139
6.3 Materials .....	140
6.4 Methods .....	141
6.4.1 Fabrication of Nano-Aperture Arrays.....	141
6.4.2 Optical Transmission Spectra .....	141
6.4.3 Single-Photon Detection Setup.....	141
6.5 Results and Discussion .....	142
6.5.1 Design and Fabrication for the SIBA Arm.....	142
6.5.2 Fluorescent Marker Selection for FRET.....	145
6.5.3 Design for the FRET-Enhancing Arm.....	147
6.6 Conclusion and Future Work.....	147
6.7 References.....	148
Chapter 7: Conclusion .....	150
References.....	152
Publications.....	153
Conference Presentations/Proceedings .....	153

## List of Tables

Table 3.1: Noise-level, limit of detection, and limit of quantification for CPR and the corresponding RI values.....	78
Table 4.1: Solutions tested in the whisky tongue.....	90
Table 4.2: Example table of the data analysed for organic solvent differentiation and whisky differentiation.....	91
Table 4.3: Coefficients for the first, second, and third principal components of the monometallic and bimetallic whisky tongues (using the full tongue arrays consisting of all 6 and all 3 sensing regions, respectively).....	107
Table 4.4: Classification accuracy from LDA using leave-one-out cross validation to test accuracy.....	113

## List of Figures

Figure 1.1: SPR propagation and dispersion curve .....	16
Figure 1.2: Prism coupling configurations for SPP .....	17
Figure 1.3: Schematic of the localised surface plasmon resonance (LSPR). .....	18
Figure 1.4: Rendering of nanostructure arrays .....	23
Figure 1.5: Extraordinary light transmission diagram.....	24
Figure 2.1: Yee Lattice diagram .....	35
Figure 2.2: Schematic of e-beam lithography tool and vector scanning .....	37
Figure 2.3: Scattering of electrons by resist and substrate. ....	38
Figure 2.4: SEM images of alignment markers using geometric squares and correlation Penrose patterns .....	39
Figure 2.5: Schematic of e-beam-lithography-mediated metal fabrication steps .....	43
Figure 2.6: Schematic of silicon nitride micro-region fabrication process .....	45
Figure 2.7: Schematic of HSQ micro-region layer fabrication process.....	47
Figure 2.8: Schematic of the nanoaperture fabrication process.....	48
Figure 2.9: Schematic of a double-beam UV-VIS-NIR spectrophotometer.....	51
Figure 2.10: Microspectrophotometer optical diagram and photograph. ....	52
Figure 2.11: Determination of the transmission trough using MATLAB .....	53
Figure 2.12: CIE 1931 chromaticity diagram .....	55
Figure 3.1: FDTD simulation schematic for optimisation of the nitride encapsulated layer of the device .....	63
Figure 3.2: FDTD simulation schematic of the full multilayered device .....	64
Figure 3.3: FDTD Simulation for silicon nitride thickness .....	66
Figure 3.4: FDTD of electric field for 100 nm x 100 nm x 50 nm Au nanostructure with 100 nm nitride deposited on top.....	67

Figure 3.5: FDTD simulation of the effect of altering the distance between two gold nanostructure array layers .....	68
Figure 3.6: Analysis of device fabrication using a silicon nitride encapsulated layer .....	69
Figure 3.7: Surface planarisation by HSQ .....	71
Figure 3.8: Schematic and SEM/AFM images of multilayered sensing device .....	72
Figure 3.9: Silicon nitride deposition effect on the plasmonic response .....	73
Figure 3.10: Corrected Position Response (CPR) .....	74
Figure 3.11: Experimental data from multi-layered device .....	76
Figure 3.12: Real-time response of sensor to changes in refractive index .....	77
Figure 3.13: Real-time biosensing of the biotin-avidin interaction .....	79
Figure 3.14: FDTD simulation of the multilayered device .....	82
Figure 4.1: Surface chemistry diagram .....	89
Figure 4.2: FDTD simulation of different periodicities between Al and Au nanostructures in bimetallic arrays .....	93
Figure 4.3: SEM of monometallic and bimetallic sensors .....	94
Figure 4.4: FDTD simulation of effect on electric field by changes to distance between Al and Au nanostructures in a bimetallic array .....	95
Figure 4.5: Schematic, bright field microscopy image, SEM image and transmission response of a bimetallic plasmonic device .....	96
Figure 4.6: The effect of surface chemistry on transmission .....	97
Figure 4.7: Comparison of the effect of surface chemistry on sensitivity of sensors consisting of (a) monometallic and (b) bimetallic Au and Al nanoarrays .....	99
Figure 4.8: PCA for organic solvent differentiation using mono- and bimetallic sensors .....	100
Figure 4.9: 3D PCA for organic solvent differentiation .....	101
Figure 4.10: PCA for organic solvent differentiation using bimetallic sensor regions .....	102
Figure 4.11: 2D PCA for whisky differentiation .....	105
Figure 4.12: 3D PCA for whisky differentiation .....	105
Figure 4.13: PCA scree plots from (a) mono- and (b) bimetallic tongues for whisky differentiation .....	106
Figure 4.14: LDA classification of whisky using (a) mono- and (b) bimetallic tongue devices .....	108
Figure 4.15: PCA plots for 11 whisky tongues .....	110
Figure 4.16: Scree plots for 11 whisky tongues .....	111
Figure 4.17: LDA for 11 whisky tongues .....	112
Figure 5.1: FDTD simulation of nano-pixel electric field .....	121
Figure 5.2: FDTD simulation of nano-pixel arm-length and periodicity .....	122
Figure 5.3: Effects of etching .....	125
Figure 5.4: Nano-pixel properties .....	126
Figure 5.5: Bright-field microscope images showing the switchable nature of the information displayed by a single set of nano-pixels .....	128
Figure 5.6: Bright-field microscope images showing the smallest discernible pixel array size by standard microscopy .....	129
Figure 5.7: Bright-field and SEM images of a switchable QR-code .....	130

*List of Figures*

Figure 5.8: Angle-dependence response for long-arm nano-pixels..... 132  
Figure 5.9: Angle-dependence response for short-arm nano-pixels ..... 133  
Figure 5.10: Bright-field microscope images showing the incident light angle-dependence  
for switchable information displayed by a single set of nano-pixels..... 134

Figure 6.1: Optical diagram of single-photon detection setup. .... 142  
Figure 6.2: Colour Palette from Chapter 5 ..... 143  
Figure 6.3: Transmission and Single-Photon Detection of Preliminary Devices ..... 144  
Figure 6.4: Normalised excitation/emission for Cy3B and Alexa Fluor 594 ..... 146  
Figure 6.5: Transmission of Selected Nano-Pixels for Alexa Fluor 594 Emission..... 147

## Acknowledgements

I would like to begin by thanking my supervisors Dr. Alasdair W. Clark and Dr. Steven L. Neale for their continued professional and personal support throughout this process. It has been a pleasure working with both of you, and I appreciate the opportunity.

I would also like to thank Dr. Gerard Macias, Dr. Esmaeil Heydari, Dr. Julien Reboud, Dr. Manlio Tassieri, Dr. William A. Peveler, Professor Jonathan M. Cooper, and Dr. Andrew Glidle for their input and guidance. A special thanks also goes to the JWNC staff for all their hard work and support. The work outlined in this thesis would not have been possible without them.

To Dr. Maria Dienerowitz, Dr. Michael Börsch, and the team at Universitätsklinikum Jena, it was fantastic getting to work with you. Thank you for your scientific input and for hosting me in Jena.

I would also like to thank the Bill and Margaret Nicol Trust for awarding me the Bill Nicol Engineering Scholarship and the Royal Society of Edinburgh for awarding me the J.M. Lessell's Travel Scholarship in Engineering. Both these awards assisted me in my studies and research, and I am truly grateful for their support.

Finally, I would like to thank my family back in the US for the support they have given me throughout my PhD (and their patience with me). Being so far away with a huge time difference has been tough, but you've always been there for me no matter the time of day (or night).

## Author's Declaration

'I declare that, except where explicit reference is made to the contribution of others, this thesis is the result of my own work and has not been submitted for any other degree at the University of Glasgow or any other institution.'

Signed: \_\_\_\_\_

Date: \_\_\_\_\_

Justin Ryan Sperling  
University of Glasgow

## Chapter 1: Introduction and Theory

### 1.1 Introduction

This Chapter briefly describes the theory behind and reviews applications of the interaction between light and metal at the nanoscale. These interactions are the underlying phenomena that drive the technology presented in this thesis. An overview of surface plasmon resonance (SPR), localised surface plasmon resonance (LSPR), extraordinary transmission (EOT) of light, and applications of these phenomena as sensors and colour image displays are introduced.

### 1.2 Plasmonics

Plasmonics is the field of science dedicated to the study of the oscillations of mobile conduction electrons in materials, like noble metals, with fixed positive ion cores. When electromagnetic (EM) radiation interacts with these free charges, a variety of effects can occur depending on the frequency of the interacting photons [1-3]. As EM radiation approaches the near-infrared to visible (NIR-VIS) range of the spectrum, when coupled, it begins to interact with the mobile conduction electrons of metals. This interaction creates a resonant condition for the free electrons. There are two kinds of plasmonic resonance—surface plasmon resonance (SPR) and localised surface plasmon resonance (LSPR)—both of which will be discussed in Chapter 1.2.2. The dispersive properties of this resonance can be described by a complex dielectric function  $\epsilon_m(\omega)$  [3]. To properly understand this phenomenon, the dielectric function of metals will first be derived.

#### 1.2.1 Derivation of the Dielectric Function of Metals

In this section, the dielectric function of metals will be derived from Maxwell's Equations and the Plasma Model.

##### *1.2.1.1 Maxwell's Equations*

The complex dielectric properties of metals and their subsequent interactions with the EM spectra are defined by the differential forms of Maxwell's equations of macroscopic electromagnetism [3].

These four equations are given by Gauss's law for electricity:

$$\nabla \cdot \mathbf{D} = \rho_{ext}, \quad (1.1a)$$

Gauss's law for magnetism:

$$\nabla \cdot \mathbf{B} = 0, \quad (1.1b)$$

Faraday's law of induction:

$$\nabla \times \mathbf{E} = -\frac{\partial \mathbf{B}}{\partial t}, \quad (1.1c)$$

and Ampere's law:

$$\nabla \times \mathbf{H} = \mathbf{J}_{ext} + \frac{\partial \mathbf{D}}{\partial t} \quad (1.1d)$$

where  $\mathbf{D}$  is the dielectric displacement,  $\rho_{ext}$  is the external charge density,  $\mathbf{B}$  is the magnetic induction,  $\mathbf{E}$  is the electric field,  $\mathbf{H}$  is the magnetic field, and  $\mathbf{J}_{ext}$  is the external current density. The total current and charge densities ( $\mathbf{J}_{total}$ ,  $\rho_{total}$ ) are the sum of the external ( $\mathbf{J}_{ext}$ ,  $\rho_{ext}$ ) and internal ( $\mathbf{J}$ ,  $\rho$ ) densities.

For linear, isotropic, and nonmagnetic media, the following relations apply:

$$\mathbf{D} = \epsilon_0 \mathbf{E} + \mathbf{P} \quad (1.2a)$$

$$= \epsilon_m \epsilon_0 \mathbf{E} \quad (1.2b)$$

$$\mathbf{B} = \mu_m \mu_0 \mathbf{H} = \mu_0 \mathbf{H} \quad (1.3)$$

$$\mathbf{J} = \sigma \mathbf{E} \quad (1.4)$$

where  $\mathbf{P}$  is polarisation,  $\sigma$  is conductivity,  $\epsilon_0$  is the electric permittivity of vacuum,  $\epsilon_m$  is the relative permittivity (or dielectric value) of the medium,  $\mu_0$  is the magnetic permeability of vacuum, and  $\mu_m$  is the relative permeability of the medium (for nonmagnetic media,  $\mu_m = 1$ ) [3]. From these equations, it can be seen that defining  $\epsilon_m$  in terms of frequency would provide a dielectric function of the material (in this case, metal).

### 1.2.1.2 Plasmon Resonance and the Plasma Model

After defining and relating Maxwell's equations of macroscopic electromagnetism, the next step is to connect them to the plasma model of electronic conduction. In the plasma model, metals consist of a plasma of  $n$  freely moving electrons surrounding a positive ion core [1, 3-4]. An applied electromagnetic field  $\mathbf{E}$  disrupts the electrons and causes them to oscillate with motion  $\mathbf{x}$ . By free movement and collisions in the plasma, the electrons eventually restore to their equilibrium states.

The plasma model assumes aspects of the band structure of electrons are incorporated in the optical mass ( $m$ ) of each electron, rather than considering lattice potential and electron-electron interactions [3]. The motion of an electron disrupted by an external electric field  $\mathbf{E}$  can thus be defined by:

$$m \frac{\partial^2 \mathbf{x}}{\partial t^2} + m \frac{\partial \mathbf{x}}{\partial t} \gamma = -e \mathbf{E} \quad (1.5)$$

where  $e$  is electron charge and  $\gamma$  is the collision frequency of the free electron gas (which is about 100 THz at room temperature) [3].

A harmonic external electric field  $\mathbf{E}$  with frequency  $\omega$  (defined by the time-domain equation  $\mathbf{E}(t) = \mathbf{E}_0 e^{-i\omega t}$ ) will oscillate an electron with the same frequency (defined by the time-domain equation  $\mathbf{x}(t) = \mathbf{x}_0 e^{-i\omega t}$ ). Substituting these time-domain equations into **Equation 1.5** yields:

$$\mathbf{x}(t) = \frac{e}{m(\omega^2 + i\gamma\omega)} \mathbf{E}(t) \quad (1.6)$$

which defines electron oscillation with relation to the incident electric field.

To relate the electron displacement back to Maxwell's equations, the relationship between polarisation  $\mathbf{P}$  and displacement  $\mathbf{x}$  must be defined. From a macroscopic approach, it is  $\mathbf{P} = -n e \mathbf{x}$ . Thus, the macroscopic polarisation  $\mathbf{P}$  by electric field  $\mathbf{E}$  is:

$$\mathbf{P} = -\frac{ne^2}{m(\omega^2+i\gamma\omega)}\mathbf{E} \quad (1.7)$$

Inserting this into **Equation 1.2a**:

$$\mathbf{D} = \varepsilon_0\left(1 - \frac{ne^2}{\varepsilon_0m(\omega^2+i\gamma\omega)}\right)\mathbf{E} \quad (1.8)$$

### 1.2.1.3 Dielectric Function of Metals

Comparing **Equation 1.2b** with **Equation 1.8**, the dielectric function of metals  $\varepsilon_m(\omega)$  is:

$$\varepsilon_m(\omega) = 1 - \frac{ne^2}{\varepsilon_0m(\omega^2+i\gamma\omega)} \quad (1.9)$$

For a given metal, the term  $\frac{ne^2}{\varepsilon_0m}$  is a constant defined as the material dependent plasmon frequency  $\omega_p$  given by the relationship: [3]

$$\omega_p^2 = \frac{ne^2}{\varepsilon_0m} \quad (1.10)$$

which alters **Equation 1.8** to:

$$\mathbf{D} = \varepsilon_0\left(1 - \frac{\omega_p^2}{(\omega^2+i\gamma\omega)}\right)\mathbf{E} \quad (1.11)$$

and **Equation 1.9** to:

$$\varepsilon_m(\omega) = 1 - \frac{\omega_p^2}{(\omega^2+i\gamma\omega)} \quad (1.12)$$

**Equation 1.12** is known as the Drude Model [3, 5]. Splitting  $\varepsilon_m(\omega)$  into its real and imaginary components defined as  $\varepsilon_1$  and  $i\varepsilon_2$ , respectively, gives:

$$\varepsilon_1 = 1 - \frac{\omega_p^2}{(\omega^2+\gamma^2)} \quad (1.13a)$$

$$\varepsilon_2 = \frac{\omega_p^2\gamma}{\omega(\omega^2+\gamma^2)} \quad (1.13b)$$

The real part  $\epsilon_1$  refers to the magnitude of polarisation [3, 5-7], and the imaginary part  $\epsilon_2$  refers to a phase-shift delay in dielectric response [3, 5-7]. For bulk plasmas, EM radiation below and above  $\omega_p$  are reflected and transmitted, respectively [2, 6, 8]. Both planar surfaces and nanoparticles of plasmonic-supporting materials exhibit surface plasmon resonance modes and will be discussed in the following section.

### 1.2.2 Propagating and Localised Plasmon Resonance

Depending on the dimensions of the material, the plasmon resonance can propagate or remain localised. The propagation of the plasmon resonance along the surface and surrounding dielectric interface of a bulk metal material is called SPR [3]. When the metal material has nano-scale dimensions with sizes at or below that of the excitation EM wavelength, the SPR becomes localised around the nanostructure—hence termed LSPR [3].

#### 1.2.2.1 Surface Plasmon Resonance (SPR)

The simplest geometry supporting SPR is a single flat metal-dielectric interface [3]. In **Figure 1.1a**, SPR propagations occur along the plasmonic material surface (x-axis) and are known as surface plasmon polaritons (SPP) [2-3, 5, 9]. The distance of the SPP in the x- and y-directions is determined by the geometry and absorption of the material [2-3, 5, 9].

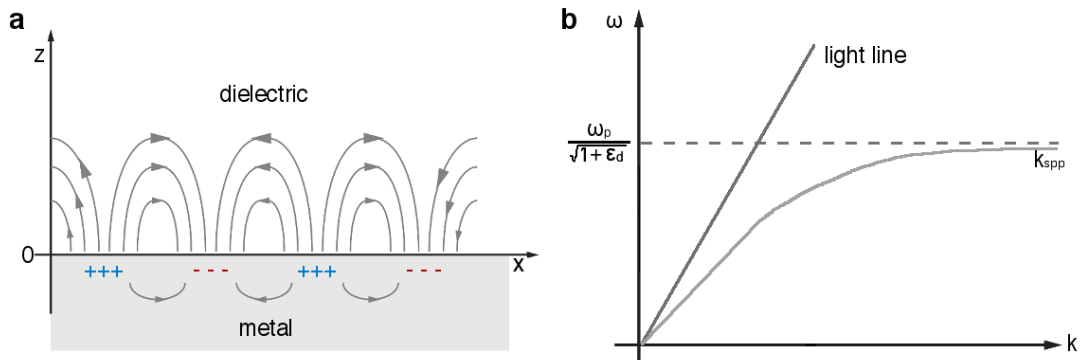


**Figure 1.1: SPR propagation and dispersion curve. (a)** The SPR propagates along the x-axis and is called a surface plasmon polariton (SPP). The dielectric-metal boundary is at  $z = 0$ , where  $z > 0$  is the dielectric and  $z < 0$  is the metal. This figure is from [2]. **(b)** Dispersion curve of SPR, where  $\omega_p$  is the plasma frequency of free electrons in the metal.

SPP is characterised in terms of its dispersion. The dispersion of SPPs propagating at the interface between a single flat metal and dielectric is given by the wavevector of the surface plasmon ( $k_{SPP}$ ):

$$k_{SPP} = k_0 \sqrt{\frac{\epsilon_m \epsilon_d}{\epsilon_m + \epsilon_d}} \quad (1.14)$$

where  $\epsilon_d$  is the real part of the dielectric ( $z > 0$ ),  $\epsilon_m$  is the dielectric of the metal ( $z < 0$ ), and  $k_0$  is the free-space wavevector ( $k_0 = \frac{\omega}{c}$ ) [3]. As mentioned previously, the metal dielectric constant  $\epsilon_m$  is defined by a frequency-dependent equation. When the frequency of the SPP approaches the value  $\frac{\omega_p}{\sqrt{1+\epsilon_d}}$  (which is called the surface plasmon frequency and denoted by  $\omega_{SPP}$ ),  $k_{SPP}$  approaches infinity. When the frequency approaches zero,  $k_{SPP}$  approaches  $k_0 \sqrt{\epsilon_d}$  (which is called the dielectric light line) [3]. The dispersion curve for SPP is show in **Figure 1.1b**.

**Equation 1.14** indicates two things: (1) SPP may exist over a wide range of  $\omega$ , and (2) For freely propagating light, the wavevector of the SPP mode is always greater than that of the light in the dielectric region. This means that freely propagating light is unable to couple to the SPP modes. Therefore, to couple light to the SPP node, a prism or Bragg scattering block is needed [3, 5]. Effectively, a prism creates a ‘sandwiching’ of the metal between two media with different dielectric values, where the prism has the higher dielectric value, resulting in total internal reflection. A beam reflected at the interface of the higher dielectric constant, and the metal will have enough momentum to excite SPP mode at the interface between the metal and the lower dielectric medium.

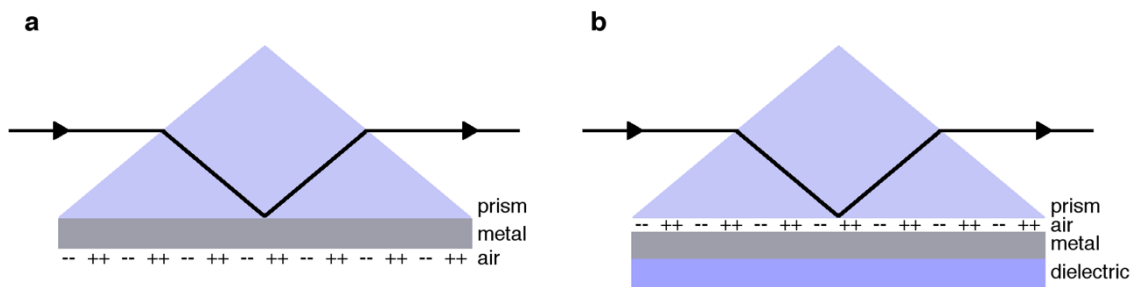


**Figure 1.2: Prism coupling configurations for SPP.** (a) The Kretschmann configuration [10] has direct contact between the metal and the prism. (b) The Otto configuration [11] has a thin air-gap between the prism and the metal. Both configuration cause total internal reflection and give rise to the momentum necessary to achieve SPP. The black arrow in both (a) and (b) represents EM radiation (light)

The two most-common configurations for this coupling are the Kretschmann [10] and the Otto [11] configurations. To achieve the necessary momentum of light, the Kreschmann

configuration (**Figure 1.2a**) uses a thin layer of metal evaporated directly onto the prism, and the Otto configuration (**Figure 1.2b**) uses a thin air-gap between the metal and prism.

The  $x$ - and  $y$ - propagation of SPP is on the order of tens to hundreds of microns along the interface between the metal and the dielectric; the  $z$ -direction, however, yields an exponential decay circa 200 nm [2]. For prism-coupled SPR, thickness of the metallic layer is very important [12]. Too thin a layer results in a decrease in sensitivity to reflectance changes (a broadening of the response curve) and too thick a layer narrows the linear range (a shallowing and thinning of the response curve) [13].

Additionally, a periodic nano-aperture array (NAA) in a thin metal film can be used to excite SPR modes by acting as a two-dimensional grating. Chapter 1.2.4.2 will discuss NAA in detail.

### 1.2.2.2 Localised Surface Plasmon Resonance (LSPR)

When EM radiation interacts with particles of a plasmon-supporting material that are much smaller than the incident wavelength of light, the electrons in the conduction band of the nanoparticle interact with the oscillating EM field (**Figure 1.3**) [2].

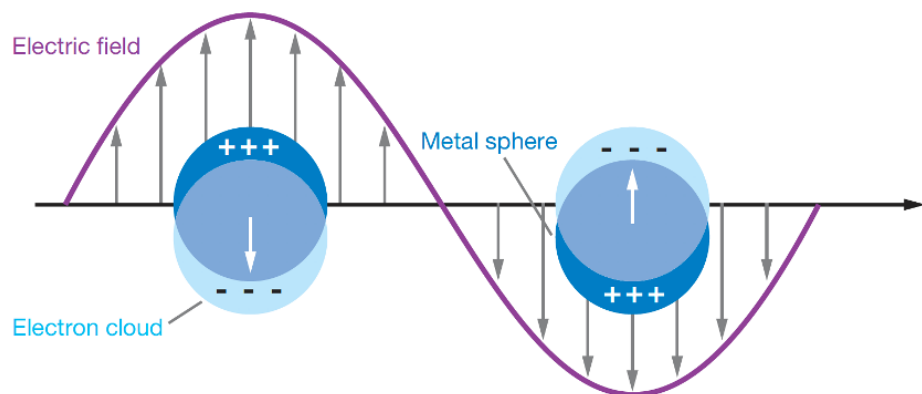


**Figure 1.3: Schematic of the localised surface plasmon resonance (LSPR).** The oscillating EM field displaces the free electrons surrounding the ion core of the nanoparticles, giving rise to a localised plasmon resonance at the surface of the nanostructures. This figure is from [2].

The dislocation and restoration of the electrons effectively makes the nanoparticle a dipole. When the frequency of the exciting EM field matches the natural resonant oscillatory frequency of the nanoparticle, LSPR occurs. In LSPR, the oscillations are confined to the nanoparticle and arise without the need of a mode-coupling dielectric material. The

interaction between the conduction electrons and the incident EM field results in the enhancement of the oscillations of the electrons around their fixed ion core, creating oscillations with higher energy than the incident EM field and resulting in preferential absorption and scattering of different wavelengths of light [5-6, 8]. Compared to SPR, the decay length of LSPR from the metal surface is much shorter, on the orders of tens of nanometers [14].

For a nanoparticle with a size much less than the incident excitation wavelength, a quasistatic approximation can be made because the phase of the EM wave is effectively constant over the entire particle. Using this approximation, the polarisability of the nanoparticle approximately has a dipole moment  $\mathbf{p}$  given by:

$$\mathbf{p} = \epsilon \epsilon_0 \alpha \mathbf{E} \quad (1.15)$$

where  $\alpha$  is the polarisability of the particle [3]. Assuming the collective response of the nanoparticle is uniform across the nanoparticle, the dipolar quasistatic approximation of polarizability of the metal nanoparticle is [7]:

$$\alpha = (1 + \kappa) \epsilon_0 V \frac{\epsilon_m - \epsilon_d}{\epsilon_m + \kappa \epsilon_d} \quad (1.16)$$

where  $V$  is the volume of the particle,  $\kappa$  is the shape factor that incorporates the dependence of polarisability on geometry of the surface that defines the electron oscillations,  $\epsilon_d$  represents the dielectric function of the surrounding dielectric medium, and  $\epsilon_m$  represents the dielectric function of the metal. By **Equation 1.16**, it is clear that the polarizability is highly sensitive to size, shape, and material of the particle and the local environment surrounding it. Larger particles have a bigger polarizability and display stronger LSPR.

Resonance is achieved when  $\alpha$  is maximised, which occurs when  $\epsilon_m + \kappa \epsilon_d$  is minimised. In this instance, the resonance can be simplified to the Fröhlich condition [7] given by:

$$\text{Re}[\epsilon_m] = -\kappa \epsilon_d \quad (1.17)$$

For further simplification, a spherical particle with radius  $R$  ( $\kappa = 2$ ,  $V = R^3\pi\frac{4}{3}$ ) [6] will be considered because it sufficiently details some important characteristics of LSPR. For a spherical particle, **Equation 1.16** and **Equation 1.17** become:

$$\alpha = 4\pi R^3 \frac{\varepsilon_m - \varepsilon_d}{\varepsilon_m + 2\varepsilon_d} \quad (1.18a)$$

$$\text{Re}[\varepsilon_m] = -2\varepsilon_d \quad (1.18b)$$

As a spherical particle increases in size beyond the limit where the quasistatic approximation can be used ( $R > 50$  nm), things ignored by the approximation, such as interband transitions, become more pronounced and the size of the particle has more effect on plasmonic frequency. Increases to the size of the nanoparticle typically results in a redshift in the plasmon resonance frequency.

As mentioned, the oscillations of the bulk plasmon of the metal create a dipole. This dipole is able to induce an electric potential distinct from that of the applied electric field, which is known as photonic excitation.

The near-field strength of LSPR can be mathematically understood by the polar form of the electric field strength ( $\mathbf{E}_{LSPR}$ ). For a spherical particle, this is given by:

$$\mathbf{E}_{LSPR} = E_0 \cos \theta + \frac{E_0 R^3 \cos \theta}{r^3} \left( \frac{\varepsilon_m - \varepsilon_d}{\varepsilon_m + 2\varepsilon_d} \right) \quad (1.19)$$

where  $E_0$  is the electric field strength of the light source,  $\cos \theta$  is the direction of light polarisation,  $r$  is the radial distance from the particle [3]. As can be seen by **Equation 1.19**, the induced electric field and electromagnetic field enhancement decay as  $1/r^3$  with distance from the surface of the nanoparticle.

Another way to determine the LSPR of particles is by their efficiency to scatter and absorb light. The scattering and absorption cross sections of a nanoparticle are derived using a time-averaged Poynting vector expression [3-4]. Using a spherical assumption, the scattering cross section ( $\sigma_{sca}$ ) and absorption cross section ( $\sigma_{abs}$ ) are given by:

$$\sigma_{sca} = \frac{8\pi}{3} f^4 r^6 \left| \frac{\varepsilon_m - \varepsilon_d}{\varepsilon_m + 2\varepsilon_d} \right|^2 \quad (1.20a)$$

$$\sigma_{abs} = 4\pi f r^3 \text{Im} \left[ \frac{\varepsilon_m - \varepsilon_d}{\varepsilon_m + 2\varepsilon_d} \right] \quad (1.20b)$$

where  $f = 2\pi/\lambda$  [3-4]. The scattering and absorption cross sections quantify the radiative and non-radiative transfer processes involved in LSPR, respectively. From **Equation 1.20a** and **Equation 1.20b**, it is observed that for small particles absorption dominates and scattering becomes more important as the particles' size increases.

The sum of the scattering and absorption cross sections quantify the total energy transfer process in LSPR. This sum represented by the extinction cross section ( $\sigma_{ext}$ ) [3-4]

$$\sigma_{ext} = \sigma_{sca} + \sigma_{abs} \quad (1.21)$$

The extinction cross section is also derived via a time-average Poynting vector expression [3-4]. Using a spherical assumption, the extinction cross section ( $\sigma_{ext}$ ) is:

$$\sigma_{ext} = 9 \frac{\omega}{c} \varepsilon_d^{3/2} V \frac{\varepsilon_2}{(\varepsilon_1 + 2\varepsilon_d)^2 + \varepsilon_2^2} \quad (1.22)$$

where  $V$  is the volume of the sphere and  $\varepsilon_1$  and  $\varepsilon_2$  are the respective real and imaginary parts of the complex dielectric function of the metal as defined by **Equation 1.13a** and **Equation 1.13b**.

The proximity of other plasmonic structures can also affect the LSPR [3-6, 8, 15-16]. When two plasmonic structures are separated by a very small distance, coupling of the LSPR between the two nanoparticles occurs. The response of the shift depends on the polarisation of the particles [3-6, 8, 15-16]. Regardless of the surrounding medium, particle shape, metal composition, and diameter, plasmonic nanoparticles exhibit a near-field coupling strength  $\Delta\lambda/\lambda$  and falls almost exponentially over a distance of about 0.2 times the particle diameter as governed by **Equation 1.23** [6]

$$\frac{\Delta\lambda}{\lambda} = p e^{-\frac{s}{0.2D}} \quad (1.23)$$

where  $s/D$  is the interparticular gap ( $s$ ) normalized by the particle size ( $D$ ) and  $p$  is the maximum plasmon shift for a particle pair depending on composition, environment, shape, etc.

In summary, LSPR is highly sensitive to the local environment (the surrounding substrate on which it is built and the medium which surrounds it) [3-4, 16-17], nanoparticle geometry (size, shape, and surface roughness) [2-5, 15, 18-21], proximity to nearby nanoparticles [3-6, 8, 15-16], and nanoparticle material composition [2-3, 5-6, 18, 22], making nanoplasmonic structures highly tuneable to interact with wavelengths throughout the VIS-NIR spectrum and highly useful for sensing applications.

### 1.2.3 Appropriate Metals

The free electrons and complex permittivity of metals make them ideal for use as surface plasmon resonant materials [5, 8]. Silver (Ag) has the lowest intrinsic losses through intraband excitations [23] in the visible range of the EM spectrum and has been used in a variety of applications [2]. However, its high likelihood to oxidise and corrode makes it difficult for long-term use and biological applications [24]. Gold (Au) is much more chemically and physically stable than Ag (and also offers very low intrinsic losses through intraband excitations) [23]. Au is also highly compatible with biological samples. However, its use is often limited by its expense and significant optical loss below 600 nm wavelengths [23]. Aluminium (Al) is able to be tuned across the UV-VIS-NIR spectrum [23, 25-26] and is much cheaper than the aforementioned materials. Unlike Ag, Al forms a self-protecting oxidising layer which makes it more stable than Ag.

In this thesis, Au was chosen to build self-referencing sensors demonstrated for biological sensing applications, both Au and Al were chosen for use as bimetallic sensors for mixture discrimination, and Al was chosen to make plasmonic nano-pixels for high-density optical image-encoding. The two types of plasmonic structure arrays fabricated from these metals were nano-particle arrays (NPA) and nano-aperture arrays (NAA).

### 1.2.4 Types of Nano-Plasmonic Structures

**Figure 1.4** shows the difference between these types of nanostructures. NPAs typically act as band-stop filters where they have high transmission across most wavelengths and attenuate the signal at their plasmonic peaks. NAAs, on the other hand, typically act as band-

pass filters where they only have high-transmission at their plasmonic peak. Applications of nanostructure arrays will be discussed in Chapter 1.3.

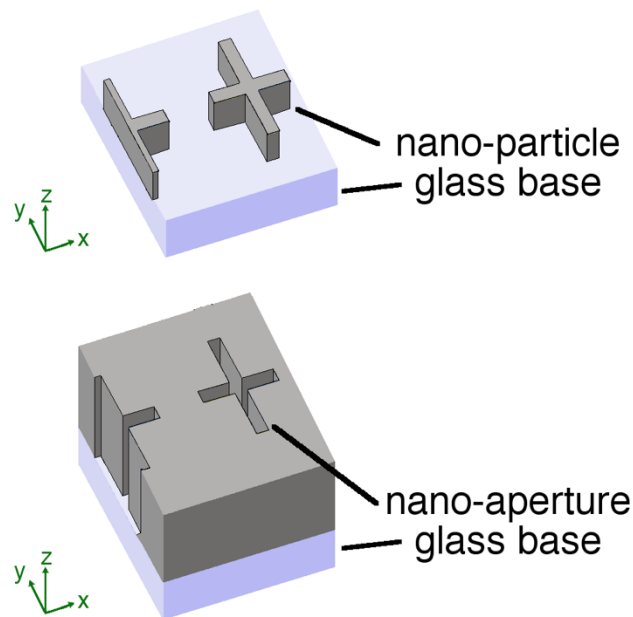


**Figure 1.4: Rendering of nanostructure arrays.** The nanostructure arrays in this thesis consisted of (top) positive nanostructures referred to as nano-particles and (bottom) negative nanostructures referred to as nano-apertures.

#### 1.2.4.1 Nanoparticle Array (NPA)

NPAs are governed by LSPR. These types of arrays can be fabricated from either a bottom-up or top-down approach. Bottom-up processes typically involve direct chemical synthesis that produces metal nanoparticles [5]. Whereas top-down approaches involve using expensive equipment, such as electron-beam lithography or focused ion-beam milling, to produce nanostructures in ordered arrays [5]. Bottom-up approaches do not require highly expensive equipment and can produce nanoparticles quite quickly, whereas top-down approaches are much better at making consistent, ordered array patterns at arbitrary size, shape, and complexity. In this thesis, the top-down electron-beam lithography approach was used because high-resolution and ordered nanostructure arrays with good reproducibility were desired.

#### 1.2.4.2 Nano-Aperture Array (NAA) and Extraordinary Transmission (EOT) of Light

NAAs are governed by SPR and the phenomenon known as extraordinary transmission (EOT) of light. Classic theory states that when plane wave light encounters a circular

aperture perforated into an optically opaque and perfectly conducting screen, the transmission  $T$  is proportional to radius  $R$  and wavelength  $\lambda$  [3]

$$T \propto \left(\frac{R}{\lambda}\right)^4 \quad (1.24)$$

**Equation 1.24** indicates a very weak total transmission as wavelength increases. However, for metals, this is not the case. In fact, subwavelength NAAs in thin metallic sheets allow transmittance per unit hole much higher (on the order of magnitudes) than that predicted by classic diffraction theory [27]. This ‘extraordinary light transmission’ arises from a combination of SPR and constructive interference [3, 28]. In other words, plasmonics provides the ability to overcome the diffraction limit of light, which is on the hundreds-of-nanometers-scale [5].

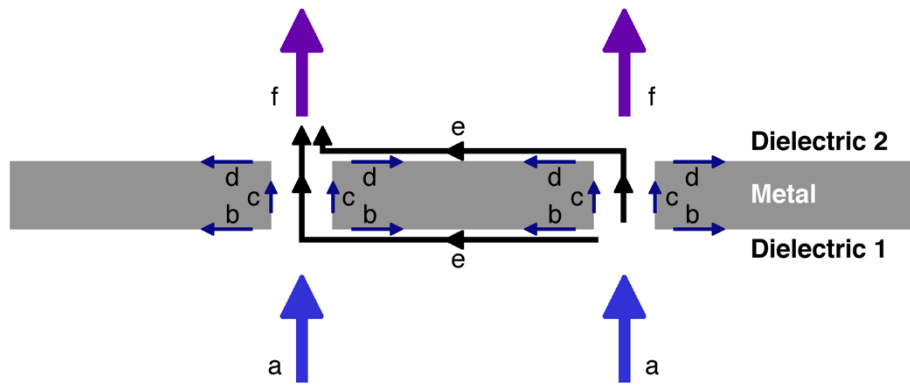


**Figure 1.5: Extraordinary light transmission diagram.** When (a) incident light hits the metal surface at the metal-dielectric-1 interface, a SPR wave arises that (b) propagates laterally along the metal-dielectric-1 interface, (c) tunnels vertically through the nano-aperture, and (d) propagates laterally along the metal-dielectric-2 interface. (e) Interference of the laterally propagating surface waves from neighbouring apertures occurs and affects (f) the radiant light from the decaying SPR that is observed as transmitted light.

**Figure 1.5** shows a diagram of the light coupling that arises from EOT. When (a) light encounters a periodic, subwavelength NAA in a metal structure, (b) SPR occurs laterally at the incident interface, (c) tunnels through the nano-aperture vertically, and (d) travels laterally along the backside interface. This generates (e) interference between the front and back SPR, producing (f) radiant photons. The dimensions of the apertures in a NAA determine the coupling wavelength and the periodicity of the NAA determines the interference between the front and back SPR. Both dimension and periodicity thus affect the observed transmitted light [3]. NAAs of circular shape [29-30], rectangular shape [31],

elliptical shape [32], and triangular bowtie shape [33] have all been demonstrated to produce different types of interference modes and patterns for EOT. As shapes become asymmetrical, polarisation-dependent modes arise in the EOT [34-35].

### 1.3 Applications of Plasmonics

A multitude of applications exist for plasmonic nanoarrays. For the purposes of this thesis and the work presented herein, the applications of plasmonic sensors and colour image displays will be briefly introduced.

#### 1.3.1 Plasmonic Sensors

The high-sensitivity to changes in the local environment and label-free detection capabilities of nanoplasmonic structures makes them a useful tool for chemical and biological sensing compared to other techniques [1, 4, 36-38]. For example, gold-standard biological detection techniques like enzyme-linked immunosorbent assays (ELISA) and molecular fluorophore-coupled polymerase chain reaction (PCR) are susceptible to photobleaching and contamination, have broad absorption/emission bands, and rely on relatively expensive equipment for detection that also hinders their portability. [1, 39] Additionally, the target antigen is often not directly detected but rather a secondary molecule is detected. [1] Plasmonic-based sensors, on the other hand, can be used for the direct detection of a target molecule, allowing for continuous, real-time measurements of binding kinetics. [1, 40] Changes in the refractive index of the surrounding environment produce a characteristic shift in the optical response [4]. The shift in optical response per refractive index unit (nm per RIU or  $\text{nm}\cdot\text{RIU}^{-1}$ ) is referred to as the bulk refractive index sensitivity and is used to compare plasmonic sensors to one another. The sensitivity range of plasmonic sensors depends highly on the nanostructure morphology, geometry, and close-proximity-coupling. It can typically range anywhere from  $90 \text{ nm}\cdot\text{RIU}^{-1}$  to  $1000 \text{ nm}\cdot\text{RIU}^{-1}$  [1, 36, 41-42]. The refractive index sensitivity, however, does not consider precision issues that arise when the line-width of the plasmonic peak is large. To account for both the refractive index sensitivity and the peak line-width of different sensors, a Figure of Merit ( $FoM$ ) [43] is used. The  $FoM$  is defined by the ratio of the refractive index sensitivity ( $m$ ) to the full-width half-max ( $FWHM$ ) of the peak:

$$FoM = \frac{m \text{ (nm}\cdot\text{RIU}^{-1}\text{)}}{FWHM \text{ (nm)}} \quad (2.25)$$

and can typically range anywhere from 0.8 to 5.4 [1, 36, 41-42].

Another advantage of plasmonic sensors is that their response, through modifications of the surface, can be tailored to specific analytes or events, such as protein-substrate binding [1, 4, 36, 44], antibody-antigen binding [42, 45-46], and DNA base pairing [36, 47-49]. Resonance shifts in plasmonic sensor can also occur from changes in the external environment such as temperature shifts and light-intensity fluctuations. To account for this, a reference is used to determine if a detected event is from a desired signal or some sort of drift [50].

Plasmonics has also been demonstrated as useful in optical sensor arrays due to their high stability, easy surface modification, and tuneable physiochemical properties [37]. Optical sensor arrays serve as excellent tools for the recognition and discrimination of a variety of liquid and gas mixtures by pattern-based recognition from signals across multiple sensing regions. As the use of optical sensor arrays progresses towards rapid, highly personalised diagnosis and component identification devices, plasmonic structure offer a label-free, highly stable, and reusable platform for each element of the array [37].

Further applications of plasmonic structures include their use as a means to simultaneously trap and sense individual molecules by techniques such as Self-Induced Back-Action [30, 33, 51]. Additionally, the highly-confined electric fields of the nanostructures can be used to enhance the spectroscopic sensing techniques of both Raman scattering [4] and fluorescence [1, 52]. These aforementioned applications are not covered in the scope of this thesis.

### 1.3.2 Coloured Image Displays

As shown mathematically in previous sections, plasmons can enhance and confine electric fields and preferentially scatter and absorb different wavelength of light. Thus, structures can be engineered to interact with white light such that they appear a particular colour. This has led to their research and development for applications in coloured image display, colour filtering, and optical image encoding [53]. The high-density capabilities and high-stability of plasmonic structures for colour applications offers advantages over using dyes and other organic pigments, which fade over time and have limitations to their resolution capabilities. Plasmonic colour filters based on positive nanostructures [54-61], filters based on nano-

apertures [29, 34, 62-64], and filters based on combinations of both of these designs [65-67] have been widely used for subwavelength colour printing [54-56, 58, 67-68], anti-counterfeiting measures [69-70], and red-green-blue splitting for image sensors [29, 63, 71-72].

## 1.4 Research Work Described Herein

The experimental work of this thesis explores the optical properties of periodic metal nanoarrays and their relative applications in optical sensing, display, and encoding. The research covered can be divided into three major areas: (1) development of a novel LSPR self-referencing sensor based on NPA, (2) development of a novel LSPR bimetallic optical sensor array based on NPA, and (3) development of highly-condensed, dual-state nano-pixel arrays (i.e. NAAs) for the all-optical encoding of two information states in the same space.

### 1.4.1 Development of a Novel LSPR Self-Referencing Sensor

As previously discussed in 1.3.1, plasmonic sensing applications have inherent advantages over other techniques. They also require a reference in order to detect a shift in signal and to determine if a signal detected arises from the desired event. For applications where only single measurements are taken, referencing can be done immediately prior to the measurement and the likelihood of signal drift is minimal. For applications where multiple measurements are taken in succession over an extended period of time, the initial reference may not be adequate as signal drift from baseline due to external factors, such as light intensity fluctuations, may occur [50]. While many different approaches have been made to produce self-referencing within the detection channel [50, 73-81], an approach using multiple layers of plasmonic NPA has yet to be explored. NPAs are ideal for this application because they inherently act as band-stop filters (as opposed to NAAs which act as bandpass filters). By working in this way, two layers with different plasmonic signal peaks can be utilised. Chapter 3 explores a proof-of-concept design for the utilisation of a multilayered, self-referencing NPA sensor.

### 1.4.2 Development of a Novel Bimetallic Optical Sensor Array

As also mentioned in 1.3.1, optical sensor arrays are powerful tools in differentiating between many different liquid and gas mixtures [37]. Compared to polymer and ligand-based counterparts which are one-time use, NPAs have been demonstrated in this field to be highly tuneable, reusable, and easily modified for specific sensor array applications [37].

However, as the use of optical sensor arrays progresses towards rapid, highly personalised diagnosis and component identification devices, reduction in complexity and data-acquisition time is key [37]. One way to achieve this is in the reduction of elements in the array without compromising the differential capabilities of the device. Given enough distance between individual components in NPAs, each metallic structure in the array can yield a response to the local environment independent to that of its neighbour. Therefore, combinations of different metal structures and surface chemistries within the same NPA can yield multiple, distinct signals from each element of the sensing array. Thus, using multiple metal structures in one region has the potential to reduce the number of elements in a sensor array while still providing the same amount of data necessary to allow for successful differentiation. Chapter 4 explores the use of a novel prototype device consisting of Au and Al NPAs with altered surface chemistries.

#### 1.4.3 Development of Dual-State Pixels for High-Density Optical Encoding

As reviewed in 1.3.2, nanostructures can be employed in a variety of applications where their high-tunability, high-stability, and age-longevity make them advantageous over standard dye and pigment techniques for creating images. In Chapter 5, a new approach to high-density image encoding, based on dual-state plasmonic pixels with polarisation-dependence, is demonstrated. While previous studies using plasmonics for colour display applications employed colour or position switching in fixed images [60, 82], these techniques only altered the colour of the same image or ‘hid’ the image. The design utilised here, on the other hand, shows two fully independent optical states of completely separate images and information states that can be encoded in the same single array of nano-pixels.

#### 1.5 References

- [1] Mayer, K. M.; Hafner, J. H. Localized Surface Plasmon Resonance Sensors. *Chem. Rev.* **2011**, *111* (6), 3828-3857, DOI: 10.1021/cr100313v.
- [2] Willets, K. A.; Van Duyne, R. P. Localized Surface Plasmon Resonance Spectroscopy and Sensing. *Annual Review of Physical Chemistry* **2007**, *58*, 267-297, DOI: 10.1146/annurev.physchem.58.032806.104607.
- [3] Maier, S. A. *Plasmonics: Fundamentals and Applications*, Springer Science+Business Media LLC: New York, 2007.
- [4] Langer, J.; Novikov, S. M.; Liz-Marzan, L. M. Sensing Using Plasmonic Nanostructures and Nanoparticles. *Nanotechnology* **2015**, *26* (32), DOI: 10.1088/0957-4484/26/32/322001.

- [5] Murray, W. A.; Barnes, W. L. Plasmonic Materials. *Advanced Materials* **2007**, *19* (22), 3771-3782, DOI: 10.1002/adma.200700678.
- [6] Jain, P. K.; El-Sayed, M. A. Plasmonic Coupling in Noble Metal Nanostructures. *Chem. Phys. Lett.* **2010**, *487* (4-6), 153-164, DOI: 10.1016/j.cplett.2010.01.062.
- [7] Kreibig, U.; Vollmer, M. *Optical Properties of Metal Clusters*, Springer: Berlin, 1995; Vol. 25.
- [8] Pelton, M.; Aizpurua, J.; Bryant, G. Metal-Nanoparticle Plasmonics. *Laser & Photonics Reviews* **2008**, *2* (3), 136-159, DOI: 10.1002/lpor.200810003.
- [9] Raether, H. Surface-Plasmons on Smooth and Rough Surfaces and on Gratings. *Springer Tracts Mod. Phys.* **1988**, *111*, 1-133.
- [10] Kretschmann, E.; Raether, H. Radiative Decay of Non Radiative Surface Plasmons Excited by Light. *Zeitschrift Fur Naturforschung Part a-Astrophysik Physik Und Physikalische Chemie* **1968**, *A 23* (12), 2135-&.
- [11] Otto, A. Excitation of Nonradiative Surface Plasma Waves in Silver by Method of Frustrated Total Reflection. *Zeitschrift Fur Physik* **1968**, *216* (4), 398-&, DOI: 10.1007/bf01391532.
- [12] Homola, J.; Yee, S. S.; Gauglitz, G. Surface Plasmon Resonance Sensors: Review. *Sens. Actuators, B* **1999**, *54* (1-2), 3-15, DOI: [https://doi.org/10.1016/S0925-4005\(98\)00321-9](https://doi.org/10.1016/S0925-4005(98)00321-9).
- [13] Ekgasit, S.; Thammacharoen, C.; Yu, F.; Knoll, W. Influence of the Metal Film Thickness on the Sensitivity of Surface Plasmon Resonance Biosensors. *Applied Spectroscopy* **2005**, *59* (5), 661-667.
- [14] Haes, A. J.; Zou, S.; Schatz, G. C.; Van Duyne, R. P. A Nanoscale Optical Biosensor: The Long Range Distance Dependence of the Localized Surface Plasmon Resonance of Noble Metal Nanoparticles. *J. Phys. Chem. B* **2004**, *108*, 109-116.
- [15] Liz-Marzan, L. M. Tailoring Surface Plasmons through the Morphology and Assembly of Metal Nanoparticles. *Langmuir* **2006**, *22* (1), 32-41, DOI: 10.1021/la0513353.
- [16] Malinsky, M. D.; Kelly, K. L.; Schatz, G. C.; Van Duyne, R. P. Nanosphere Lithography: Effect of Substrate on the Localized Surface Plasmon Resonance Spectrum of Silver Nanoparticles. *J. Phys. Chem. B* **2001**, *105* (12), 2343-2350.
- [17] Perez-Juste, J.; Pastoriza-Santos, I.; Liz-Marzan, L. M.; Mulvaney, P. Gold Nanorods: Synthesis, Characterization and Applications. *Coordination Chemistry Reviews* **2005**, *249* (17-18), 1870-1901, DOI: 10.1016/j.ccr.2005.01.030.
- [18] Haes, A. J.; Zou, S. L.; Schatz, G. C.; Van Duyne, R. P. Nanoscale Optical Biosensor: Short Range Distance Dependence of the Localized Surface Plasmon Resonance of Noble Metal Nanoparticles. *J. Phys. Chem. B* **2004**, *108* (22), 6961-6968, DOI: 10.1021/jp036261n.
- [19] Liz-Marzan, L. M.; Perez-Juste, J.; Pastoriza-Santos, I. Plasmonics of Gold Nanorods. Considerations for Biosensing. *Nanomaterials for Applications in Medicine and Biology* **2008**, 103-111, DOI: 10.1007/978-1-4020-6829-4\_9.
- [20] Pecharroman, C.; Perez-Juste, J.; Mata-Osoro, G.; Liz-Marzan, L. M.; Mulvaney, P. Redshift of Surface Plasmon Modes of Small Gold Rods Due to Their Atomic Roughness and End-Cap Geometry. *Physical Review B* **2008**, *77* (3), DOI: 10.1103/PhysRevB.77.035418.
- [21] Rodriguez-Fernandez, J.; Funston, A. M.; Perez-Juste, J.; Alvarez-Puebla, R. A.; Liz-Marzan, L. M.; Mulvaney, P. The Effect of Surface Roughness on the Plasmonic Response of Individual Sub-Micron Gold Spheres. *Physical Chemistry Chemical Physics* **2009**, *11* (28), 5909-5914, DOI: 10.1039/b905200n.

- [22] Knight, M. W.; King, N. S.; Liu, L.; Everitt, H. O.; Nordlander, P.; Halas, N. J. Aluminum for Plasmonics. *Acs Nano* **2014**, *8* (1), 834-840, DOI: 10.1021/nn405495q.
- [23] Zoric, I.; Zach, M.; Kasemo, B.; Langhammer, C. Gold, Platinum, and Aluminum Nanodisk Plasmons: Material Independence, Subradiance, and Damping Mechanisms. *Acs Nano* **2011**, *5* (4), 2535-2546, DOI: 10.1021/nn102166t.
- [24] Graedel, T. E. Corrosion Mechanisms for Silver Exposed to the Atmosphere. *J. Electrochem. Soc.* **1992**, *139* (7), 1963-1970, DOI: 10.1149/1.2221162.
- [25] Li, W.; Qiu, Y.; Zhang, L.; Jiang, L.; Zhou, Z.; Chen, H.; Zhou, J. Aluminum Nanopyramid Array with Tunable Ultraviolet-Visible-Infrared Wavelength Plasmon Resonances for Rapid Detection of Carbohydrate Antigen 199. *Biosensors and Bioelectronic* **2016**, (79), 500-507, DOI: 10.1016/j.bios.2015.12.038.
- [26] Langhammer, C.; Schwind, M.; Kasemo, B.; Zoric, I. Localized Surface Plasmon Resonances in Aluminum Nanodisks. *Nano Lett.* **2008**, *8* (5), 1461-1471, DOI: 10.1021/nl080453i.
- [27] Ebbesen, T. W.; Lezec, H. J.; Ghaemi, H. F.; Thio, T.; Wolff, P. A. Extraordinary Optical Transmission through Sub-Wavelength Hole Arrays. *Nature* **1998**, *391* (6668), 667-669, DOI: 10.1038/35570.
- [28] Liu, H.; Lalanne, P. Microscopic Theory of the Extraordinary Optical Transmission. *Nature* **2008**, *452* (7188), 728-731, DOI: 10.1038/nature06762.
- [29] Burgos, S. P.; Yokogawa, S.; Atwater, H. A. Color Imaging Via Nearest Neighbor Hole Coupling in Plasmonic Color Filters Integrated onto a Complementary Metal-Oxide Semiconductor Image Sensor. *Acs Nano* **2013**, *7* (11), 10038-10047, DOI: 10.1021/nn403991d.
- [30] Juan, M. L.; Gordon, R.; Pang, Y.; Eftekhari, F.; Quidant, R. Self-Induced Back-Action Optical Trapping of Dielectric Nanoparticles. *Nature Physics* **2009**, *5* (12), 915-919, DOI: 10.1038/nphys1422.
- [31] Ren, X. F.; Zhang, P.; Guo, G. P.; Huang, Y. F.; Wang, Z. W.; Guo, G. C. Polarization Properties of Subwavelength Hole Arrays Consisting of Rectangular Holes. *Applied Physics B-Lasers and Optics* **2008**, *91* (3-4), 601-604, DOI: 10.1007/s00340-008-3027-1.
- [32] Gordon, R.; Brolo, A. G.; McKinnon, A.; Rajora, A.; Leathem, B.; Kavanagh, K. L. Strong Polarization in the Optical Transmission through Elliptical Nanohole Arrays. *Physical Review Letters* **2004**, *92* (3), DOI: 10.1103/PhysRevLett.92.037401.
- [33] Mestres, P.; Berthelot, J.; Acimovic, S. S.; Quidant, R. Unraveling the Optomechanical Nature of Plasmonic Trapping. *Light-Science & Applications* **2016**, *5*, DOI: 10.1038/lsa.2016.92.
- [34] Li, Z. B.; Clark, A. W.; Cooper, J. M. Dual Color Plasmonic Pixels Create a Polarization Controlled Nano Color Palette. *Acs Nano* **2016**, *10* (1), 492-498, DOI: 10.1021/acsnano.5b05411.
- [35] Heydari, E.; Sperling, J. R.; Neale, S. L.; Clark, A. W. Plasmonic Color Filters as Dual-State Nanopixels for High-Density Microimage Encoding. *Adv. Funct. Mater.* **2017**, *27* (35), DOI: 10.1002/adfm.201701866.
- [36] Unser, S.; Bruzas, I.; He, J.; Sagle, L. Localized Surface Plasmon Resonance Biosensing: Current Challenges and Approaches. *Sensors* **2015**, *15* (7), 15684-15716, DOI: 10.3390/s150715684.
- [37] Bigdeli, A.; Ghasemi, F.; Golmohammadi, H.; Abbasi-Moayed, S.; Nejad, M. A. F.; Fahimi-Kashani, N.; Jafarinejad, S.; Shahrajabian, M.; Hormozi-Nezhad, M. R. Nanoparticle-Based Optical Sensor Arrays. *Nanoscale* **2017**, *9* (43), 16546-16563, DOI: 10.1039/c7nr03311g.

- [38] Gordon, R.; Sinton, D.; Kavanagh, K. L.; Brolo, A. G. A New Generation of Sensors Based on Extraordinary Optical Transmission. *Accounts of Chemical Research* **2008**, *41* (8), 1049-1057, DOI: 10.1021/ar800074d.
- [39] Rosi, N. L.; Mirkin, C. A. Nanostructures in Biodiagnostics. *Chem. Rev.* **2005**, *105*, 1547-1562, DOI: 10.1021/cr030067f.
- [40] Mayer, K. M.; Hao, F.; Lee, S.; Nordlander, P.; Hafner, J. H. A Single Molecule Immunoassay by Localized Surface Plasmon Resonance. *Nanotechnology* **2010**, *21* (25), DOI: 10.1088/0957-4484/21/25/255503.
- [41] Szunerits, S.; Boukherroub, R. Sensing Using Localised Surface Plasmon Resonance Sensors. *Chem. Commun. (Cambridge)* **2012**, *48* (72), 8999-9010, DOI: 10.1039/c2cc33266c.
- [42] Acimovic, S. S.; Sipova, H.; Emilsson, G.; Dahlin, A. B.; Antosiewicz, T. J.; Kall, M. Superior Lspr Substrates Based on Electromagnetic Decoupling for on-a-Chip High-Throughput Label-Free Biosensing. *Light: Sci. Appl* **2017**, *6*, DOI: 10.1038/lsa.2017.42.
- [43] Sherry, L. J.; Chang, S. H.; Schatz, G. C.; Van Duyne, R. P.; Wiley, B. J.; Xia, Y. N. Localized Surface Plasmon Resonance Spectroscopy of Single Silver Nanocubes. *Nano Lett.* **2005**, *5* (10), 2034-2038, DOI: 10.1021/nl0515753.
- [44] Sagle, L. B.; Ruvuna, L. K.; Ruellemele, J. A.; Van Duyne, R. P. Advances in Localized Surface Plasmon Resonance Spectroscopy Biosensing. *Nanomedicine* **2011**, *6* (8), 1447-1462, DOI: 10.2217/nnm.11.117.
- [45] Fernandez, F.; Garcia-Lopez, O.; Tellechea, E.; Asensio, A. C.; Cornago, I. Lspr Cuvette for Real-Time Biosensing by Using a Common Spectrophotometer. *IEEE Sens. J.* **2016**, *16* (11), 4158-4165, DOI: 10.1109/jsen.2016.2544953.
- [46] Acimovic, S. S.; Ortega, M. A.; Sanz, V.; Berthelot, J.; Garcia-Cordero, J. L.; Renger, J.; Maerkl, S. J.; Kreuzer, M. P.; Quidant, R. Lspr Chip for Parallel, Rapid, and Sensitive Detection of Cancer Markers in Serum. *Nano Lett.* **2014**, *14* (5), 2636-2641, DOI: 10.1021/nl500574n.
- [47] Sonnichsen, C.; Reinhard, B. M.; Liphardt, J.; Alivisatos, A. P. A Molecular Ruler Based on Plasmon Coupling of Single Gold and Silver Nanoparticles. *Nat. Biotechnol.* **2005**, *23* (6), 741-745, DOI: 10.1038/nbt1100.
- [48] Yoo, S. Y.; Kim, D.-K.; Park, T. J.; Kim, E. K.; Tamiya, E.; Lee, S. Y. Detection of the Most Common Corneal Dystrophies Caused by Bigh3 Gene Point Mutations Using a Multispot Gold-Capped Nanoparticle Array Chip. *Anal. Chem.* **2010**, *82* (4), 1349-1357, DOI: 10.1021/ac902410z.
- [49] Verdoold, R.; Gill, R.; Ungureanu, F.; Molenaar, R.; Kooyman, R. P. N. Femtomolar DNA Detection by Parallel Colorimetric Darkfield Microscopy of Functionalized Gold Nanoparticles. *Biosens. Bioelectron.* **2011**, *27* (1), 77-81, DOI: 10.1016/j.bios.2011.06.019.
- [50] Wadell, C.; Langhammer, C. Drift-Corrected Nanoplasmonic Hydrogen Sensing by Polarization. *Nanoscale* **2015**, *7* (25), 10963-10969, DOI: 10.1039/c5nr01818h.
- [51] Kotnala, A.; Gordon, R. Quantification of High-Efficiency Trapping of Nanoparticles in a Double Nanohole Optical Tweezer. *Nano Lett.* **2014**, *14* (2), 853-856, DOI: 10.1021/nl404233z.
- [52] Brolo, A. G.; Kwok, S. C.; Moffitt, M. G.; Gordon, R.; Riordon, J.; Kavanagh, K. L. Enhanced Fluorescence from Arrays of Nanoholes in a Gold Film. *J. Am. Chem. Soc.* **2005**, *127* (42), 14936-14941, DOI: 10.1021/ja0548687.
- [53] Shao, L.; Zhuo, X.; Wang, J. Advanced Plasmonic Materials for Dynamic Color Display. *Advanced Materials* **2018**, *30* (16), DOI: 10.1002/adma.201704338.
- [54] Miyata, M.; Hatada, H.; Takahara, J. Full-Color Subwavelength Printing with Gap-Plasmonic Optical Antennas. *Nano Lett.* **2016**, *16* (5), 3166-3172, DOI: 10.1021/acs.nanolett.6b00500.

- [55] Tan, S. J.; Zhang, L.; Zhu, D.; Goh, X. M.; Wang, Y. M.; Kumar, K.; Qiu, C.-W.; Yang, J. K. W. Plasmonic Color Palettes for Photorealistic Printing with Aluminum Nanostructures. *Nano Lett.* **2014**, *14* (7), 4023-4029, DOI: 10.1021/nl501460x.
- [56] Kumar, K.; Duan, H.; Hegde, R. S.; Koh, S. C. W.; Wei, J. N.; Yang, J. K. W. Printing Colour at the Optical Diffraction Limit. *Nature Nanotechnology* **2012**, *7* (9), 557-561, DOI: 10.1038/nnano.2012.128.
- [57] Roberts, A. S.; Pors, A.; Albrechtsen, O.; Bozhevolnyi, S. I. Subwavelength Plasmonic Color Printing Protected for Ambient Use. *Nano Lett.* **2014**, *14* (2), 783-787, DOI: 10.1021/nl404129n.
- [58] Olson, J.; Manjavacas, A.; Liu, L.; Chang, W.-S.; Foerster, B.; King, N. S.; Knight, M. W.; Nordlander, P.; Halas, N. J.; Link, S. Vivid, Full-Color Aluminum Plasmonic Pixels. *Proceedings of the National Academy of Sciences* **2014**, *111* (40), 14348-14353, DOI: 10.1073/pnas.1415970111.
- [59] Chen, T. H.; Reinhard, B. M. Assembling Color on the Nanoscale: Multichromatic Switchable Pixels from Plasmonic Atoms and Molecules. *Advanced Materials* **2016**, *28* (18), 3522-+, DOI: 10.1002/adma.201506179.
- [60] Goh, X. M.; Zheng, Y.; Tan, S. J.; Zhang, L.; Kumar, K.; Qiu, C.-W.; Yang, J. K. W. Three-Dimensional Plasmonic Stereoscopic Prints in Full Colour. *Nature Communications* **2014**, *5*, DOI: 10.1038/ncomms6361.
- [61] Huang, Y. W.; Chen, W. T.; Tsai, W. Y.; Wu, P. C.; Wang, C. M.; Sun, G.; Tsai, D. P. Aluminum Plasmonic Multicolor Meta-Hologram. *Nano Lett.* **2015**, *15* (5), 3122-3127, DOI: 10.1021/acs.nanolett.5b00184.
- [62] Shrestha, V. R.; Lee, S.-S.; Kim, E.-S.; Choi, D.-Y. Aluminum Plasmonics Based Highly Transmissive Polarization-Independent Subtractive Color Filters Exploiting a Nanopatch Array. *Nano Lett.* **2014**, *14* (11), 6672-6678, DOI: 10.1021/nl503353z.
- [63] Zheng, B. Y.; Wang, Y. M.; Nordlander, P.; Halas, N. J. Color-Selective and Cmos-Compatible Photodetection Based on Aluminum Plasmonics. *Advanced Materials* **2014**, *26* (36), 6318-6323, DOI: 10.1002/adma.201401168.
- [64] Rajasekharan, R.; Balaur, E.; Minovich, A.; Collins, S.; James, T. D.; Djalalian-Assl, A.; Ganesan, K.; Tomljenovic-Hanic, S.; Kandasamy, S.; Skafidas, E.; Neshev, D. N.; Mulvaney, P.; Roberts, A.; Praver, S. Filling Schemes at Submicron Scale: Development of Submicron Sized Plasmonic Colour Filters. *Sci. Rep.* **2014**, *4*, DOI: 10.1038/srep06435.
- [65] Ahn, M.-S.; Chung, T.; Jeong, K.-H. Structural Coloration of Transmission Light through Self-Aligned and Complementary Plasmonic Nanostructures. *Nanoscale* **2018**, *10* (14), 6313-6317, DOI: 10.1039/c8nr01006d.
- [66] Lochbihler, H.; Ye, Y.; Xu, Y. Complementary Aluminum Nanopatch/Nanohole Arrays for Broad Palettes of Colors. *Plasmonics* **2018**, *1-7*, DOI: 10.1007/s11468-018-0733-3.
- [67] James, T. D.; Mulvaney, P.; Roberts, A. The Plasmonic Pixel: Large Area, Wide Gamut Color Reproduction Using Aluminum Nanostructures. *Nano Lett.* **2016**, *16* (6), 3817-3823.
- [68] Gu, Y.; Zhang, L.; Yang, J. K. W.; Yeo, S. P.; Qiu, C.-W. Color Generation Via Subwavelength Plasmonic Nanostructures. *Nanoscale* **2015**, *7* (15), 6409-6419, DOI: 10.1039/c5nr00578g.
- [69] Smith, A. F.; Patton, P.; Skrabalak, S. E. Plasmonic Nanoparticles as a Physically Unclonable Function for Responsive Anti-Counterfeit Nanofingerprints. *Adv. Funct. Mater.* **2016**, *26* (9), 1315-1321, DOI: 10.1002/adfm.201503989.
- [70] Zheng, Y. H.; Jiang, C.; Ng, S. H.; Lu, Y.; Han, F.; Bach, U.; Gooding, J. J. Unclonable Plasmonic Security Labels Achieved by Shadow-Mask-Lithography-

- Assisted Self-Assembly. *Advanced Materials* **2016**, *28* (12), 2330-2336, DOI: 10.1002/adma.201505022.
- [71] Chen, Q.; Das, D.; Chitnis, D.; Walls, K.; Drysdale, T. D.; Collins, S.; Cumming, D. R. S. A Cmos Image Sensor Integrated with Plasmonic Colour Filters. *Plasmonics* **2012**, *7* (4), 695-699, DOI: 10.1007/s11468-012-9360-6.
- [72] Frey, L.; Parrein, P.; Raby, J.; Pellé, C.; Hérault, D.; Marty, M.; Michailos, J. Color Filters Including Infrared Cut-Off Integrated on Cmos Image Sensor. *Optics Express* **2011**, *19* (14), 13073-13080, DOI: 10.1364/OE.19.013073.
- [73] Lu, H. B.; Homola, J.; Campbell, C. T.; Nenninger, G. G.; Yee, S. S.; Ratner, B. D. Protein Contact Printing for a Surface Plasmon Resonance Biosensor with on-Chip Referencing. *Sens. Actuators, B* **2001**, *74* (1-3), 91-99, DOI: 10.1016/S0925-4005(00)00716-4.
- [74] Boozer, C.; Yu, Q. M.; Chen, S. F.; Lee, C. Y.; Homola, J.; Yee, S. S.; Jiang, S. Y. Surface Functionalization for Self-Referencing Surface Plasmon Resonance (Spr) Biosensors by Multi-Step Self-Assembly. *Sens. Actuators, B* **2003**, *90* (1-3), 22-30, DOI: 10.1016/S0925-4005(03)00017-0.
- [75] Levy, R.; Ruschin, S. Design of a Single-Channel Modal Interferometer Waveguide Sensor. *IEEE Sens. J.* **2009**, *9* (1-2), 146-153, DOI: 10.1109/jSEN.2008.2011075.
- [76] Kashif, M.; Bakar, A. A. A.; Hashim, F. H. Analysing Surface Plasmon Resonance Phase Sensor Based on Mach-Zehnder Interferometer Technique Using Glycerin. *Opt. Commun.* **2016**, *380*, 419-424, DOI: 10.1016/j.optcom.2016.06.033.
- [77] Wu, S. Y.; Ho, H. P.; Law, W. C.; Lin, C. L.; Kong, S. K. Highly Sensitive Differential Phase-Sensitive Surface Plasmon Resonance Biosensor Based on the Mach-Zehnder Configuration. *Opt. Lett.* **2004**, *29* (20), 2378-2380, DOI: 10.1364/OL.29.002378.
- [78] Hao, N.; Zhang, Y.; Zhong, H.; Zhou, Z.; Hua, R.; Qian, J.; Liu, Q.; Li, H.; Wang, K. Design of a Dual Channel Self-Reference Photoelectrochemical Biosensor. *Anal. Chem.* **2017**, *89* (19), 10133-10136, DOI: 10.1021/acs.analchem.7b03132.
- [79] Wang, X.; Chang, T.-W.; Lin, G.; Gartia, M. R.; Liu, G. L. Self-Referenced Smartphone-Based Nanoplasmonic Imaging Platform for Colorimetric Biochemical Sensing. *Anal. Chem.* **2017**, *89* (1), 611-615, DOI: 10.1021/acs.analchem.6b02484.
- [80] Wersall, M.; Verre, R.; Svedendahl, M.; Johansson, P.; Kall, M.; Shegai, T. Directional Nanoplasmonic Antennas for Self-Referenced Refractometric Molecular Analysis. *J. Phys. Chem. C* **2014**, *118* (36), 21075-21080, DOI: 10.1021/jp5064929.
- [81] Rivero, P. J.; Ibanez, E.; Goicoechea, J.; Urrutia, A.; Matias, I. R.; Arregui, F. J. A Self-Referenced Optical Colorimetric Sensor Based on Silver and Gold Nanoparticles for Quantitative Determination of Hydrogen Peroxide. *Sens. Actuators, B* **2017**, *251*, 624-631, DOI: 10.1016/j.snb.2017.05.110.
- [82] Li, X. P.; Zhang, Q. M.; Chen, X.; Gu, M. Giant Refractive-Index Modulation by Two-Photon Reduction of Fluorescent Graphene Oxides for Multimode Optical Recording. *Sci. Rep.* **2013**, *3*, 4, DOI: 10.1038/srep02819.

## Chapter 2: Materials and Methods

### 2.1 Introduction

This Chapter provides an overview of the numerical and experimental techniques used in the course of the research of this thesis. Specific implementation of the protocols is introduced in the relevant experimental chapters. All the fabrication steps, SEM, and AFM were carried out in the James Watt Nanofabrication Centre at the University of Glasgow. Optical transmission data acquisition was carried out in the Rankine Building at the University of Glasgow.

### 2.2 Materials

1-decanethiol (DT)	Sigma-Aldrich
1-Ethyl-3-(3-dimethylaminopropyl)-carbodiimide (EDC)	Sigma-Aldrich
1H,1H,2H,2H-perfluoro-1-decanethiol (PFDT)	Sigma-Aldrich
2-[methoxy (polyethyleneoxy)6-9 propyl] trimethoxysilane (PEG6-9)	Sigma-Aldrich
Absolut® Vodka	
Acetone	Fisher Scientific
AR-PC 5091 (Electra-92) conductive protective coating	AllResist
Avidin	Sigma-Aldrich
Biotin hydrazide	Sigma-Aldrich
Borosilicate glass, 4-inch wafers, 500 µm thick	University Wafer, Inc.
Bovine serum albumin (BSA)	Sigma-Aldrich
Deionised (DI) water	Sigma-Aldrich
Electron beam evaporated aluminium (Al) metal	Kurt J. Lesker Company
Electron beam evaporated gold (Au) metal	Pi-KEM, Ltd.
Electron beam evaporated titanium (Ti) metal	Kurt J. Lesker Company
Ethanol	Sigma-Aldrich
Ethanolamine	Sigma-Aldrich
Glass slides and coverslips	Thermo-Fischer
Glen Marnoch® Bourbon Cask	
Glen Marnoch® Rum Cask	
Glen Marnoch® Sherry Cask,	
Glenfiddich® 12 Year	
Glenfiddich® 15 Year	
Glenfiddich® 18	
Hexamethyldisilazane (HMDS)	Sigma-Aldrich
Hydrogen silsesquioxane (HSQ) Fox 16 Flowable Oxide	Dow Corning, Co.
Isopropyl Alcohol	Scientific Laboratory Supplies, Ltd.
Laphroaig® 10 Year	
Linear polarisers	Thorlabs
Mercaptoundecanoic acid (MUA)	Sigma-Aldrich
Methyl isobutyl ketone (MIBK)	Merck Chemicals
Microposit MF CD-26	Shipley
Microposit Remover 1165	Shipley
O-xylene	Sigma-Aldrich
Phosphate buffer solution (PBS)	Sigma-Aldrich
Polydimethylsiloxane (PDMS)	Sigma-Aldrich
Polymethyl Methacrylate (PMMA)	Lucite International, Inc.

Sodium hydroxide (NaOH)	Sigma-Aldrich
Sucrose	Sigma-Aldrich
Tetramethylammonium hydroxide (TMAH) 25%	Chestech, Ltd.
Tween-20	Sigma-Aldrich
ZEP520A	ZEON, Ltd.

## 2.3 Simulation Techniques

### 2.3.1 Finite-Difference Time-Domain (FDTD) Simulations

In Chapter 1, Maxwell equations are used to define the interactions of electromagnetic waves with their surrounding environment and objects. A common method to model this interaction is the numerical calculation method of finite-difference time-domain (FDTD). As its name implies, FDTD uses a finite-difference approximation to the continuous derivatives in both the spatial and temporal domains, in the Cartesian coordinate system. This allows the use of the central-difference (rather than partial-differential) forms of the time-dependent Maxwell equations. 3D FDTD analysis divides the computational space into cubic grids called Yee Lattices [1]. The magnetic field vector components of the Yee Lattice originate at the centre of each grid face and are directionally perpendicular to each face, and the electric field vector components of the Yee Lattice originate at the centre of each grid edge and are directionally parallel to each edge (see **Figure 2.1**).

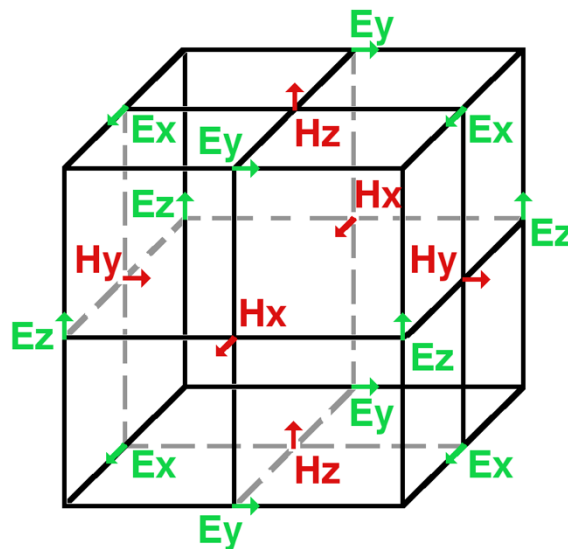


**Figure 2.1: Yee Lattice diagram.** The vector components of the electric (green) and magnetic (red) fields as defined by the Yee Lattice [1].

Defining the electric and magnetic fields in this way results in each component being separated spatially by a ‘half-step.’ This allows for discrete calculations of the field components in a cyclic pattern, where the electric field is solved at one time-point followed

by the magnetic field at the subsequent time-point. This cyclic pattern repeats until all the fields in the whole space are solved [2].

### 2.3.2 Lumerical FDTD

Throughout this research, Lumerical FDTD Solutions was used to model the optical transmission and resonant field distributions. 3D simulation models were built by defining the structural dimensions and materials of each object in the model using data from the included materials database and data measured by ellipsometry. The interface between the base glass of each sample and the first fabricated structure was always positioned at  $Z = 0$  nm. The dielectric values of gold and titanium were obtained from the CRC library [3] and of glass and aluminium were obtained from the Palik library [4].

After building the model, simulation boundaries were then defined with certain dimensions in X, Y, and Z. The simulation region provided the ability to define background index, meshing accuracy, and boundary conditions. Depending on what was being simulated, the background index was modified accordingly. Since each fabricated device in this work consists of periodic arrays across the surface of the device (defined in the X and Y plane), the X-Y plane was defined with periodic boundary conditions (representing an infinite array). The simulation model was therefore built for one period-worth of nanoplasmonic structures. The boundary condition in Z was set as a perfectly-matched-layer (PML) boundary condition. For all simulations, a mesh override was added to increase the accuracy of the simulation.

A linearly polarised plane wave was defined for the simulation area originating from the negative Z-axis near the lower Z-boundary of the simulation region, propagating in the +Z direction so that it transmitted through the sample. The wave intensity and phase, polarisation, and wavelength range were each altered depending on the device simulated. To monitor transmission, a frequency domain and power monitor was positioned in the positive Z-axis near the upper Z-boundary of the simulation region. To monitor the electric field, a frequency domain field monitor was used, intersecting the regions of interest.

Details on the parameters used to simulate each device explored in this work can be found in the subsequent chapters.

## 2.4 Fabrication Tools

### 2.4.1 Electron-Beam (E-Beam) Lithography

Electron-beam (e-beam) lithography is a process used for the fabrication of patterns with the capabilities of nanometer resolution [5]. E-beam lithography systems use a focused beam of electrons to expose a polymer film called a resist. Depending on if the resist is a positive or negative, the exposure to the e-beam will either break long-chains in the polymer or cross-link short-chains to long, less soluble chains, respectively. After e-beam exposure, resist is chemically developed. Exposed positive resist and unexposed negative resist are removed while unexposed positive resist and exposed negative resist remain. An example of positive resist (PMMA) is found in Chapter 2.5.3 and negative (HSQ) is found in Chapter 2.5.5. Additionally, e-beam lithography is a direct-writing system which means it only exposes one area at a time (unlike using photolithography where the full pattern is exposed all at once).

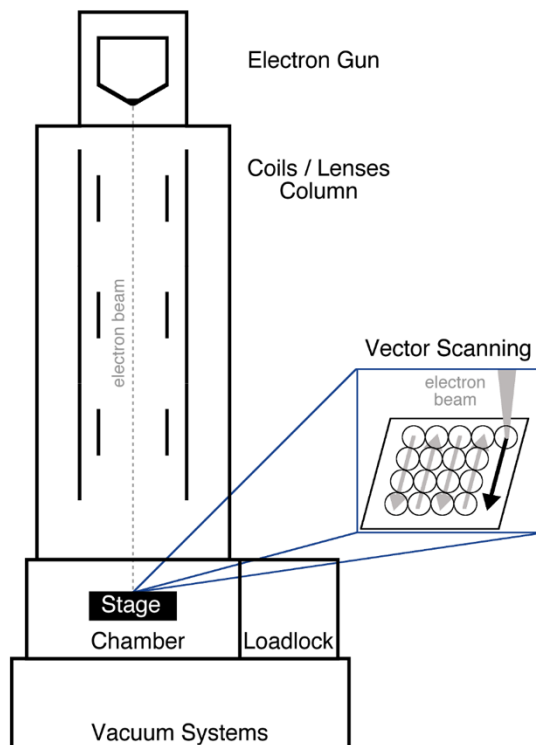


**Figure 2.2: Schematic of e-beam lithography tool and vector scanning.** The e-beam tool operates at high-vacuum. The electron gun generates an electron beam (dashed-grey line) that is focused and deflected by a series of coils and lenses in the column. The stage can be moved between the chamber (where exposure to the e-beam occurs) and loadlock (where loading/unloading at atmospheric pressure occurs). (**inset**) The pattern is written by vector scanning as indicated by the arrows.

While there are slight differences in configuration between different e-beam tools, the typical e-beam tool consists of a high-voltage electron gun, beam focusing parts, sample holder(s), and a vacuum/pumping system. **Figure 2.2** shows a schematic of the tool. Free electrons are produced by the electron gun through either thermal or field emission, and a strong electric field with high voltage accelerates the free electrons into a beam. As the e-beam travels through the column, it is focused by a series of electromagnetic lenses and deflection coils. The designed pattern is then written by vector scanning movement of the stage (see inset of Figure 2.2).

To properly write a pattern into the resist, the correct exposure dose (electron charge density per area measured in  $\mu\text{C}\cdot\text{cm}^{-2}$ ) is necessary. A common method to determine the proper dose is to expose multiple iterations of the same pattern with varied doses. This method is commonly referred to as a ‘dose test.’

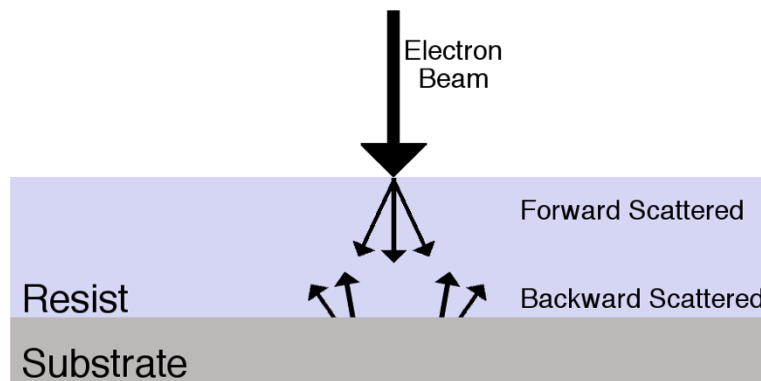


**Figure 2.3: Scattering of electrons by resist and substrate.** Forward scattering of electrons by molecules in the resist and backward of electrons scattering by molecules of the substrate results in lateral exposure of the resist.

E-beam exposure is not only dependent on the dose, but also on the scattering of the focused electrons once they have made contact with the substrate. To prevent charge build-up, the substrate must be conductive to allow electron dissipation. Otherwise, accumulation of electrons will occur on the substrate surface, which will repel incoming electrons, distort the e-beam, and alter the pattern shape and resolution. For non-conductive substrates, such as the glass ones used in this research, a thin layer of metal or charge-conductive polymer is necessary to act as a conduction layer. Additionally, the molecules of the substrate can backward scatter electrons, and the molecules of the resist can forward scatter electrons. Both types of scattering result in electrons travelling laterally through the resist layer and

expose adjacent areas of the resist (see **Figure 2.3**). This lateral exposure, referred to as ‘proximity effects,’ enlarges the exposed pattern and is especially prominent when making very small features in relatively thick resist layers [6]. To overcome this, the doses across the pattern extent can be varied.

For nanofabrication jobs where multiple e-beam lithography steps are warranted and high-accuracy of each pattern on the substrate is important, the process of alignment is a crucial step [7]. Alignment markers allow for finding the exact location on the substrate for e-beam exposure and correcting location, rotation, keystone, and scale in both X and Y. One type of alignment markers involves using simple geometric shapes. However, this method relies on scanning the beam across a pair of parallel edges. If any two parallel sides are not even, a marker may not be ‘found.’ If one marker is slightly larger than another, it may result in altered position, rotation, keystone, and/or scale (in X, Y, or both). Correlation-based alignment with Penrose patterns has been demonstrated to be less susceptible to these potential defects, with sub-5 nm alignment, even when up to 80% of the marker pattern is missing [8]. **Figure 2.4** shows local registration markers of geometric and Penrose patterns. The work in this research utilised both types of markers. For the devices of Chapter 3, geometric markers were used. The devices in Chapter 4 required more accurate alignment, and therefore, Penrose markers were used.

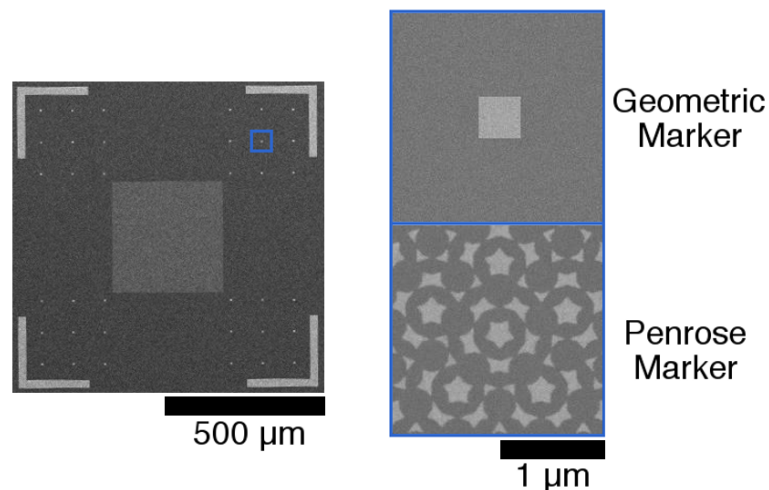


**Figure 2.4: SEM images of alignment markers using geometric squares and correlation Penrose patterns.** Geometric markers are susceptible to marker-edge defects. Penrose markers are much less susceptible and can still achieve sub-5 nm resolution, even with up to 80% of the pattern missing [8].

The e-beam tool used in this work is a Vistec VB6 Ultra High Resolution Extra Wide Field (UHR EWF) electron-beam lithography tool. The VB6 operates at 100 kV and has a minimum beam size of 4 nm. To ensure full exposure of resist and an acceptable writing time, the beam size for writing should be slightly larger than the beam step size (BSS). BSS is defined as the distance between two consecutive exposure spots and is the product of the resolution and an integer number called the variable resolution unit (VRU):  $BSS = Resolution \times VRU$ . Writing time for a pattern can be estimated by  $Time = \frac{(Exposure\ Dose) \times (Exposure\ Area)}{(Beam\ Current)}$ .

#### 2.4.2 Electron-Beam Metal Evaporation

An electron-beam metal evaporation process is used for the controlled linear deposition of metal onto a substrate. The sample is loaded into a load-lock chamber at high-vacuum. An electron beam is generated at 9.7 kV and a magnetic field is used to deflect and direct the beam onto a metal in a lower chamber. By controlling the current, the metal is rapidly heated and changes to the vapour state. The vapour state then evaporates onto the sample with high-linear directionality (as opposed to that in a sputtering process), which is highly beneficial for metallisation/lift-off techniques (see Chapter 2.5.3). Evaporation rate and film thickness are monitored by oscillation frequency detection of a quartz crystal. In this work, a Plassys MEB 550S and Plassys MEB 400S machine were used.

#### 2.4.3 Plasma Enhanced Chemical Vapour Deposition (PECVD) of SiO<sub>2</sub>

Plasma Enhanced Chemical Vapour Deposition (PECVD) [9] is a thin-film deposition technique that uses plasma to react chemicals in the gas state to deposit dielectric, metal oxide, and metal nitride thin films in the solid state. For the PECVD process, a sample is placed in a high-vacuum chamber and a specific mixture of gases is then flowed into the chamber at a controlled rate so that pressure in the chamber is maintained. The gas selected for this process is chosen based on the desired material for deposition. Power is supplied to parallel electrode plates (positioned above and below, but isolated from, the sample) in the chamber, which ignites the gas and generates an ionized plasma. The electrons in the plasma move along an EM field and accumulate, forming a voltage bias. The voltage bias maintains the plasma and accelerates the ions between the vertical plates, which is critical in depositing the formed solid materials on the surface. The substrate table is brought to high temperature to help with the deposition process. The PECVD process carried out in this work was for the deposition of SiO<sub>2</sub> (see Chapter 2.5.6 which refers to the sample fabrication process for

devices from Chapter 5). An Oxford Instrument System 100 Plasma Deposition Tool was used with the recipe  $\text{SiH}_4/\text{N}_2\text{O}/\text{N}_2 = 7/146/85$  sccm, 15 W, 1000 mTorr, 300° C which resulted in a deposition rate around 65 nm/min.

#### 2.4.4 Inductively Coupled Plasmon Chemical Vapour Deposition (ICP-CVD) of $\text{SiN}_x$

Inductively Coupled Plasmon Chemical Vapour Deposition (ICP-CVD) is similar to PECVD (see Chapter 2.4.3). However, the inductively coupled plasma in ICP-CVD is generated by a strong magnetic field via inductance coils [10]. This allows for film deposition at room temperature [11]. The ICP-CVD process carried out in this work was for the deposition of silicon nitride (see Chapter 2.5.4 which refers to the sample fabrication process for devices from Chapter 3). An Oxford Instruments System 100 ICP 180 PECVD was used with a recipe of  $\text{SiH}_4/\text{N}_2 = 7/6$  sccm, ICP/Platen = 100/0 W, 4 mTorr, 25° C which resulted in a deposition rate of around 16 nm/min.

#### 2.4.5 Reactive-Ion Etching (RIE) of Aluminium

Reactive-Ion Etching (RIE), commonly referred to as “dry-etching,” uses plasma from gases to chemically react with and physically remove materials on a substrate [12-13]. For the RIE process, a sample is placed in a high-vacuum chamber and a specific gas or mixture of gases is then flowed into the chamber at a controlled rate so that pressure in the chamber is maintained. The gas selected for this process is chosen based on its ability to etch the desired material. Power is supplied to parallel electrode plates (positioned above and below, but isolated from, the sample) in the chamber, which ignites the gas and generates an ionized plasma. The electrons in the plasma move along an EM field and accumulate, forming a voltage bias. The voltage bias maintains the plasma and accelerates the ions between the vertical plates, which is critical in removing the materials on the surface in an anisotropic etching process. Since the RIE process is anisotropic, a mask (made of resist, nitride, or metal) can be used to confine etching to a specific area on the substrate. Alterations to chamber pressure, power, and gas-flow-rate result in different etch rates and structural profiles.

In this work, an Oxford Instrument Plasmalab System 100 T-Gate Reactive Ion Etch Tool was used to etch nano-apertures into 100 nm aluminium (see Chapter 2.5.6 which refers to the sample fabrication process for devices from Chapter 5). ZEP520A was used as the

etching mask and SiCl<sub>4</sub> plasma was used in the RIE with the parameters of 18 sccm, 250 W, 9 mTorr, 20° C.

## 2.5 Fabrication Processes

### 2.5.1 Design Software

For e-beam lithography, L-Edit Software (Tanner Research, Inc.) was used to design a graphical data system (GDS) file with 0.125 nm resolution. Layout Beamer Software (GenlSys GmbH) was then used to extract each layer in the GDS file and generate corresponding VEP format files for each. A custom Java program called Belle was used to then generate a TXT file that instructed the e-beam tool position, exposure dose, beam size VRU, and which design to pattern on the sample. Jobs written with specific alignment requirements to previous patterns on the sample (registration jobs) were also defined in the Belle-generated TXT file. All plasmonic structures were written with a 1 nA, 4 nm beam size with a VRU value of 8. All markers were written with a 64 nA, 33 nm beam size with VRU of 50.

### 2.5.2 Device Cleaning

Glass samples were ultrasonically cleaned for 5 minutes in acetone then IPA to remove organic/inorganic contaminants and then blow dried by nitrogen. Samples were then O<sub>2</sub> plasma cleaned in a Gala Plasma Prep 5 Oxygen Barrel Asher for 3 minutes at 150 W and  $3 \times 10^{-1}$  mTorr.

### 2.5.3 Metal Structure Fabrication

A ‘top-down’ (see Chapter 1.2.4) approach was used for the fabrication of the metal markers and nanostructure arrays on the devices from Chapter 3 and Chapter 4. The nanostructure arrays for the final devices used for these two Chapters were fabricated using the registration job local-field alignment (as discussed in Chapter 2.4.1).

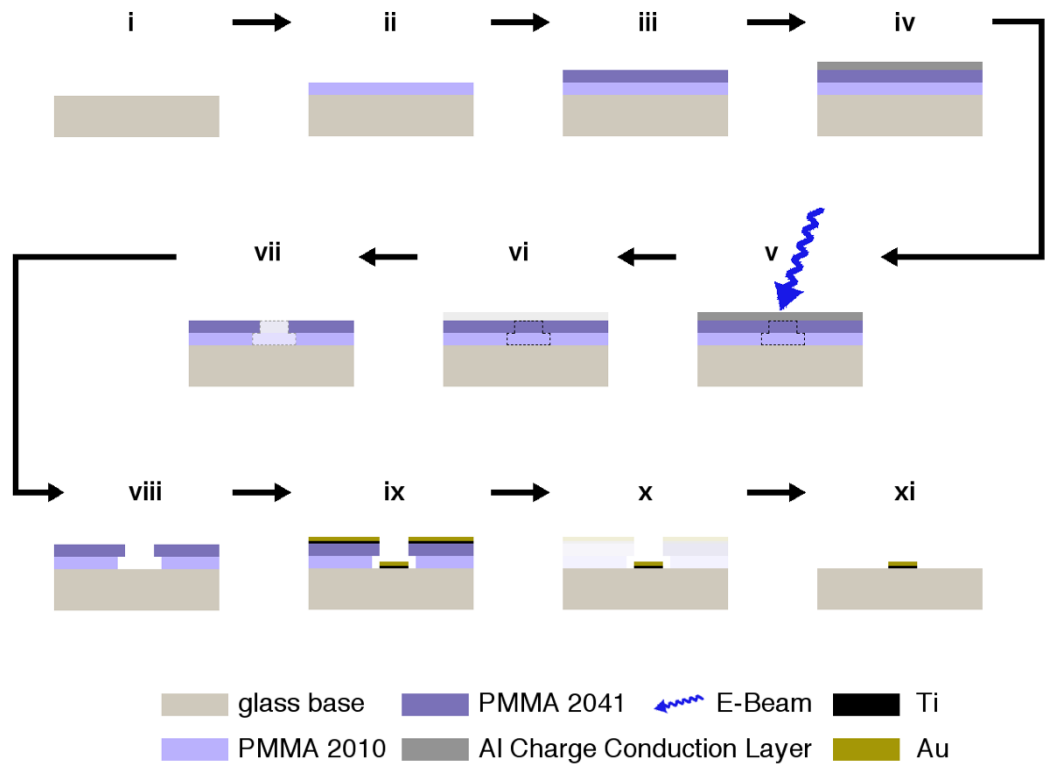


**Figure 2.5: Schematic of e-beam-lithography-mediated metal fabrication steps.** The fabrication process involves **(i)** cleaning a glass substrate, **(ii-iii)** spinning a resist bilayer and hotplate baking after each layer is spun on, **(iv)** depositing a charge conduction layer, **(v)** exposing the sample with e-beam tool, **(vi)** removing the charge conduction layer, **(vii)** developing the sample, **(viii)** removing resist residue with an O<sub>2</sub> plasma asher, **(ix)** e-beam metal evaporation for 50 nm Al or 2:50 nm Ti: Au (in this Figure, Ti: Au is shown), **(x)** lift-off of resist and metal not deposited on the substrate base, and **(xi)** a final O<sub>2</sub> plasma ash clean.

**Figure 2.5** shows a schematic of the fabrication steps. Once the glass base surface of the device was **(i)** cleaned, **(ii-iii)** a positive resist bi-layer of 4% poly(methyl methacrylate) resist (PMMA) 2010 and 2.5% PMMA 2041 was spun onto the surface at 5000 RPM for 60 seconds (total thickness around 100 nm and 50 nm, respectively). Between each PMMA spun layer, the device was hotplate baked at 180° C for 15 seconds to evaporate the O-xylene solvent out of the PMMA layer. 4% PMMA 2010 was chosen because its 5000 RPM spun-on height is well above the desired height of the metal markers and nanostructures. A bilayer was used in order to gain an undercut profile necessary for good metal lift-off and nanostructure definition. PMMA 2010 has a lower molecular weight and is therefore more sensitive to the electron beam, resulting in a larger area cleared by the same dose beam when compared to PMMA 2041. **(iv)** To prevent charge build-up and allow for electron conduction during the e-beam lithography process, a 10 nm Al charge conduction layer was deposited

by electron-beam metal evaporation. Either a Plassys MEB 550S or Plassys MEB 400S was used for this step. During the metallisation process, the substrate was upside-down in the load-lock chamber and the process was automatically controlled by the machine software (0.3 nm/s deposition rate). **(v)** The sample was then submitted for e-beam lithography. In order to determine the correct electron dose for writing, a substrate consisting of the same pattern with varying doses was written and examined by SEM. Too low of a dose results in incomplete patterns and loss of sharp edges. Too high a dose results in oversized patterns. After dose testing, markers and large patterns were written with a 64 nA, 33 nm diameter beam at a dose of 600  $\mu\text{C}/\text{cm}^2$  at 50 variable-resolution-unit (VRU) and nanoarrays were written with a 1 nA, 4 nm diameter beam at a dose of 1150  $\mu\text{C}/\text{cm}^2$  at 8 VRU. **(vi)** Post-lithography, CD-26 solution (2.5% TMAH) was used to remove the Al charge conduction layer. **(vii)** The substrate was next developed in 2.5:1 IPA:MIBK solution at 23° C for 45 seconds followed by a 30-second IPA rinse and N<sub>2</sub> drying. As can be seen in the Figure, areas of the positive-tone resist exposed to the e-beam are more soluble and wash away during development. **(viii)** To remove any undeveloped resist residues on the surface, an O<sub>2</sub> plasma ash gently etched away several nanometres of the resist layer. A barrel asher set at 80 W /  $3 \times 10^{-1}$  mTorr for 20 seconds was used. **(ix)** As in (iv), either a Plassys MEB 550S or Plassys MEB 400S was used for Ti/Au and Al evaporation. The entire deposition recipe process was automatically controlled by the software for the machines using evaporation rates of 0.3 nm/s. As mentioned in Chapter 2.4.2, electron-beam evaporation allows for linear control in the metal deposition process, where only areas on the substrate normal to the metal vapor have metal deposited on them. A sputtering process could result in metal deposited along the edge walls of the resist and result in problems with the lift-off step. Thickness of Au and Al was 50 nm. For Au deposition, a 2 nm Ti layer was first deposited to promote surface adhesion. This is the metallisation process shown in (ix). For Al deposition, this was not necessary. **(x)** The sample was next placed in 50° C acetone, which dissolved the PMMA bilayer and lifted-off the metal deposited only on the resist. The undercut between the two layers of resist prevented the metal deposited on the base substrate and on the resist from being continuous. It also allowed for the acetone to effectively get ‘under’ the resist layer, which promoted a clean lift-off process. A pipette was used to vigorously agitate the sample, and the sample underwent multiple washes with fresh acetone. **(xi)** Once the lift-off process was complete, the sample was rinsed with a mixture of acetone/DI water, rinsed with IPA, and then N<sub>2</sub> dried. A final O<sub>2</sub> plasma ash clean was then completed at 150 W /  $3 \times 10^{-1}$  mTorr for 3 minutes.

## 2.5.4 Silicon Nitride Micro-Region Fabrication

Similar to Chapter 2.5.3, the registration job local-field alignment e-beam lithography technique was used to fabricate the silicon-nitride micro-regions of the devices in Chapter 3.

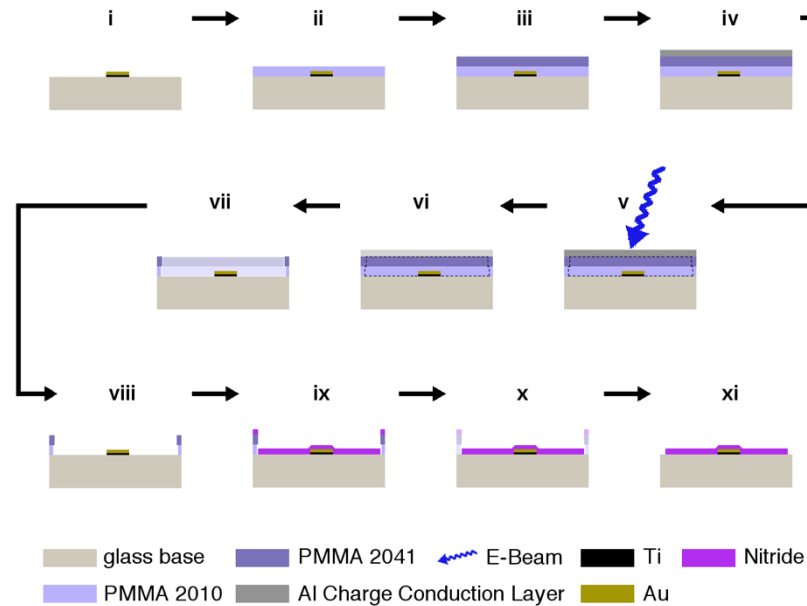


**Figure 2.6:** Schematic of silicon nitride micro-region fabrication process. The fabrication process involves (i)  $O_2$  plasma ash cleaning a substrate, (ii-iii) spinning a resist bilayer and hotplate baking after each layer is spun on, (iv) depositing a charge conduction layer, (v) exposing the sample with e-beam tool, (vi) removing the charge conduction layer, (vii) developing the sample, (viii) removing resist residue with an  $O_2$  plasma ash, (ix) nitride deposition, (x) lift-off of resist and nitride not deposited on the substrate base, and (xi) a final  $O_2$  plasma ash clean.

**Figure 2.6** shows a schematic of the fabrication steps. Once the glass base with metal nanostructures of the device was (i)  $O_2$  plasma cleaned at  $150\text{ W} / 3 \times 10^{-1}\text{ mTorr}$  for 3 minutes, (ii-iii) a positive resist bi-layer of 8% poly(methyl methacrylate) resist (PMMA) 2010 and 4% PMMA 2041 was spun onto the surface at 5000 RPM for 60 seconds (total thickness around 200 nm and 100 nm, respectively). Between each PMMA spun layer, the device was hotplate baked at  $180^\circ\text{ C}$  for 15 seconds to evaporate the O-xylene solvent out of the PMMA layer. 8% PMMA 2010 was chosen because its 5000 RPM spun-on height is well above the desired height of the nitride deposition. As previously mentioned in Chapter 2.5.3, a bilayer was used in order to aid in the lift off step, post development. (iv) To prevent charge build-up and allow for electron conduction during the e-beam lithography process, a 10 nm Al charge conduction layer was deposited by electron-beam metal evaporation. Either a Plassys MEB 550S or Plassys MEB 400S was used for this step. During the metallisation

process, the substrate was upside-down in the load-lock chamber and the process was automatically controlled by the machine software (0.3 nm/s deposition rate). **(v)** The sample was then submitted for e-beam lithography using a 64 nA, 33 nm diameter beam at a dose of  $650 \mu\text{C}/\text{cm}^2$  at 50 VRU to open a  $375 \mu\text{m} \times 375 \mu\text{m}$  window over the nanostructure array region. **(vi)** Post-lithography, CD-26 solution (2.5% TMAH) was used to remove the Al charge conduction layer. **(vii)** The substrate was next developed in 2.5:1 IPA:MIBK solution at  $23^\circ \text{C}$  for 45 seconds followed by a 30-second IPA rinse and air drying. As can be seen in the Figure, the bilayer resist has an undercut, and the areas of the positive-tone resist exposed to the e-beam are more soluble and wash away during development. **(viii)** To remove any undeveloped resist residues on the surface, an  $\text{O}_2$  plasma ash gently etched away several nanometres of the resist layer. A barrel asher set at  $80 \text{ W} / 3 \times 10^{-1} \text{ mTorr}$  for 20 seconds was used. **(ix)** The 85 nm to 100 nm silicon nitride layer was deposited using an Oxford Instruments System 100 ICP 180 PECVD nitride deposition tool ( $\text{SiH}_4/\text{N}_2 = 7/6 \text{ sccm}$ , ICP/Platen =  $100/0 \text{ W}$ ,  $4 \text{ mTorr}$ ,  $25^\circ \text{C}$ ) with a deposition rate of 16 nm/min. **(x)** The sample was next placed in  $50^\circ \text{C}$  acetone, which dissolved the PMMA bilayer and lifted-off the nitride deposited only on the resist. The undercut between the two layers of resist prevented the nitride deposited on the base substrate and on the resist from being continuous. It also allowed for the acetone to effectively get ‘under’ the resist layer, which promoted a clean lift-off process. A pipette was used to vigorously agitate the sample, and the sample underwent multiple washes with fresh acetone. **(xi)** Once the lift-off process was complete, the sample was rinsed with a mixture of acetone/DI water, rinsed with IPA, and then  $\text{N}_2$  dried. A final  $\text{O}_2$  plasma ash clean was then completed at  $150 \text{ W} / 3 \times 10^{-1} \text{ mTorr}$  for 3 minutes.

### 2.5.5 HSQ Micro-Region Fabrication

Similar to Chapter 2.5.3 and Chapter 2.5.4, the registration job local-field alignment e-beam lithography technique was used to fabricate the HSQ micro-regions of the devices in Chapter 3.

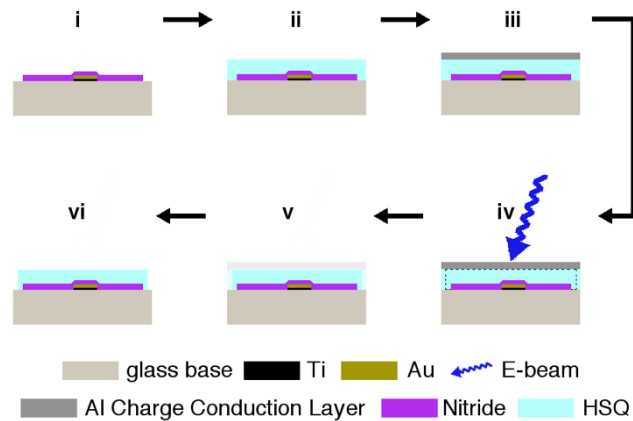


**Figure 2.7: Schematic of HSQ micro-region layer fabrication process.** The fabrication process involves (i)  $O_2$  plasma ash cleaning a substrate, (ii) spinning HSQ resist and hotplate baking, (iii) depositing a charge conduction layer, (iv) exposing the sample with e-beam tool, (v) removing the charge conduction layer and developing the sample, and (vi) a final  $O_2$  plasma ash clean.

**Figure 2.7** shows a schematic of the fabrication steps. Once the device with glass base, metal nanostructures and silicon nitride was (i)  $O_2$  plasma cleaned at  $150\text{ W} / 3 \times 10^{-1}\text{ mTorr}$  for 3 minutes, (ii) a negative resist HSQ (neat) was spun onto the sample at 6000 RPM for 60 seconds (total thickness around 320 nm). The sample was then hotplate baked at  $90^\circ\text{ C}$  for 2 minutes to evaporate off the MIBK solvent. (iii) To prevent charge build-up and allow for electron conduction during the e-beam lithography process, a 10 nm Al charge conduction layer was deposited by electron-beam metal evaporation. Either a Plassys MEB 550S or Plassys MEB 400S was used for this step. During the metallisation process, the substrate was upside-down in the load-lock chamber and the process was automatically controlled by the machine software ( $0.3\text{ nm/s}$  deposition rate). (iv) The sample was then submitted for e-beam lithography using a 64 nA, 33 nm diameter beam at a dose of  $1000\ \mu\text{C}/\text{cm}^2$  at 50 VRUs to write a  $375\ \mu\text{m} \times 375\ \mu\text{m}$  HSQ window over the nanostructure array region. High-dose, over-exposure was used to promote cross-linking of the HSQ. (v) Post-lithography, 25% TMAH was used to remove the Al charge conduction layer (30 seconds) and develop the HSQ resist (30 seconds). As can be seen in the Figure, areas of the negative-tone resist exposed to the e-beam are less soluble and unexposed areas wash away during development. The device was immediately rinsed in two separate IPA baths for 30 seconds, then  $N_2$  dried. (vi) A final  $O_2$  plasma ash clean was then completed at  $150\text{ W} / 3 \times 10^{-1}\text{ mTorr}$  for 3 minutes.

### 2.5.6 Nano-Aperture Fabrication

The nanoaperture arrays from the devices in Chapter 5 were also fabricated using the e-beam lithography tool. However, no registration job lithography technique was required because these devices were not fabricated with multiple, high-resolution alignment lithography cycles.

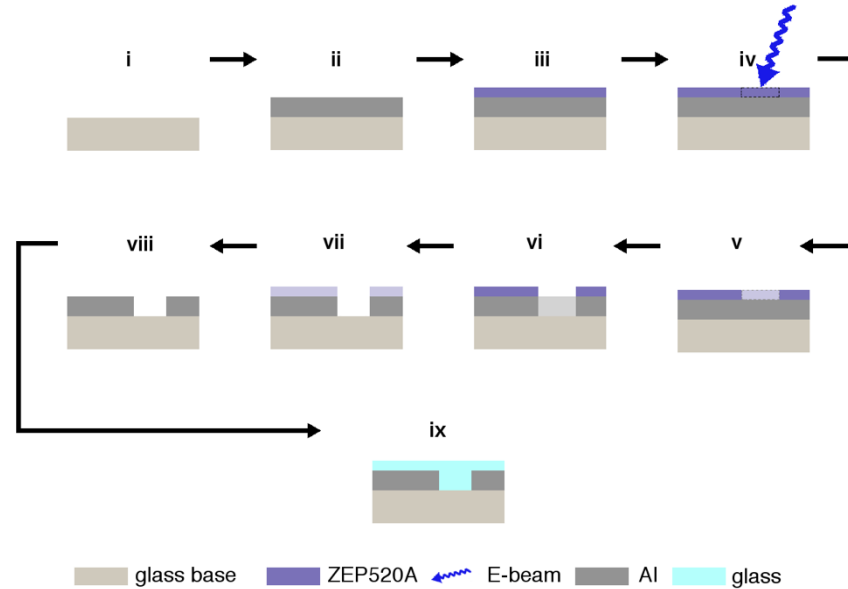


**Figure 2.8: Schematic of the nanoaperture fabrication process.** The fabrication process involves (i) cleaning a glass substrate and spinning on primer, (ii) 100 nm Al deposition, (iii) spinning a resist layer and oven baking, (iv) exposing the sample with e-beam tool, (v) developing the sample, (vi) O<sub>2</sub> plasma ash and reactive-ion etching of the metal, (vii) stripping of the resist, (viii) O<sub>2</sub> plasma ash clean, and (ix) silicon dioxide deposition.

**Figure 2.8** shows a schematic of the fabrication steps. (i) MCC 80/20 Primer was spun onto a cleaned piece of glass at 5000 RPM for 60 seconds to act as an adhesion layer for Al metal deposition. (ii) Either a Plassys MEB 550S or Plassys MEB 400S was used to electron-beam evaporate 100 nm of Al at a 0.3 nm/sec rate. During the metallisation process, the substrate was upside-down in the load-lock chamber and the process was automatically controlled by the machine software. (iii) The positive resist ZEP520A in a 2:1 dilution with anisole was spun on at 3000 RPM for 60 seconds (approximate 200 nm thickness), followed by a 180° C bake in the oven for 40 minutes. ZEP520A was chosen due to its high etch-resistance. (iv) The sample was then submitted for e-beam lithography. In order to determine the correct electron dose for writing, a substrate consisting of the same pattern with varying doses was written and examined by SEM. The final parameters of 1 nA, 4 nm diameter beam at a dose of 1000  $\mu\text{C}/\text{cm}^2$  at 8 VRUs. (v) Post-exposure, the resist was developed in O-xylene for 45 seconds, immediately followed by a 60 second IPA rinse and N<sub>2</sub> dried. As can be seen in the Figure, areas of the positive-tone resist exposed to the e-beam are more soluble and wash

away during development. **(vi)** Developed substrates were then taken to an Oxford System 100 T-Gate reactive-ion etching tool. Samples were cleaned by O<sub>2</sub> Plasma Ash at 10 sccm, 10 W, 50 mTorr followed by 100 nm Al etch using SiCl<sub>4</sub> gas at 18 sccm, 250 W, 9 mTorr at 20° C. **(vii)** Microposit Remover 1165 at 80° C was used to strip any remaining ZEP520A from the surface. **(viii)** A final O<sub>2</sub> plasma ash clean was then completed at 150 W / 3x10<sup>-1</sup> mTorr for 3 minutes. **(ix)** An Oxford Instrument Plasmalab 80Plus PECVD tool was used to deposit silicon dioxide using SiH<sub>4</sub>/N<sub>2</sub>O/N<sub>2</sub> = 7/146/85 sccm, 15 W, 1000 mTorr, 300° C with a deposition rate around 65 nm/min.

### 2.5.7 Surface Modifications

Various surface modifications were made to both Au and Al nanostructures. For the real-time biotin-avidin interaction observed in Chapter 3, the surface was modified by thiolation of the Au nanostructures with 11-mercaptoundecanoic acid (MUA) followed by modifications to the non-bound end of the MUA by 1-Ethyl-3-(3-dimethylaminopropyl)-carbodiimide then biotin hydrazide [14]. In Chapter 4, sensors in the optical tongue arrays were modified by thiolation of Au with 1-decanethiol and 1H,1H,2H,2H-perfluoro-1-decanethiol [15-16] and by silanisation of Al with 2-[methoxy (polyethyleneoxy)6-9 propyl] trimethoxysilane and hexamethyldisilazane [17-18]. Further details and information relating to the steps for each surface modification can be found in Chapter 3.3 and Chapter 4.3, respectively.

## 2.6 Characterisation Tools and Techniques

### 2.6.1 Atomic Force Microscopy (AFM)

Atomic Force Microscopy (AFM) allows for highly-accurate surface profiling, capable of viewing surface topology and roughness. A cantilever with a pyramid-shaped probing tip is moved across the surface of a sample in a raster pattern. The reflection of a laser off the backside of the cantilever is measured by a photodiode array and used to determine vertical displacement of the tip from (and thus the height of) the surface of the sample. In this work, an Icon AFM in ‘tapping’ mode was used to measure the surface roughness of the multilayered devices fabricated in Chapter 3. Tapping mode reduces potential damage of the tip and the sample during scanning by using high-frequency oscillations of the cantilever to ‘tap’ the surface rather than be in constant contact [19].

### 2.6.2 Ellipsometry

Ellipsometry is used to determine the thickness and dielectric (n,k) values of a material deposited on a sample [20-21]. The ellipsometer measures the change in polarisation of light reflected from a surface. By using fitting functions, the measurements from the ellipsometer can be used to then determine the aforementioned values. In this work, a J.A. Woollam Mark II Variable Angle Spectroscopic Ellipsometer was used for measuring the silicon nitride layer deposited on the devices of Chapter 3.

### 2.6.3 Scanning Electron Microscopy (SEM)

Scanning electron microscopy (SEM) allows for higher resolution image capturing when compared to light microscopy because the focused electron beam is orders of magnitude smaller than a focused region capable with light.

An SEM works in the following way: An electron gun generates a beam of electrons in a high-vacuum column. Electromagnetic lenses focus the beam and coils deflect it to scan the surface of an area. Modifying the lenses and apertures of the SEM allow for the control of beam size. To produce a high-resolution image, a secondary electron (SE) detector is used to detect the signal from the surface of the sample. Additionally, some SEMs have back-scattering electron detectors (BSE) and X-ray detectors (XRD) that allow for better resolved images and even chemical analysis. The combination between voltage, current, and working-distance from the sample affect the resolution of the image. Adjusting the focal distance and stigma in X and Y fine-tunes the resolution of the image. For samples that are not conductive, typically a conductive layer is sputtered over the sample to prevent charge build-up and allow for clear image generation.

In this work, images of structures were taken using both a Hitachi S4700 SEM tool and a Hitachi SU8240 SEM tool. Depending on if a spun-on polymer charge conduction layer was used, the SEM tools were operated at either 5 kV / 10  $\mu$ A (without) or 10 kV / 20  $\mu$ A (with). The charge-conduction polymer used was Electra-92, spun onto the sample at 4000 RPM for 60 seconds followed by a 2-minute hotplate bake at 90° C. The Hitachi SU8240 was always operated with both SE and BSE.

### 2.6.4 Spectrophotometry

A spectrophotometer is a device that is used to measure the transmission, reflection, or absorption of a sample as a function of either wavelength, electron volts, or wavenumber. For this research, only transmission measurements were used. Transmittance is the ratio of the intensity of light that is able to transmit (pass through) a sample to the intensity of the reference light without passing through the sample. Depending on the spectrophotometer, either a diffraction grating at the light source can be rotated to generate monochromatic light of different wavelengths (and a photodetector can measure each wavelength individually) or a diffraction grating at the detector can be used to split the light monochromatically and simultaneously measure each wavelength.

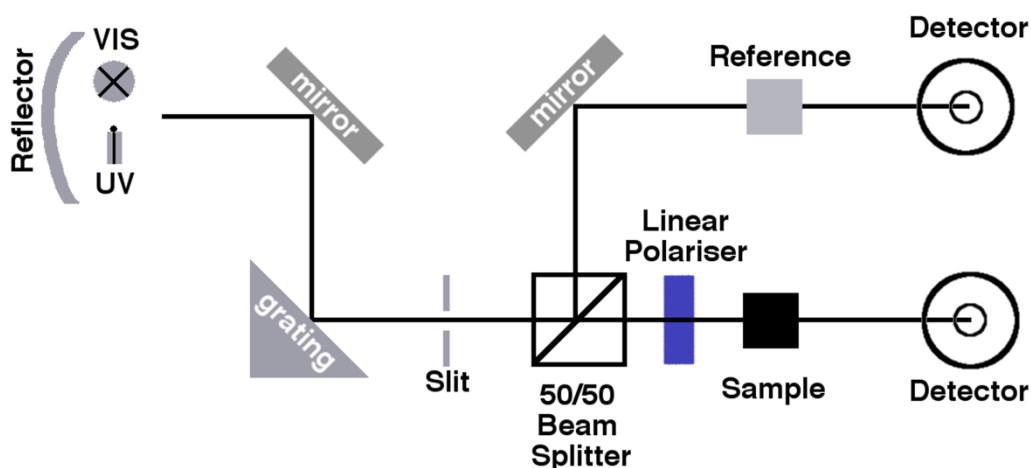


**Figure 2.9:** Schematic of a double-beam UV-VIS-NIR spectrophotometer. A grating is used to diffract light into subsequent wavelengths and transmitted through a reference and sample. The beam-width is controlled by the slit and the polarisation is controlled by the linear polariser.

Transmission measurements on the millimetre scale were measured on a Shimadzu UV3101PC spectrophotometer (see **Figure 2.9**). This spectrophotometer used a double beam of UV-VIS-NIR light and rotated a diffraction grating at the light source. This was mostly used for measuring the transmission spectra of the substrates from Chapter 5. Substrates were attached to a vertical stage and aligned to a 1 mm hole. A diffraction grating generating monochromatic light in the UV-VIS-NIR spectrum was used (350 nm to 1000 nm). A change in the grating occurred at 894 nm, resulting in a slight discontinuity around that wavelength. Prior to measurements, a baseline scan was used to calibrate the detectors, and the 1 mm pinholes of two empty holders were aligned in the reference and sample

positions. To take measurements of actual samples, Blu-Tack was used to adhere them flush against the holder in the sample position. Blank glass was adhered, in the same fashion, to the holder in the reference position. The test sample was rotated to the parallel and perpendicular positions relative to the incident polarisation.

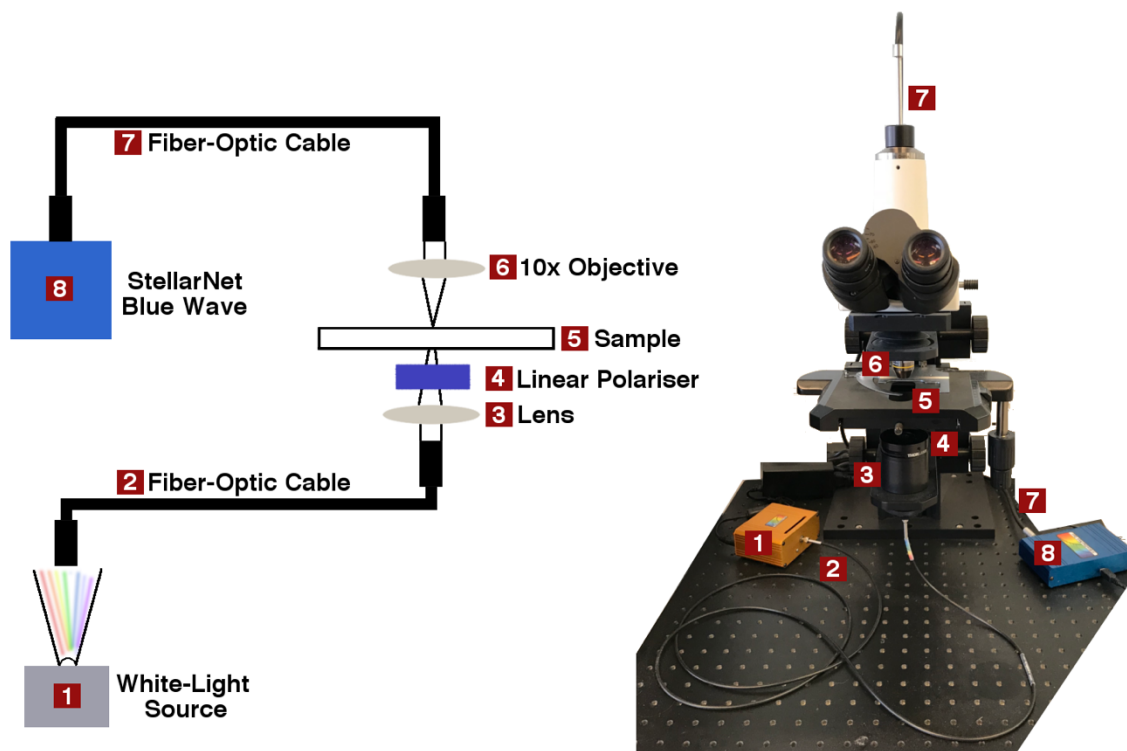


**Figure 2.10: Microspectrophotometer optical diagram and photograph.** Fiber-optic cables and lenses are used to focus white light on a sample and measure the transmission of light through it using the StellarNet Blue Wave box. The numbering in the schematic (left) correlates with the numbered labels in the photograph (right).

Transmission measurements on the micro-scale were measured on a custom-built microspectrophotometer. Light from a VIS-NIR light source (tungsten-halogen 400 to 1200 nm wavelength) was used to probe the sensor. **Figure 2.10** shows a schematic of the optics and photo of the microspectrophotometry device. A 10x objective was used to couple the transmitted light into an optical fibre attached to a StellarNet Microspectrophotometer (StellarNet Blue Wave, 0.5 nm resolution) with a diffraction grating at the detector for the simultaneous measurement of monochromatic wavelengths of light. This resulted in a spot size of approximately 45  $\mu\text{m}$ . Prior to taking measurements of actual samples, a light reference (a spot from a blank region of the sample) and dark reference (measurement when the shutter was closed) were taken. Integration time and number of scans to average varied depending on whether or not a linear polarisation filter was used. This set up was used for the real-time measurements of Chapter 3, optical tongue measurements of Chapter 4, and

the angle-dependency measurements of Chapter 5 (see the Section 3 of these chapters for details on the parameter settings of the microspectrophotometer).

For polarisation-dependent measurements on either spectrophotometer, a Thorlabs linear polariser was placed between the incident light and the sample.

## 2.7 Data Analysis Techniques

### 2.7.1 Transmission Trough Determination

MATLAB and Origin were used to analyse of the transmission spectra for each series of the real-time measurements.

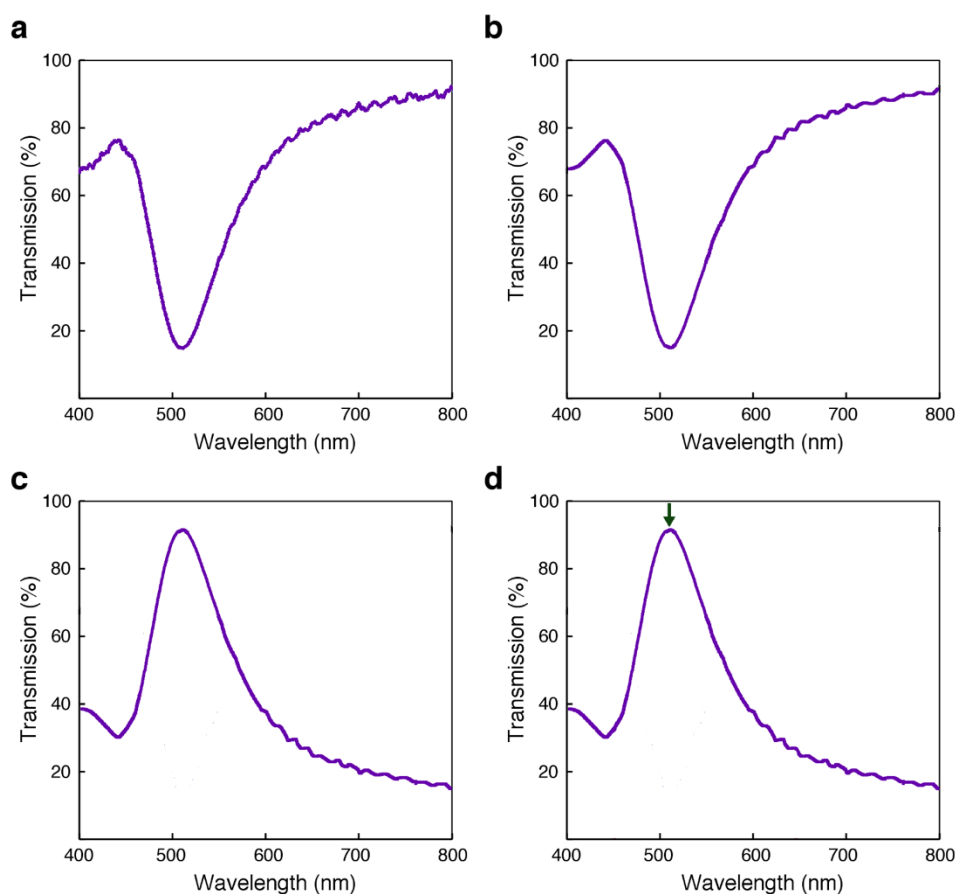


**Figure 2.11: Determination of the transmission trough using MATLAB.** (a) Raw data was (b) smoothed (20 points, mean-average) and interpolated (0.5 nm to 0.01 nm), (c) then inverted. (d) Next, the MATLAB findpeaks function (minimum peak distance 100 nm, minimum peak prominence of 0.1) was used to obtain the position of the ‘peak.’

The wavelength in nanometers and transmission value of the two minima were determined using MATLAB. The raw spectrum data (**Figure 2.11a**) was smoothed (20 points, mean-

average smoothing) and interpolated (from the 0.5 nm resolution of the microspectrophotometer to 0.01 nm) (**Figure 2.11b**). The spectrum was then inverted to make the troughs become peaks (**Figure 2.11c**). Next, the *findpeaks* function with a minimum peak distance of 100 nm and minimum peak prominence of 0.1 was used to determine the resonance position (**Figure 2.11d**).

The FWHM values were determined using inherent functions in Origin.

### 2.7.2 Principal Component Analysis (PCA) and Linear Discriminant Analysis (LDA)

Principal Component Analysis (PCA) is a multivariate analysis technique used to look at the structure of a set of data. Denoting the dataset as an  $n$  by  $p$  matrix called  $\mathbf{X}$ , the  $n$  rows are considered ‘objects’ or ‘observations,’ and the  $p$  columns are considered ‘variables’ that contain the measurements made on the  $n$  objects. PCA is commonly used to do the following: dimensionally reduce the  $p$  variables of matrix  $\mathbf{X}$  to the most-important components, identify outliers, delineate classes, model the data, and predict outcomes from measurements made on unknown objects [22].

In PCA,  $\mathbf{X}$  is transformed into a new coordinate system (the *score* matrix  $\mathbf{T}$ ) based on the variance (from greatest to least) of each component by an orthogonal linear transformation. The orthogonal linear transformation works in the following way: Each row of  $\mathbf{X}$  denoted as  $\mathbf{x}_{(i)}$ , is mapped to a new vector of principal component (PC) scores  $\mathbf{t}_{(i)}$  by a unit vector  $\mathbf{w}_{(k)}$  (called *loadings*) such that each component of the resulting score vector  $\mathbf{t}_{(i)}$  inherits the maximum possible variance from  $\mathbf{x}$ . The matrix of loading vectors  $\mathbf{W}$  is defined as the eigenvectors of  $\mathbf{X}^T\mathbf{X}$ , and the full matrix of scores  $\mathbf{T}$  is thus defined by  $\mathbf{T} = \mathbf{X}\mathbf{W}$  [22]. For the resulting score matrix  $\mathbf{T}$ , the rows correspond to the same  $n$  observations as in  $\mathbf{X}$ , and the columns correspond to the components of the dataset.

Quantification of the capabilities of a PCA is determined by its dimensionality, the distance between the groupings of repetition measurements, and ‘tightness’ within each grouping. The dimensionality of the PCA is measured by the number of components required to achieve 95% cumulative variance.

LDA is a supervised technique similar to PCA. It is typically applied to data to generate new “scores” that maximise the ratio of between sample variance of known groups whilst minimising variance within each group. Unlike PCA, LDA is a biased technique in that the

classification of each sample is known beforehand and taken into account during analysis [23].

In Chapter 4, PCA and LDA are used to analyse the optical tongue and determine its ability to classify different concentrations of organic solvents and different whiskies. An example data matrix for PCA and LDA are found in Chapter 4.3.6.

### 2.7.3 CIE XYZ Spectra

The International Commission on Illumination (CIE) 1931 [24] chromaticity diagram (**Figure 2.12**) is a graphical representation of the link between perceived human colour vision and the electromagnetic spectrum of visible light. Using the chromaticity values of X, Y, and Z, any colour can be calculated based on the colour matching functions [25].

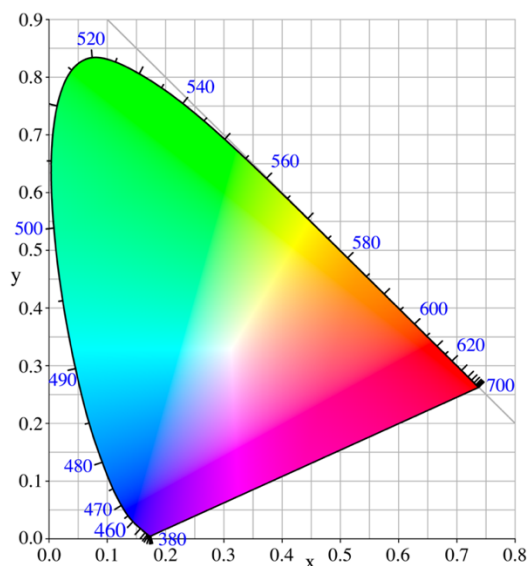


**Figure 2.12: CIE 1931 chromaticity diagram.** The CIE diagram is a graphical representation of the link between perceived human colour vision and the electromagnetic spectrum of visible light.

The CIE figures found in Chapter 5 were produced by loading measured transmission spectra into CIE1931xy.V.1.6.0.2a software.

## 2.8 Conclusion

This chapter contained an overview of the materials and fabrication processes used for making the plasmonic structures described in this work. Additionally, characterisation tools,

simulation techniques, and data analysis techniques were presented and explained. More specific details can be found in the subsequent experimental chapters.

## 2.9 References

- [1] Yee, K. S. Numerical Solution of Initial Boundary Value Problems Involving Maxwells Equations in Isotropic Media. *Ieee Transactions on Antennas and Propagation* **1966**, *AP14* (3), 302-&.
- [2] Taflove, A.; Hagness, S. C.; Picket-May, M. Computational Electromagnetics: The Finite-Difference Time-Domain Method. *Electrical Engineering Handbook* **2005**, 629-670, DOI: 10.1016/b978-012170960-0/50046-3.
- [3] Rumble, J. R.; Lide, D. R.; Bruno, T. J. *Crc Handbook of Chemistry & Physics*, 98 ed.; CRC Press: Boca Raton, USA, 2017.
- [4] Palik, E. D. *Handbook of Optical Constants of Solids*, Academic Press: 1997; Vol. I-III.
- [5] Cumming, D. R. S.; Thoms, S.; Weaver, J. M. R.; Beaumont, S. P. 3 Nm Nicr Wires Made Using Electron Beam Lithography and Pmma Resist. *Microelectron. Eng.* **1996**, *30* (1-4), 423-425, DOI: 10.1016/0167-9317(95)00278-2.
- [6] Mohammad, M. A.; Muhammad, M.; Dew, S. K.; Stepanova, M. Fundamentals of Electron Beam Exposure and Development. In *Nanofabrication*; Stepanova, M.; Dew, S. K., Eds.; Springer-Verlang: Wien, 2012; Chapter 2.
- [7] Miyauchi, S.; Tanaka, K.; Russ, J. C. Automatic Pattern Positioning of Scanning Electron Beam Exposure. *Ieee Transactions on Electron Devices* **1970**, *ED17* (6), 450-&, DOI: 10.1109/t-ed.1970.17008.
- [8] Docherty, K. E.; Lister, K. A.; Romijn, J.; Weaver, J. M. R. High Robustness of Correlation-Based Alignment with Penrose Patterns to Marker Damage in Electron Beam Lithography. *Microelectron. Eng.* **2009**, *86* (4-6), 532-534, DOI: 10.1016/j.mee.2008.11.037.
- [9] Martinu, L.; Poitras, D. Plasma Deposition of Optical Films and Coatings: A Review. *J. Vac. Sci. Technol. A* **2000**, *18* (6), 2619-2645, DOI: 10.1116/1.1314395.
- [10] Lee, J. W.; Mackenzie, K. D.; Johnson, D.; Sasserath, J. N.; Pearton, S. J.; Ren, F. Low Temperature Silicon Nitride and Silicon Dioxide Film Processing by Inductively Coupled Plasma Chemical Vapor Deposition. *J. Electrochem. Soc.* **2000**, *147* (4), 1481-1486, DOI: 10.1149/1.1393382.
- [11] Elgaid, K.; Zhou, H.; Wilkinson, C. D. W.; Thayne, I. G. Low Temperature High Density Si<sub>3</sub>n<sub>4</sub> Mim Capacitor Technology for Mmic and Rf-Mems Applications. *Microelectron. Eng.* **2004**, *73-4*, 452-455, DOI: 10.1016/j.mee.2004.03.016.
- [12] Oehrlein, G. S. Reactive-Ion Etching. *Phys. Today* **1986**, *39* (10), 26-33, DOI: 10.1063/1.881066.
- [13] Sendra, J. R.; Anguita, J.; Perezcamacho, J. J.; Briones, F. Reactive Ion-Beam Etching of Aluminum Indium-Antimonide, Gallium Indium-Antimonide Heterostructures in Electron-Cyclotron-Resonance Methane/Hydrogen/Nitrogen/Silicon Tetrachloride Discharges at Room-Temperature. *Applied Physics Letters* **1995**, *67* (22), 3289-3291, DOI: 10.1063/1.115223.
- [14] Lopez-Munoz, G. A.; Estevez, M. C.; Cristina Pelaez-Gutierrez, E.; Homs-Corbera, A.; Carmen Garcia-Hernandez, M.; Ignacio Imbaud, J.; Lechuga, L. M. A Label-Free Nanostructured Plasmonic Biosensor Based on Blu-Ray Discs with Integrated

- Microfluidics for Sensitive Biodetection. *Biosens. Bioelectron.* **2017**, *96*, 260-267, DOI: 10.1016/j.bios.2017.05.020.
- [15] Poirier, G. E. Coverage-Dependent Phases and Phase Stability of Decanethiol on Au(111). *Langmuir* **1999**, *15* (4), 1167-1175, DOI: 10.1021/la981374x.
- [16] Pflaum, J.; Bracco, G.; Schreiber, F.; Colorado, R.; Shmakova, O. E.; Lee, T. R.; Scoles, G.; Kahn, A. Structure and Electronic Properties of CH<sub>3</sub>- and CF<sub>3</sub>-Terminated Alkanethiol Monolayers on Au(111): A Scanning Tunneling Microscopy, Surface X-Ray and Helium Scattering Study. *Surf. Sci.* **2002**, *498* (1-2), 89-104, DOI: 10.1016/s0039-6028(01)01495-9.
- [17] Tasaltin, N.; Sanli, D.; Jonas, A.; Kiraz, A.; Erkey, C. Preparation and Characterization of Superhydrophobic Surfaces Based on Hexamethyldisilazane-Modified Nanoporous Alumina. *Nanoscale Res. Lett.* **2011**, *6*, 8, DOI: 10.1186/1556-276x-6-487.
- [18] Popat, K. C.; Mor, G.; Grimes, C. A.; Desai, T. A. Surface Modification of Nanoporous Alumina Surfaces with Poly(Ethylene Glycol). *Langmuir* **2004**, *20* (19), 8035-8041, DOI: 10.1021/la049075x.
- [19] Garcia, R.; Perez, R. Dynamic Atomic Force Microscopy Methods. *Surf. Sci. Rep.* **2002**, *47* (6-8), 197-301, DOI: 10.1016/s0167-5729(02)00077-8.
- [20] Rothen, A. The Ellipsometer, an Apparatus to Measure Thicknesses of Thin Surface Films. *Rev. Sci. Instrum.* **1945**, *16* (2), 26-30, DOI: 10.1063/1.1770315.
- [21] Thompkins, H.; Harber, E. A., *Handbook of Ellipsometry*. William Andrew Publishing: NY, 2005.
- [22] Wold, S.; Esbensen, K.; Geladi, P. Principal Component Analysis. *Chemometrics and Intelligent Laboratory Systems* **1987**, *2* (1-3), 37-52, DOI: 10.1016/0169-7439(87)80084-9.
- [23] Stewart, S.; Ivy, M. A.; Anslyn, E. V. The Use of Principal Component Analysis and Discriminant Analysis in Differential Sensing Routines. *Chem. Soc. Rev.* **2014**, *43* (1), 70-84, DOI: 10.1039/c3cs60183h.
- [24] Smith, T.; Guild, J. The Cie Colorimetric Standards and Their Use. *Trans. Opt. Soc.* **1932**, *33*, 73.
- [25] Fairman, H. S.; Brill, M. H.; Hemmendinger, H. How the Cie 1931 Color-Matching Functions Were Derived from Wright-Guild Data. *Color Research and Application* **1997**, *22* (1), 11-23, DOI: 10.1002/(sici)1520-6378(199702)22:1<11::aid-col4>3.0.co;2-7.

## Chapter 3: Multilayered Nanoplasmonic Arrays for Self-Referenced Biosensing

### 3.1 Introduction

When it comes to molecular-based sensing, as mentioned in Chapter 1.3.1, plasmonic-based techniques have advantage over other techniques. SPR, especially has long been used as a label-free optical biosensing technique [1]. While a powerful tool for sensing, the use of SPR sensors in point-of-care devices is typically hindered by miniaturisation problems and complex supporting optics [2-3]. As an alternative, sensors based on LSPR have been demonstrated to have similar performance to SPR sensors [4]. While SPR relies on the propagation of surface plasmon polaritons on a continuous metal film, LSPR is localised to structures on the nanoscale. Therefore, LSPR allows for the use of more compact optics, does not need precise temperature control, and thus has the potential to be miniaturised beyond the capabilities of SPR sensors [5]. For example, LSPR sensors were demonstrated in the parallel biosensing of 32 independent sensor elements on the same chip [2].

Sensors based on LSPR offer unprecedented advantage as real-time, label-free, and easily miniaturised chemical and biological detectors [2-3, 5-15]. As previously discussed in Chapter 1, the resonance peaks of plasmonic nanostructures are highly sensitive to local refractive index changes and shift by different amounts when subject to different biological and chemical environments. Modifications to the nanostructure surface can also allow for detection of specific molecules and chemicals with shifts so sensitive that the presence of single molecules can be detected. This highly localised sensing minimises bulk refractive index (RI) effects [3, 6-7] and has been used for real-time, label-free detection of nanoscale biochemical events such as protein-substrate binding [5-6, 8-9], antibody-antigen binding [2-3, 10], and DNA base pairing [5, 11-13]. However, this extreme sensitivity has its drawbacks. Resonance shifts also occur due to light intensity fluctuations and other environmental factors.

Since LSPR is highly responsive to a multitude of changes on the nano-scale, a reference is required to determine if a detected event is from a desired signal or some sort of drift [14]. This is especially problematic for devices designed for point of care applications, where a sensor is more likely to be exposed to environments where precise control of external

factors—such as intensity fluctuations of the light source, temperature, and humidity, for example—is not possible. A separate reference channel is typically used to address this issue. However, a two-channel design often makes devices at least twice as big, requires two light sources and detectors (or complex optical setups) to obtain sensing and reference signals, requires the injection of potentially expensive or of limited quantity samples into a non-capturing channel, and subjects the reference to potential biofouling [15-16].

To address this challenge, a variety of self-referencing sensor technologies have been explored. Examples include dual-metal SPR sensors [17-18], modified Mach-Zehnder Interferometer phase sensors [19-21], porous silicon double layer sensors [22-23], photochemical sensors [24], nanohole LSPR sensors [25], refractometric LSPR sensors [26], dual-metal suspended colloid LSPR sensors [27], and polarisation-dependent sensors [14], to name a few.

In this chapter, a proof-of-concept multilayered LSPR sensor with internal-referencing that self-corrects for baseline drift is explored. Comprised of both an encapsulated and an exposed nanoplasmonic layer, this device exhibits two distinct peaks: a reference peak from the encapsulated layer and a sensing peak from the exposed layer. The presence of the reference layer directly below the sensing layer allows for the correction of any drift that may occur during real-time chemical and biosensing experiments using single measurement from a single beam of light.

Additionally, utilising one channel rather than separate sensing and referencing channels allows for a more compact design and eliminates the need to inject potentially expensive samples into a parallel reference channel [17].

This design also offers advantage over the other technologies in that the self-referencing mechanism does not require spatial control over different surface modifications [17-18] and is not subject to fouling because the reference layer is isolated from the sensing region [17-18, 22-26]. Additionally, this device self-corrects rather than just recognising “unreliable data” [24], can be regenerated and thus reused in multiple detection events rather than being consumed during detection [27], and doesn’t require multiple detectors [26] or a beam-splitter [14].

The first section of this chapter reviews the device design and fabrication steps. The second section discusses device characterisation and calibration. The third and fourth sections of this chapter discuss experimental analysis of the device in the real-time detection of chemical and biological molecules, respectively. The final section of this chapter compares FDTD simulation of the final design of the device and to the experimental results.

The majority of work detailed in this chapter was published by J.R. Sperling, G. Macias, S.L. Neale, and A.W. Clark (2018) [28].

## 3.2 Materials

The materials used are available in Chapter 2.

## 3.3 Methods

### 3.3.1 Fabrication of Multilayered Sensor

Devices were fabricated using electron-beam lithography as covered in Chapter 2.5 (See Metal Nanostructure Fabrication, Silicon Nitride Micro-Region Fabrication, and HSQ Micro-Region Fabrication). For both the reference and sensing nano-antenna layers, a resist bi-layer of PMMA 2010 and PMMA 2041 (total thickness 150 nm) was patterned using a Vistec VB6 UHR EWF electron beam lithography tool. Following development of the pattern, a 2/50 nm Ti/Au layer was evaporated onto the sample using a Plassys MEB 400S/550S electron-beam evaporation tool. The silicon nitride layer was deposited using an Oxford Instruments System 100 ICP 180 PECVD nitride deposition tool at room temperature. For devices with a hydrogen silsesquioxane (HSQ, Fox 16) layer, HSQ was spun on and then cross-linked using the electron-beam lithography tool. The final sensing nano-antenna layer was then fabricated on top of the device, following the same procedure as the fabrication steps of the reference layer. More detailed descriptions for each step of the fabrication process can be found in Chapter 2.

### 3.3.2 Experimental Setup

A polydimethylsiloxane (PDMS) microfluidic channel was placed on top of the device and a positive crankcase ventilation (PVC) valve was used to allow for sample injection without disrupting flow. The flow rate from the microfluidic pump was set to 100  $\mu\text{L}\cdot\text{min}^{-1}$ . A

custom-built microspectrophotometer was used to measure the real-time transmission spectra (0.5 nm resolution). Light from a visible to near-infrared light source (tungsten-halogen 400 to 1200 nm wavelength) was used to probe the sensor. A 10x objective was used to couple the transmitted light into an optical-fibre attached to a StellarNet Microspectrophotometer (StellarNet Blue Wave).

### 3.3.3 Peak Analysis

MATLAB and Origin were used to analyse of the transmission spectra for each series of the real-time measurements. The transmission spectrum was smoothed (20 points, mean-average smoothing) and interpolated (from 0.5 nm to 0.01 nm). The peak position value of the two minima peaks and full-width half-max (FWHM) values were determined. The corrected position response (CPR) was calculated by subtracting the position of the sensing peak from the reference peak.

### 3.3.4 Sensor Calibration

For the calibration experiments, water containing varying concentrations of dissolved sucrose (Sigma Aldrich), from 0.5% to 50% (w/w) was introduced to the device. The refractive index of the surrounding medium was, thus, altered from 1.333 to 1.4201 [29]. A sample rate of 7.5 seconds was used to capture a 30-measure-averaged transmission response.

### 3.3.5 Device Functionalisation

The sensor was immersed in a 10 mM ethanolic solution of 11-mercaptoundecanoic acid (MUA, Sigma Aldrich) overnight, rinsed three times with ethanol, dried under a stream of nitrogen, and assembled with the microfluidic system. A constant flow rate of  $100 \mu\text{L} \cdot \text{min}^{-1}$  was maintained throughout the functionalisation steps. The channel was flushed with water for 20 min prior to the injection of 500  $\mu\text{L}$  of 200 mM 1-Ethyl-3-(3-dimethylaminopropyl)-carbodiimide (EDC, Sigma Aldrich) in MES buffer at pH 5.5 and rinsed with deionised (DI) water for 15 min. 500  $\mu\text{L}$  of 500  $\mu\text{g} \cdot \text{mL}^{-1}$  biotin hydrazide (Sigma Aldrich) in DI water was then injected, followed by a DI water rinse for a further 15 min. Finally, unreacted sites were blocked with 500  $\mu\text{L}$  of 1 M ethanolamine (Sigma Aldrich) in DI water and rinsed with DI water for 15 min.

### 3.3.6 Biological Sensing

0.1% Tween-20 in phosphate buffer saline (PBS) was used as the flowing solution throughout the experiments. Prior to the biological sensing, the device was stabilized by flowing the PBS solution at  $100 \mu\text{L}\cdot\text{min}^{-1}$  for 30 min. Throughout the experiments, the flow rate was kept constant at  $100 \mu\text{L}\cdot\text{min}^{-1}$  and at least 10 min of baseline were acquired before the biomolecule injection. Sensor regeneration was achieved by injecting 500  $\mu\text{L}$  of 20 mM sodium hydroxide in DI water. As a non-specific control, 500  $\mu\text{L}$  of  $100 \mu\text{g}\cdot\text{mL}^{-1}$  bovine serum albumin was injected. Finally, 0.1, 1, 100 and 500  $\mu\text{g}\cdot\text{mL}^{-1}$  of avidin in 0.1% Tween-20 PBS was injected at a constant volume of 500  $\mu\text{L}$  in order to test the specificity and dose-dependency of the device. A sample rate of 3.5 seconds was used to capture a 30-measure-averaged transmission response.

### 3.3.7 FDTD Simulations

FDTD simulations were performed using Lumerical FDTD Solutions software.

#### 3.3.7.1 Optimisation Simulations

The optimisation simulation layout is shown in **Figure 3.1**. A linearly polarised plane wave was defined for a unit area cell with a period of 300 nm x 300 nm. For the form-following layer of silicon nitride, the dielectric values ( $n_2$ ,  $k_2$ ) as measured by ellipsometry for device 2 (shown in **Figure 3.9b**) were used with varying heights. For the simulation to determine the effect of nitride thickness on plasmonic response (depicted in **Figure 3.1** and investigated in Chapter 3.4.1.1), a rough-estimate of nitride deposition was used, where the side profile of nitride deposited on the nanostructures was 1/3 the height of the deposition. For the simulation to determine the effect of vertical distance between nanostructure arrays (investigated in Chapter 3.4.1.2), the nitride layer was simulated as a flat surface. The dielectric values of Au and titanium were obtained from the CRC library [30] and glass was obtained from the Palik library [31]. Periodic boundary conditions were used in the X-axis and Y-axis, and a perfectly-matched-layers (PML) boundary was used in the Z-axis. A uniform mesh size of 5 nm was used in all axes.

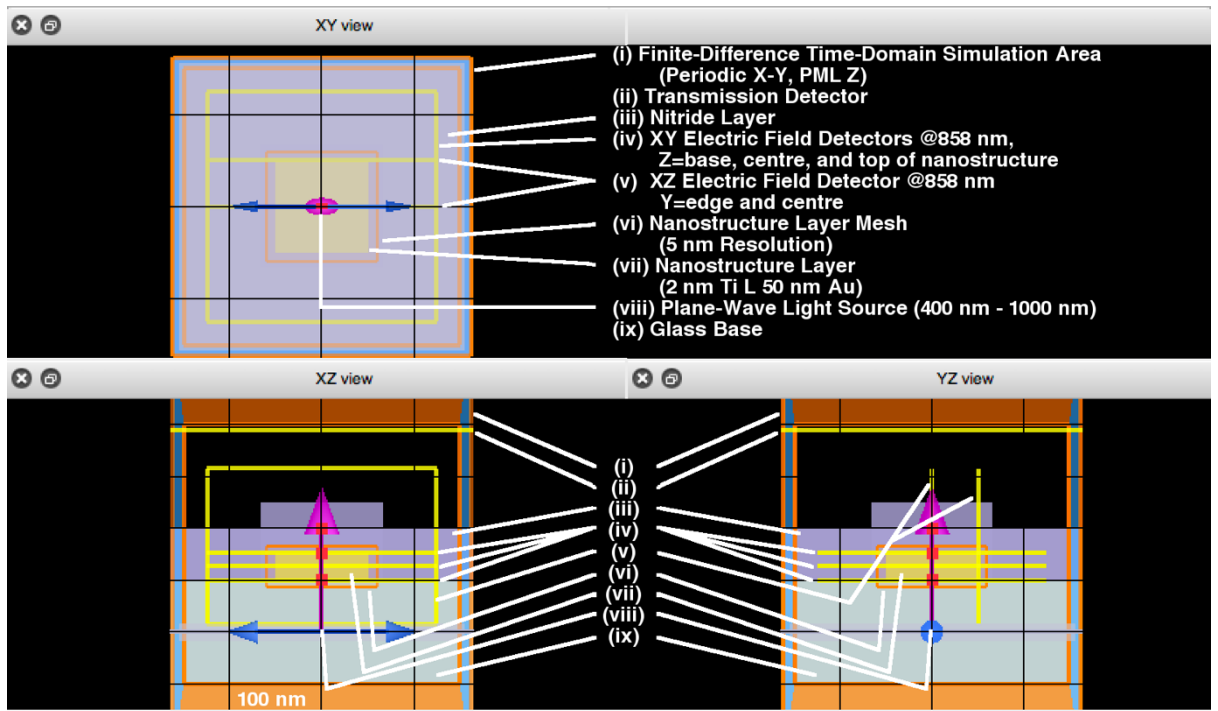


**Figure 3.1: FDTD simulation schematic for optimisation of the nitride encapsulated layer of the device.** The grid in each view is 100 nm x 100 nm. (i) FDTD simulation area of 300 nm x 300 nm. The FDTD area is simulated as periodic in X-Y and PML (perfectly-matched-layer) in Z. (ii) Transmission detector. (iii) Silicon nitride layer conforming to the array layer. The dielectric constants and thickness used came from measurements of the nitride layer deposited on the actual device ( $(n_2, k_2)$  from **Figure 3.4**). (iv) XY electric field detector for wavelength of 858 nm for Z at the nanostructure base, nanostructure centre, and nanostructure top. (v) XZ electric field detector for wavelength of 858 nm for Y at the nanostructure edge and nanostructure centre. (vi) 5 nm resolution mesh for the nanostructure. (vii) Nanostructure layer (2 nm Ti : 50 nm Au) with dielectric constants from the CRC library [30]. (viii) Plane-wave light source (400 nm to 1000 nm). (ix) Glass base with dielectric constants from the Palik library [31].

### 3.3.7.2 Full Device Simulation

The full device simulation is shown in **Figure 3.2**. A linearly polarised plane wave was defined for a unit area cell with a period of 300 nm x 300 nm. For the form-following layer of silicon nitride, the dielectric values ( $n_2, k_2$ ) and thickness as measured by ellipsometry for device 2 (shown in **Figure 3.9b**) were used. Unlike the optimisation simulations, the nitride layer was simulated as gradual rather than as a square block. The 320 nm thick HSQ layer was given a dielectric constant value of 1.4. The dielectric values of Au and titanium were obtained from the CRC library [30] and glass was obtained from the Palik library [31]. Periodic boundary conditions were used in the X-axis and Y-axis, and a perfectly-matched-layers (PML) boundary was used in the Z-axis. A uniform mesh size of 2.5 nm was used in all axes. In order to simulate both water and a range of sucrose solutions, the refractive index values of the surrounding medium altered between 1.333 and 1.4201 [29].

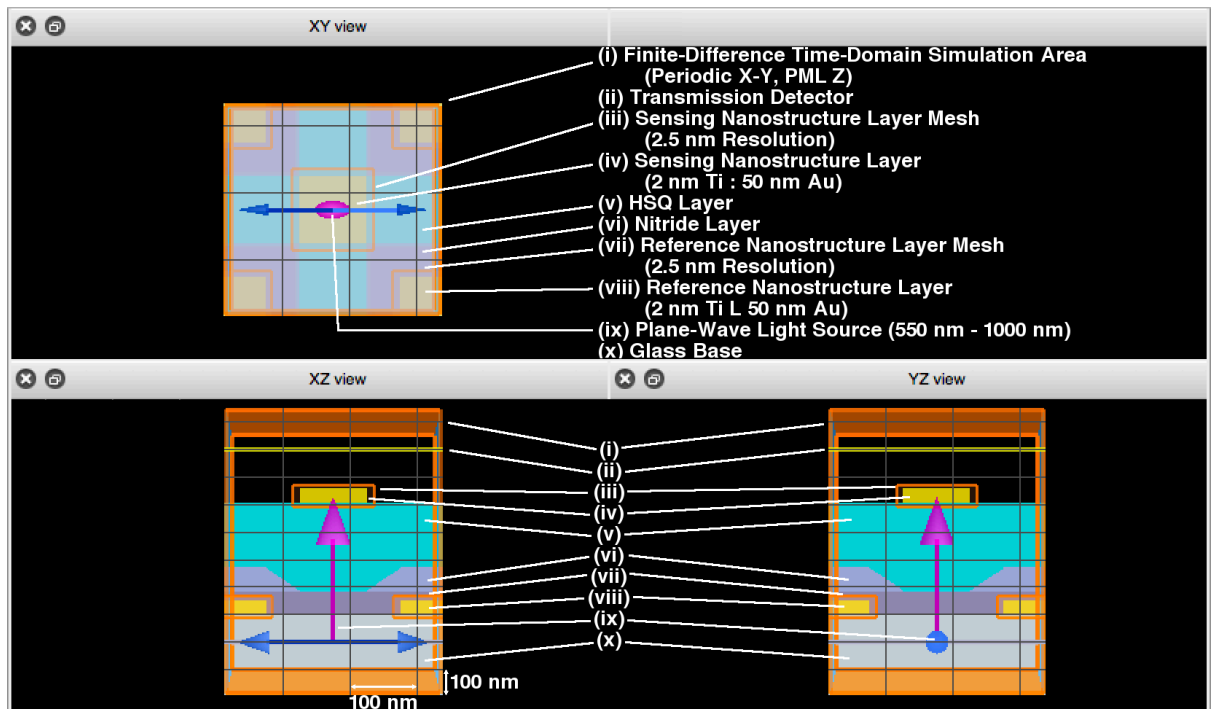


**Figure 3.2: FDTD simulation schematic of the full multilayered device.** The grid in each view is 100 nm x 100 nm. **(i)** FDTD simulation area of 300 nm x 300 nm. The FDTD area is simulated as periodic in X-Y and PML (perfectly-matched-layer) in Z. **(ii)** Transmission detector. **(iii)** 2.5 nm X-Y-Z resolution mesh for sensing layer. **(iv)** Sensing nanostructure layer (2 nm Ti : 50 nm Au) with dielectric constants from the CRC library [30]. **(v)** 320 nm thick HSQ layer with dielectric constant of 1.4. **(vi)** Silicon nitride layer conforming to the reference array layer. The dielectric constants and thickness used came from measurements of the nitride layer deposited on the actual device ( $(n_2, k_2)$  from **Figure 3.4**). **(vii)** 2.5 nm resolution mesh for the reference layer. **(viii)** Reference nanostructure layer (2 nm Ti : 50 nm Au) offset 150 nm in both X and Y from the sensing layer with dielectric constants from the CRC library [30]. **(ix)** Plane-wave light source (550 nm to 1000 nm). **(x)** Glass base with dielectric constants from the Palik library [31].

### 3.3.8 Surface Planarisation

Various thicknesses of HSQ were spun on to 50 nm tall nanostructures. AFM was used to measure surface roughness in order to determine the minimum thickness necessary for planarisation.

### 3.3.9 Nitride Characteristics

A J.A. Woollam Mark II Variable Angle Spectroscopic Ellipsometer was used to determine the thickness and dielectric (n,k) values of the nitride.

## 3.4 Results and Discussion

### 3.4.1 Design and Fabrication of Multilayer Sensor

The multilayer substrate design consists of two Au nanoarrays—an encapsulated reference array and exposed sensing array (**Figure 3.2**)—with a 2 nm thick titanium adhesion layer. Nanosquare shapes were chosen for this proof-of-concept design because (1) the design allows for easy, repeatable fabrication, (2) the symmetrical shape is not subject to a polarisation-dependent response, and (3) the shape maximises the surface area coverage for a given periodicity (and thus maximises the plasmonic signal). A periodicity of 300 nm was chosen to provide a significant enough distance between nanostructures to make plasmon coupling negligible [32] while still providing a strong plasmonic signal (>90% transmission-attenuation).

#### 3.4.1.1 FDTD Determination of Minimum Nitride Thickness

To determine the minimum thickness of nitride necessary to isolate the reference layer from detecting refractive index changes of the region above it, FDTD simulation of varying nitride thickness for different sized nano-prism shapes was carried out. **Figure 3.3a** shows (i) XY and (ii) XZ renderings of the various parameters simulated, where  $s$  is the length and width of the structure,  $t$  is the metal thickness,  $P$  is the period of the array, and  $h$  is the thickness of the nitride. For these simulations, the minimum thickness of nitride where peak resonance shifts are no longer observed signifies that the electric field of the structure is isolated from the refractive index of the region immediately above the nitride layer. **Figure 3.3b(i)** shows the simulated transmission of a nanostructure array where  $s = 100$  nm,  $t = 50$  nm,  $P = 300$  nm, and  $h$  is varied from 0 nm to 120 nm. The transmission peak red-shifts from  $h = 0$  to 80 nm and remains the same after 80 nm, signifying that for this structure, isolation occurs at  $h > 80$  nm. To further expand on this, simulations with varied  $h$  were also done for additional nanostructure prisms with  $s \times t$  (nm) of 50x25, 75x25, 100x25, 50x50, and 75x50. As seen by the plateaued regions in **Figure 3.3b(ii)**, the thickness of nitride where the resonance no longer shifts was also found to be at  $h > 80$  nm for the other simulated structures. Therefore, for electric field isolation, the nitride layer must be greater than 80 nm thick. The inset of **Figure 3.3b(ii)** shows the transmission value at the resonance peak. From the transmission plot in **Figure 3.3b(i)** and the transmission at peak plot in the inset of **Figure 3.3b(ii)**, the  $s = 100$ ,  $t = 50$  structure has the most attenuation with well-defined peaks for  $h = 0$  nm and  $h > 80$  nm (which would represent the sensing and reference regions, respectively). Thus, this structure was chosen for the proof-of-concept design. As the purpose of this design is to

evaluate the viability of the multilayer design for self-referencing, neither the geometry of the nanostructures nor the array periodicity was optimized to produce the most sensitive device.

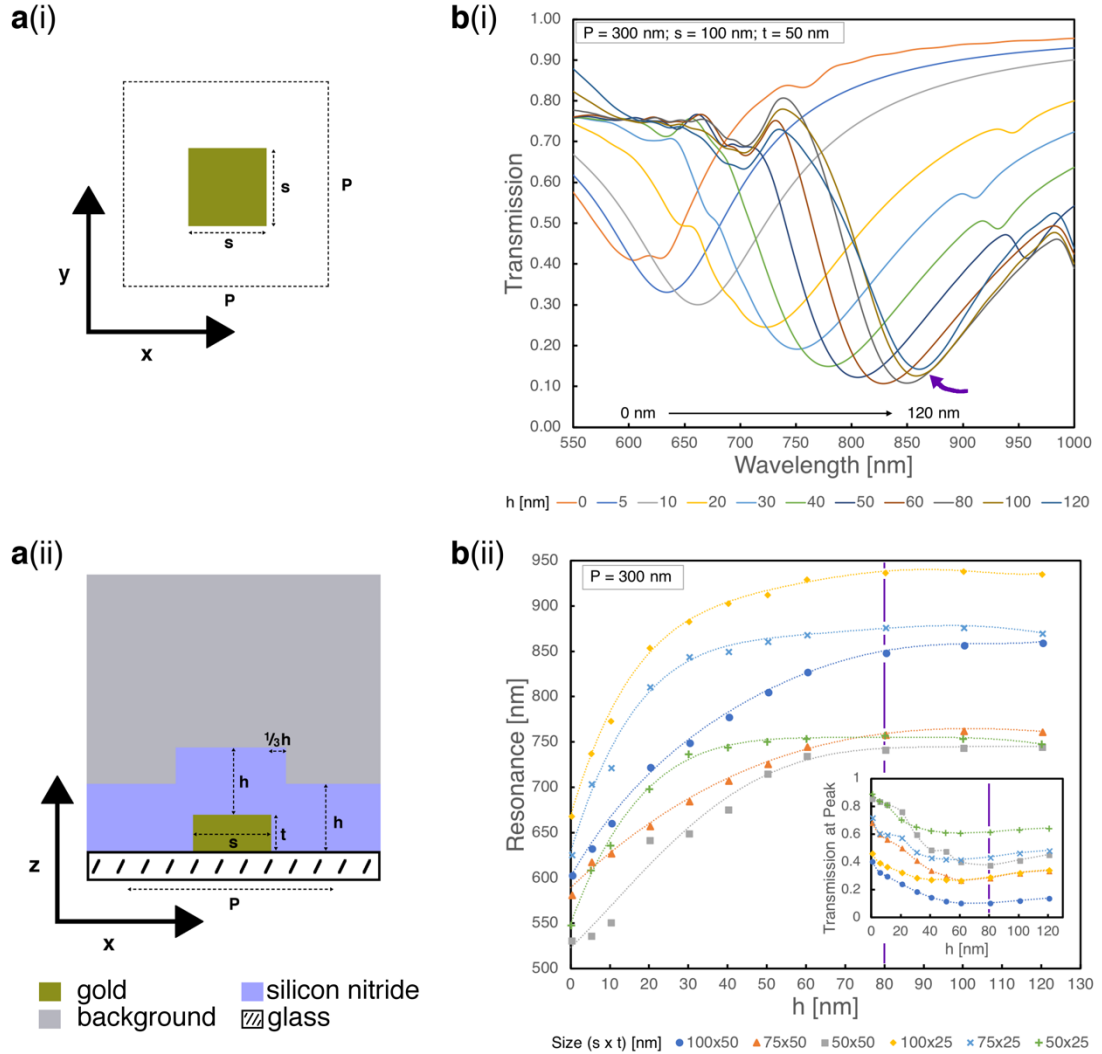


**Figure 3.3: FDTD Simulation for silicon nitride thickness.** (a) Rendering of the simulation in (i) XY and (ii) XZ for Au nanostructures with dimensions  $s$  by  $s$  by  $t$  and periodicity of  $P = 300$  nm. The height of nitride deposited ( $h$ ) was varied from 0 nm to 120 nm. The side-wall coverage for the nitride deposition is roughly  $1/3 h$ . (b)(i) Transmission response for  $s = 100$  nm and  $t = 50$  nm for increased nitride height  $h$ . After 80 nm of nitride, the peak position does not shift (purple arrow). (ii) Resonance position for square nanostructures with varying  $s$  (50 nm, 75 nm, and 100 nm) and  $t$  (25 nm and 50 nm), versus nitride thickness  $h$ . For  $h > 80$  nm (after the purple line), the resonance position plateaus, indicating the ideal thickness for isolation of the nanostructure. (inset) Transmission at peak for each of the nanostructures versus nitride thickness  $h$ . The  $s = 100$  nm,  $t = 50$  nm structure has the most attenuation at  $h=0$  nm and in the plateau region of  $h > 80$  nm (after the purple line).

The simulated electric field of the chosen structure ( $s = 100$  nm,  $t = 50$  nm, and  $P = 300$  nm) with  $h = 100$  nm (Figure 3.4a) shows how the electric field propagates and attenuates in the

nitride layer. As can be seen by the XY slices (**Figure 3.4b**) where Z is sliced at (i) the interface between the bottom of the nanostructure and glass base, (ii) the centre of the nanostructure, and (iii) at the interface between the top of the nanostructure and surrounding nitride, the high electric field is found at the corners of the nanostructure shape. As can be seen by the XZ slices (**Figure 3.4c**) where Y is sliced at (i) the centre and (ii) the edge of the structure, the high electric field is found at the top corners of the structure shape.

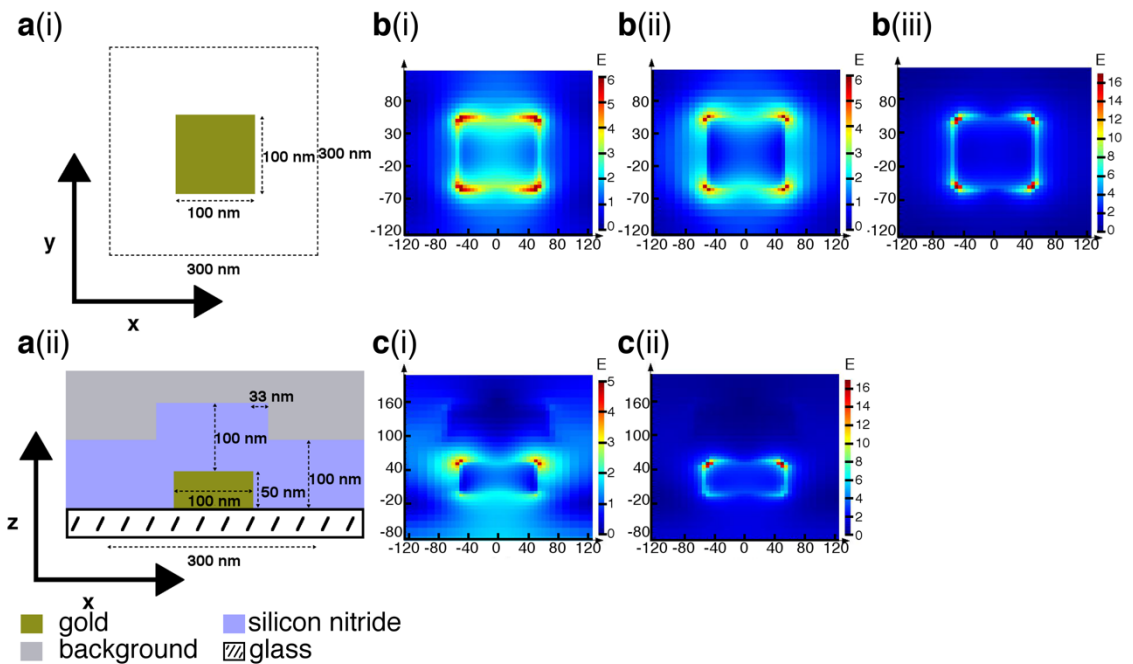


**Figure 3.4: FDTD of electric field for 100 nm x 100 nm x 50 nm Au nanostructure with 100 nm nitride deposited on top. (a) Rendering showing (i) XY and (ii) XZ views of the simulated region. The electric field at a wavelength of 858 nm was simulated for 100 x 100 x 50 nm (L x W x H) structures, with 100 nm nitride, and a periodicity of 300 nm. (b) The electric field in XY at slices in Z for at (i) the interface between the bottom of the structure and glass base, (ii) the centre of the structure, and (iii) the interface between the top of the structure and the surrounding nitride. (c) The electric field in XZ at slices in Y at (i) the centre of the structure and (ii) the edge of the structure. As can be seen by the electric field for each slice, the corners generate the highest electric field, especially at the interface between the nanostructure and the surrounding nitride.**

#### 3.4.1.2 FDTD Determination of Minimum Distance Between Nanoarray Layers

The FDTD simulation used to determine minimum nitride thickness was slightly altered to determine the minimum distance between the sensing and reference layer necessary to prevent plasmonic coupling between the layers. In this FDTD simulation, two arrays of 100 nm x 100 nm x 50 nm (L x W x H) Au nanostructures were simulated as shown in the rendering in **Figure 3.5a**. The thickness of nitride was varied to alter the distance  $D$  between

the nanostructures ( $10 \text{ nm} < D < 400 \text{ nm}$ ). To simplify the simulation, the silicon nitride layer was considered to be planar.

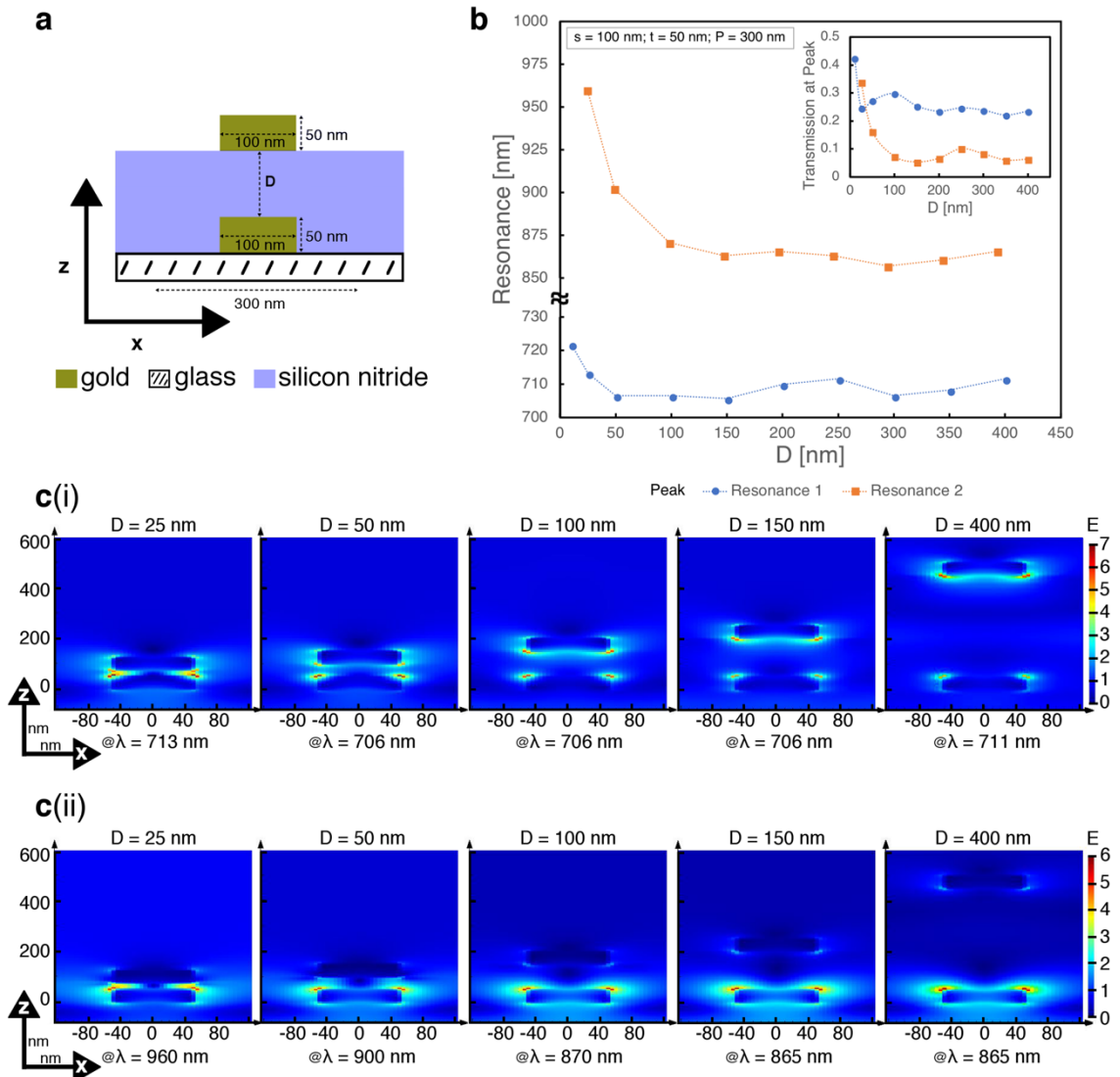


**Figure 3.5: FDTD simulation of the effect of altering the distance between two gold nanostructure array layers. (a)** Rendering of the device. The distance  $D$  between the structures was altered from  $10 \text{ nm}$  to  $400 \text{ nm}$ . **(b)** The resonance of the two most-significant peaks of the structure versus the distance between each structure. **(inset)** The transmission at the peak for each resonance. **(c)** The  $XZ$  electric field sliced where  $Y$  is at the centre of the nanostructures for wavelengths corresponding to **(i)** Resonance 1 and **(ii)** Resonance 2 from **(b)** for distance  $D$ . The resonant wavelength is indicated below each subfigure. In both **(b)** and **(c)**, coupling effects are minimal when  $D > 100 \text{ nm}$ .

**Figure 3.5b** shows the results of the simulation for the two resonant peaks in the transmission. **Figure 3.5c** shows the  $XZ$  electric field for each resonant peak where  $Y$  is at the centre of the nanostructure. Both confirm that coupling effects are minimal when the distance between array layers is at least  $100 \text{ nm}$ .

## 3.4.1.3 Determination of Minimum HSQ Thickness

Initially, a device consisting of 100 nm x 100 nm x 50 nm (L x W x H) Au nanostructure arrays with a 300 nm periodicity was made, where the sensing layer was directly fabricated on top of the nitride layer (**Figure 3.6a(i)**). The transmission in water of the nano-array layer on glass (blue line), nano-array layer encapsulated in nitride (orange line), and fully fabricated device (green line) are shown in **Figure 3.6a(ii)**.

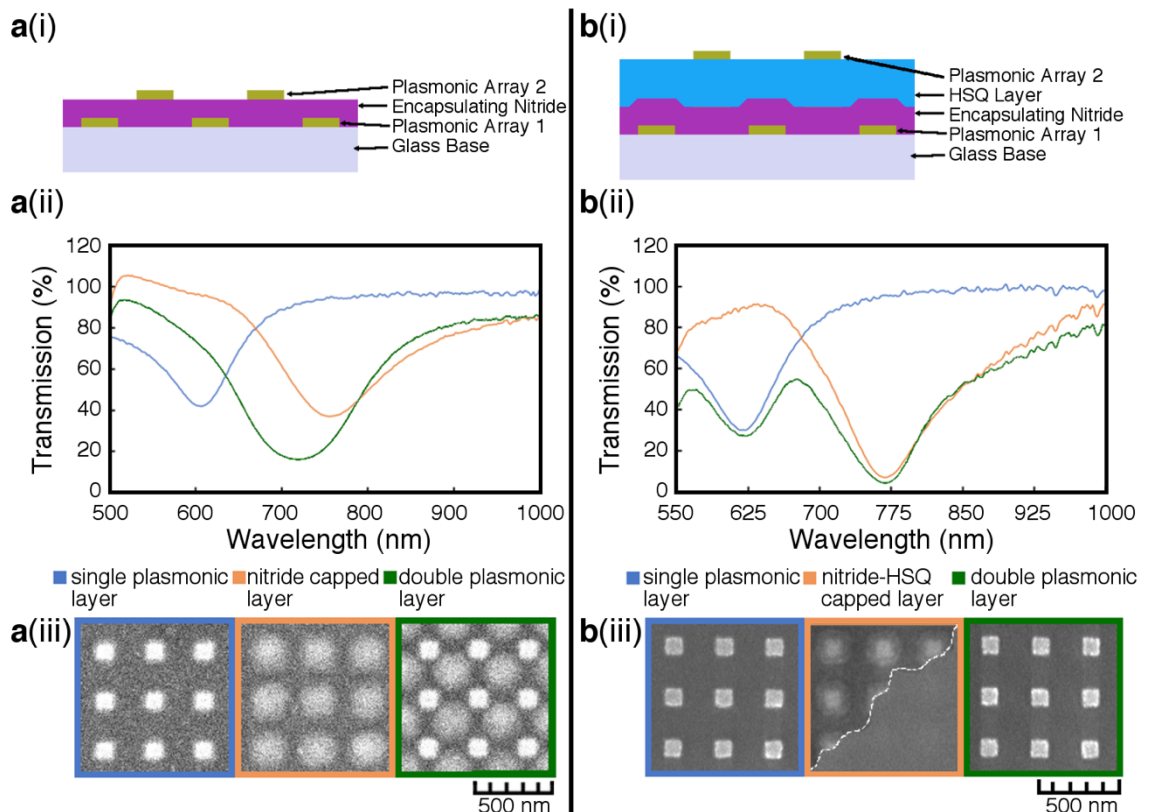


**Figure 3.6: Analysis of device fabrication using a silicon nitride encapsulated layer.** The multi-layered device where the reference layer is encapsulated in silicon nitride and the sensing layer is fabricated **(a)** directly on the nitride layer and **(b)** on an HSQ planarisation layer. The nanostructures for these devices were 100 nm x 100 nm x 50 nm (L x W x H) Au nanostructures. For both **(a)** and **(b)**, **(i)** a rendering showing the multi-layered device design; **(ii)** the transmission response, in water, immediately after fabrication of the first plasmonic layer (blue), encapsulating layer(s) (orange), and second plasmonic layer (green); and **(iii)** the corresponding SEM images taken after each layer is fabricated. The orange-boxed SEM image in **b(iii)** shows two SEM images combined, diagonally. The first just after the nitride deposition (top-left-half) and second just after the HSQ deposition (bottom-right-half). The nanoarrays for the layers in devices **(a)** and **(b)** were 100 nm x 100 nm x 50 nm Au with a period of 300 nm.

As expected, the transmission spectra of the nanostructure array red-shifts when it is encapsulated in nitride. However, the transmission of the fully fabricated device has only

one peak where two (one from each the encapsulated and exposed nano-arrays) were expected.

The transmission response of the full device in **Figure 3.6a** is best understood by examining the corresponding SEM images at each stage of the fabrication process (**Figure 3.6a(iii)**). The SEM images show that the nitride layer conforms to the nano-array layer below it and is not planar. By fabricating the sensing array directly on top of the nitride layer, each nanostructure of the sensing array was surrounded by nitride on all sides. The increased value of the refractive index surrounding the sensing layer resulted in a red-shifted transmission compared to that of the same designed nano-array on a planar surface. Thus, for device (a), the transmission signal from the reference and sensing plasmonic layers merged and produced a single-peak transmission (as shown in the green line of the transmission spectra of **Figure 3.6a(ii)**).

To resolve this, an HSQ planarisation step was added to the fabrication process. The device shown in **Figure 3.6b(i)** has an HSQ layer deposited between the nitride layer and second nanoarray layer. The transmission in water of the nanoarray layer on glass (blue line), nanoarray layer encapsulated in nitride and capped by HSQ (orange line), and fully fabricated device (green line) are shown in **Figure 3.6b(ii)**. Just like the device of **Figure 3.6a**, the transmission spectra of the nanoarray layer encapsulated in nitride is red-shifted from that of the structure prior to encapsulation. Unlike that of the device in **Figure 3.6a**, the transmission of the full device in **Figure 3.6b(ii)** has two, distinct peaks that match up with the signal from the nanoarray layer on glass (blue) and the nitride-encapsulated layer (orange). The SEM images in **Figure 3.6b(iii)** reveal that the HSQ layer planarises the conforming nitride layer and allows for the second nanoarray to be fully open to the environment surrounding each structure. This explains the two distinct peaks in **Figure 3.6b(ii)** for the multi-layered device (green plot) that align with that of the single layer (blue) and capped single layer (orange) transmission resonances. Thus, it was concluded that the HSQ layer was necessary for the design of the device.

To determine the minimum HSQ thickness necessary to planarise the surface, various HSQ thicknesses were spun on to structures of 50 nm x 50 nm x 50 nm (L x W x H) and 100 nm x 100 nm x 50 nm (L x W x H), as shown in **Figure 3.7**. For both sizes of structures, an HSQ thickness of 200 nm was found sufficient to planarise the nitride layer.

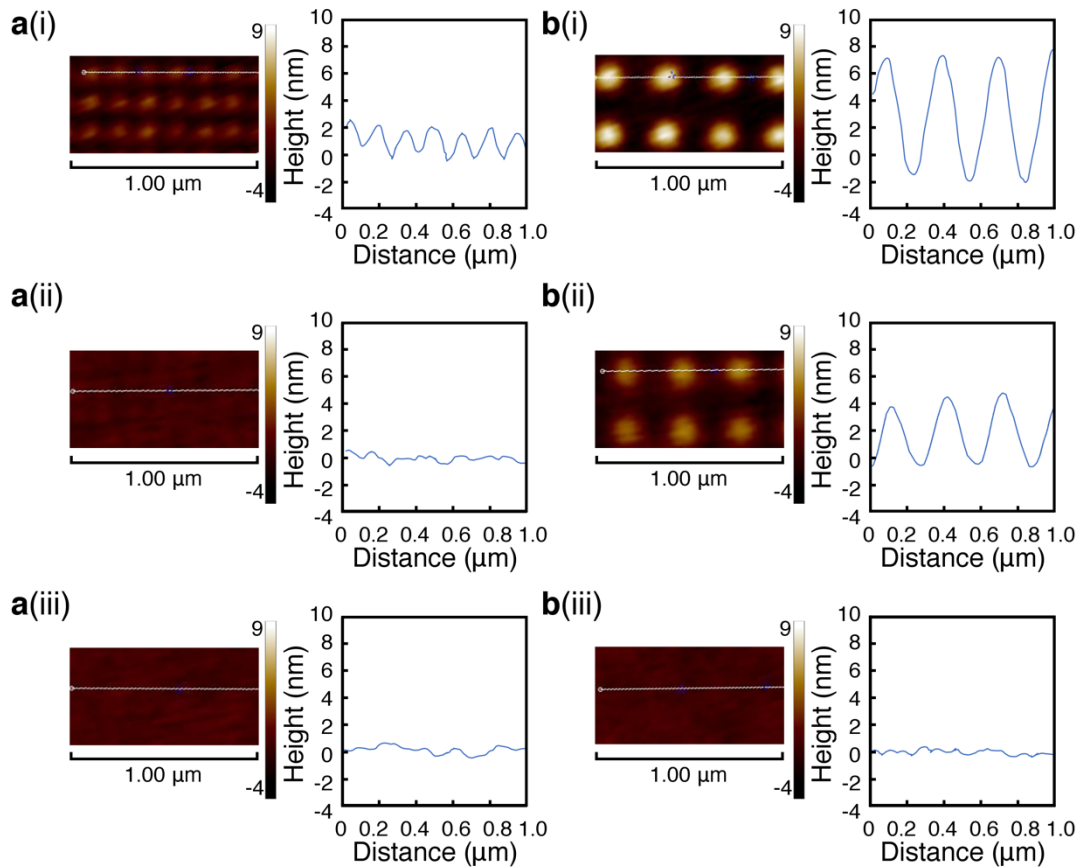


**Figure 3.7: Surface planarisation by HSQ.** (a) AFM image and height profile for HSQ layer with thickness of (i) 52 nm, (ii) 100 nm, and (iii) 200 nm spun onto nanostructures with dimensions of 50 nm x 50 nm x 50 nm ( $L \times W \times H$ ). (b) AFM image and height profile for HSQ layer with thickness of (i) 52 nm, (ii) 100 nm, and (iii) 200 nm spun onto nanostructures with dimensions of 100 nm x 100 nm x 50 nm ( $L \times W \times H$ ). For both nanostructure shapes, planarisation occurs when there is at least 200 nm of HSQ.

To support a microfluidic channel for real-time fluid flow testing, the same design as that of **Figure 3.6b** was fabricated on a glass slide and both SEM and AFM images and measurements were taken during the fabrication process (**Figure 3.8**). For this new device, the resulting nitride thickness was measured by ellipsometry to be 86 nm. After each stage of the fabrication process (i-iv) as indicated in the rendering of **Figure 3.8a**, brightfield microscopy, SEM, and AFM images were taken. **Figure 3.8b** shows corresponding bright-field microscopy/SEM images; **Figure 3.8c** shows SEM images of the corner of the device; and **Figure 3.8d** shows corresponding SEM/AFM images. The AFM images further confirm that the HSQ planarises the non-planar nitride layer.

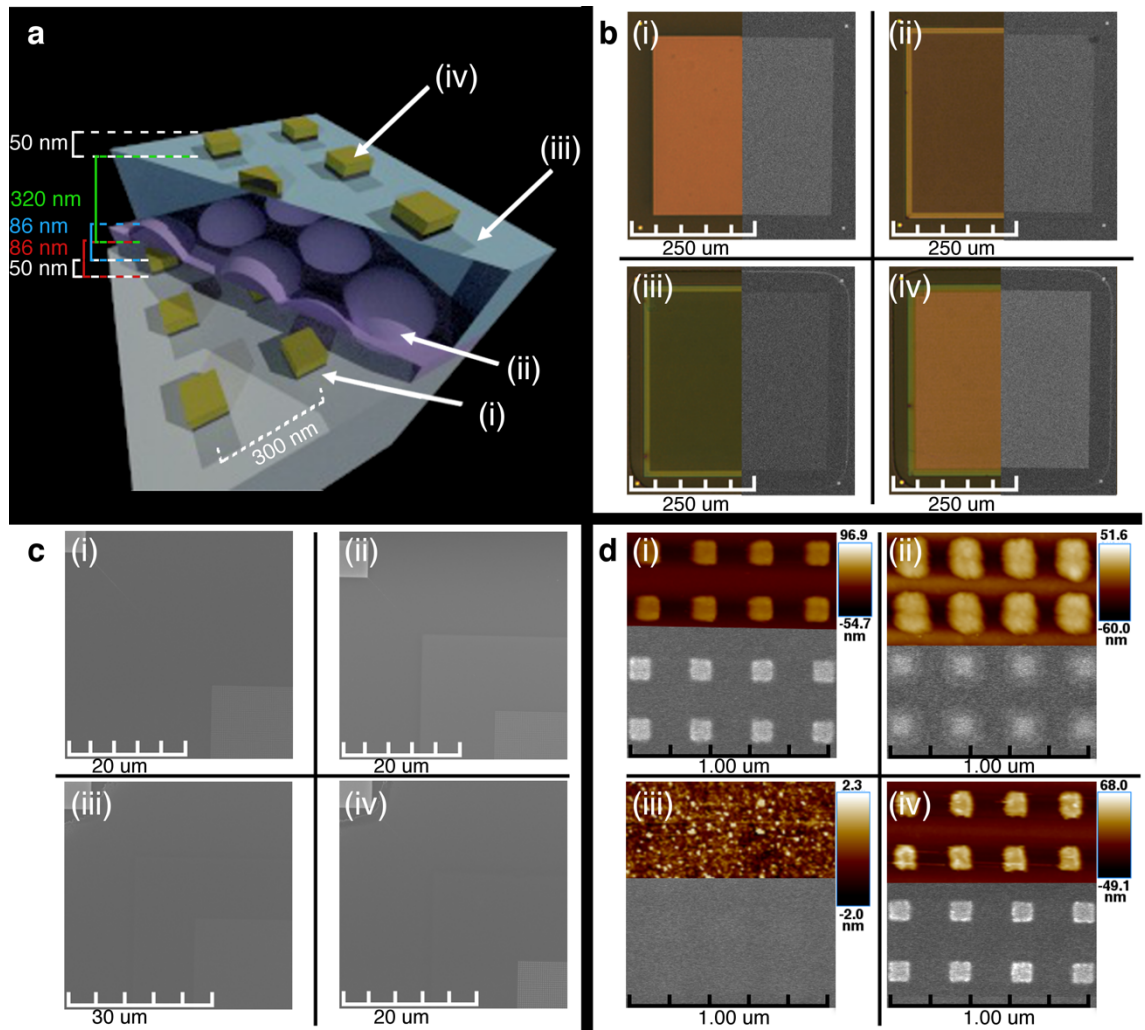


**Figure 3.8: Schematic and SEM/AFM images of multilayered sensing device.** (a) Schematic showing the multilayered device. (i) An Au nanostructure LSPR reference layer encapsulated in (ii) a conforming silicon nitride with (iii) a HSQ planarisation layer, and (iv) a gold LSPR sensing layer. The heights of each layer and periodicity of the arrays are labelled. Both nanostructure arrays consist of elements that are 100 nm x 100 nm x 50 nm (LxWxH). (b) Bright field and low magnification SEM images of each layer of the device taken at time of deposition. (c) Further magnified SEM images of (i-iv). (d) AFM (top) and SEM (bottom) images of each of the device layers (i-iv) taken at the time of deposition. The AFM images confirm that the HSQ layer planarised the nitride layer. Parts (a) and (d) were published in Sperling, et.al. (2018) [28].

#### 3.4.1.4 Consistency of Nitride Deposition

**Figure 3.9a** compares the transmission of the device from Figure 3.6b (labelled as ‘1’) to that of Figure 3.8 (labelled as ‘2’). While both devices have two distinct sets of peaks, the resulting transmissions are different, most noticeably around the second peak corresponding to the nitride-encapsulated nanostructures. The two of devices shown in Figure 3.6 and the third device shown in Figure 3.8 went through two, separate nitride depositions. Despite having requested for a 100 nm deposition with the same process and parameters (as can be

seen by the resulting  $(n,k)$  values for each deposition in **Figure 3.9b**) two different nitrides were deposited. Additionally, the measured thickness of the nitride layer for Device 1 and Device 2 were  $89.50 \pm 0.07$  nm and  $86.59 \pm 0.04$  nm (out of the requested 100 nm), respectively. Device 1 has a blue-shifted second peak because the nitride layer deposited on this sample has a lower  $(n,k)$  refractive index. Device 2 was used for the experiments in the subsequent sections of this chapter.

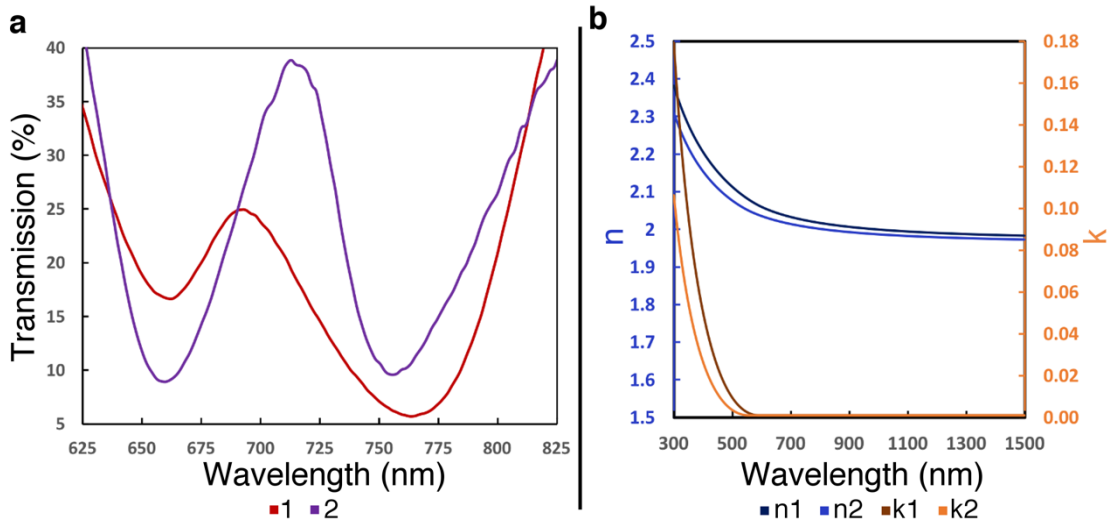


**Figure 3.9: Silicon nitride deposition effect on the plasmonic response.** (a) The transmission of two multilayered devices with different silicon nitride depositions. The right-most peak corresponds to the encapsulated reference layer of the device. (b) The corresponding  $(n,k)$  values of the nitride layers for each device as measured by ellipsometry. The thickness of deposition requested was 100 nm. The measured thickness for Device 1 and Device 2 were  $89.50 \pm 0.067$  nm and  $86.59 \pm 0.042$  nm, respectively. Device 2 was used for real-time measurements.

### 3.4.2 Multilayer Sensor Calibration

As previously demonstrated, the transmission of the sensor has two peaks. Here, they will be denoted as  $P_1$  and  $P_2$ , as shown in **Figure 3.10**, corresponding to the sensing peak and reference peak, respectively.

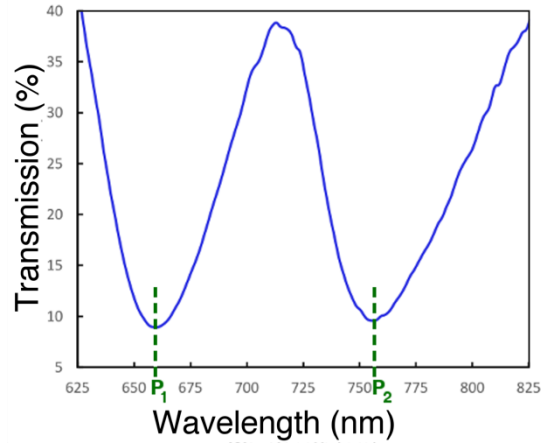


**Figure 3.10: Corrected Position Response (CPR).** CPR is defined as the difference between the sensing peak ( $P_1$ ) and encapsulated reference peak ( $P_2$ ). This Figure was published in Sperling, et.al. (2018) [28].

To correct for drift in peak position, the CPR was calculated by subtracting the position of the sensing peak from that of the reference peak [14, 22]:

$$CPR [nm] = P_2 - P_1 \quad (3.1)$$

To measure the spectral response of this sensor, the custom-made microspectrophotometer described in Chapter 2 was used to measure the transmission as fluid flowed over the device through a polydimethylsiloxane (PDMS) microfluidic channel.

**Figure 3.11** demonstrates the stability of the reference peak. In **Figure 3.11a**, changing the refractive index surrounding the sensor from that of water (RI = 1.333) to that of 20% (w/w) sucrose solution (RI = 1.3639) [29] results in a clear shift in  $P_1$ . The position of  $P_2$  remains constant. The contour plot in **Figure 3.11b** further expands upon this. It shows the transmission (dark-to-light-blue colour profile) between wavelengths of 600 nm and 850 nm (X-axis) to the refractive indexes of 1.333, 1.3405, 1.3478, 1.3555, 1.3639, and 1.4201 (Y-axis). The refractive indexes used correspond to that of 0%, 5%, 10%, 15%, 20%, and 50% (w/w) sucrose solutions in water [29]. The reference peak (right-most dashed line) does not exhibit a shift in response with varying refractive index while the sensing peak (left-most dashed line) does. This indicates that the encapsulated peak is a viable reference, independent from the refractive index changes of the sensing region. Therefore, the reference peak can be used to correct the position of the sensing layer's peak.

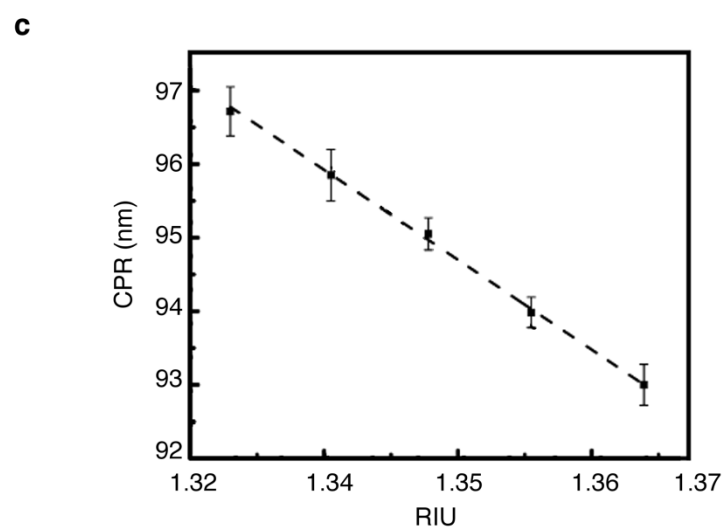
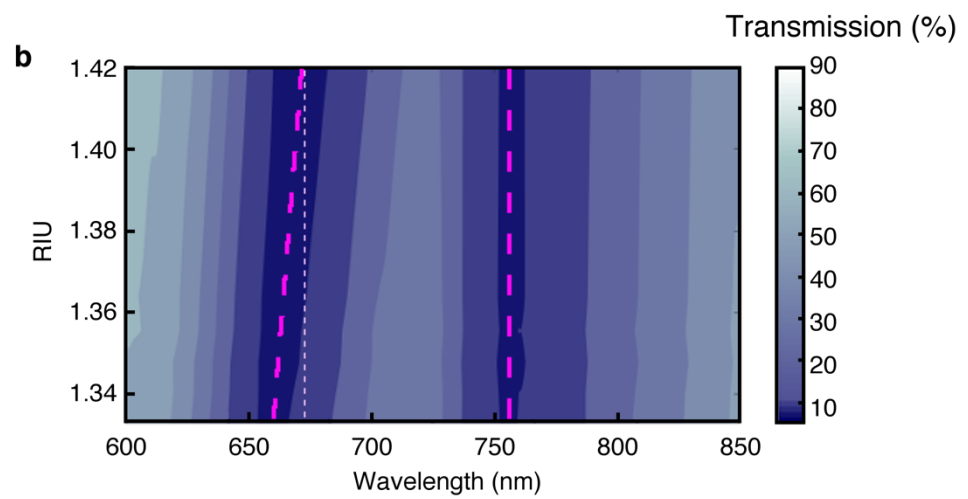
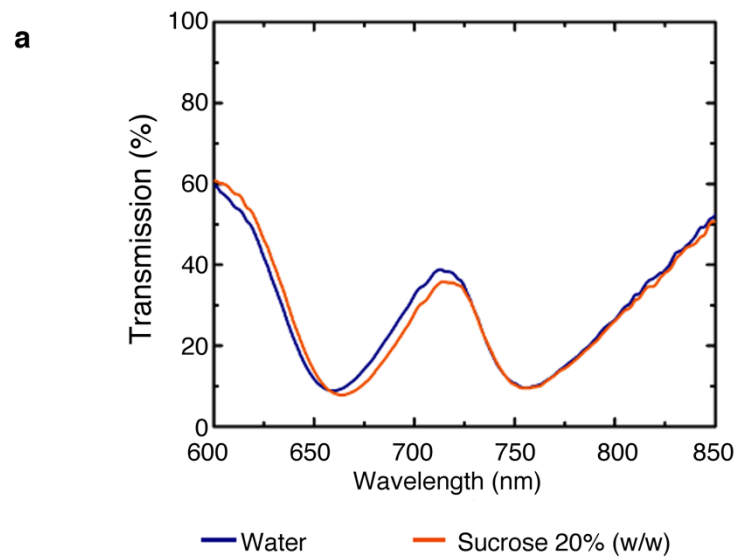


**Figure 3.11: Experimental data from multi-layered device.** (a) Transmission plot of the device in response to water ( $RIU = 1.333$ ) and 20% sucrose (w/w) ( $RIU = 1.3639$ ). (b) Contour plot of the transmission of multi-layered sensor in 0%, 5%, 10%, 15%, 20%, and 50% (w/w) sucrose solutions. Significantly, the encapsulated reference peak (right-most dashed line) does not exhibit a shift in response with varying refractive index while the uncapped sensing peak (left-most dashed line) does. (c) Experimental results of the CPR to changes in the refractive index. The experimental CPR has a sensitivity of  $122 \pm 3 \text{ nm} \cdot RIU^{-1}$ , respectively. A linear fit best describes the CPR because it has an adjusted  $R^2$  value well above 99%. This figure was published in Sperling, et.al. (2018) [28].

The sensitivity of the sensor was determined by taking the slope of the CPR-Refractive Index curves shown in **Figure 3.11c**. The CPR sensitivity of  $122 \pm 3 \text{ nm} \cdot RIU^{-1}$  and Figure of Merit (FoM) [33] of 1.3 makes it close to sensitivity shown for silver nanocubes [34], but overall, at the lower sensitivity range of other LSPR sensing devices, which range from  $90 \text{ nm} \cdot RIU^{-1}$  to  $1000 \text{ nm} \cdot RIU^{-1}$  and FoM of 0.8 to 5.4 [3, 5-7]. Conceptually, this design shows potential as a means to self-reference. To improve the device, tuning the nanostructure material, size, and/or shape may alter the plasmonic properties and result in a higher sensitivity (see Chapter 1) [6-8].

### 3.4.3 Multilayer Device for Real-Time RI Sensing

To further demonstrate the stability, real-time measurements of induced refractive index changes were measured. **Figure 3.12a** shows the real-time position response of P1 (black), P2 (red), and CPR (blue) of the sensor to injections of sucrose solutions with varying RIs (green dashed lines).

The injections of sucrose solutions (in water w/w) for (i) the first run were 0%, 5%, 10%, 15%, 20%, and 50; (ii) the second run were 0%, 0.5%, 1.0%, 2.5%, 5%, 10%, 15%, and 20%; and (iii) the third run were 0%, 5%, 15%, and 20%. For each run, the device was left to stabilise at baseline and injections of sucrose were only started following 10 minutes of stabilised response. The measurements in **Figure 3.12a(ii)** and **Figure 3.12a(iii)** were taken in quick succession. As a result, for the first ten minutes of these runs, the sensor was still returning to baseline from the sucrose injection from the previous run. **Figure 3.12b** shows the shift in (i) P1, (ii) P2, and (iii) CPR from the baseline measurements for the five injections shown in **Figure 3.12a(i)**. Both the sensing peak position and CPR show a stepwise change in response when higher concentrations of sucrose water are injected into the system, where the reference does not.

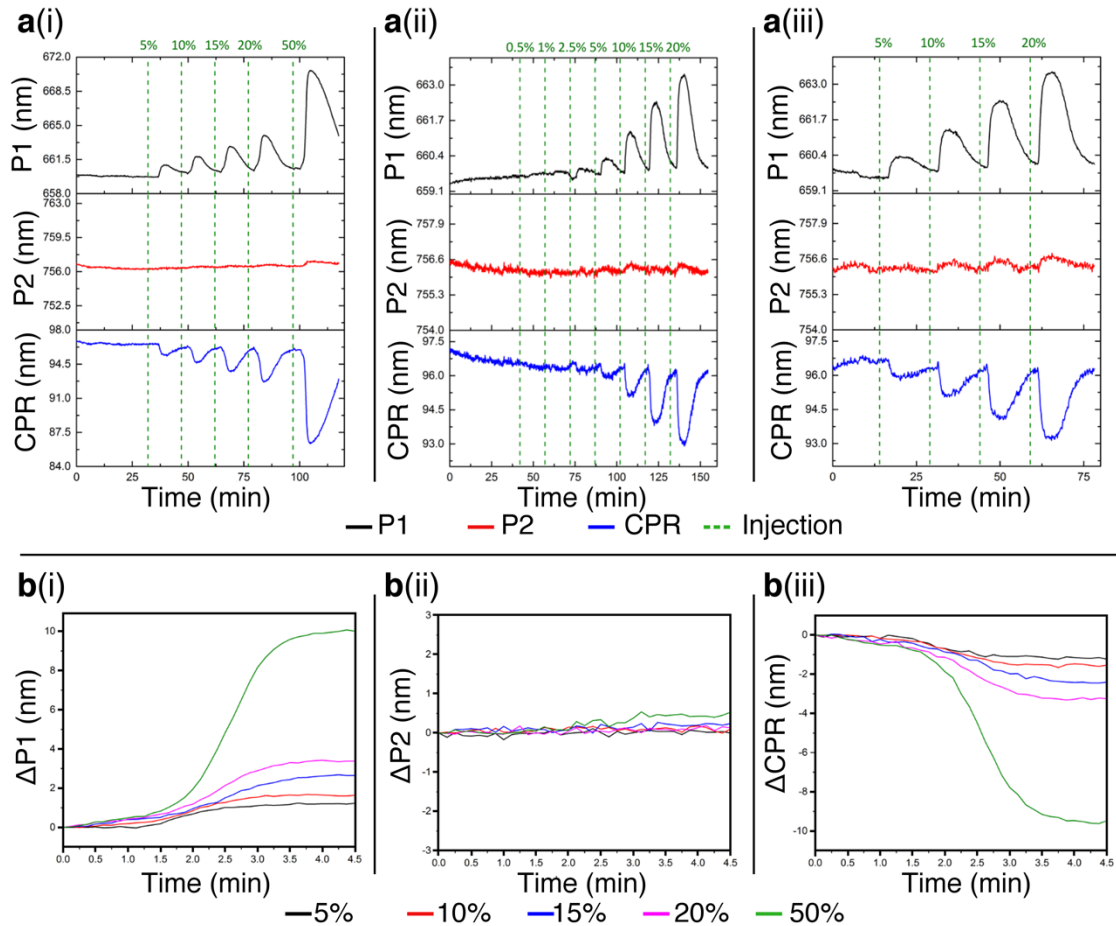


**Figure 3.12: Real-time response of sensor to changes in refractive index. (a)** The real-time response of P1 (black), P2 (red), and CPR (blue) to varying refractive index changes using sucrose solutions (w/w in water) of (i) 0%, 5%, 10%, 15%, 20%, and 50%; (ii) 0%, 0.5%, 1.0%, 2.5%, 5%, 10%, 15%, and 20%; and (iii) 0%, 5%, 10%, 15%, and 20%. The dotted green lines indicated the time at which sucrose was injected into the system. For each run, during the first 10 minutes, the device is stabilising at baseline. The measurements in (a)ii and (a)iii were taken in immediate succession of the previous run. In the first ten minutes of the measurement, the sensor was returning to baseline from the last sucrose injection of the previous run. **(b)** The shift in peak for (i) P1, (ii) P2, and (iii) CPR for the five injections from (a)i: 5% ( $t=35.5-40$  minutes), 10% ( $t=50-54.5$  minutes), 15% ( $t=64.5-69$  minutes), 20% ( $t=80-84.5$  minutes), and 50% ( $t=100.25-104.75$  minutes). This figure was published in Sperling, et.al. (2018) [28].

As the measurements from the second run (**Figure 3.12a(ii)**) have the most fluctuation, this run was used to determine the noise, limit of detection, and limit of quantification of the sensor. Using the full ten minutes prior to the first injection of this run as the baseline, the standard deviation of the baseline (noise), limit of detection (2x noise), and limit of quantification (3x noise) were determined from the CPR (**Table 3.1**). The values of 2x and 3x for limits of detection and quantification, respectively, are chosen from the ‘based on signal to noise’ analysis by *T.A. Little (2015)* [35].

**Table 3.1:** Noise-level, limit of detection, and limit of quantification for CPR and the corresponding RI values. This table was published in Sperling, et.al. (2018) [28].

	$\Delta\text{CPR}$	$\Delta\text{RIU (CPR)}$
Noise-Level	$9.28 \times 10^{-2}$	$7.59 \times 10^{-4}$
Limit of Detection	$1.86 \times 10^{-2}$	$1.52 \times 10^{-3}$
Limit of Quantification	$2.78 \times 10^{-2}$	$2.28 \times 10^{-3}$

The sensitivity for CPR was then used to calculate the corresponding change in RIU. The limit of detection and limit of quantification for the sensor are changes of  $1.52 \times 10^{-3}$  RIU and  $2.28 \times 10^{-3}$  RIU respectively. Although these values are also on the lower end of other published LSPR sensor devices [6-7, 36], we have successfully demonstrated a new design for self-referencing devices that can now be modified with much more sensitive nanostructure arrays. By simply modifying the size, shape, and material of the nanoplasmonic structures based on their well-known characteristics (see Chapter 1), more sensitive devices with better limits of detection and quantification can be achieved.

#### 3.4.4 Multilayer Device for Real-Time Biosensing

A biochemical binding assay was performed in order to demonstrate the applicability of the self-correcting device for biosensing applications. For this purpose, the well-known biotin-avidin interaction was used as a model. The sensing region of the device was functionalised with 11-mercaptoundecanoic acid (MUA) [36-37]. This treatment provided a self-assembled monolayer (SAM) with carboxylic acid moieties that were further used to covalently attach biotin-hydrazide via ethyl-carbodiimide cross linking [37]. Unreacted sites on the nanostructures were blocked with ethanolamine [36], and Tween-20 was added to the PBS solution used during the biosensing experiment to prevent avidin from binding to unblocked regions of the glass base of the device.

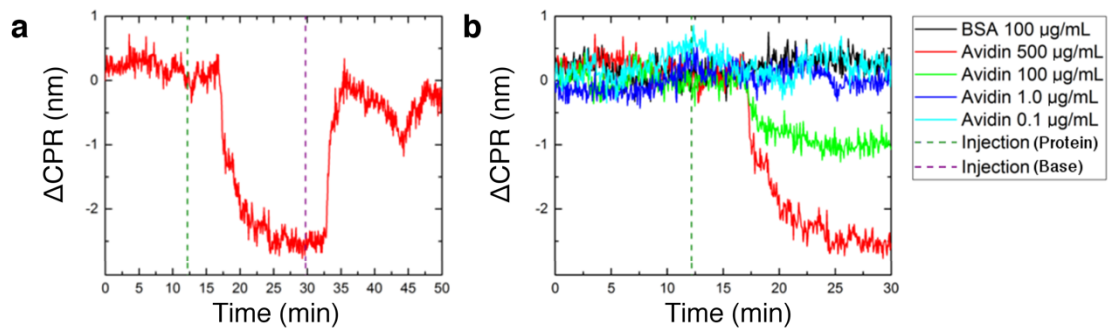


**Figure 3.13: Real-time biosensing of the biotin-avidin interaction.** (a) The real-time change of CPR to the specific binding and pH-mediated release of  $500 \mu\text{g}\cdot\text{mL}^{-1}$  avidin to biotin. The dotted green line denotes the time at which the protein was injected into the system. The dotted purple line denotes when NaOH was injected to release any bound proteins. The fluctuation after NaOH injection is present because of the change of the refractive index of solutions flowing through the device. Prior to injecting any other concentrations of protein into the device, the device was allowed a long flush ( $>30$  minutes) with PBS buffer to return the signal to baseline. (b) The real-time change of CPR to the non-specific interaction of BSA ( $100 \mu\text{g}\cdot\text{mL}^{-1}$ ) and the specific binding of avidin ( $0.1, 1, 100,$  and  $500 \mu\text{g}\cdot\text{mL}^{-1}$ ) with biotin. The dotted green line denotes the time at which the protein was injected into the system. This figure was published in Sperling, et.al. (2018) [28].

**Figure 3.13a** shows the change in CPR to an injection of  $500 \mu\text{g}\cdot\text{mL}^{-1}$  avidin (green dotted line). To regenerate the surface after protein binding,  $20 \text{ mM}$  NaOH was injected into the device (purple dotted line). In order to verify the suitability of the sensor in providing a dose-dependent response, three additional concentrations of avidin ( $0.1, 1,$  and  $100 \mu\text{g}\cdot\text{mL}^{-1}$ ) were also injected into the device. Additionally, the specificity of the sensor was tested by injecting bovine serum albumin (BSA) at a concentration of  $100 \mu\text{g}\cdot\text{mL}^{-1}$ . **Figure 3.13b** shows the shift in CPR to BSA and all four concentrations of avidin. The BSA injection did not produce a significant shift in the response of the sensor, thus demonstrating specificity to avidin. Avidin, though, was detected in a dose-dependent manner, and the concentrations of avidin where a significant shift could be observed were  $100 \mu\text{g}\cdot\text{mL}^{-1}$  and  $500 \mu\text{g}\cdot\text{mL}^{-1}$ . The sensitivity may be improved by investigating different antenna geometries.

#### 3.4.5 Full Device FDTD Simulation

To better understand the trends in the sensor, FDTD simulations were performed using Lumerical FDTD Solutions software (see 3.3.7 for simulation parameters used).

The simulation results in **Figure 3.14a** show that increasing the refractive index surrounding the sensor from  $1.333$  (water) to  $1.3639$  ( $20\% \text{ w/w}$  sucrose in water [29]) results in a clear shift in  $P_1$  and a stable  $P_2$ . Additionally, the contour plot in **Figure 3.14b** shows the

transmission (dark-to-light blue colour profile) between wavelengths of 600 nm to 900 nm (X-axis) to RI = 1.333, 1.3343, 1.335, 1.337, 1.3405, 1.3478, 1.3555, 1.3639, 1.3812, 1.3999, and 1.4201, respectively (Y-axis). Just like the experimental results shown in **Figure 3.11**, the sensing peak (left-most dashed line) exhibits a shift in response with varying refractive index while the reference peak (right-most dashed line) does not. **Figure 3.14c** shows the sensitivity curve of simulated CPR for the aforementioned refractive indexes. The simulated CPR has a sensitivity of  $269 \pm 2 \text{ nm} \cdot \text{RIU}^{-1}$ .

Significantly, the FDTD results confirm the self-referencing characteristic seen in the experimental results—a stable reference peak and a negative, linear sensitivity curve for CPR. However, compared to the experimental results, the simulation has a reference peak that is more red-shifted and is twice as sensitive.

These discrepancies are attributed to the physical differences between the simulated and the fabricated device. First, the silicon nitride layer in the simulation was approximated to be a flat, uniformly deposited layer that conformed to the shape of the surface below with dielectric values ( $n_2$ ,  $k_2$ ) as measure by ellipsometry (Figure 3.3). In the real sample, the gas-induced sputtering deposition at room temperature most likely produces edge effects of the silicon nitride particles that are deposited on the metal nanostructures on the sample, resulting in a non-uniform dielectric environment. This most likely accounts for why the simulated reference peak is much more red-shifted compared to that of the experimental reference peak. Additionally, the fabricated plasmonic nano-antennae, unlike the FDTD nano-antennae, were not perfectly square (see Figure 3.4), and shape has a major effect on plasmonic response [8, 38-39]. Altogether, these discrepancies yield a different response between the simulated and experimental results.

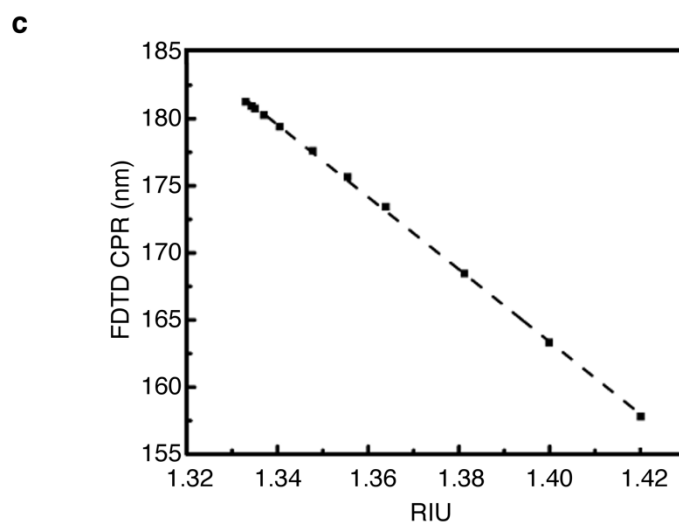
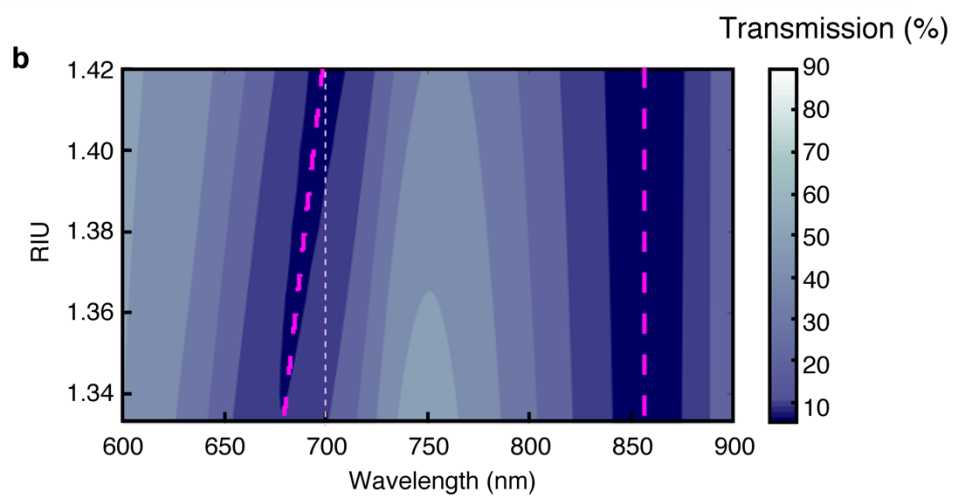
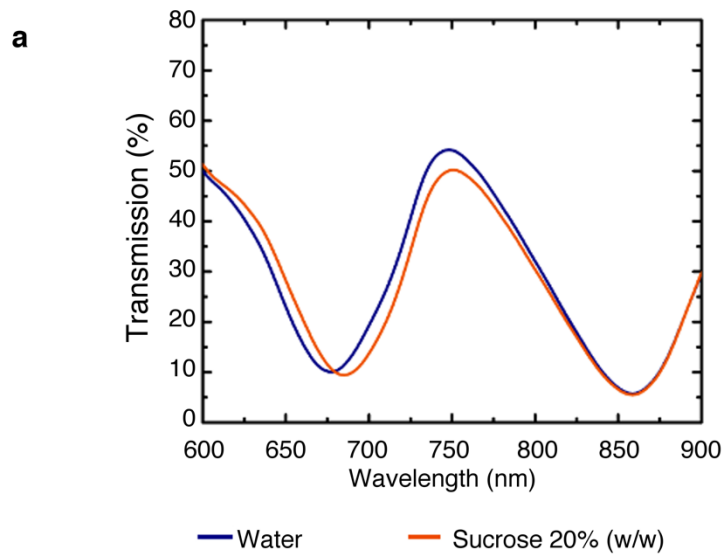


**Figure 3.14: FDTD simulation of the multilayered device. (a)** FDTD transmission to water (RIU = 1.333) and 20% sucrose (w/w) (RIU = 1.3639). **(b)** Contour plot of the transmission of the FDTD simulation for the multilayered sensor in 0%, 0.5%, 1%, 2.5%, 5%, 10%, 20%, 30%, 40%, and 50% (w/w) sucrose solutions. Just like the in the experimental data (see **Figure 3.11**), the encapsulated reference peak (right-most dashed line) does not exhibit a shift in response with varying refractive index while the uncapped sensing peak (left-most dashed line) does. **(c)** FDTD simulation of the CPR to changes in the refractive index. The FDTD CPR has sensitivities of  $269 \pm 2 \text{ nm} \cdot \text{RIU}^{-1}$ .

### 3.5 Conclusion and Future Work

In summary, a proof-of-concept multilayered LSPR device with an encapsulated reference region was demonstrated to self-correct for drift and detect, with selectivity and dose-dependence, the biotin-avidin interaction. The inclusion of both the reference and sensing regions within the same physical space allows for a more compact design, eliminates the need to inject samples that are potentially expensive or of limited quantity into a non-capturing parallel reference channel, and allows for the use of a single detector rather than multiple detectors. This is especially of interest for point-of-care diagnostic devices because the self-referencing design accounts for limitations in resources and sample quantity, operates in transmission-mode (standard UV-Vis instrumentation at point of care is generally carried out in this mode) [5], and can be incorporated into multiplexed microfluidic systems with different, more sensitive LSPR structures.

### 3.6 References

- [1] Homola, J. Surface Plasmon Resonance Sensors for Detection of Chemical and Biological Species. *Chem. Rev.* **2008**, *108* (2), 462-493, DOI: 10.1021/cr068107d.
- [2] Acimovic, S. S.; Ortega, M. A.; Sanz, V.; Berthelot, J.; Garcia-Cordero, J. L.; Renger, J.; Maerkl, S. J.; Kreuzer, M. P.; Quidant, R. Lspr Chip for Parallel, Rapid, and Sensitive Detection of Cancer Markers in Serum. *Nano Lett.* **2014**, *14* (5), 2636-2641, DOI: 10.1021/nl500574n.
- [3] Acimovic, S. S.; Sipova, H.; Emilsson, G.; Dahlin, A. B.; Antosiewicz, T. J.; Kall, M. Superior Lspr Substrates Based on Electromagnetic Decoupling for on-a-Chip High-Throughput Label-Free Biosensing. *Light: Sci. Appl* **2017**, *6*, DOI: 10.1038/lsa.2017.42.
- [4] Svedendahl, M.; Chen, S.; Dmitriev, A.; Kall, M. Refractometric Sensing Using Propagating Versus Localized Surface Plasmons: A Direct Comparison. *Nano Lett.* **2009**, *9* (12), 4428-4433, DOI: 10.1021/nl902721z.
- [5] Unser, S.; Bruzas, I.; He, J.; Sagle, L. Localized Surface Plasmon Resonance Biosensing: Current Challenges and Approaches. *Sensors* **2015**, *15* (7), 15684-15716, DOI: 10.3390/s150715684.

- [6] Mayer, K. M.; Hafner, J. H. Localized Surface Plasmon Resonance Sensors. *Chem. Rev.* **2011**, *111* (6), 3828-3857, DOI: 10.1021/cr100313v.
- [7] Szunerits, S.; Boukherroub, R. Sensing Using Localised Surface Plasmon Resonance Sensors. *Chem. Commun. (Cambridge)* **2012**, *48* (72), 8999-9010, DOI: 10.1039/c2cc33266c.
- [8] Langer, J.; Novikov, S. M.; Liz-Marzan, L. M. Sensing Using Plasmonic Nanostructures and Nanoparticles. *Nanotechnology* **2015**, *26* (32), DOI: 10.1088/0957-4484/26/32/322001.
- [9] Sagle, L. B.; Ruvuna, L. K.; Ruennele, J. A.; Van Duyne, R. P. Advances in Localized Surface Plasmon Resonance Spectroscopy Biosensing. *Nanomedicine* **2011**, *6* (8), 1447-1462, DOI: 10.2217/nnm.11.117.
- [10] Fernandez, F.; Garcia-Lopez, O.; Tellechea, E.; Asensio, A. C.; Cornago, I. Lspr Cuvette for Real-Time Biosensing by Using a Common Spectrophotometer. *IEEE Sens. J.* **2016**, *16* (11), 4158-4165, DOI: 10.1109/jsen.2016.2544953.
- [11] Sonnichsen, C.; Reinhard, B. M.; Liphardt, J.; Alivisatos, A. P. A Molecular Ruler Based on Plasmon Coupling of Single Gold and Silver Nanoparticles. *Nat. Biotechnol.* **2005**, *23* (6), 741-745, DOI: 10.1038/nbt1100.
- [12] Yoo, S. Y.; Kim, D.-K.; Park, T. J.; Kim, E. K.; Tamiya, E.; Lee, S. Y. Detection of the Most Common Corneal Dystrophies Caused by Bigh3 Gene Point Mutations Using a Multispot Gold-Capped Nanoparticle Array Chip. *Anal. Chem.* **2010**, *82* (4), 1349-1357, DOI: 10.1021/ac902410z.
- [13] Verdoold, R.; Gill, R.; Ungureanu, F.; Molenaar, R.; Kooyman, R. P. N. Femtomolar DNA Detection by Parallel Colorimetric Darkfield Microscopy of Functionalized Gold Nanoparticles. *Biosens. Bioelectron.* **2011**, *27* (1), 77-81, DOI: 10.1016/j.bios.2011.06.019.
- [14] Wadell, C.; Langhammer, C. Drift-Corrected Nanoplasmonic Hydrogen Sensing by Polarization. *Nanoscale* **2015**, *7* (25), 10963-10969, DOI: 10.1039/c5nr01818h.
- [15] Liu, Y.; Liu, Q.; Chen, S.; Cheng, F.; Wang, H.; Peng, W. Surface Plasmon Resonance Biosensor Based on Smart Phone Platforms. *Sci. Rep.* **2015**, *5*, DOI: 10.1038/srep12864.
- [16] Nenninger, G. G.; Clendenning, J. B.; Furlong, C. E.; Yee, S. S. Reference-Compensated Biosensing Using a Dual-Channel Surface Plasmon Resonance Sensor System Based on a Planar Lightpipe Configuration. *Sens. Actuators, B* **1998**, *51* (1-3), 38-45, DOI: 10.1016/s0925-4005(98)00218-4.
- [17] Lu, H. B.; Homola, J.; Campbell, C. T.; Nenninger, G. G.; Yee, S. S.; Ratner, B. D. Protein Contact Printing for a Surface Plasmon Resonance Biosensor with on-Chip Referencing. *Sens. Actuators, B* **2001**, *74* (1-3), 91-99, DOI: 10.1016/s0925-4005(00)00716-4.
- [18] Boozer, C.; Yu, Q. M.; Chen, S. F.; Lee, C. Y.; Homola, J.; Yee, S. S.; Jiang, S. Y. Surface Functionalization for Self-Referencing Surface Plasmon Resonance (Spr) Biosensors by Multi-Step Self-Assembly. *Sens. Actuators, B* **2003**, *90* (1-3), 22-30, DOI: 10.1016/s0925-4005(03)00017-0.
- [19] Levy, R.; Ruschin, S. Design of a Single-Channel Modal Interferometer Waveguide Sensor. *IEEE Sens. J.* **2009**, *9* (1-2), 146-153, DOI: 10.1109/jsen.2008.2011075.
- [20] Kashif, M.; Bakar, A. A. A.; Hashim, F. H. Analysing Surface Plasmon Resonance Phase Sensor Based on Mach-Zehnder Interferometer Technique Using Glycerin. *Opt. Commun.* **2016**, *380*, 419-424, DOI: 10.1016/j.optcom.2016.06.033.
- [21] Wu, S. Y.; Ho, H. P.; Law, W. C.; Lin, C. L.; Kong, S. K. Highly Sensitive Differential Phase-Sensitive Surface Plasmon Resonance Biosensor Based on the Mach-Zehnder Configuration. *Opt. Lett.* **2004**, *29* (20), 2378-2380, DOI: 10.1364/ol.29.002378.

- [22] Pacholski, C.; Sartor, M.; Sailor, M. J.; Cunin, F.; Miskelly, G. M. Biosensing Using Porous Silicon Double-Layer Interferometers: Reflective Interferometric Fourier Transform Spectroscopy. *J. Am. Chem. Soc.* **2005**, *127* (33), 11636-11645, DOI: 10.1021/ja0511671.
- [23] Pacholski, C.; Yu, C.; Miskelly, G. M.; Godin, D.; Sailor, M. J. Reflective Interferometric Fourier Transform Spectroscopy: A Self-Compensating Label-Free Immunosensor Using Double-Layers of Porous SiO<sub>2</sub>. *J. Am. Chem. Soc.* **2006**, *128* (13), 4250-4252, DOI: 10.1021/ja056702b.
- [24] Hao, N.; Zhang, Y.; Zhong, H.; Zhou, Z.; Hua, R.; Qian, J.; Liu, Q.; Li, H.; Wang, K. Design of a Dual Channel Self-Reference Photoelectrochemical Biosensor. *Anal. Chem.* **2017**, *89* (19), 10133-10136, DOI: 10.1021/acs.analchem.7b03132.
- [25] Wang, X.; Chang, T.-W.; Lin, G.; Gartia, M. R.; Liu, G. L. Self-Referenced Smartphone-Based Nanoplasmonic Imaging Platform for Colorimetric Biochemical Sensing. *Anal. Chem.* **2017**, *89* (1), 611-615, DOI: 10.1021/acs.analchem.6b02484.
- [26] Wersall, M.; Verre, R.; Svedendahl, M.; Johansson, P.; Kall, M.; Shegai, T. Directional Nanoplasmonic Antennas for Self-Referenced Refractometric Molecular Analysis. *J. Phys. Chem. C* **2014**, *118* (36), 21075-21080, DOI: 10.1021/jp5064929.
- [27] Rivero, P. J.; Ibanez, E.; Goicoechea, J.; Urrutia, A.; Matias, I. R.; Arregui, F. J. A Self-Referenced Optical Colorimetric Sensor Based on Silver and Gold Nanoparticles for Quantitative Determination of Hydrogen Peroxide. *Sens. Actuators, B* **2017**, *251*, 624-631, DOI: 10.1016/j.snb.2017.05.110.
- [28] Sperling, J. R.; Macias, G.; Neale, S. L.; Clark, A. W. Multilayered Nanoplasmonic Arrays for Self-Referenced Biosensing. *ACS Applied Materials & Interfaces* **2018**, DOI: 10.1021/acsami.8b12604.
- [29] ChemBuddy Refractive Indices of Sucrose Solutions at 20 °C, 589.29 Nm. <http://www.refractometer.pl/refraction-datasheet-sucrose> (accessed 2017/08/01).
- [30] Rumble, J. R.; Lide, D. R.; Bruno, T. J. *Crc Handbook of Chemistry & Physics*, 98 ed.; CRC Press: Boca Raton, USA, 2017.
- [31] Palik, E. D. *Handbook of Optical Constants of Solids*, Academic Press: 1997; Vol. I-III.
- [32] Jain, P. K.; El-Sayed, M. A. Plasmonic Coupling in Noble Metal Nanostructures. *Chem. Phys. Lett.* **2010**, *487* (4-6), 153-164, DOI: 10.1016/j.cplett.2010.01.062.
- [33] Sherry, L. J.; Chang, S. H.; Schatz, G. C.; Van Duyne, R. P.; Wiley, B. J.; Xia, Y. N. Localized Surface Plasmon Resonance Spectroscopy of Single Silver Nanocubes. *Nano Lett.* **2005**, *5* (10), 2034-2038, DOI: 10.1021/nl0515753.
- [34] Galush, W. J.; Shelby, S. A.; Mulvihill, M. J.; Tao, A.; Yang, P.; Groves, J. T. A Nanocube Plasmonic Sensor for Molecular Binding on Membrane Surfaces. *Nano Lett.* **2009**, *9* (5), 2077-2082, DOI: 10.1021/nl900513k.
- [35] Little, T. A. Method Validation Essentials, Limit of Blank, Limit of Detection, and Limit of Quantitation. *BioPharm Int.* **2015**, *28* (4), 48-51.
- [36] Lopez-Munoz, G. A.; Estevez, M. C.; Cristina Pelaez-Gutierrez, E.; Homs-Corbera, A.; Carmen Garcia-Hernandez, M.; Ignacio Imbaud, J.; Lechuga, L. M. A Label-Free Nanostructured Plasmonic Biosensor Based on Blu-Ray Discs with Integrated Microfluidics for Sensitive Biodetection. *Biosens. Bioelectron.* **2017**, *96*, 260-267, DOI: 10.1016/j.bios.2017.05.020.
- [37] Haes, A. J.; Van Duyne, R. P. A Nanoscale Optical Biosensor: Sensitivity and Selectivity of an Approach Based on the Localized Surface Plasmon Resonance Spectroscopy of Triangular Silver Nanoparticles. *J. Am. Chem. Soc.* **2002**, *124* (35), 10596-10604, DOI: 10.1021/ja020393x.
- [38] Liz-Marzan, L. M.; Murphy, C. J.; Wang, J. Nanoplasmonics. *Chem. Soc. Rev.* **2014**, *43* (11), 3820-3822, DOI: 10.1039/c4cs90026j.

- [39] Haes, A. J.; Zou, S. L.; Schatz, G. C.; Van Duyne, R. P. Nanoscale Optical Biosensor: Short Range Distance Dependence of the Localized Surface Plasmon Resonance of Noble Metal Nanoparticles. *J. Phys. Chem. B* **2004**, *108* (22), 6961-6968, DOI: 10.1021/jp036261n.

## Chapter 4: Bimetallic Nano-Plasmonics for the Optical Tasting of Whisky

### 4.1 Introduction

Today's electronic sensing devices have evolved to strongly resemble the senses of animals [1]. Photodetectors and filter algorithms found in digital cameras and video recorders [2-4], pressure and temperature sensors [5-6], and microphones [7] can all be related to the biological counterparts of vision, touch, and hearing, respectively. However, there are still two senses that science hasn't yet been able to sufficiently replicate: smell and taste [8-9].

While chromatography is the gold-standard technology to identify, detect, and quantify the components in a gas [10] or liquid [11] mixture, it requires efficient separation of the mixture's components prior to analysis using specialist laboratory equipment. Therefore, to provide accurate results necessitates a complex, costly, time-consuming, and highly-wasteful process [12], which makes this equipment unsuitable for applications where speed, cost, and portability are important, such as point-of-care diagnostics or food and beverage testing. To address these issues, recent efforts have turned to modelling detection and identification technologies on the senses of taste and smell leading to the development of optical and electronic "tongues" and "noses." [8, 13-17] Compared to the aforementioned, laboratory-based tools [10-11], these artificial noses and tongues are portable, do not require component isolation, and can be fabricated relatively cheaply [18]. In particular they have shown great effect in the detection of small changes in complex mixtures [19].

Our perception of taste and smell are the product of multiple partially-selective chemoreceptors in our nose and tongue that result in distinct electro-chemical patterns for specific odours/flavours [20-21]. Artificial tongues/noses mimic this by combining the responses of multiple cross-reacting sensor, allowing them to identify flavour/odour through trained pattern recognition rather than by measuring absolute concentrations of specific components within the mixture [19, 21-24]. The more sensing regions added to the analysis, the more accurate the device is at differentiating between different mixtures (as long as the ratio of measured data to sensing elements is high, ideally greater than six to avoid over-fitting/bias) [25]. While sensor arrays require "training" to identify different mixtures [13], they are widely applicable and have found uses in a range of diverse fields including medical diagnostics, where their ability to differentiate between a variety of different conditions

provides faster, non-invasive screening methods and enhances early-detection rates [14, 26-31], environmental monitoring [32-33], and food-safety, where they are used to monitor food-spoilage [8, 15, 34].

While in some previous works olfactory proteins have been used in artificial olfactory systems, their inherent long-term instability has prevented their widespread use [35]. To provide better stability, more robust synthetic materials are used, such as nanomaterials, doped metal oxides, or fluorescent polymers, as the partially-selective sensing elements [24, 34].

Recently, devices based on plasmonic Au nanostructures have emerged as a useful platform for constructing sensor arrays, thanks to their optoelectronic properties and chemical stability [36-37]. The optical response of Au nanostructures is dictated by their localised surface plasmon resonance (LSPR), a phenomena particularly sensitive to changes in local refractive index [38]. Partial selectivity in these devices is achieved by using multiple arrays of chemically-functionalised nanostructures as individual sensing regions. By monitoring the resonance peak-shifts for each of these sensing regions upon addition of a chemical mixture, a fingerprint of that mixture can be obtained [31]. However, the need for multiple sensing regions can inevitably result in limitations to miniaturisation and data acquisition time. As a result, there are size, weight, and speed advantages associated with reducing the number of sensors and measurements that are required for successful mixture classification.

To address these issues, this Chapter presents an optical tongue device where each sensing element of the tongue-array is multiplexed, providing two of the necessary partially-selective signals from one measurement. Each region consists of two superimposed nanoplasmonic arrays featuring two distinct metals: Au and Al. In addition to providing two distinct plasmonic resonance peak shifts from a single measurement, this choice of materials that makes up a 'bimetallic' array allows the selective chemical functionalisation of each superimposed array via thiol (Au array) [39-41] and silane (Al array) [40, 42] chemistries. Compared to its monometallic counterparts, the bimetallic Al/Au sensor is shown capable of operating with halve the number of sensing elements, thus reducing device size and regions to probe (i.e. data-acquisition time), all without compromising identification and classification capabilities of the device. Furthermore, the bimetallic optical tongue is used to distinguish between seven different whiskies and three controls.

The majority of work detailed in this chapter was presented as a talk at 2019 SPIE Photonics West Conference (BiOS, Frontiers in Biological Detection: From Nanosensors to Systems XI) by J.R. Sperling [43].

## 4.2 Materials

The materials used are available in Chapter 2.

## 4.3 Methods

### 4.3.1 Simulations of Designs

Finite-difference time-domain (FDTD) simulations were performed using Lumerical FDTD Solutions software.

### 4.3.2 Fabrication of Nanostructures

Devices were fabricated using electron-beam lithography as covered in Chapter 2.5 (See Metal Nanostructure Fabrication). For the nanostructures, a resist bi-layer of poly(methyl methacrylate) resist (PMMA) 2010 and PMMA 2041 (total thickness 150 nm) was patterned using a Vistec VB6 UHR EWF electron beam lithography tool. Following development of each run, a Plassys MEB 400S/550S electron-beam evaporation tool was used to evaporate (run 1) 2/50 nm titanium/Au and (run 2) 50 nm Al. For each electron beam lithography step, alignment was carried out using Penrose makers (see Chapter 2.4.1).

### 4.3.3 Surface Chemistry Modifications

The bimetallic optical tongue device consisted of 3 Al/Au sensors. Modifications to the surface chemistry of these three sensors involved silanisation of Al and thiolation of Au. For the first sensor, no modifications were made, leaving native Al and Au (with its native oxide layer). For these regions, the base substrate remained native glass (**Figure 4.1a**).

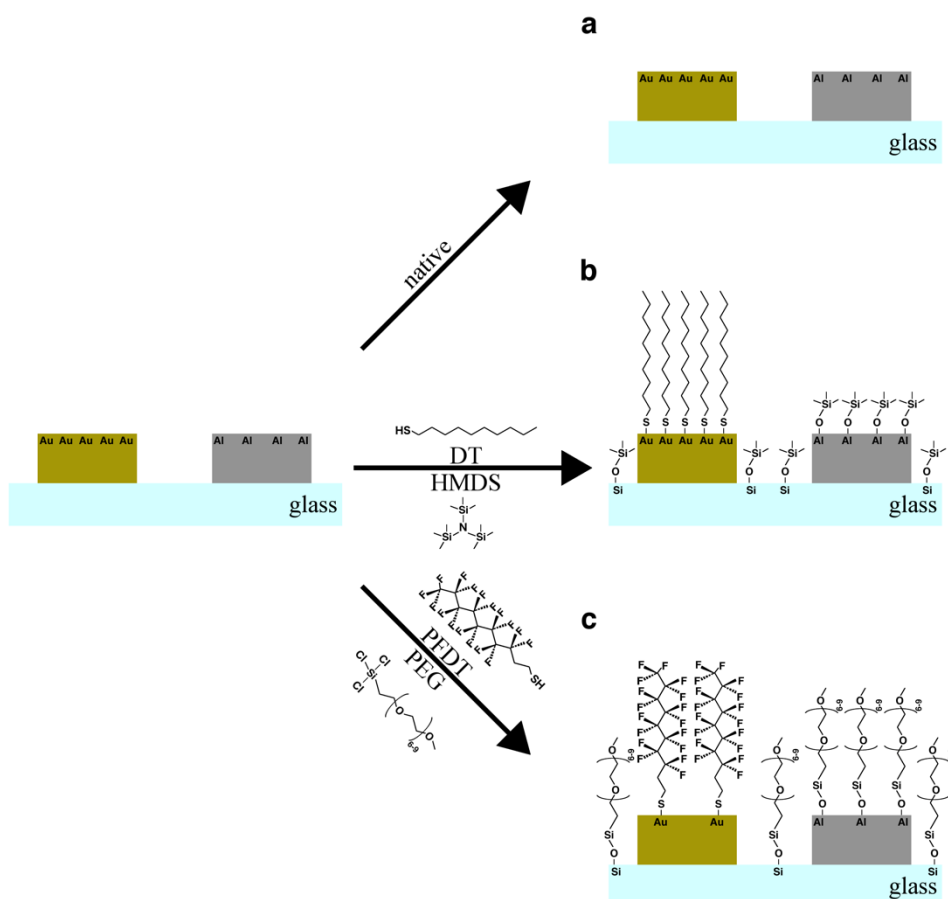


**Figure 4.1: Surface chemistry diagram.** (a) The surface chemistries of native Au and Al, (b) Au-DT and Al-HMDS, and (c) Au-PFDT and Al-PEG.

The second sensor was immersed in a 10 mM ethanolic solution of 1-decanethiol (DT, Sigma-Aldrich) for 24 hours, rinsed three times with ethanol, and dried with nitrogen. Hexamethyldisilazane (HMDS, Sigma-Aldrich) was then spun on at 4000 revolutions per minute for 60 seconds, allowed to air-dry for 2 minutes, and the excess was washed off. This produced the Al-HMDS and Au-DT surfaces (**Figure 4.1b**). For this sensor, the base substrate was modified to glass-HMDS.

The third sensor was immersed in a 10 mM ethanolic solution of 1H,1H,2H,2H-perfluoro-1-decanethiol (PFDT, Sigma Aldrich) for 24 hours, rinsed three times with ethanol, and dried with nitrogen. The sensor was then immersed in 0.5% solution (by volume) of 2-[methoxy (polyethyleneoxy)<sub>6-9</sub> propyl] trimethoxysilane (PEG, Sigma-Aldrich) in toluene for 1 hour, rinsed three times with toluene, and rinsed three times with deionised water. The sensor was then nitrogen dried and oven-baked at 100°C for 30 minutes. This produced the Al-PEG and

Au-PFDT surfaces (**Figure 4.1c**). For this sensor, the base substrate was modified to glass-PEG.

A monometallic device consisting of 6 nanoarray regions (3 Al and 3 Au) was fabricated for comparison. The same surface modifications were made to create the six sensors of Al, Au, Al-HMDS, Au-DT, Al-PEG, and Au-PFDT.

#### 4.3.4 Solution Preparation

Solutions of 10%, 20%, and 30% acetone (by volume) and 10%, 20%, 30%, and 40% ethanol (by volume) in deionised water were prepared. The selection of whiskies and vodka in **Table 4.1** were purchased from their respective distilleries.

**Table 4.1: Solutions tested in the whisky tongue.** The shape/colour for each solution in the subsequent PCA plots is denoted in the 'ID' column.

ID	Name	Serial Number	%	Type	Region	Barrel	Malt	Age
0 ○	DI H <sub>2</sub> O	-	0	Deionised Water	-	-	-	-
E ○	40% Ethanol in DI H <sub>2</sub> O (v/v)	-	40	Deionised Water / Ethanol Mixture	-	-	-	-
V ◇	Absolut®	L20180109H 16:07	40	Vodka	-	-	-	-
W1 +	Glenfiddich® 12 y	L33B46542108 0841	40	Scotch Whisky	Speyside	Amer. Oak / Eur. Sherry	Single	12
W2 △	Glenfiddich® 15 y	L33B44663005 1142	40	Scotch Whisky	Speyside	Eur. Sherry / Solera Vat	Single	15
W3 ◇	Glenfiddich® 18 y	L33B46271907 1531	40	Scotch Whisky	Speyside	Amer. Oak / Span. Oloroso	Single	18
W4 +	Glen Marnoch® Sherry Cask	LBB6B1406 021117 15:44	40	Scotch Whisky	Highland	Amer. Oak / Eur. Sherry	Single	-
W5 △	Glen Marnoch® Bourbon Cask	LBB6B1405 021117 19:42	40	Scotch Whisky	Highland	Amer. Oak / Bourbon	Single	-
W6 ◇	Glen Marnoch® Rum Cask	LBB6B1407 021117 17:53	40	Scotch Whisky	Highland	Amer. Oak / Caribbean Rum	Single	-
W7 ◇	Laphroaig® 10 y	L6262MB2 22990853	40	Scotch Whisky	Islay	Bourbon	Single	10

#### 4.3.5 Experimental Setup and Data Collection

A polydimethylsiloxane (PDMS) chamber on a glass slide was filled with each solution and samples were submerged in the chamber and slightly agitated for 2 minutes. A custom-built micro-spectrophotometer was used to measure the real-time transmission spectra (0.5 nm resolution). Light from a VIS-NIR light source (tungsten-halogen 400 to 1200 nm

wavelength) was used to probe the sensor. A 10x objective was used to couple the transmitted light into an optical-fibre attached to a StellarNet Microspectrophotometer (StellarNet Blue Wave). For the acetone and ethanol solvent differentiation, three different preparations of each solvent were made, and subsequent transmission spectra were taken. For the alcohol differentiation experimentation, thirty transmission spectra per region, for each solution, were measured. Between measurements, samples were rinsed in water, then ethanol, and nitrogen dried. A baseline measurement of a “blank” region the sample was used prior to measuring an element in one of the tongue arrays for background correction.

#### 4.3.6 Data Analysis

MATLAB was used to analyse the transmission spectra. The transmission spectrum was smoothed (20 points, mean-average smoothing) and interpolate (from 0.5 nm to 0.01 nm). The peak position value of the minima peaks (one for each monometallic sensor and two for each bimetallic sensor) was determined. The resulting transmission peak values (wavelength in nanometres) were arranged in a data matrix similar to that of **Table 4.2**, where the rows of the matrix corresponded to a particular solution and the columns corresponded to the wavelength of the resonant peaks for each chemistry—Au, Al, Au-DT, Al-HMDS, Au-PFDT, Al-PEG.

**Table 4.2: Example table of the data analysed for organic solvent differentiation and whisky differentiation.**

Solution	Transmission Peak Response (nm)					
	Al	Au	Al-HMDS	Au-DT	Al-PEG	Au-PFDT
<i>Solution 1</i>	492.79	660.17	485.49	661.4	484.11	659.04
<i>Solution 2</i>	494.03	663.36	488.69	664.59	486.19	661.61
			⋮			
<i>Solution N</i>	495.14	664.75	490.01	664.32	485.54	661.51

The data matrix was analysed using the inherent principal component analysis (PCA) function in MATLAB (by singular value decomposition algorithm). The variance for the scree plot was obtained from the MATLAB PCA result set. (See Chapter 2.7.2 for more information on PCA). For the whisky experiment, linear discriminant analysis (LDA) was then performed on the same data matrix using Systat 13 software.

## 4.4 Results and Discussion

### 4.4.1 Design and Fabrication of Bimetallic Nano-Square Sensors

The bimetallic nanoplasmonic sensor consists of two arrays of square (100 nm length by 100 nm width) nanostructures organised in a “checkboard”-like arrangement as depicted in **Figure 4.2a**; one array constructed with Au, the other with Al. This spatial configuration was chosen for its characteristic optic features, which displayed two well resolved peaks with very low transmission at their respective minima. Similar to Chapter 3, the shape of the nanostructures was chosen because (1) its design allows for easy, repeatable fabrication with the VB6 electron-beam lithography tool available, (2) the symmetrical shape is not subject to a polarisation-dependent response, and (3) the shape maximises the surface area of coverage for a given periodicity (and thus maximises the plasmonic signal).

#### 4.4.1.1 Determination of Periodicity

For optimisation of the periodicity between the Al and Au nanostructure arrays, FDTD simulations were conducted. A linearly polarised plane wave was defined for a unit area cell with various periods (**Figure 4.2b**). The dielectric values of gold and titanium were obtained from the CRC library [44], and the dielectric values of glass and aluminium were obtained from the Palik library [45]. Periodic boundary conditions were used in the X-axis and Y-axis, and a perfectly-matched-layers (PML) boundary was used in the Z-axis. A uniform mesh size of 4 nm was used in all axes and the background refractive index (RI) was set to that of water (RI=1.333).

Based on the simulation results, a period of 300 nm for each array (offset by 150 nm in X and Y) was chosen for fabrication of this device because it provides for two distinct peaks with the highest transmission attenuation with virtually no coupling between the two nanostructures at their resonance peaks (**Figure 4.2c**).

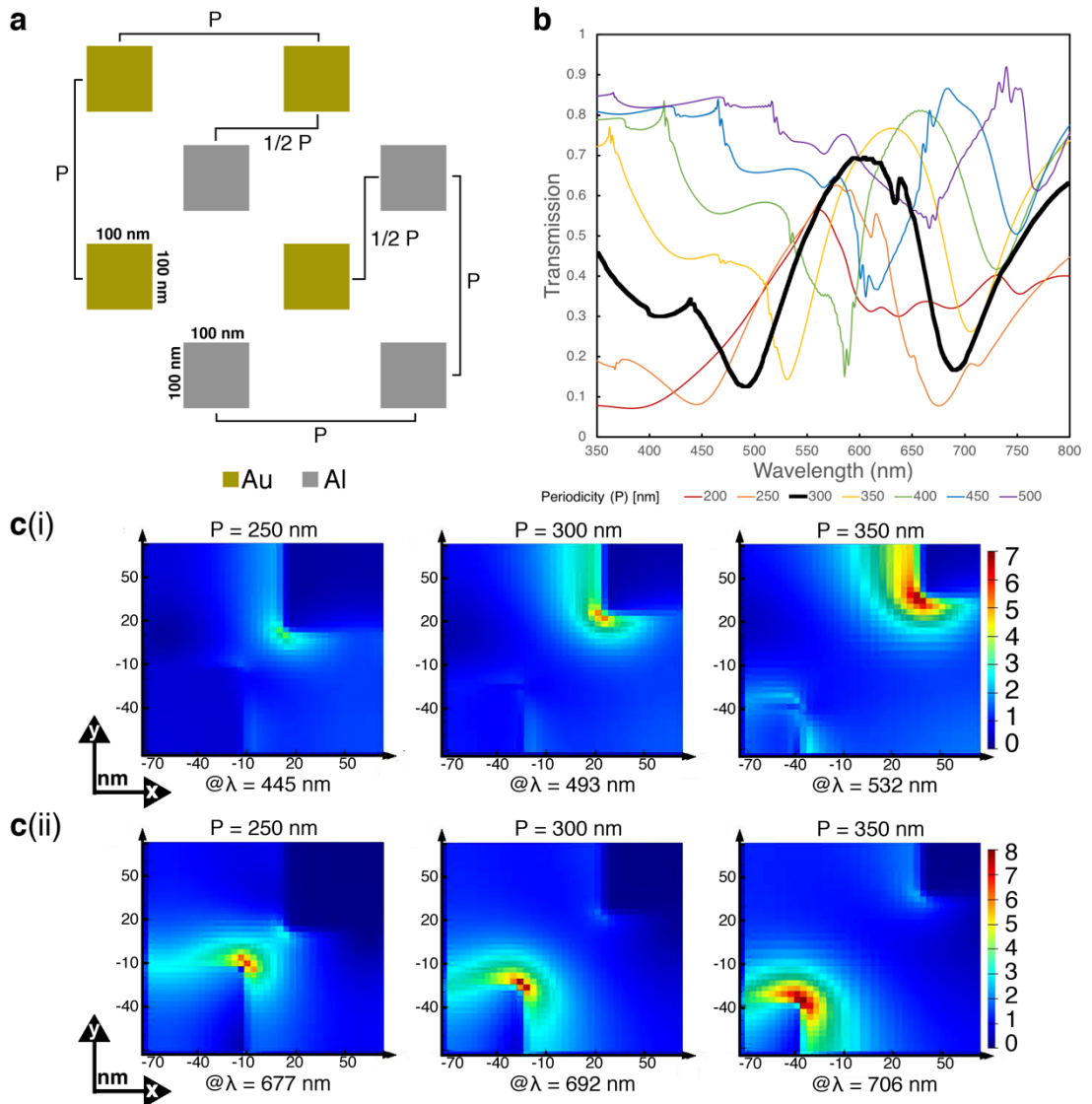


**Figure 4.2: FDTD simulation of different periodicities between Al and Au nanostructures in bimetallic arrays.** (a) Rendering of the simulation of the effect of periodicity ( $P$ ) for arrays of Au and Al nanostructures with dimensions of  $100 \times 100 \times 50$  nm (length  $\times$  width  $\times$  height). For each simulation, the nanostructures were considered to be offset by half a period in both  $X$  and  $Y$ . (b) Resulting transmission as  $P$  increases from 200 nm to 500 nm, in increments of 50 nm. (c) The  $XY$  electric field between the nanostructures for a wavelength corresponding to (i) Resonance 1 (Al) and (ii) Resonance 2 (Au) from (b) (as labelled below each subfigure) for  $P$  of 250 nm, 300 nm, and 350 nm. As indicated by the bold line in (b) and the middle electric field plots of c(i) and c(ii),  $P = 300$  nm shows two distinct peaks, with high transmission, and virtually no coupling between the nanostructures at their resonance peaks.

#### 4.4.1.2 Fabrication and Alignment

SEM images of two monometallic (top row) and ten bimetallic (bottom two rows) arrays are shown in **Figure 4.3**. The two metals can be differentiated by the shade of grey due to their distinct electron diffraction properties, Au being ‘brighter’ and Al being ‘darker.’ [46] While the bimetallic arrays were written with the same programmed pattern alignment, variations

in alignment of between the two metallic arrays within each region is clearly visible. While within tolerance of the e-beam tool, this variation in alignment can cause the two metal arrays to become within close proximity with one another and produce coupling effects on the resonance peaks for each metal.

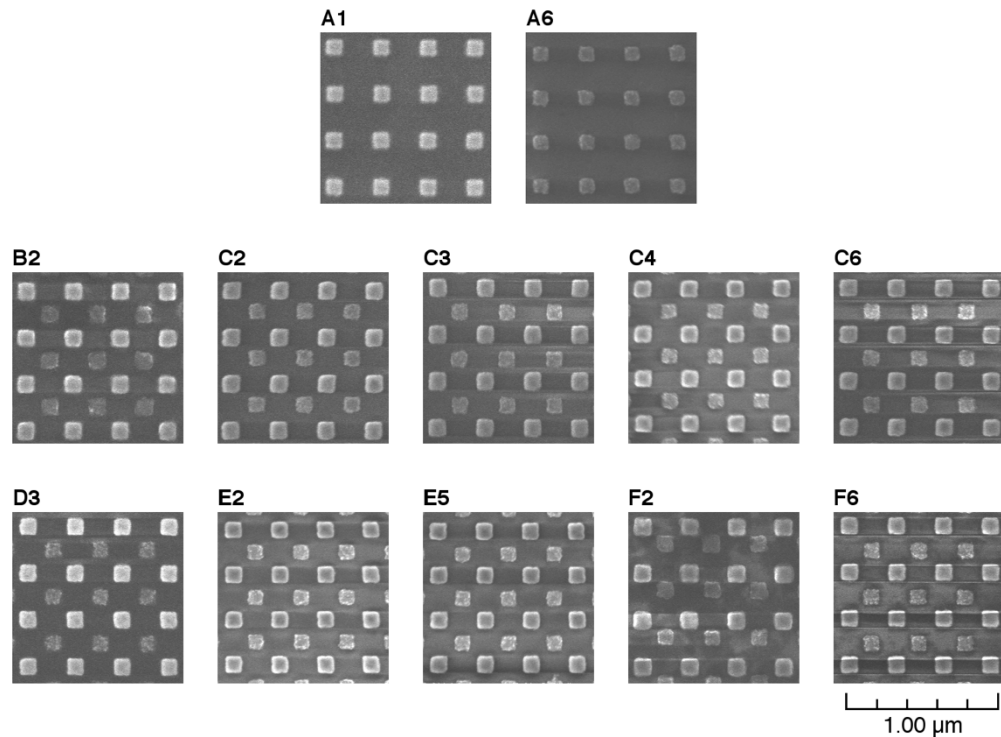


**Figure 4.3: SEM of monometallic and bimetallic sensors.** A1 and A6 are monometallic sensors of Au and Al, respectively. B2, C2, C3, C4, C6, D3, E2, E5, F2, and F6 are all bimetallic Al/Au sensors. For each bimetallic SEM, the outer 4x4 array is Au and the offset, inner 3x3 array is of Al. Although the alignment between the two metal arrays is within fabrication tolerance of the e-beam lithography tool, there is a slight difference in the alignment between each metallic array in each bimetallic sensor.

#### 4.4.1.3 Effect of Al-Au Nanostructure Distance for Bimetallic Array

To understand the effects of alignment during fabrication on the electric field between the nanostructures, FDTD simulation was carried out. A linearly polarised plane wave was defined for a unit area cell with a period of 300 nm in both X and Y. Both nanostructures were defined with dimensions of 100 nm x 100 nm x 50 nm (length by width by height). The distance between the Au and Al nanostructures was decreased from largest distance possible between structures (150 nm in X and Y for a period of 300 nm) to ‘touching,’ as shown in **Figure 4.4a**. The dielectric values of Au and titanium were obtained from the CRC library [44], and the dielectric values of glass and Al were obtained from the Palik library [45]. Periodic boundary conditions were used in the X-axis and Y-axis, and a perfectly-matched-

layers (PML) boundary was used in the Z-axis. A uniform mesh size of 4 nm was used in all axes and the background refractive index (RI) was set to that of water (RI=1.333).

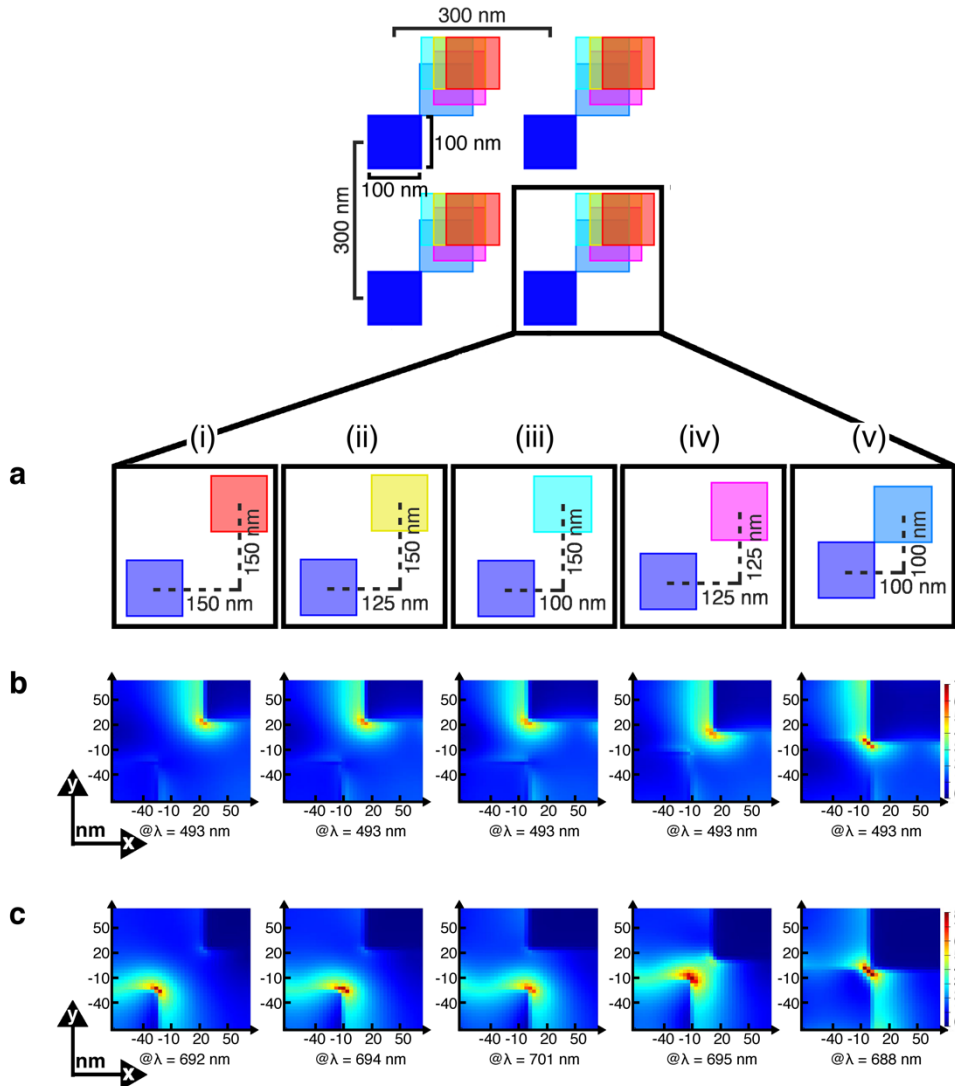


**Figure 4.4: FDTD simulation of effect on electric field by changes to distance between Al and Au nanostructures in a bimetallic array. (a) Rendering of the simulations and resulting XY electric fields for the resonance peaks corresponding to (b) Al and (c) Au as the distance between the metal nanostructures is decreased. Simulation for nanostructures separated in (X, Y) by (i) (150 nm, 150 nm), (ii) (125 nm, 150 nm), (iii) (100 nm, 150 nm), (iv) (125 nm, 125 nm), and (v) (100 nm, 100 nm) are shown. The nanostructures of Au and Al are 100 nm x 100 nm x 50 nm (length x width x height) with an X-Y period of 300 nm between each Au-Al pair and a mesh size of 4 nm in X-Y-Z was used. The resulting electric fields indicate strong coupling when alignment is off by more than 25 nm in either X or Y.**

As seen by the resulting electric field at the resonance associated with Al (**Figure 4.4b**) and Au (**Figure 4.4c**), strong coupling occurs when the alignment between nanostructure arrays is off by more than 25 nm (iii-v).

The E2 region is well within the tolerance as determined by simulation and is therefore used for the analysis to compare arrays of monometallic and bimetallic sensors as optical tongue devices in the subsequent sections.

#### 4.4.1.4 Transmission Response of Bimetallic Array

**Figure 4.5a** shows a schematic of the device; and **Figure 4.5b-c** shows bright-field microscopy (10x) and SEM images of the E2 region, respectively. **Figure 4.5d** shows a typical transmission spectrum for a bimetallic plasmonic sensor (solid, black line) compared to equivalent, single-metal sensors of Al (dotted, blue line) and Au (dotted, red line). As confirmed by the spectra of the two monometallic sensors, the two distinct and separate peaks in the bimetallic transmission spectrum at 500 nm and 660 nm correspond to Al and Au, respectively.

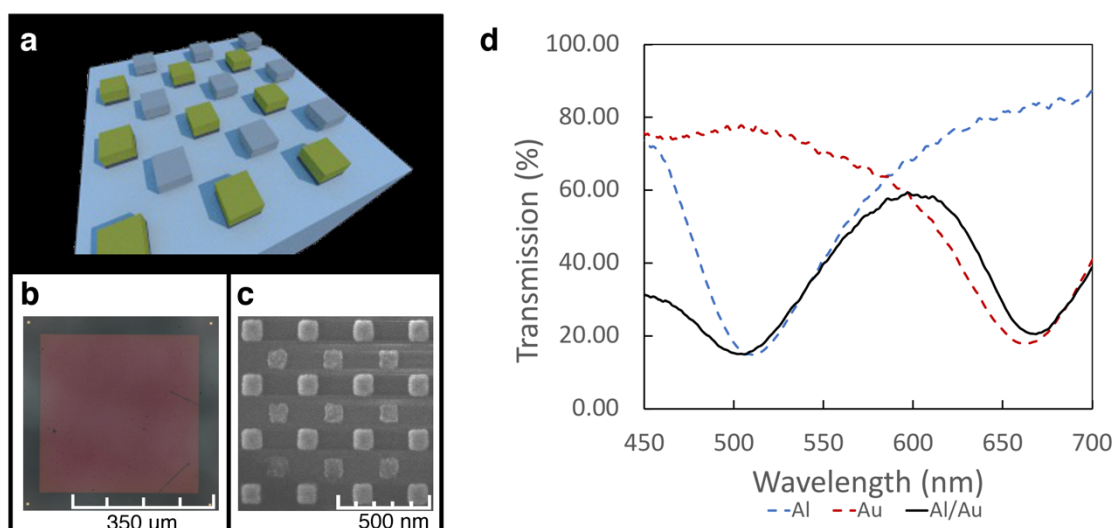


**Figure 4.5: Schematic, bright field microscopy image, SEM image and transmission response of a bimetallic plasmonic device. (a) Schematic showing the Au and Al bimetallic device. (b) Bright field microscopy image of the bimetallic device. (c) SEM image of the bimetallic sensor. (d) Transmission response of arrays of Al (dotted-blue), Au (dotted-red), and Al/Au (black solid) in water.**

#### 4.4.1.5 Analysis of Surface Chemistries

Both Au and Al can support selective functionalisation of their surfaces. While Au nanostructures can be readily modified by thiol chemistry [39-41], the native oxide layer present on the Al nanostructures displays -OH groups which enables the use of silane chemistry for functionalisation [40, 42]. The use of organic ligands in this way has previously been reported to change the sensitivity Au nanostructure based electronic noses,

in response to contact with certain organic molecules [36]. However, as these devices consisted of monometallic sensing regions, only one organic ligand per sensing region was reported. The bimetallic device designed here enables two ligand groups to be present in the same region, which has yet to be explored for plasmonic nose/tongues devices.

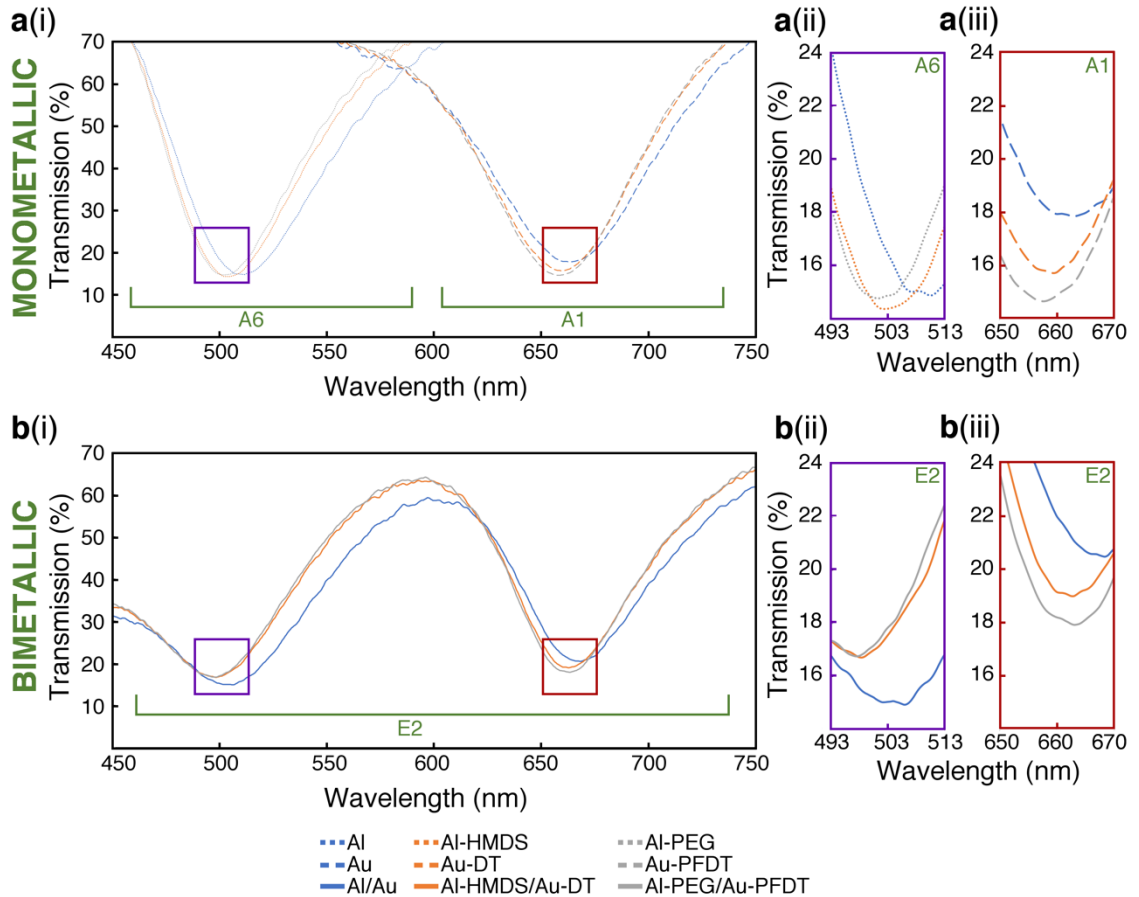


**Figure 4.6: The effect of surface chemistry on transmission.** The transmission response in water from (a) six monometallic sensors (Al, Au, Al-HMDS, Au-DT, Al-PEG, and Au-PFDT) and (b) three bimetallic sensors (Al/Au, Al-HMDS/Au-DT, and Al-PEG/Au-PFDT) for the wavelength ranges of (i) 450 nm to 750 nm, (ii) 493 nm to 513 nm (a zoom-in corresponding to the Al-type nanostructure peaks), and (iii) 650 nm to 670 nm (a zoom-in corresponding to the Au-type nanostructure peaks). Both the surface chemistry present on the metallic nanostructures and the type of sensor (mono- versus bimetallic) results in unique transmission responses.

To test this, 3 bimetallic sensors, each exhibiting unique surface chemistries as shown in Figure 4.1, were produced: (1) native Al/Au, (2) Al-HMDS/Au-DT, and (3) Al-PEG/Au-PFDT. These surface chemistries were chosen to represent varied levels of hydrophobicity. Altering the hydrophobicity of the LSPR nanostructures affects how individual components in a mixture interact with the local environment of the nanostructure (and thus the plasmonic response). In addition to these bimetallic sensors, 6 comparable monometallic sensors were produced: (1) native Al, (2) native Au, (3) Al-HMDS, (4) Au-DT, (5) Al-PEG, (6) Au-PFDT.

**Figure 4.6** shows the effect of the altered surface chemistries on the transmission response in water for **(a)** the 6 monometallic sensors and **(b)** the 3 bimetallic sensors. As expected, alterations to the surface chemistry cause a clear change in affinity for water.

#### 4.4.2 Organic Solvent Differentiation

To determine whether the surface chemistry modifications actually alter the sensing capabilities of the plasmonic region and change affinities for organic solvents (rather than simply ‘shifting’ the resonance peak), the resulting 6 monometallic (**Figure 4.7a**) and 3 bimetallic (**Figure 4.7b**) sensors were tested against varying refractive index media adjusted with **(i)** ethanol and **(ii)** acetone. The resulting resonance shifts from water (RIU=1.333) were compared using RIU values for acetone [47] and ethanol [48] solutions.

In all cases (regardless of the organic solvent used to alter the refractive index, the metal of the nanostructure, or if the region is mono- or bimetallic), it can be observed that organic ligand present on the nanostructures alters the sensitivity curves. (i.e. Al, Al-HMDS, and Al-PEG curves in **Figure 4.7a(i)** are different.)

However, for sensors with the same metallic base and organic ligand (regardless if the region is mono- or bimetallic), the sensitivity curve depends on the organic solvent used to alter the refractive index. (i.e. The sensitivity curves for a monometallic array of Au-DT in acetone (**Figure 4.7a(i)**) and ethanol (**Figure 4.7a(ii)**) are different).

Additionally, the sensitivity curves for regions with the same metallic base, organic ligand, and organic solvent differ depending on if the sensor region is monometallic or bimetallic. (i.e. Au-PFDT sensitivity curves in **Figure 4.7a(i)** and **Figure 4.7b(i)** are not the same.)

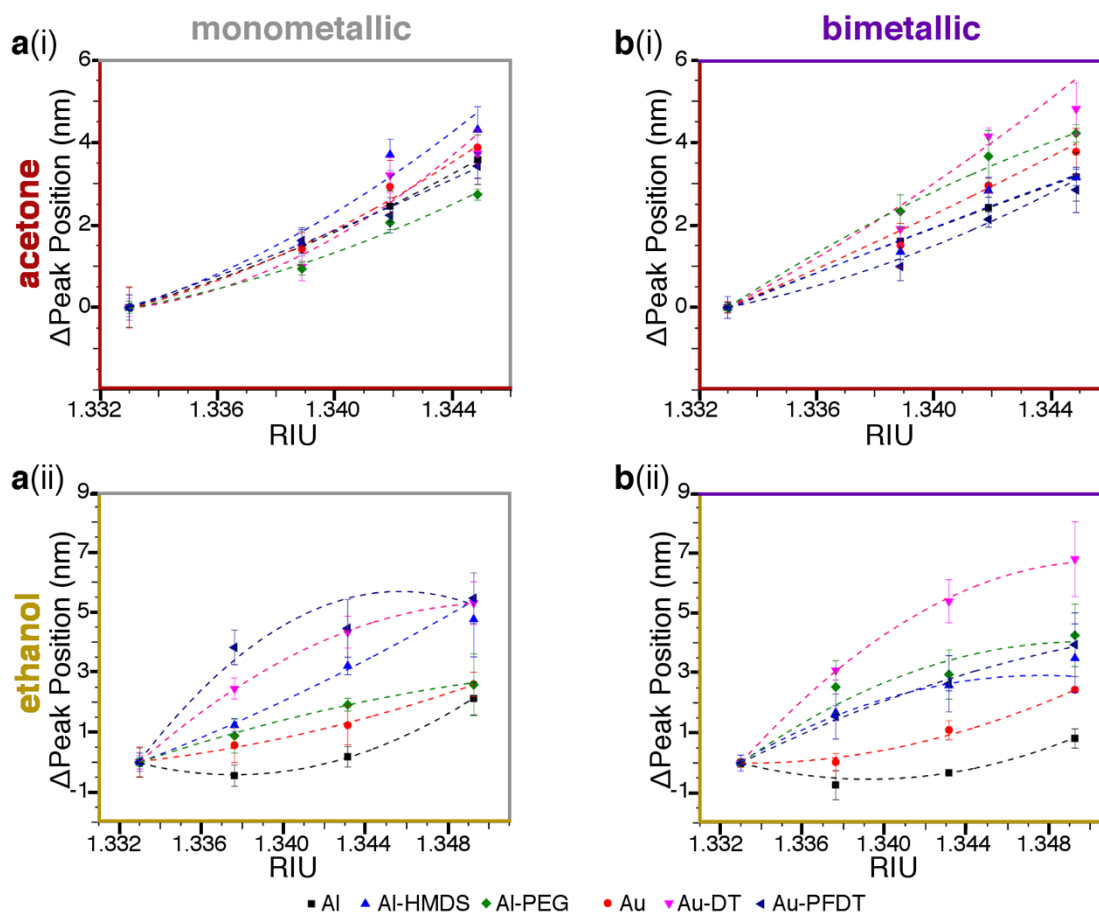


**Figure 4.7: Comparison of the effect of surface chemistry on sensitivity of sensors consisting of (a) monometallic and (b) bimetallic Au and Al nanoarrays.** Each plot in the figure shows the shift from water of the plasmonic peaks in 10%, 20%, and 30% solutions (v/v) of (i) acetone and (ii) ethanol, in RIUs. The different surface chemistries (native Al, Al-HMDS, Al-PEG, native Au, Au-DT, and Au-PFDT) alter the plasmonic peak of the nanostructures when exposed to the same organic solvent. The RIUs for acetone and ethanol solutions were obtained from S.S. Kurtz, *et al.* (1965) [47] and T.A. Scott (1946) [48], respectively. The error bars can be attributed to the multiple preparation of solutions as each chemistry combination was tested individually with 3 different sets of each solution.

These observed behaviours are attributed to the segregation of the solvent at the solid liquid interface and corresponding changes to the local refractive index. Solvent segregation depends on the chemical groups present at the interface; [49] using different metals and different ligands on the surface results in different segregation behaviours, which likely explains the different plasmonic responses. This is especially important when comparing the mono- and bimetallic responses; the presence of a second metal and second ligand results in a unique solvent segregation behaviour different than that which occurs for the two, separate monometallic counterparts. These results are in good agreement with previous reports [36], and they confirm that the partial-selectivity of a sensor can be tuned via silane and thiol chemistries.

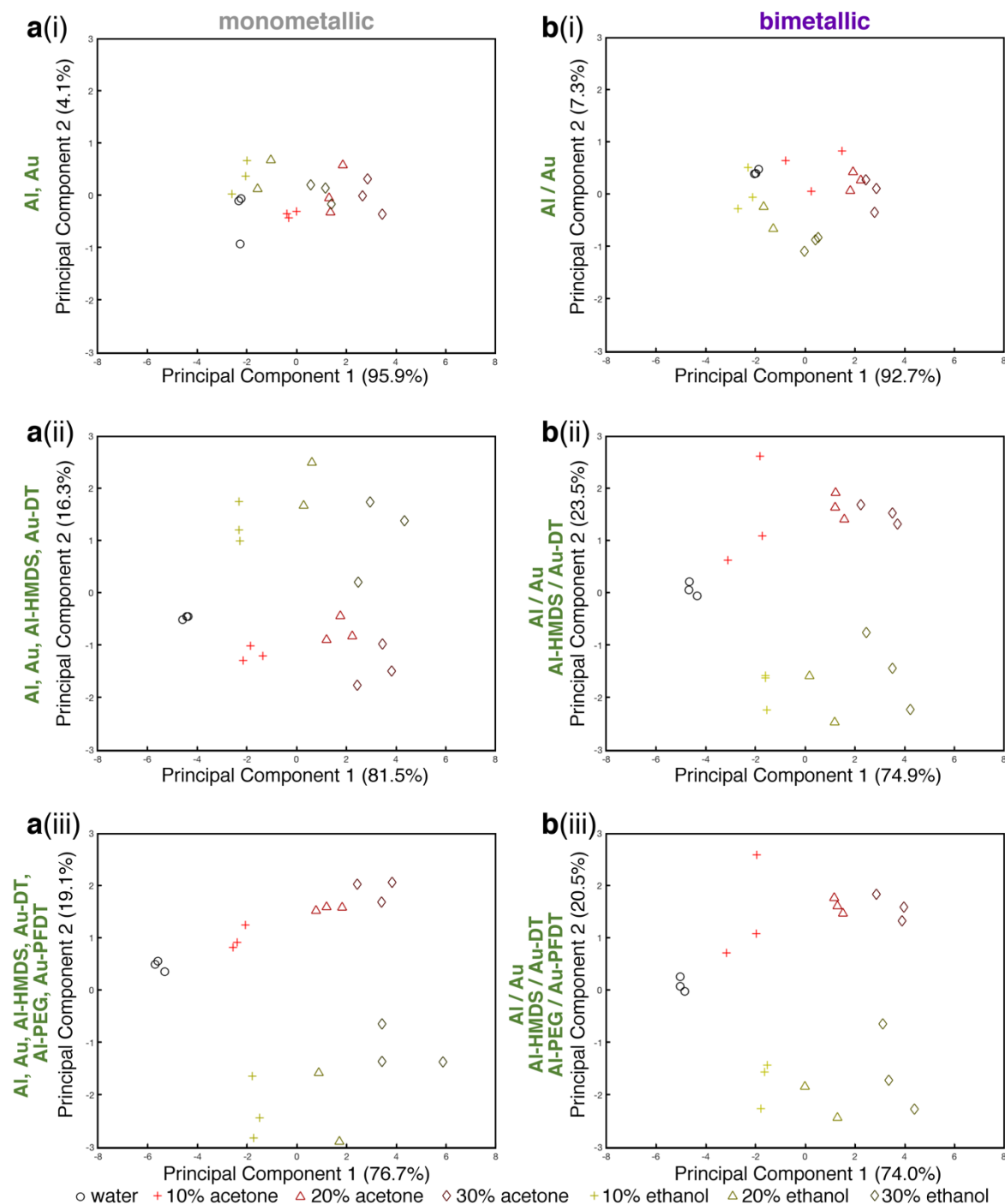


**Figure 4.8: PCA for organic solvent differentiation using mono- and bimetallic sensors.** The resulting PCA for (a) individual, separate regions with Au and Al arrays (elements A1/A6) and (b) bimetallic arrays of Au and Al (element E2) as the responses from more sensors are added to the PCA: (i) Al and Au, only; (ii) Al, Au, Al-HMDS, and Au-DT; and (iii) Al, Au, Al-HMDS, Au-DT, Al-PEG, and Au-PFDT. As the responses from more sensors are added to the PCA, the optical tongue is better able to distinguish the difference between water and 10%, 20%, and 30% (v/v) acetone and ethanol.

To further verify the applicability of the bimetallic approach for artificial tongue development, the resulting transmission peaks from the acetone/ethanol test for one group of bimetallic sensors (E2 from **Figure 4.3**) were analysed using PCA [17, 50] and compared to that of a comparable group of monometallic sensors (A1 and A6 from **Figure 4.3**). For the PCA data matrix, the resulting transmission peaks were arranged in a matrix similar to that shown in **Table 4.2**.

**Figure 4.8** shows PCA scatterplots of the first two principal components for **(a)** monometallic Al and Au sensors (A1 and A6 from **Figure 4.3**) and **(b)** bimetallic sensors (E2 from **Figure 4.3**). To demonstrate the effect of adding more partially-selective responses of additional sensors to the analysis, PCA was calculated using the transmission peaks from the columns in the data matrices corresponding to **(i)** Al and Au, only; **(ii)** Al, Au, Al-HMDS, and Au-DT; and **(iii)** Al, Au, Al-HMDS, Au-DT, Al-PEG, and Au-PFDT. In each PCA, black dots represent DI water, red dots represent acetone-based media and yellow dots represent ethanol-based media.

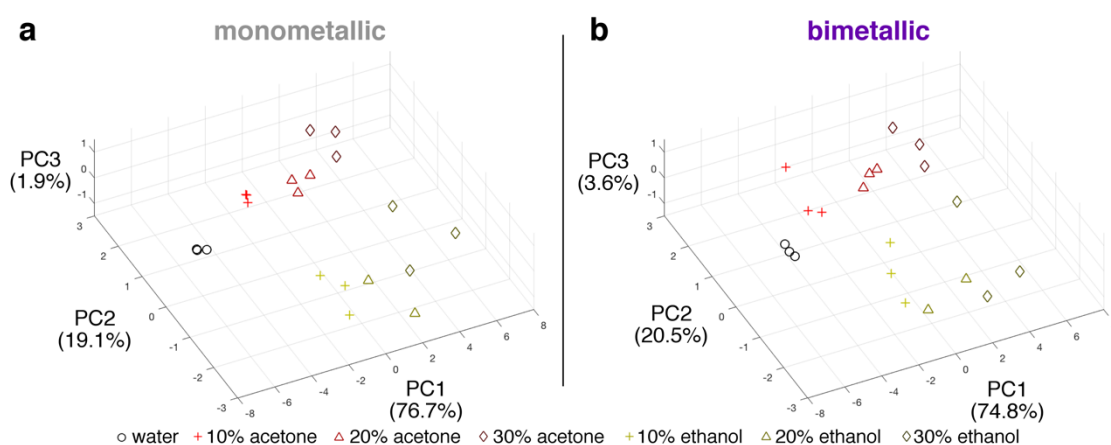


**Figure 4.9: 3D PCA for organic solvent differentiation.** Plot of the first (PCA1), second (PCA2), and third (PCA3) principal components of organic solvent sensing for **(a)** monometallic and **(b)** bimetallic sensor arrays from **Figure 4.8a(iii)** and **Figure 4.8b(iii)**. The third component further helps display the clustering of the data.

From **Figure 4.8**, it is observed that as the responses from more partially-selective elements are added to the PCA, further clustering occurs among responses to the same solution and further separation occurs between the clusters corresponding to different solutions. Further separation and clustering is shown in the PCA of the first three principal components for all six chemistries (**Figure 4.9**).

This clustering and separation are further demonstrated when looking across all 10 bimetallic ‘tongues’ from **Figure 4.3**. **Figure 4.10** shows the PCA of the first two principal components (that explain 87.3% of the total variance) for all 6 chemistries across all 10 bimetallic ‘tongues’ shown in **Figure 4.3** (each tongue consisting of 3 sensing regions).

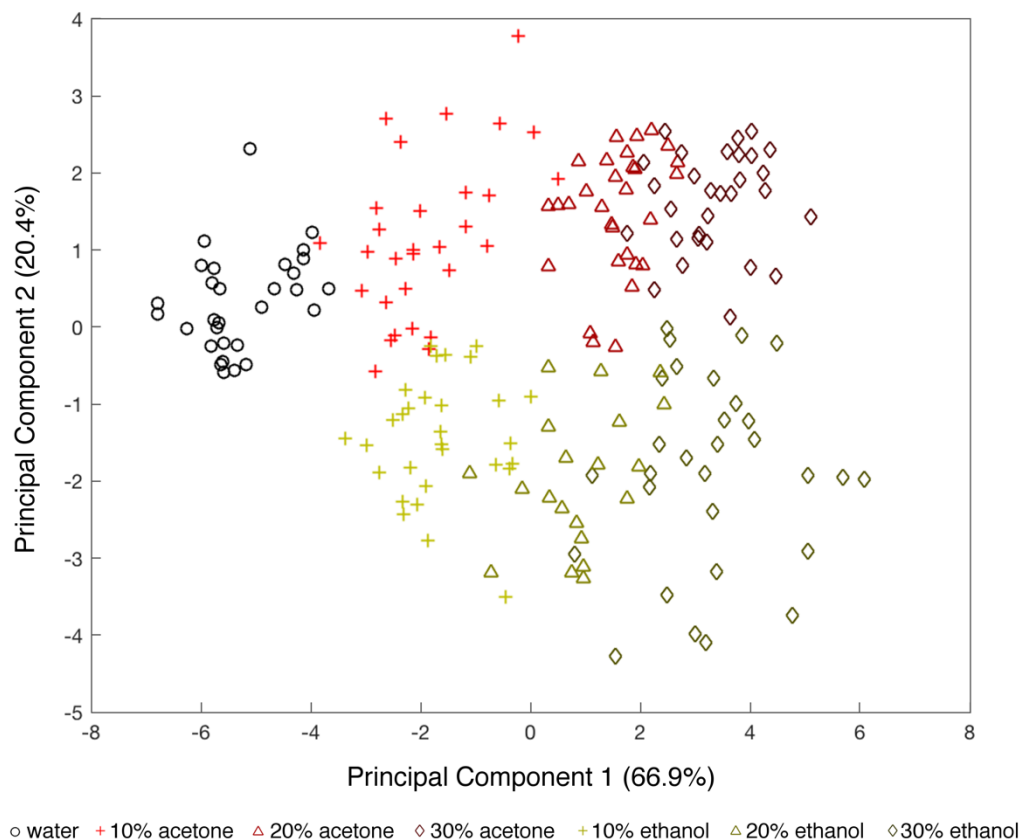


**Figure 4.10: PCA for organic solvent differentiation using bimetallic sensor regions.** The transmission peaks of 10 bimetallic optical-tongue arrays (30 sensing regions) in 10%, 20%, and 30% acetone and ethanol solutions were used to generate a PCA with each sensor as a new row of the PCA. The resulting PCA shows distinguishable groupings for the differentiation of the organic solvents.

While delineation of classes (acetone/ethanol and the v/v percent of each) is shown, it is important to note that this PCA analysed the results across 10 different optical tongue devices. A close look at SEM images from the 10 bimetallic sensors in **Figure 4.3** revealed that, while within the specifications of the e-beam lithography tool (i.e. 20 nm spatial resolution), the X-Y distances between the two metals was slightly different in each device. Given the high sensitivity of plasmonic nanostructures to their near-field environment, such minute misalignments can result in sensitivity differences from sensor to sensor [51-52], and this is confirmed by simulation in **Figure 4.4**. Additionally, the positioning between the Al and Au nanostructures can effectively alter the full surface wettability and segregation properties, which are intended to be used as part of the surface chemistry modifications

within this design for a plasmonic tongue [53]. This is because the distribution of hydrophobic and hydrophilic groups is dependent on the position of the metals and their uniquely modified surface chemistries within the array [53]. Thus, the spread of point within each class in the PCA is most likely attributed to this fabrication resolution. Regardless, the PCA shows clustering of the different solutions by combining the response from three sensing regions (even across 10 different tongue devices), which constitutes the very basic requirement for the development of an artificial tongue.

#### 4.4.3 Whisky Differentiation

To further demonstrate the capabilities of bimetallic tongue, the ten sensor arrays (as shown in **Figure 4.3**) were tested with seven whiskies with identical alcohol contents (40%), a 40% vodka, and 40% ethanol in water, with water as the control (as shown in **Table 4.1**). This test was performed on each of the bimetallic tongues, individually, to minimise the variance between sensors that would increase the noise within the data.

First, the PCA resulting response from the three sensors that the bimetallic tongue E2 comprises of will be compared to that of the equivalent six sensors that make-up the monometallic tongue using A1 and A6. Then, the resulting PCAs from all 10 bimetallic sensor arrays will be compared to one another to examine the effects of the different ‘within-spec’ alignments between the metal arrays.

##### 4.4.3.1 Monometallic Sensor Array v. Bimetallic Sensor Array

The resulting PCA for the first two principal components for monometallic (elements A1 and A6 from **Figure 4.3**) and bimetallic (element E2 from **Figure 4.3**) sensing arrays are shown in **Figure 4.11a** and **Figure 4.11b**, respectively. The colours and symbols used in the PCA are identified by the first column of **Table 4.1**. To demonstrate the effect of adding more partially-selective responses of additional sensors to the analysis, PCA was calculated using the transmission peaks from the columns in the data matrices corresponding to **(i)** Al and Au, only; **(ii)** Al, Au, Al-HMDS, and Au-DT; and **(iii)** Al, Au, Al-HMDS, Au-DT, Al-PEG, and Au-PFDT. The boxed region in **(iii)**, which contains the alcohol solutions, is enlarged in **(iv)**. Similar to the organic solvent tests, further delineation of class (clustering of each solution and increasing distance between clusters) occurs as more elements are added to the PCA.

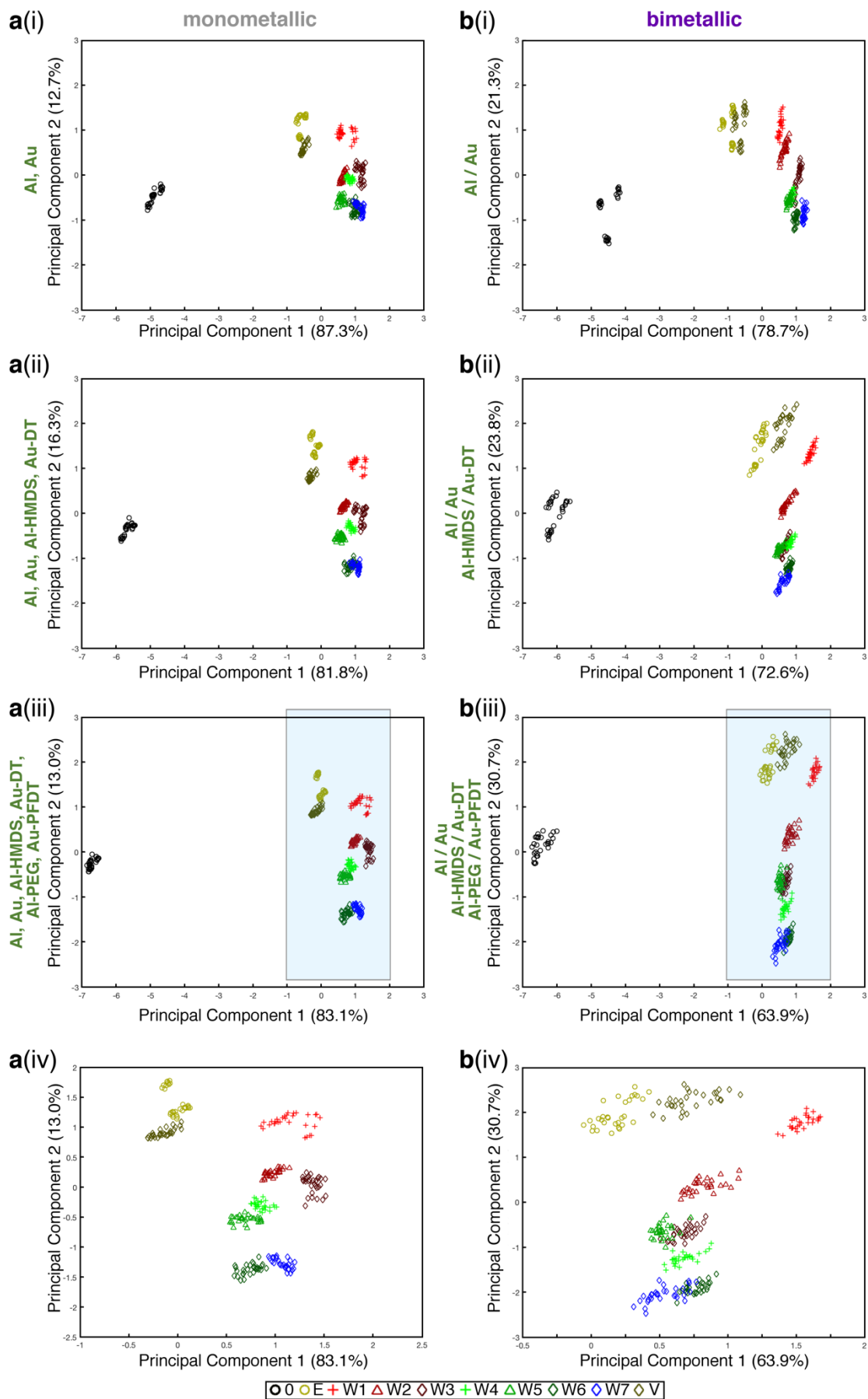


**Figure 4.11: 2D PCA for whisky differentiation.** This figure shows scatterplots of the first and second principal components of the plasmonic peaks from an optical-tongue sensor consisting of (a) monometallic Au and Al sensors (elements A1/A6 from **Figure 4.3**) and (b) bimetallic arrays of Au/Al (element E2 from **Figure 4.3**) as the responses from more sensors are added to the PCA: (i) Al and Au; (ii) Al, Au, Au-DT, and Al-HMDS; and (iii) Al, Au, Au-DT, Al-HMDS, Au-PFDT, and Al-PEG. (iv) Zoomed-in plot of the box from (iii) to show more closely the clustering of and separation between the whiskies in the PCA. For identification of the solutions, the colours of and symbols correspond to Column 1 of **Table 4.1**.

To further exhibit the achieved clustering and delineation of class, the first (PC1), second (PC2), and third (PC3) principal components for all chemistries (as shown in **Figure 4.11 a(iii)** and **Figure 4.11 b(iii)**, representing >95% variance) are shown in **Figure 4.12** for the (a) mono- and (b) bimetallic arrays. The inset in each figure shows a magnified view of the region of the PCA containing only the alcohol elements.

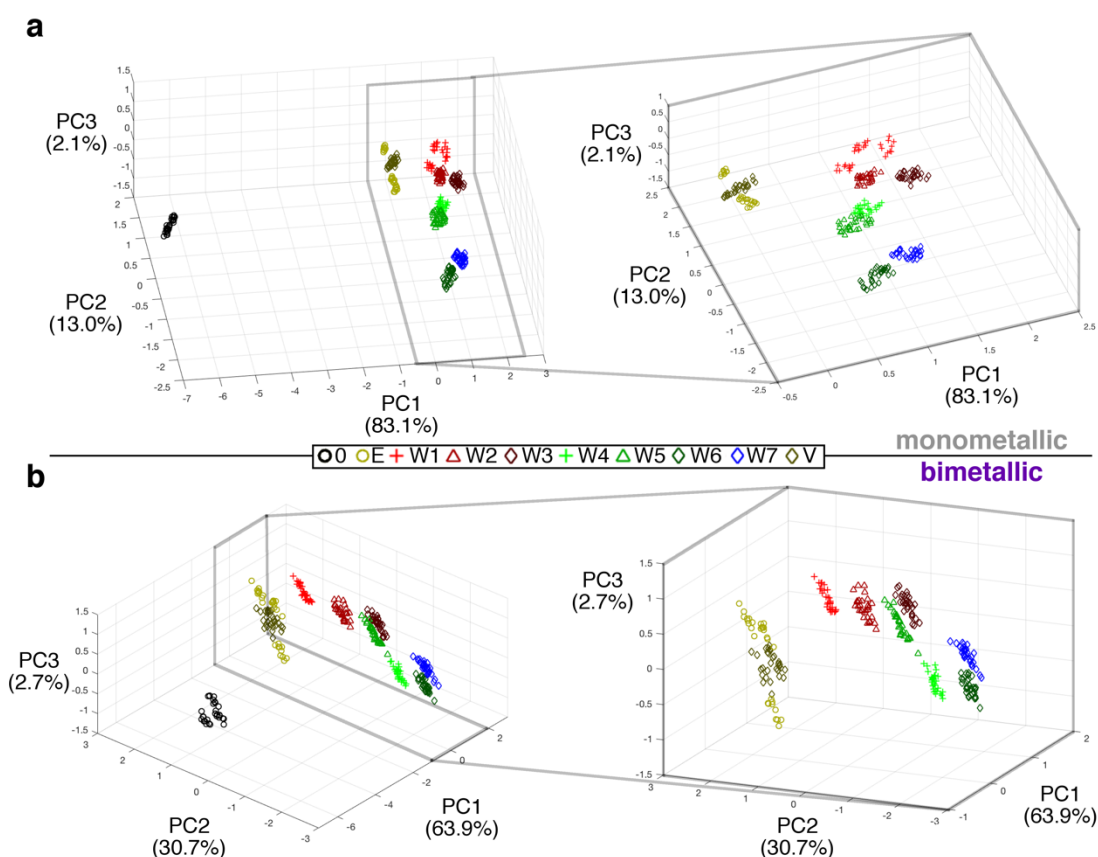


**Figure 4.12: 3D PCA for whisky differentiation.** Scatterplots show the PCA results using all 6 partially-selective responses from the optical tongue consisting of (a) 6 monometallic sensors (A1/A6) and (b) 3 bimetallic sensors (E2). (right) Zoomed-in plot of the boxed region indicated in the corresponding PCA to the left. For identification of the solutions, the colours of and symbols correspond to Column 1 of **Table 4.1**.

Similar to the organic solvent PCA above, it is observed that as the responses from more partially-selective elements are added to the PCA, further clustering occurs among responses corresponding to the same solution and further separation occurs between the clusters corresponding to different solutions.

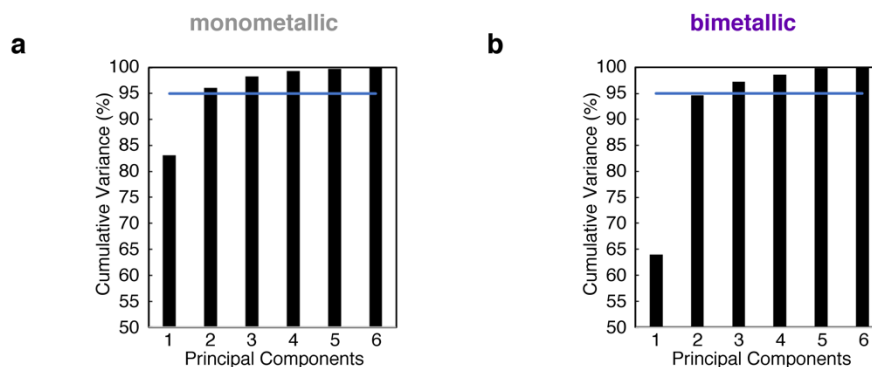


**Figure 4.13:** PCA scree plots from (a) mono- and (b) bimetallic tongues for whisky differentiation.

Sensor performance is determined by the dimensionality of the PCA, the distance between the groupings, and ‘tightness’ of the groupings. The dimensionality is measured by the number of components required to account for 95% of measurement variance, as shown in **Figure 4.13a** and **Figure 4.13b**. For the plasmonic tongue comprised of six monometallic sensors (A1/A6), two dimensions (principal components) contained >95% variance; and for the plasmonic tongue comprised of three bimetallic sensors (E2), >95% of the variance was spread over three dimensions. The overall difference between the cumulative variance of monometallic and bimetallic tongues with two principal components is very small. In both cases, the important qualitative point is that the PCA algorithm shows distinct clustering of the different test solutions. However, the main difference between the monometallic and bimetallic tongues is best explained by observing what happens when comparing the device classification capabilities based on using one versus two principal components.

To better understand how each partially-selective element in the sensing array affects the PCA, the resulting coefficients for the first (PC1), second (PC2), and third (PC3) principal components for the monometallic (A1/A6) and bimetallic (E2) whisky tongues are shown in **Table 4.3**. These PCs are derived from using the full transmission peak response matrix for the monometallic and bimetallic tongues (i.e. all 6 partially-selective responses).

**Table 4.3: Coefficients for the first, second, and third principal components of the monometallic and bimetallic whisky tongues (using the full tongue arrays consisting of all 6 and all 3 sensing regions, respectively).**

	PC	Al	Au	Al-HMDS	Au-DT	Al-PEG	Au-PFDT	% variance
<i>monometallic</i> (A1/A6)	1	0.341	0.667	0.213	0.349	0.325	0.407	83.1
	2	0.515	-0.568	0.582	0.019	0.269	-0.034	13.0
	3	-0.236	0.223	0.081	-0.437	0.725	-0.414	2.1
<i>bimetallic</i> (E2)	1	0.215	0.673	0.474	0.397	0.088	0.333	63.9
	2	0.454	-0.467	0.390	-0.015	0.648	-0.057	30.7
	3	0.087	0.473	-0.531	-0.367	0.593	0.024	2.7

In both PCAs (mono- versus bimetallic) the pattern of water versus whisky and ethanol/vodka versus whisky is largely similar. W1 (Glenfiddich® 12y) in particular gives a markedly different signal to the other spirits tested. Analysis of the principal components in each tongue give an indication of the elements contributing to each PC. For the monometallic tongue, PC1 is from the transmission peaks corresponding to the Au nanostructures, particularly Au and Au-PFDT that separate water from ethanolic solutions. Al-HMDS contributes to the PC2, along with Al which has the most separation of the whiskies/controls. In the bimetallic tongue, many regions contribute to the PC1, but PC2 is dominated by Al and Al-PEG, demonstrating that by combining the surface chemistries in a single device, very different behaviour is observed.

In this sensor configuration, it is hypothesised that the organic aromatic components in the whiskies (phenols, terpenes and vanillin) and aliphatics (lactones) interacting with the bare or coated metal surfaces, as well as factors such as pH/ionic strength will all contribute to the subtle changes seen on the sensor chips.

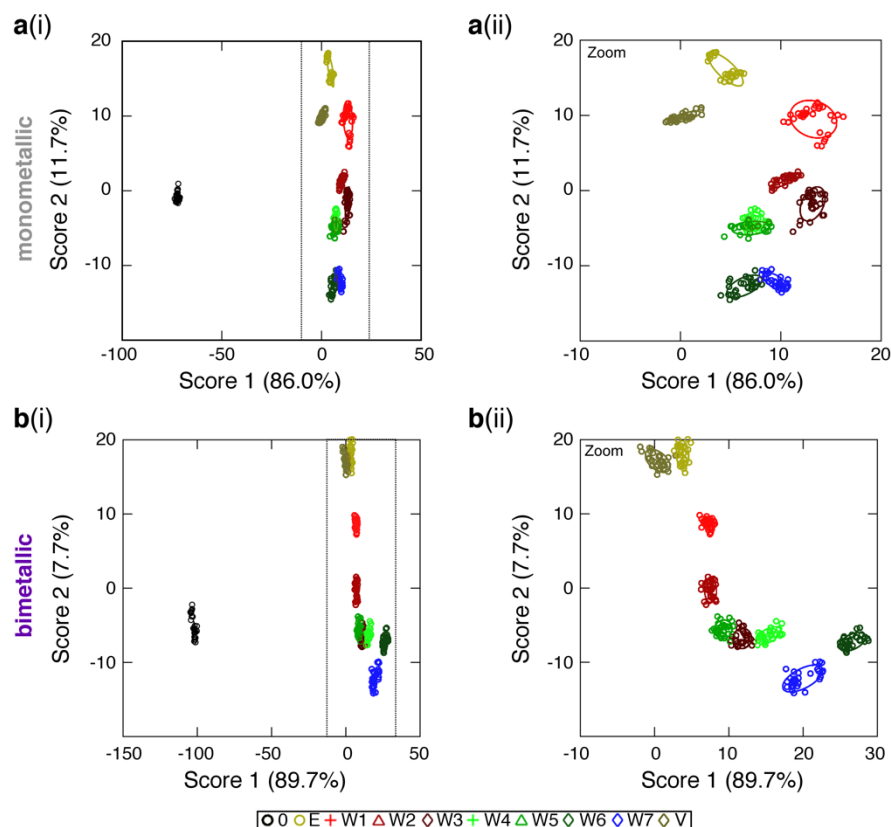


**Figure 4.14: LDA classification of whisky using (a) mono- and (b) bimetallic tongue devices.** For both analyses, (i) shows the full LDA and (ii) shows a zoomed in LDA of only the alcoholic solutions. For the monometallic device, classification had 100% accuracy. W4 and W5 are well separated in Score 3 (1.1%). For the bimetallic device, classification had 99.7% accuracy (W3 and W5 had one point misclassified). W4 is well separated out by Score 3 (1.9%). The ellipses are one standard deviation.

After analysing the PCA and clustering capabilities of both mono- and bimetallic tongues, it was concluded that both tongues are able to cluster and are sensitive to the functional groups present on their surface. However, bimetallic tongues are more sensitive to the functional groups on the surface while providing similar clustering capabilities. To investigate whether full classification was possible, linear discriminant analysis (LDA), a supervised technique, was applied to the data to generate new “scores” (in a similar methodology to PCA) to maximise separation between known clusters whilst minimising variance within each cluster [54]. Both the mono (**Figure 4.14a**) and bimetallic (**Figure 4.14b**) tongues could classify (using leave-one-out cross validation to test accuracy) 100% and 99.7% of the data, respectively. Although the bimetallic tongue performed fractionally worse than the monometallic tongue (confusing one instance of W3 for W5), this was compensated for by the bimetallic device in its ability to provide two signals from one measurement and therefore fewer measurements required to collect the data.

#### 4.4.3.2 Analysis of 10 Bimetallic Sensor Arrays

Examination of the effects of ‘within-spec’ fabrication alignment of the bimetallic tongue is best understood by comparing and analysing all 10 bimetallic tongues shown in **Figure 4.3**. The PCA, scree plots, and LDA for each sensor array are shown in **Figure 4.15**, **Figure 4.16**, and **Figure 4.17**, respectively.

Applying the same critical analysis as in the previous section, it can be observed regardless of any ‘within spec’ differences in alignment for the bimetallic tongue sensors, delineation and differentiation are achieved. However, some of the bimetallic tongues performed better than others. Classification accuracy (using leave-one-out cross validation to test accuracy) across all ten tongues ranged between 97% and 100% (see **Table 4.4**). As previously mentioned, due to the relatively close proximity of the nanostructure design, the ‘within-spec’ misalignment from the fabrication for the bimetallic tongues may result in undesired coupling between the individual structures and may additionally alter their full surface wettability and segregation properties. It is probable that this is the reason for the difference in both PCA and LDA between the different bimetallic tongues. Regardless, the bimetallic devices demonstrate the capability of distinguishing between different alcohols, using half the number of elements of the comparable monometallic tongue.

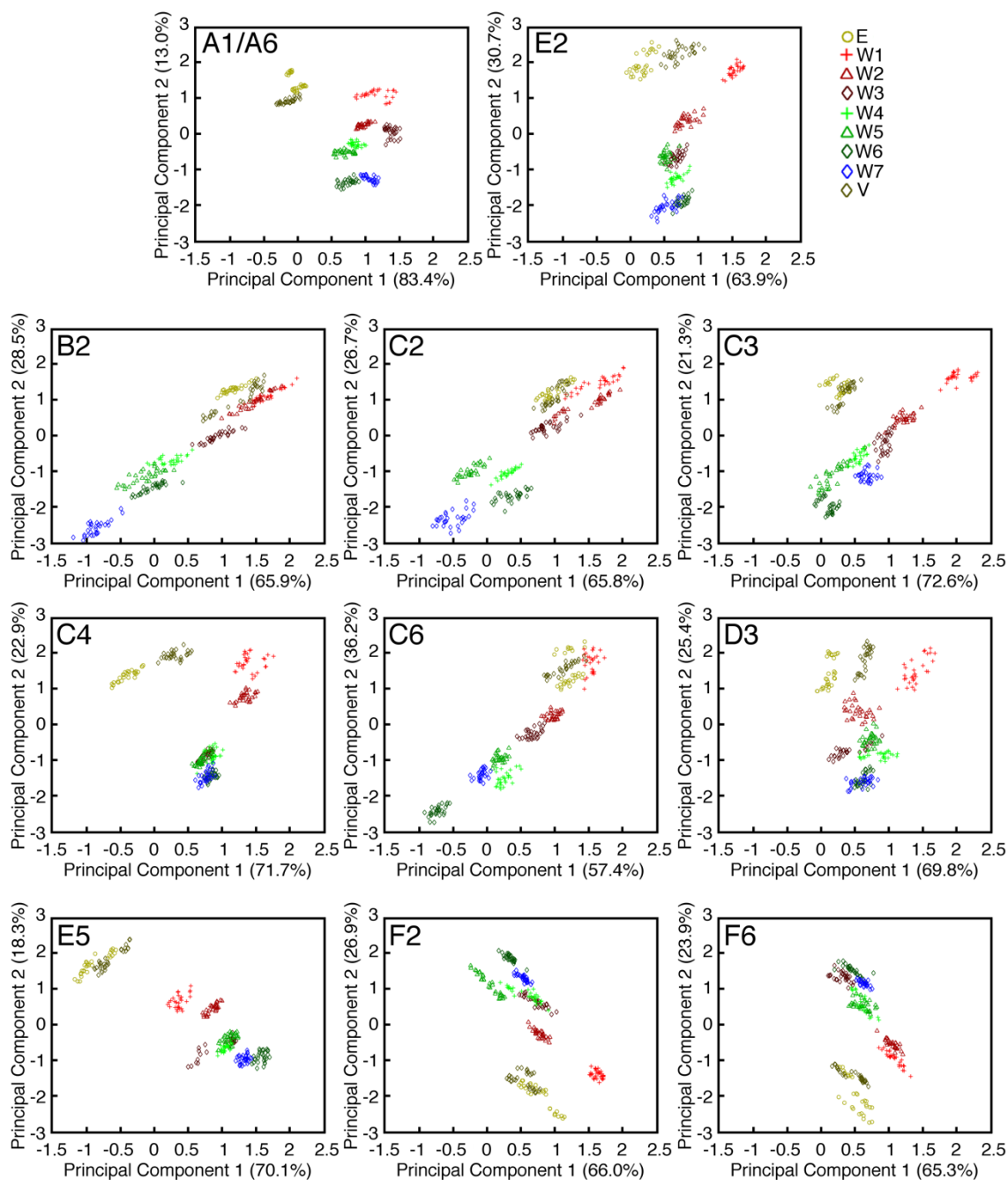


**Figure 4.15: PCA plots for 11 whisky tongues.** Zoomed in PCA of the first and second principal components (all six chemistries) for the monometallic (6 sensors) and all 10 bimetallic (3 sensors) tongues (SEMs shown in **Figure 4.3**). For better viewing, water is not shown and the PCAs are all zoomed in to the area containing the dataset for the eight alcoholic solutions. For identification of the alcohols from the key, see **Table 4.1**.

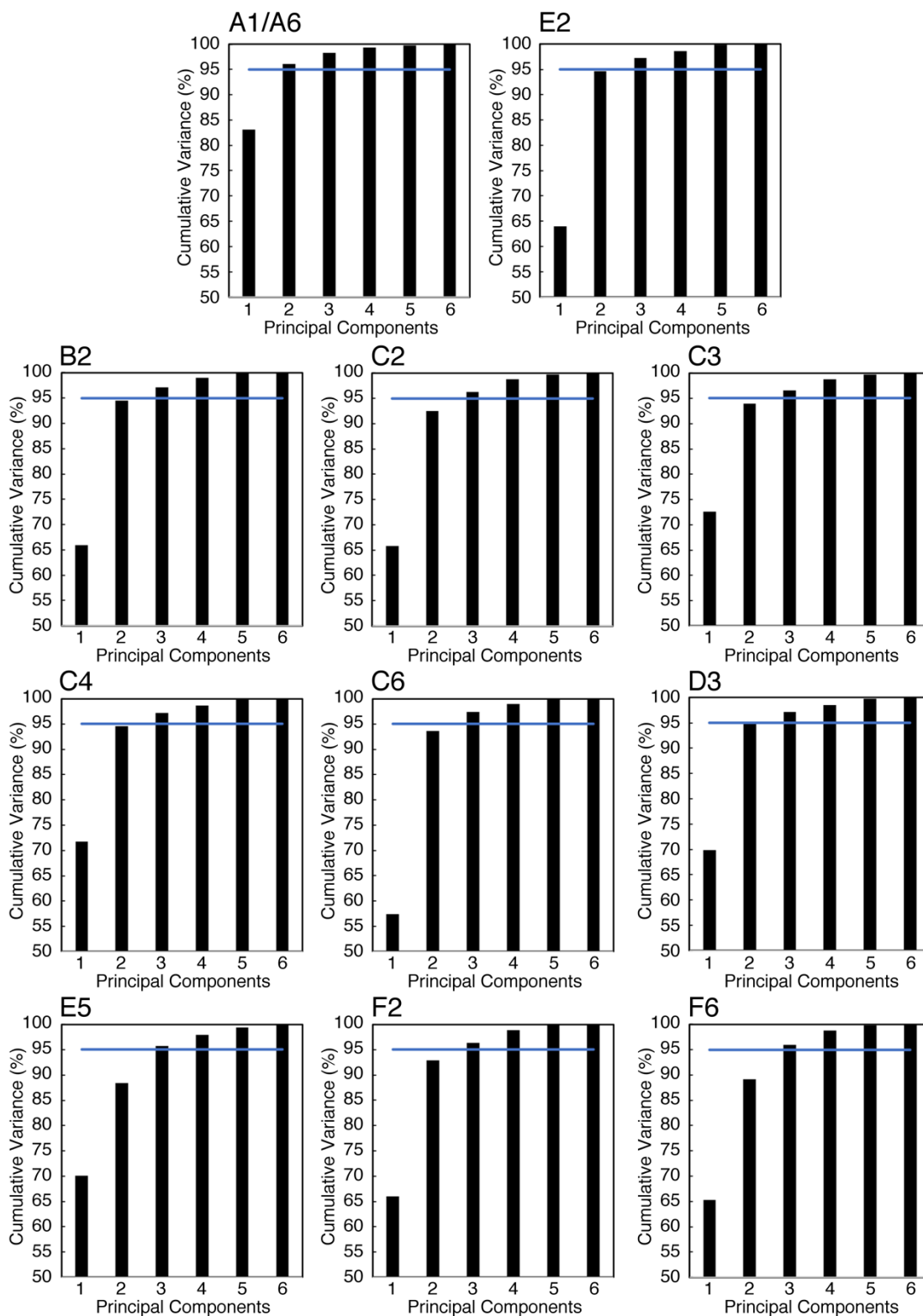


**Figure 4.16: Scree plots for 11 whisky tongues.** The corresponding scree plot for the PCAs of the monometallic and all 10 bimetallic tongues shown in Figure 4.15. The blue line denotes 95% cumulative variance.

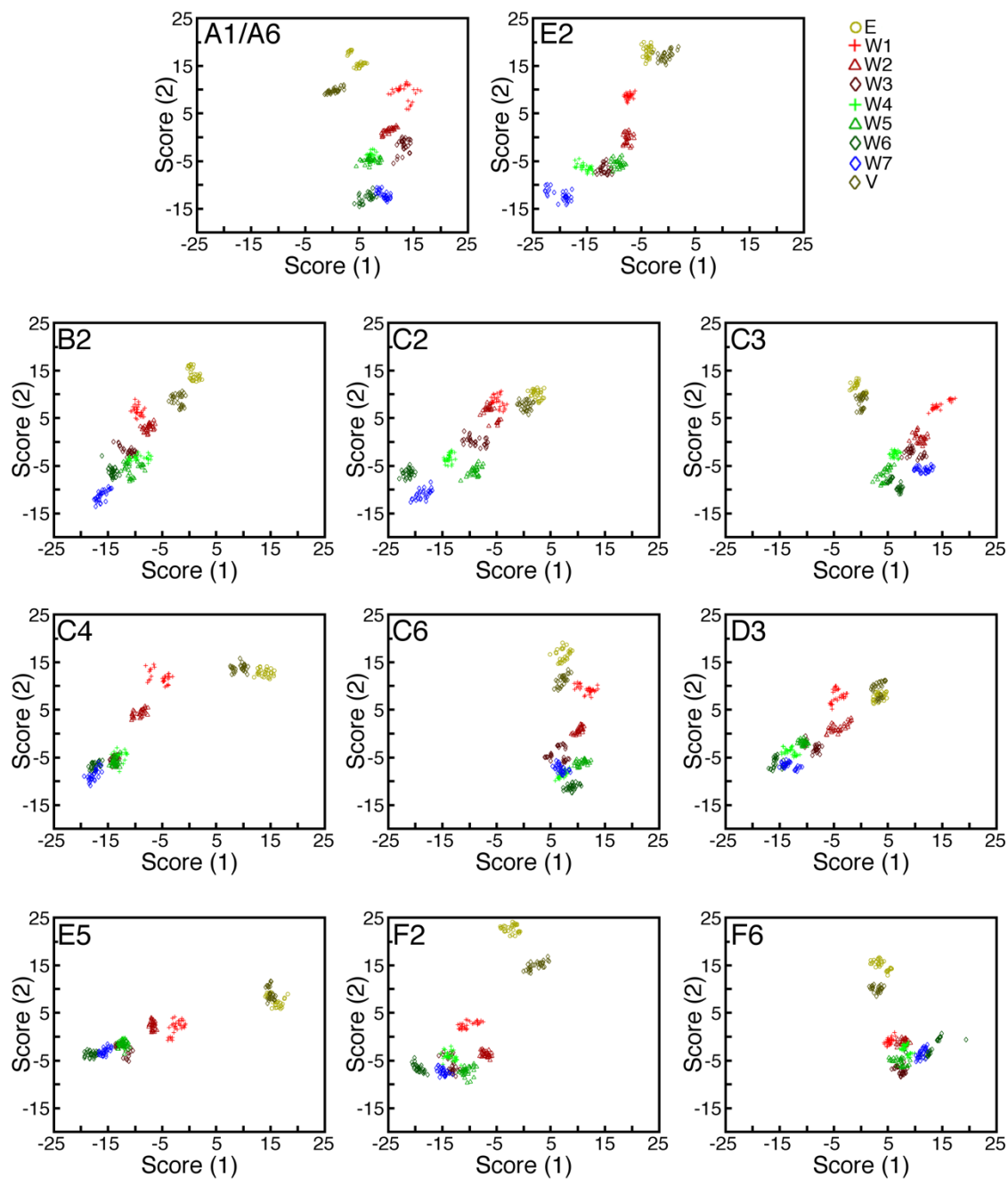


**Figure 4.17: LDA for 11 whisky tongues.** The corresponding LDA plots for the monometallic and all 10 bimetallic tongues shown in Figure 4.15.

**Table 4.4: Classification accuracy from LDA using leave-one-out cross validation to test accuracy.**

Device	% Accuracy	Instances of Misclassification
A1/A6	100.0%	-
E2	99.7%	W3 as W5
B2	100.0%	-
C2	100%	-
C3	99.7%	W2 as W3
C4	99.0%	W5 as W3 (x3)
C6	100%	-
D3	99.3%	W4 as W5; W3 as W5
E5	100.0%	-
F2	97.0%	W3 as W4 (x8); W4 as W7
F6	99.3%	W1 as W2; W6 as W4

#### 4.5 Conclusion and Future Work

This Chapter presented a bimetallic approach for the development of an optical tongue device. Compared to other devices which produce only one partially selective signal per element, each element of the bimetallic device provides two partially-selective signals. This unique feature effectively halves the number of elements necessary to provide the same amount of data as previous devices. Thus, device size and data acquisition time are halved while still providing dataset clustering upon PCA and successful classification with LDA. Additionally, the partial-selectivity to organic solvents is demonstrated to be tuned by altering the surface chemistry of the two different metals of the nanostructures within each element of the sensing array. To develop a high quality nanoplasmonic tongue for a given application, simple alterations to the surface ligands present in a region or change of metallic base components of one (or both) of the superimposed nanoarrays can yield new moieties with unique chemical responses. The technology presented here has applications in a number of fields that rely on assays for identification/classification of mixtures with multiple analytes, such as point of care diagnostics, food and drink processing, environmental monitoring, and the defence industry.

#### 4.6 References

- [1] del Valle, M. Bioinspired Sensor Systems. *Sensors* **2011**, *11* (11), 10180-10186, DOI: 10.3390/s111110180.

- [2] Stockmann, F. Photodetectors, Their Performance and Their Limitations. *Applied Physics* **1975**, 7 (1), 1-5, DOI: 10.1007/bf00900511.
- [3] Laux, E.; Genet, C.; Skauli, T.; Ebbesen, T. W. Plasmonic Photon Sorters for Spectral and Polarimetric Imaging. *Nature Photonics* **2008**, 2 (3), 161-164, DOI: 10.1038/nphoton.2008.1.
- [4] Dong, X.; Huang, X.; Zheng, Y.; Shen, L.; Bai, S. Infrared Dim and Small Target Detecting and Tracking Method Inspired by Human Visual System. *Infrared Physics & Technology* **2014**, 62, 100-109, DOI: 10.1016/j.infrared.2013.11.007.
- [5] Lipomi, D. J.; Vosgueritchian, M.; Tee, B. C. K.; Hellstrom, S. L.; Lee, J. A.; Fox, C. H.; Bao, Z. Skin-Like Pressure and Strain Sensors Based on Transparent Elastic Films of Carbon Nanotubes. *Nature Nanotechnology* **2011**, 6 (12), 788-792, DOI: 10.1038/nnano.2011.184.
- [6] Lumelsky, V. J.; Shur, M. S.; Wagner, S. Sensitive Skin. *IEEE Sens. J.* **2001**, 1 (1), 41-51, DOI: 10.1109/jsen.2001.923586.
- [7] Zhang, Y.; Bauer, R.; Jackson, J. C.; Whitmer, W. M.; Windmill, A. F. C.; Uttamchandani, D. A Low-Frequency Dual-Band Operational Microphone Mimicking the Hearing Property of Ormia Ochracea. *Journal of Microelectromechanical Systems* **2018**, 27 (4), 667-676, DOI: 10.1109/jmems.2018.2845680.
- [8] Rodriguez-Mendez, M. L.; De Saja, J. A.; Gonzalez-Anton, R.; Garcia-Hernandez, C.; Medina-Plaza, C.; Garcia-Cabezón, C.; Martín-Pedrosa, F. Electronic Noses and Tongues in Wine Industry. *Frontiers in Bioengineering and Biotechnology* **2016**, 4, DOI: 10.3389/fbioe.2016.00081.
- [9] Guerrini, L.; Garcia-Rico, E.; Pazos-Perez, N.; Alvarez-Puebla, R. A. Smelling, Seeing, Tasting-Old Senses for New Sensing. *Acs Nano* **2017**, 11 (6), 5217-5222, DOI: 10.1021/acsnano.7b03176.
- [10] Jennings, W.; Shibamoto, T. *Qualitative Analysis of Flavor and Fragrance Volatiles by Glass Capillary Gas Chromatography*, 1 ed.; Elsevier: 2012.
- [11] Ng, S. C.; Ong, T. T.; Fu, P.; Ching, C. B. Enantiomer Separation of Flavour and Fragrance Compounds by Liquid Chromatography Using Novel Urea-Covalent Bonded Methylated Beta-Cyclodextrins on Silica. *Journal of Chromatography A* **2002**, 968 (1-2), 31-40, DOI: 10.1016/s0021-9673(02)00840-3.
- [12] Welch, C. J.; Wu, N.; Biba, M.; Hartman, R.; Brkovic, T.; Gong, X.; Helmy, R.; Schafer, W.; Cuff, J.; Pirzada, Z.; Zhou, L. Greening Analytical Chromatography. *Trac-Trends in Analytical Chemistry* **2010**, 29 (7), 667-680, DOI: 10.1016/j.trac.2010.03.008.
- [13] Kermani, B. G.; Schiffman, S. S.; Nagle, H. T. Performance of the Levenberg-Marquardt Neural Network Training Method in Electronic Nose Applications. *Sens. Actuators, B* **2005**, 110 (1), 13-22, DOI: 10.1016/j.snb.2005.01.008.
- [14] D'Amico, A.; Pennazza, G.; Santonico, M.; Martinelli, E.; Roscioni, C.; Galluccio, G.; Paolesse, R.; Di Natale, C. An Investigation on Electronic Nose Diagnosis of Lung Cancer. *Lung Cancer* **2010**, 68 (2), 170-176, DOI: 10.1016/j.lungcan.2009.11.003.
- [15] Han, J.; Ma, C.; Wang, B.; Bender, M.; Bojanowski, M.; Hergert, M.; Seehafer, K.; Herrmann, A.; Bunz, U. H. F. A Hypothesis-Free Sensor Array Discriminates Whiskies for Brand, Age, and Taste. *Chem* **2017**, 2 (6), 817-824, DOI: 10.1016/j.chempr.2017.04.008.
- [16] Hou, C.; Dong, J.; Zhang, G.; Lei, Y.; Yang, M.; Zhang, Y.; Liu, Z.; Zhang, S.; Huo, D. Colorimetric Artificial Tongue for Protein Identification. *Biosens. Bioelectron.* **2011**, 26 (10), 3981-3986, DOI: 10.1016/j.bios.2010.11.025.

- [17] Askim, J. R.; Mahmoudi, M.; Suslick, K. S. Optical Sensor Arrays for Chemical Sensing: The Optoelectronic Nose. *Chem. Soc. Rev.* **2013**, *42* (22), 8649-8682, DOI: 10.1039/c3cs60179j.
- [18] Persaud, K.; Dodd, G. Analysis of Discrimination Mechanisms in the Mammalian Olfactory System Using a Model Nose. *Nature* **1982**, *299* (5881), 352-355, DOI: 10.1038/299352a0.
- [19] Peveler, W. J.; Yazdani, M.; Rotello, V. M. Selectivity and Specificity: Pros and Cons in Sensing. *Acs Sensors* **2016**, *1* (11), 1282-1285, DOI: 10.1021/acssensors.6b00564.
- [20] Vosshall, L. B.; Stocker, R. E. Molecular Architecture of Smell and Taste in *Drosophila*. *Annual Review of Neuroscience* **2007**, *30*, 505-533, DOI: 10.1146/annurev.neuro.30.051606.094306.
- [21] Vlasov, Y.; Legin, A.; Rudnitskaya, A.; Di Natale, C.; D'Amico, A. Nonspecific Sensor Arrays ("Electronic Tongue") for Chemical Analysis of Liquids (Iupac Technical Report). *Pure and Applied Chemistry* **2005**, *77* (11), 1965-1983, DOI: 10.1351/pac200577111965.
- [22] Bicego, M.; Tessari, G.; Tecchiolli, G.; Bettinelli, M. A Comparative Analysis of Basic Pattern Recognition Techniques for the Development of Small Size Electronic Nose. *Sens. Actuators, B* **2002**, *85* (1-2), 137-144, DOI: 10.1016/s0925-4005(02)00065-5.
- [23] Anslyn, E. V.; Rotello, V. M. Chemosensory Models: Approaches and Applications of Differential Sensing Editorial Overview. *Current Opinion in Chemical Biology* **2010**, *14* (6), 683-684, DOI: 10.1016/j.cbpa.2010.08.024.
- [24] Li, Z.; Askim, J. R.; Suslick, K. S. The Optoelectronic Nose: Colorimetric and Fluorometric Sensor Arrays. *Chem. Rev.* **2019**, *119* (1), 231-292, DOI: 10.1021/acs.chemrev.8b00226.
- [25] Goodner, K. L.; Dreher, J. G.; Rouseff, R. L. The Dangers of Creating False Classifications Due to Noise in Electronic Nose and Similar Multivariate Analyses. *Sens. Actuators, B* **2001**, *80* (3), 261-266, DOI: 10.1016/s0925-4005(01)00917-0.
- [26] Turner, A. P. F.; Magan, N. Electronic Noses and Disease Diagnostics. *Nature Reviews Microbiology* **2004**, *2* (2), 161-166, DOI: 10.1038/nrmicro823.
- [27] Brenner, H. Long-Term Survival Rates of Cancer Patients Achieved by the End of the 20th Century: A Period Analysis. *Lancet* **2002**, *360* (9340), 1131-1135, DOI: 10.1016/s0140-6736(02)11199-8.
- [28] Geng, Y.; Peveler, W. J.; Rotello, V. M. Array-Based "Chemical Nose" Sensing in Diagnostics and Drug Discovery. *Angewandte Chemie (International ed. in English)* **2018**, DOI: 10.1002/anie.201809607.
- [29] Peveler, W. J.; Landis, R. F.; Yazdani, M.; Day, J. W.; Modi, R.; Carmalt, C. J.; Rosenberg, W. M.; Rotello, V. M. A Rapid and Robust Diagnostic for Liver Fibrosis Using a Multichannel Polymer Sensor Array. *Advanced Materials* **2018**, *30* (28), DOI: 10.1002/adma.201800634.
- [30] Li, W.; Liu, H.; Xie, D.; He, Z.; Pi, X. Lung Cancer Screening Based on Type-Different Sensor Arrays. *Sci. Rep.* **2017**, *7*, DOI: 10.1038/s41598-017-02154-9.
- [31] Peng, G.; Hakim, M.; Broza, Y. Y.; Billan, S.; Abdah-Bortnyak, R.; Kuten, A.; Tisch, U.; Haick, H. Detection of Lung, Breast, Colorectal, and Prostate Cancers from Exhaled Breath Using a Single Array of Nanosensors. *British Journal of Cancer* **2010**, *103* (4), 542-551, DOI: 10.1038/sj.bjc.6605810.
- [32] Peveler, W. J.; Roldan, A.; Hollingsworth, N.; Porter, M. J.; Parkin, I. P. Multichannel Detection and Differentiation of Explosives with a Quantum Dot Array. *Acs Nano* **2016**, *10* (1), 1139-1146, DOI: 10.1021/acsnano.5b06433.

- [33] Diehl, K. L.; Anslyn, E. V. Array Sensing Using Optical Methods for Detection of Chemical and Biological Hazards. *Chem. Soc. Rev.* **2013**, *42* (22), 8596-8611, DOI: 10.1039/c3cs60136f.
- [34] El Barbri, N.; Llobet, E.; El Bari, N.; Correig, X.; Bouchikhi, B. Electronic Nose Based on Metal Oxide Semiconductor Sensors as an Alternative Technique for the Spoilage Classification of Red Meat. *Sensors* **2008**, *8* (1), 142-156, DOI: 10.3390/s8010142.
- [35] Wu, C.; Du, Y.-W.; Huang, L.; Galeczki, Y. B.-S.; Dagan-Wiener, A.; Naim, M.; Niv, M. Y.; Wang, P. Biomimetic Sensors for the Senses: Towards Better Understanding of Taste and Odor Sensation. *Sensors* **2017**, *17* (12), DOI: 10.3390/s17122881.
- [36] Peng, G.; Tisch, U.; Adams, O.; Hakim, M.; Shehada, N.; Broza, Y. Y.; Billan, S.; Abdah-Bortnyak, R.; Kuten, A.; Haick, H. Diagnosing Lung Cancer in Exhaled Breath Using Gold Nanoparticles. *Nature Nanotechnology* **2009**, *4* (10), 669-673, DOI: 10.1038/nnano.2009.235.
- [37] Saha, K.; Agasti, S. S.; Kim, C.; Li, X.; Rotello, V. M. Gold Nanoparticles in Chemical and Biological Sensing. *Chem. Rev.* **2012**, *112* (5), 2739-2779, DOI: 10.1021/cr2001178.
- [38] Maier, S. A. *Plasmonics: Fundamentals and Applications*, Springer Science+Business Media LLC: New York, 2007.
- [39] Srisombat, L.; Jamison, A. C.; Lee, T. R. Stability: A Key Issue for Self-Assembled Monolayers on Gold as Thin-Film Coatings and Nanoparticle Protectants. *Colloids and Surfaces a-Physicochemical and Engineering Aspects* **2011**, *390* (1-3), 1-19, DOI: 10.1016/j.colsurfa.2011.09.020.
- [40] Nicosia, C.; Huskens, J. Reactive Self-Assembled Monolayers: From Surface Functionalization to Gradient Formation. *Materials Horizons* **2014**, *1* (1), 32-45, DOI: 10.1039/c3mh00046j.
- [41] Sperling, J. R.; Macias, G.; Neale, S. L.; Clark, A. W. Multilayered Nanoplasmonic Arrays for Self-Referenced Biosensing. *ACS Applied Materials & Interfaces* **2018**, DOI: 10.1021/acsami.8b12604.
- [42] Jani, A. M. M.; Anglin, E. J.; McInnes, S. J. P.; Losic, D.; Shapter, J. G.; Voelcker, N. H. Nanoporous Anodic Aluminium Oxide Membranes with Layered Surface Chemistry. *Chem. Commun. (Cambridge)* **2009**, (21), 3062-3064, DOI: 10.1039/b901745c.
- [43] Sperling, J. R.; Macias, G.; Burley, G. A.; Neale, S. L.; Clark, A. W. In *Nanoplasmonic Discrimination of Organic Solvents Using a Bimetallic Optical Tongue*, SPIE BiOS, San Francisco, CA (USA), 2-7 Feb 2019; San Francisco, CA (USA), 2019.
- [44] Rumble, J. R.; Lide, D. R.; Bruno, T. J. *Crc Handbook of Chemistry & Physics*, 98 ed.; CRC Press: Boca Raton, USA, 2017.
- [45] Palik, E. D. *Handbook of Optical Constants of Solids*, Academic Press: 1997; Vol. I-III.
- [46] Goldstein, J. I.; Newbury, D. E.; Micheal, J. R.; Ritchie, N. W. M.; Scott, J. H. J.; Joy, D. C. *Scanning Electron Microscopy and X-Ray Microanalysis*, 4 ed.; Springer: 2017.
- [47] Kurtz, S. S.; Wikings, A.; Camin, D. L.; Thompson, A. R. Refractive Index and Density of Acetone-Water Solutions. *Journal of Chemical and Engineering Data* **1965**, *10* (4), 330-333, DOI: 10.1021/je60027a009.
- [48] Scott, T. A. Refractive Index of Ethanol-Water Mixtures and Density and Refractive Index of Ethanol-Water-Ethyl Ether Mixtures. *J. Phys. Chem.* **1946**, *50* (5), 406-412, DOI: 10.1021/j150449a003.

- [49] Koberstein, J. T. Molecular Design of Functional Polymer Surfaces. *Journal of Polymer Science Part B-Polymer Physics* **2004**, 42 (16), 2942-2956, DOI: 10.1002/polb.20157.
- [50] Wold, S.; Esbensen, K.; Geladi, P. Principal Component Analysis. *Chemometrics and Intelligent Laboratory Systems* **1987**, 2 (1-3), 37-52, DOI: 10.1016/0169-7439(87)80084-9.
- [51] Guo, L.; Jackman, J. A.; Yang, H.-H.; Chen, P.; Cho, N.-J.; Kim, D.-H. Strategies for Enhancing the Sensitivity of Plasmonic Nanosensors. *Nano Today* **2015**, 10 (2), 213-239, DOI: 10.1016/j.nantod.2015.02.007.
- [52] Su, K. H.; Wei, Q. H.; Zhang, X.; Mock, J. J.; Smith, D. R.; Schultz, S. Interparticle Coupling Effects on Plasmon Resonances of Nanogold Particles. *Nano Lett.* **2003**, 3 (8), 1087-1090, DOI: 10.1021/nl034197f.
- [53] Liu, X. M.; Thomason, J. L.; Jones, F. R. The Concentration of Hydroxyl Groups on Glass Surfaces and Their Effect on the Structure of Silane Deposits. *Silanes and Other Coupling Agents, Vol 5* **2009**, 25-38.
- [54] Stewart, S.; Ivy, M. A.; Anslyn, E. V. The Use of Principal Component Analysis and Discriminant Analysis in Differential Sensing Routines. *Chem. Soc. Rev.* **2014**, 43 (1), 70-84, DOI: 10.1039/c3cs60183h.

## Chapter 5: Plasmonic Nano-Apertures as Dual-State, Nanopixels for High-Density Micro-Image Encoding

### 5.1 Introduction

From painted artwork to spectral filters for modern image displays, discrete colour separation from white light is key for our ability to record and view optical information. Colour separation in these instances is typically provided by organic compounds, dyes, and pigments that absorb and scatter particular wavelengths of light, resulting in distinct colour profiles. Alternative to absorptive dyes, structured coloured systems based on engineered nanophotonic materials have recently emerged [1-16].

As briefly discussed in Chapter 1, plasmonic colour filters based on positive nanostructures [4, 8, 10, 12-13, 17-19], filters based on nano-apertures [2, 5, 20-22], and filters based on combinations of both of these designs [9, 15-16] are among these recent advances. Each of these approaches has a distinct fabrication and geometrical solution for achieving colour nanopixels for selective white-light separation. Plasmonic colour pixels offer several advantages over their microscale, dye-based counterparts. Most notably, the use of plasmonics allows for (a) ultra-dense, ultra-thin pixels arrays due to their subwavelength dimensions and (b) images that are environmentally stable and do not degrade or fade over time from radiation exposure. As a result, plasmonic colour filters have emerged as new technological solutions for subwavelength colour printing [1, 4, 8-10, 13], anti-counterfeiting measures [23-24], and red-green-blue splitting for image sensors [2, 21, 25-26]. This chapter explores a new application of polarisation-controlled plasmonic filters' dual-output, full-colour optical image encoding.

Recent developments in the engineering and manipulation of materials on the nanoscale have given rise to a number of new techniques with the potential for physically encoding images and data into optically readable surfaces and volumes [27-28]. Researchers have demonstrated novel 2D and 3D techniques (such as semiconductor quantum dots [29-31], graphene [32], and super-resolution lithography techniques [33-38]) that may enable the next generation of optical storage and encoding techniques. Additionally, plasmonic filters and particles are also among these techniques where optical data storage has been demonstrated alongside their abilities to encode images [27-28, 39-41].

In this Chapter, a new approach to high-density image encoding is demonstrated using full colour, dual-state plasmonic nanopixels based on polarisation-dependence. As opposed to previous studies that employed colour or position switching in fixed images [18, 32], this work shows two arbitrary full-colour images that can be encoded into a single array of pixels. Based on the EOT phenomenon discussed in Chapter 1, asymmetric cross-shaped nano-apertures in thin films of Al are used to encode two data sets into a single set of pixels for the first time, generating vivid, near-full sRGB (standard Red Green Blue colour space) colour images and codes with polarisation-switchable information states. Using a standard optical microscope, the smallest ‘unit’ that can be read relates to  $2 \times 2$  nano-pixels ( $370 \text{ nm} \times 370 \text{ nm}$ ). As a result, dual-state nano-pixels may prove significant for long-term, high-resolution optical image encoding, and counterfeit-prevention measures.

The majority of work detailed in this chapter was published by E. Heydari, J.R. Sperling, S.L. Neale, and A.W. Clark (2017) [6].

## 5.2 Materials

The materials used are available in Chapter 2.

## 5.3 Methods

### 5.3.1 Fabrication of Nano-Aperture Arrays

Devices were fabricated using electron-beam lithography, reactive ion etching, and inductively coupled plasma deposition as covered in Nano-Aperture Fabrication (Chapter 2.5.6). 100 nm of Al was deposited onto a  $500 \mu\text{m}$  thick borosilicate substrate by electron-beam evaporation. A Vistec VB6 UHR EWF electron-beam lithography tool was used to pattern a ZEP520A etch mask. Nano-apertures were etched into the Al using  $\text{SiCl}_4$  gas in an Oxford Instruments System 100 reactive ion etch tool. An Oxford Instrument System 100 plasma deposition tool was then used to deposit 150 nm of  $\text{SiO}_2$ .

### 5.3.2 Optical Image Capturing

Bright-field images of the pixel arrays were captured using a Zeiss Axio Imager A1 optical microscope with a Sony NEX-F3 camera. The Zeiss Epiplan-Neofluar objective lenses used included a  $20 \times 0.5 \text{ NA}$ ,  $50 \times 0.5 \text{ NA}$ , and  $100 \times 0.75 \text{ NA}$ .

### 5.3.3 Optical Transmission Spectra

Transmission spectra were collected over the visible spectrum using a linear film polariser with both a Shimadzu UV2101PC spectrophotometer and a custom-built microspectrophotometer. For the microspectrophotometer, a 10 x 0.5 NA objective was used to couple the transmitted light into an optical fibre attached to a StellarNet Microspectrophotometer (StellarNet Blue Wave).

### 5.3.4 Angled Measurements

3-D printed wedges at 5°, 10°, 15°, 20°, 30°, and 45° to normal were used to capture transmission spectra and optical images.

### 5.3.5 FDTD Simulations

FDTD simulations were modelled using Lumerical FDTD software. Further details on the parameters can be found in Chapter 5.4.1.

## 5.4 Results and Discussion

### 5.4.1 FDTD Simulations of Nano-Pixel Design

The colour pixels were designed as two nano-slit-apertures combined to form a nano-cross-aperture in a thin Al film. Al was chosen for its wide spectral plasmonic band, which can be tuned from the UV to the NIR, its low-cost, and its compatibility with current semiconductor manufacturing processes [5-6, 42].

**Figure 5.1** shows 5 nm resolution FDTD simulations of the electric field generated by 600 nm plane-wave source linearly polarised parallel to (a) the X-arm and (b) the Y-arm for a nano-aperture array in 100 nm thick Al deposited on glass. The source was transmitted through the glass-base of the sample as indicated by the red arrow labelled  $\lambda$  in **Figure 5.1a(i)** and **Figure 5.1b(i)**. The nano-aperture simulated has an arm length of 160 nm in X and 170 nm in Y, a periodicity of 310 nm in X and 300 nm in Y, and arm widths of 20 nm. The simulation was periodic in X-Y and perfectly-matched-layer (PML) in Z, and the dielectric values for both the glass and Al were obtained from the Palik library [43].

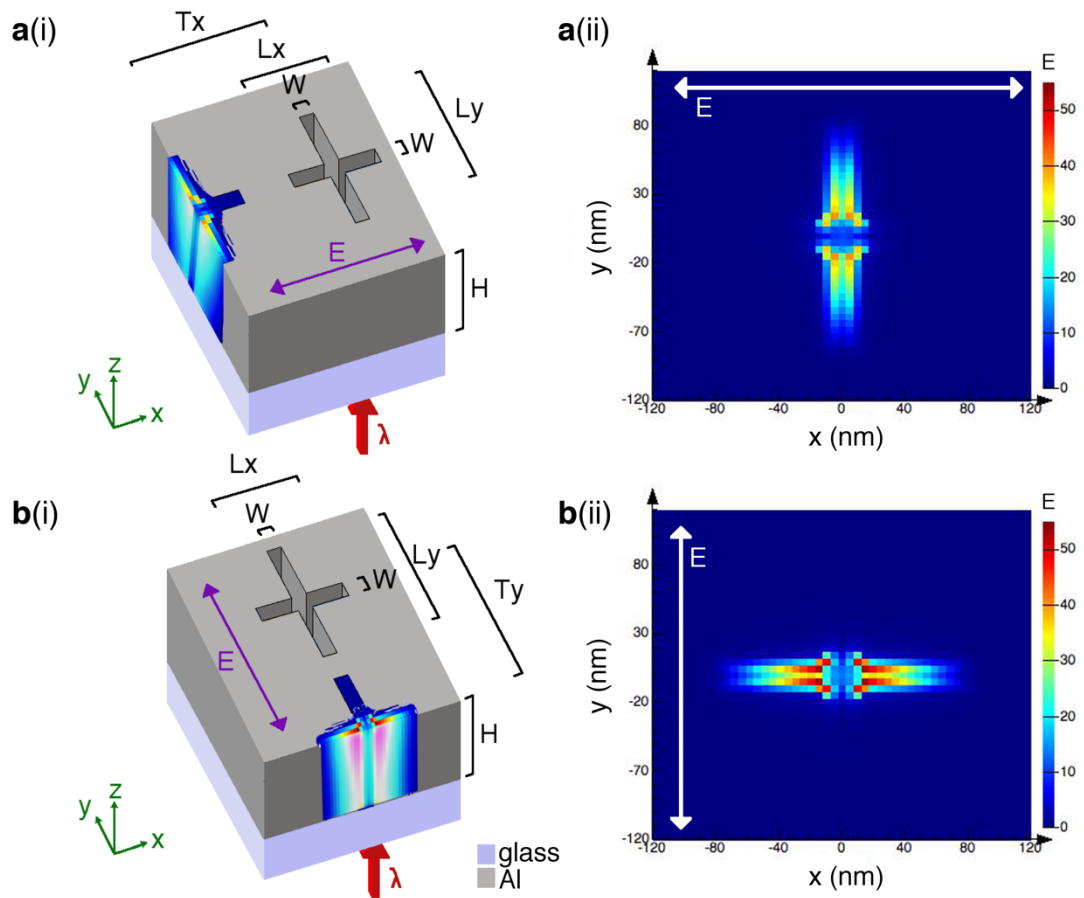


**Figure 5.1: FDTD simulation of nano-pixel electric field.** FDTD simulation (5 nm mesh, periodic in X-Y and PML in Z,  $\lambda = 600$  nm plane-wave light source) of nano-pixel array with arm lengths  $L_x = 160$  nm,  $L_y = 170$  nm; arm widths  $W = 20$  nm; and period  $T_x = 310$  nm,  $T_y = 300$  nm etched into  $H = 100$  nm of Al deposited on glass. The polarisation of the incident light source is indicated by E. The glass base and Al were simulated with dielectric constants from the Palik library [43]. (a) Linearly polarised light parallel to the x-axis generates a strong electric field in the y-arm as shown by the (i) cross section of the electric field in a 3D rendering of the simulated structure and (ii) the electric field at the surface of the Al. Whereas (b) linearly polarised light parallel to the y-axis generates a strong electric field in the x-arm as shown by the (i) cross section of the electric field in a 3D rendering of the simulated structure and (ii) the electric field at the top surface of the Al. It is important to note that the electric field in the arm parallel to the incident light is equal to that of the background, indicating that the two polarisation states are virtually independent of one another with no cross-talk.

As seen in the simulation results, linearly polarised light parallel to the X-arm generates a strong electric field in the Y-arm and linearly polarised light parallel to the Y-arm generates a strong electric field in the X-arm. It is important to note that the electric field in the arm parallel to the incident light is practically equal to that of the background, indicating that the two polarisation states are virtually independent of one another. The cross-structure itself thus enables polarisation dependence due to the selection rules for light propagating through

a nano-scale slit, which requires light to be perpendicular to the length of the slit. As a result, the two perpendicular arms can support their own resonance properties that can be tuned independently of one another, with zero cross-talk (colour-leak) between modes.

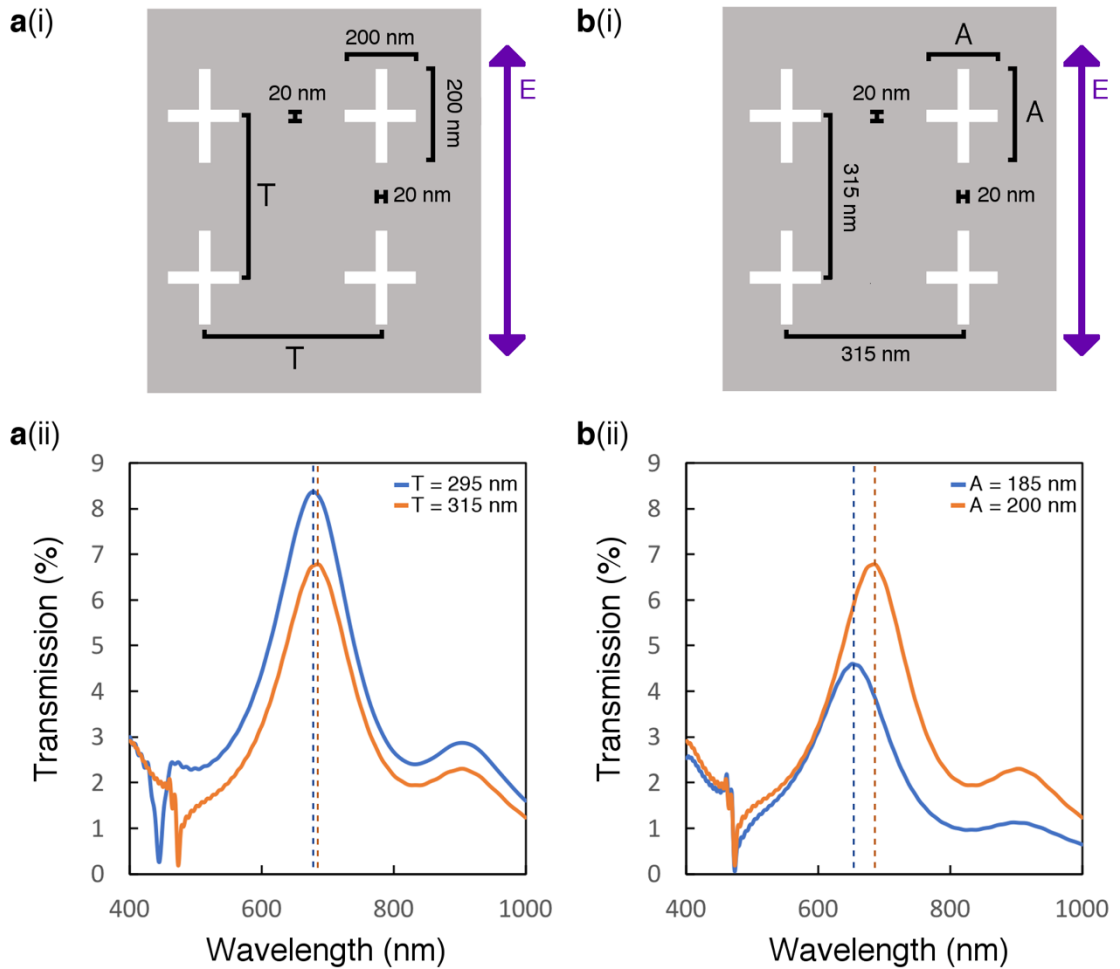


**Figure 5.2: FDTD simulation of nano-pixel arm-length and periodicity.** FDTD simulation (5 nm mesh, periodic in X-Y and PML in Z, linearly-polarised plane-wave light source) of the effect of varying periodicity ( $T$ ) and arm-length ( $A$ ) of a nano-pixel array etched into 100 nm of Al on glass. **(a)** Using a set arm-length of 200 nm and increasing the period from 295 nm to 315 nm results in a red-shift in the plasmonic peak and decrease in transmission. **(b)** Using a set period of 315 nm and increasing the arm-length from 185 nm to 200 nm yields a red-shift in the plasmonic peak and increase in transmission. For (a) and (b), part (i) is a rendering of the surface simulated and part (ii) is the transmission spectra. The glass base and Al were simulated with dielectric constants from the Palik library [43].

In **Figure 5.2**, the effects of changing (a) the period between nano-pixels and (b) the arm-length of the nano-pixel were explored by FDTD simulation (5 nm mesh, periodic in X-Y, PML in Z, linearly polarised plane-wave light source from 400 nm to 1000 nm). As can be seen from the simulation results, both the arm-length (perpendicular to the electric-field) and periodicity (parallel to the electric-field) of the nano-apertures affects the transmission.

Increasing the period from 295 nm to 315 nm results in a red-shift in the transmission peak and a decrease in transmission. Increasing the arm-length from 185 nm to 200 nm results in a red-shift in the transmission peak and an increase in transmission. Based on these simulations, it can also be concluded that variations to arm-length result in a larger peak-shift than variations to period.

#### 5.4.2 Fabricated Nano-Pixels

With the trends determined by FDTD in mind, the colour pixels were then fabricated on a borosilicate substrate using a combination of metal-evaporation, electron-beam lithography, and reactive ion etching, followed by inductively coupled plasma deposition of 150 nm of SiO<sub>2</sub> as a protective layer. Acting as a filter for white light, the colour response of the individual pixels was tuned by independently altering the arm-length and periodicity of each arm of the cross structure (**Figure 5.3 a,b**).

To determine the etch-rate for the nano-size structures, a variety of etch-times were tested. **Figure 5.3a** and **Figure 5.3b** show polarisation-switchable colour palettes using etch times of (i) 70 seconds and (ii) 120 seconds. For the colour palettes in **Figure 5.3**: Moving from top to bottom, the length of the x-arm is designed to increase from 120 nm to 220 nm, in 5 nm increments, while the period in the x-axis is designed to decrease from 350 nm to 250 nm, in 5 nm increments. Moving from left to right, the length of the y-arm is designed to decrease from 220 nm to 120 nm, in 5 nm increments, while the period in the y-axis is designed to increase from 250 nm to 350 nm, in 5 nm increments. As a result, the top-left half and bottom-right half of the palette are mirrored pixel-arrays, rotated by 90 degrees as indicated by the white diagonal line.

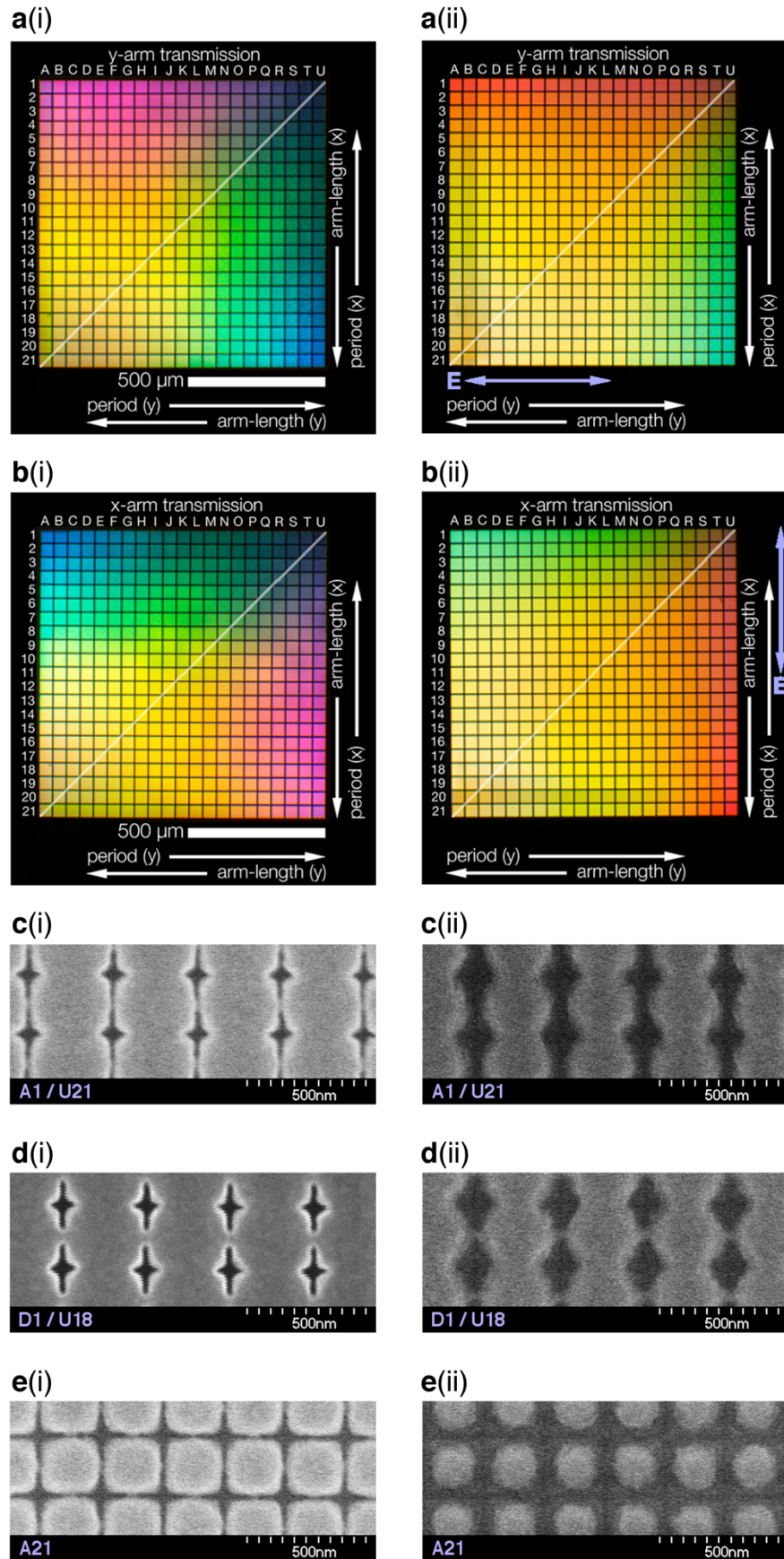


**Figure 5.3: Effects of etching.** (a,b) Bright-field microscope images showing a switchable colour palette with different colour outputs linked to different white-light polarisations with (i) 70 second and (ii) 120 reactive ion-etch times. For (a) and (b) the electric field is polarised in the X-axis and Y-axis, respectively. The geometry and period of each pixel array have been altered across the palette to produce a colour range that spans the visible spectrum, and where both extremes of the range can be encoded into the same pixel. The pixel arrays are labelled A1 – U21. Moving from top to bottom the arm length in the x-axis is increased while the x-axis period is decreased. Moving from left to right the arm-length in the y-axis is decreased while the y-axis period is increased. The arm width is fixed. The pixel arrays on either side of the diagonal line are the inverse of one another (i.e. the x-axis period and arm-length of the array in the top-left of the palette have the same values as the y-axis period and arm-length of the array in the bottom-right). SEM images of regions (c) A1/U21, (d) D1/U18, and (e) A21 of the colour palettes shown in (a) and (b). As expected, over-etching results in a red-shift of the plasmonic filter and drastically alters the shape of the nano-pixel. Figure parts a(i) and b(i) are reprinted from Heydari, et.al. (2017) [6]

The two palettes seen in **Figure 5.3a(i)** and **Figure 5.3b(i)** are in the same physical space, with each different palette activated by transmitted white-light polarised at 0-degrees and 90-degrees. **Figure 5.3 a(ii)** and **Figure 5.3 b(ii)**, just like the aforementioned palettes, occupy the same physical space and are activated by transmitting light polarised at 0-degrees and 90-degrees. As can be seen from the colour palettes, both the arm-length (perpendicular to the electric-field) and periodicity (parallel to the electric-field) of the nano-apertures affects the pixel colour. Increases to either value results in red-shifting, which matches the pattern seen in the simulation **Figure 5.2**. The sharpness of each resonance and transmission efficiency are both dictated by the periodicity (where the resonance becomes broader with decreasing inter-pixel distance and longer arms let through a higher percentage of light). As a result, there is a compromise between transmission percentage, spectral width, and peak position.

As indicated by the actual colour of the palettes and confirmed in the SEM images (**Figure 5.3 c-e**) of the selected pixels from the (i) 70 second and (ii) 120 second etches, a longer etch-time enlarges the nano-aperture width and results in a red-shifted palette. The nano-apertures also begin to merge, and shape-integrity is lost. Thus, it was concluded that in order to produce the widest range of colours and maintain the individuality of each nano-cross, the etch time of 70 seconds was warranted.

#### 5.4.3 Analysis of the Nano-Pixel Colour Palette Spectrum

For the 70 second etched samples, the actual arm-lengths were measured by SEM to range from  $112 \pm 5$  nm to  $219 \pm 9$  nm [SD] with arm widths of  $21 \pm 2$  nm. These dimensions

produced a palette encompassing the visible spectrum from deep blue to magenta. This palette demonstrates a vast selection of colours that can be accessed using the aforementioned dimensional constraints. However, it is by no means a demonstration of all the colours that can be created. Choosing a minimum pixel period of 250 nm allows the arm-length of the neighbouring pixel to be increased up to 220 nm without the two adjacent pixels merging. This translates to the widest colour gamut available while still allowing the ability to encode both colour extremes of magenta and deep-blue into a single pixel geometry.

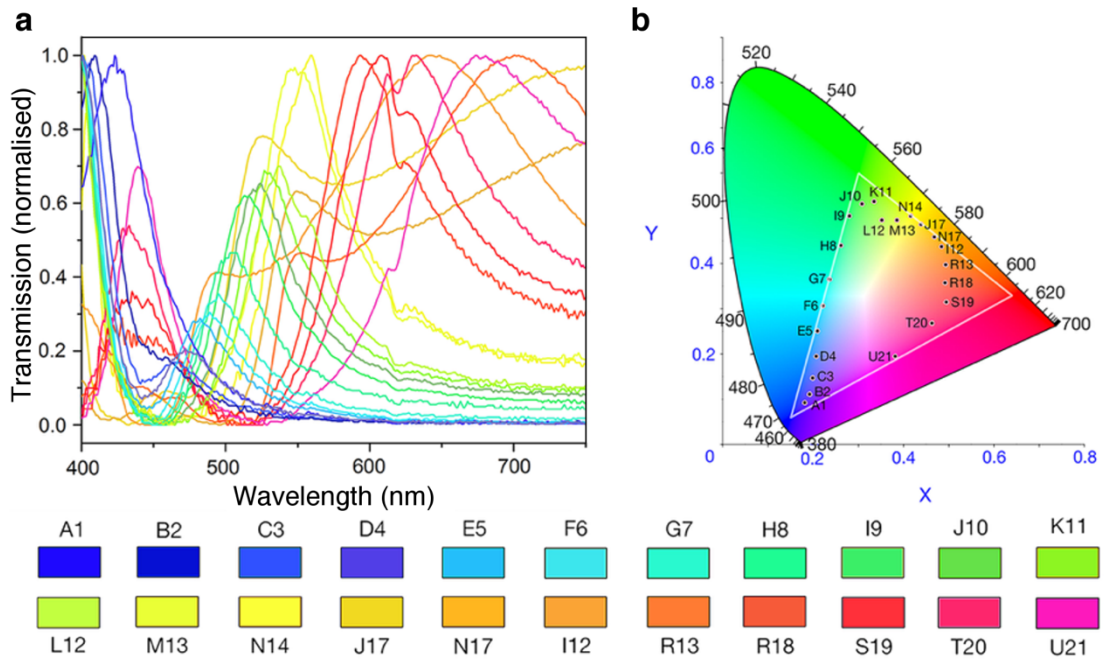


**Figure 5.4: Nano-pixel properties.** (a) Normalised  $x$ -arm transmission spectra selected from the pixel arrays shown, and labelled, in **Figure 5.3b(i)**, to best demonstrate the colour range achievable across the visible spectrum. (b) The same selection of pixel arrays plotted on a CIE  $XY$  chromaticity diagram. The  $sRGB$  colour space is marked by the white triangle. This figure is reprinted from Heydari, et.al. (2017) [6]

**Figure 5.4** shows spectral analysis of 22 nano-pixel arrays selected from **Figure 5.3b(i)** that best represent the colour range attainable using the cross-shaped nano-apertures. For a majority of the palette, the high-frequency mode either occurs below 400 nm or is so weak that its presence does not affect the perceived colour output. As a result, increasing the arm-length or period results in a predictable red-shift of the spectra and perceived colour output. However, the pixel arrays with larger transmission arm-lengths and periods can have a strong mode between 400 nm and 450 nm. This is the case for the magenta outputs. While the low-frequency peak occurs between 650 nm and 700 nm (red), the strong high-frequency (blue) peak results in a perceived mixture of the two colours (magenta). Various combinations of different arm-lengths and periodicities have the potential to encode any single pixel with any

two visible colours. For practicality purposes, only a selection of these combinations has been demonstrated. The CIE XY chromaticity diagram (**Figure 5.4b**) of the 22 selected pixels gives a clear representation of the colour range accessible using the aforementioned constraints. Coverage is shown extending across the extremities of the majority of the sRGB colour-space (marked as a white triangle on the figure).

#### 5.4.4 Nano-Pixels for Dual-Image Printing and Encoding

Each pixel holds potential for ultra-high-resolution image ‘printing’ at the nano-scale, facilitating print resolutions far beyond the diffraction limit [10]. The dual-colour capabilities for each pixel also makes them capable of encoding two full-colour image states [5-6, 44] into the same unit area using the same set of nano-pixels.

**Figure 5.5** shows an example of the ability of these nano-pixels to produce dual, polarisation-dependent information states in the same space. Bright-field microscopy (20x objective) reveals images of two distinct colour patterns produced from the same pixel array as designed by E. Heydari and fabricated by both E. Heydari and J.R. Sperling [6]. When light is transmitted through this filter, y-axis polarised light shows micro-images of the University of Glasgow crest and x-axis polarised light shows the University’s main building. The ‘arms’ of each individual cross in the micro-image have been tuned to transmit the appropriate colour for each polarisation state. Since each nano-pixel can be tuned to produce any two visible colours, this technique can be extended to encode any two arbitrary, full-colour images or information sets in the same area using the same pixels. As can be seen in the colour palettes of **Figure 5.3** and the micro-images of **Figure 5.5**, there is no colour-leaking between polarisation states.

The nano-pixel design allows for optically readable storage at the diffraction limit that, unlike magnetic or electronic methods, can provide stable, long-term data retention in scenarios where heat, humidity, or radiation damage may be of concern. This makes them, along with other nanophotonic solutions, attractive additions to the field of information storage and display [28, 39]. Compared to devices with single resonance pixels, the dual-state capabilities of these surfaces have double the information density. Additionally, the colour-based pixels allow for the stored information to be ‘read’ using white light, a standard microscope, and the human eye. The ability to encode two colour images in the same area with nano-scale resolutions may also make this technology appealing for the creation of anti-counterfeiting labels for bank notes and high-valued goods because the high-resolution and

dual-state capabilities make it much more difficult to forge than currently implemented techniques.

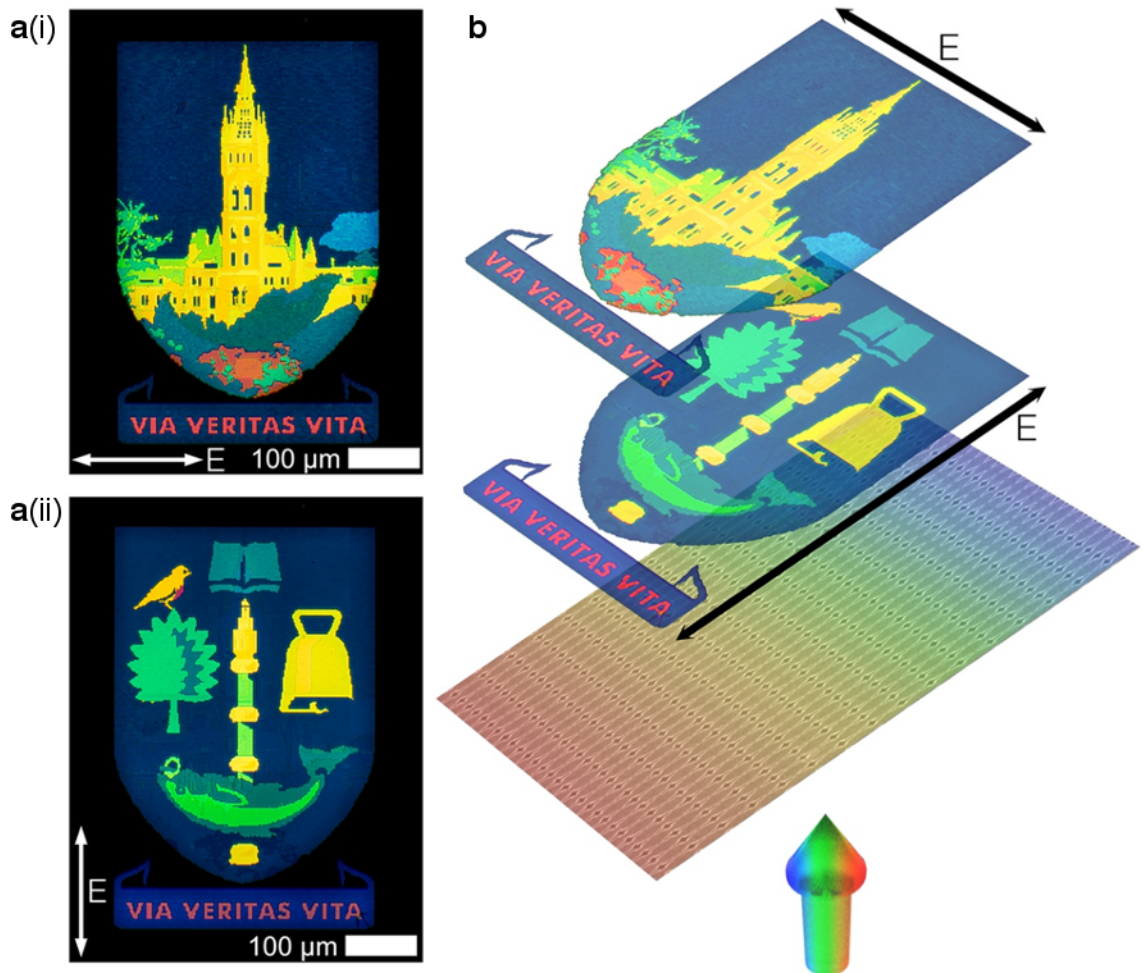


**Figure 5.5: Bright-field microscope images showing the switchable nature of the information displayed by a single set of nano-pixels. (a) Bright-field transmission images (20x objective) showing the full-colour pictures produced by the array when illuminated from the rear with white-light at different polarisations. Switching the polarisation of light causes the image displayed in the far-field to switch. (b) Schematic showing how the images were taken. A white-light source passes through a linear polariser before being selectively transmitted through the nano-apertures (pixels). At each polarisation state the aperture transmits colour corresponding to the desired display pattern. This figure is from Heydari, et.al. (2017) [6]**

As previously discussed, a wide variation in periodicity is required to achieve a full colour palette. Therefore, the pixel density (measured in pixels-per-inch or PPI) varies with colour. The PPI ranges from 101,599 PPI at its most dense to 72,568 at its most sparse. These values represent the number of physical apertures in a single inch, in any one axis (the periods in X and Y may differ depending on the desired two-colour pixel response). Since each aperture

has two arms that can be independently encoded with its own colour profile, the PPI range can be effectively doubled in terms of useful image encoding density. However, in order to determine the ultimate usable capacity of this system, the size limit below which individual groups of pixels cannot be resolved using white light must be determined.

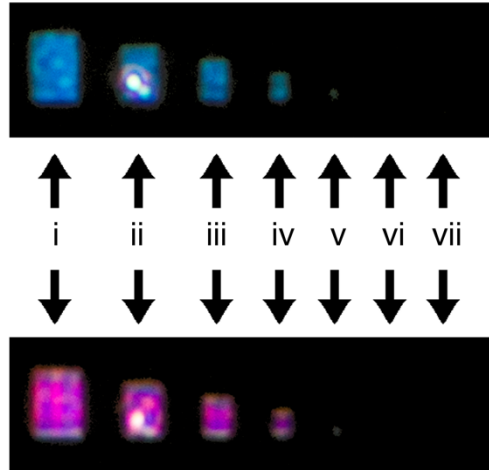


**Figure 5.6: Bright-field microscope images showing the smallest discernible pixel array size by standard microscopy.** A nano-pixel array using  $120 \text{ nm} \times 220 \text{ nm}$  designed pixels (measured by SEM as  $112 \pm 5 \text{ nm}$  by  $219 \pm 9 \text{ nm}$ ) of (i)  $10 \times 10$ , (ii)  $8 \times 8$ , (iii)  $6 \times 6$ , (iv)  $4 \times 4$ , (v)  $2 \times 2$ , (vi)  $2 \times 1$ , and (vii)  $1 \times 1$  pixel(s) with a period in (x,y) of (350 nm, 250 nm). The smallest discernible pixel array size is  $2 \times 2$  nano-pixels using a  $100 \times$  objective.

**Figure 5.6** shows seven array sizes ( $10 \times 10$ ,  $8 \times 8$ ,  $6 \times 6$ ,  $4 \times 4$ ,  $2 \times 2$ ,  $2 \times 1$ , and  $1 \times 1$  nano-pixels) of the magenta-blue pixel from the colour palette. The smallest discernible nano-pixel array size using white light and a standard optical microscope ( $100 \times$  objective) was found to be  $2 \times 2$  nano-pixels. This corresponds to a resolution of  $370 \text{ nm}$  by  $370 \text{ nm}$ .

The smallest discernible component was then used to create ultra-high-density QR codes encoded with 2 layers of information, as shown in **Figure 5.7**. QR codes are comprised of a matrix of contrasting modules, the layout of which define a 2D barcode. By using simple Boolean logic (**Figure 5.7a**), two different QR codes images were used to generate overlapping layers of shared foreground (yellow/blue), shared background (blue/yellow), QR1-only (always yellow), and QR2-only (always blue) images. These QR codes have feature sizes beyond the diffraction limit that are nevertheless visible using a simple optical microscope.

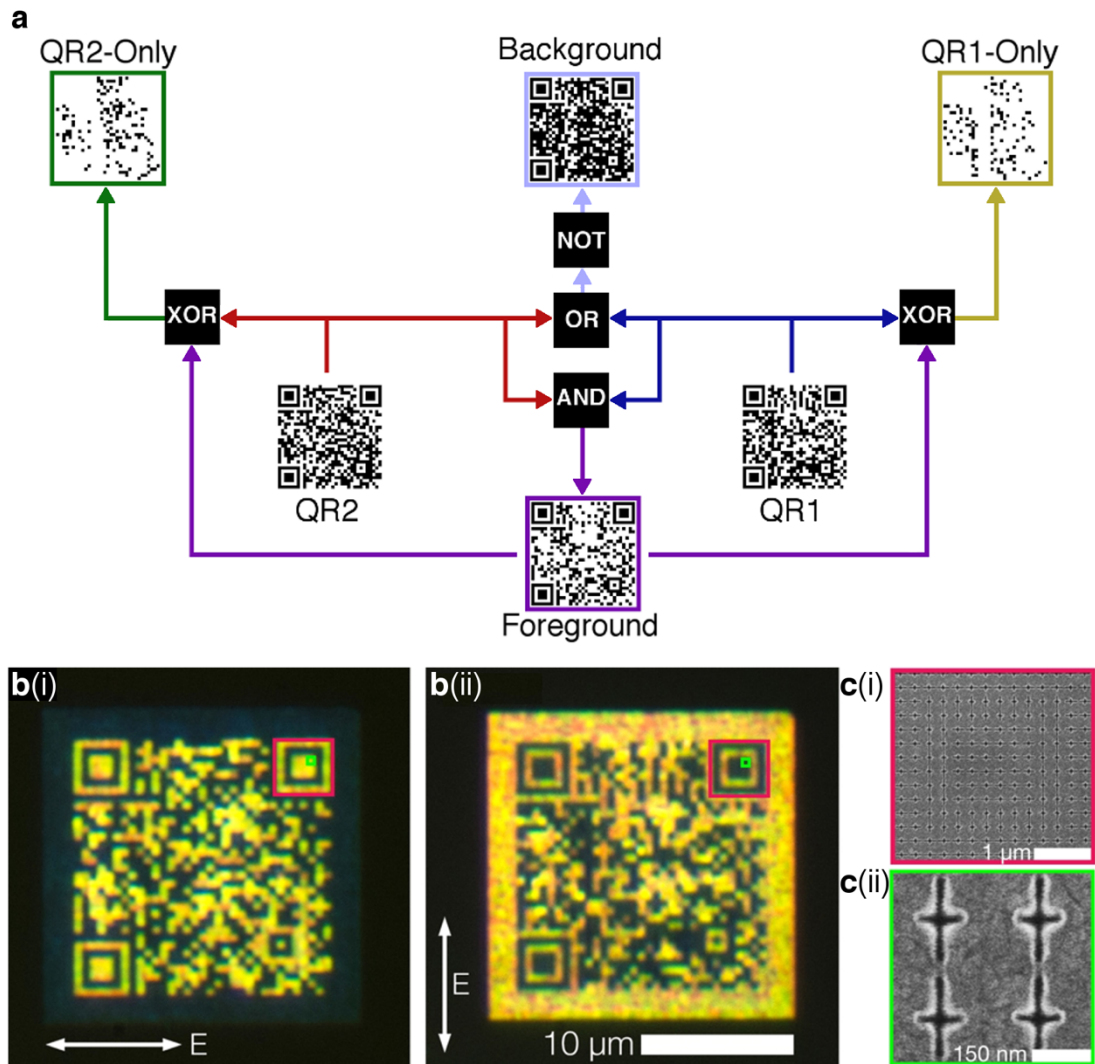


**Figure 5.7: Bright-field and SEM images of a switchable QR-code.** (a) Boolean logic used to create the pixel regions for the foreground (in **b(i)/b(ii)** yellow/blue), background (in **b(i)/b(ii)** blue/yellow), QR1-only (always yellow), and QR2-only (always blue). (b) Bright-field images (100x objective) of a 16 μm QR code (20 μm with border included) taken using a 100x objective lens when the illuminating white-light is polarised along (i) the X-axis and (ii) the Y-axes of the code. A different QR code is visible at each polarisation state. To view the information stored within the dual-state QR code, a QR reader capable of scanning reversed contrast codes, such as I-nigma, is necessary (bright patterns on dark backgrounds). (c) SEM images showing the composition of the QR-code. (i) A wide-area image showing the pattern present in the top-right corner of the QR code. (ii) The smallest unit that can be resolved optically, 2x2 pixels with a period of 250 x 250 nm. These 2x2 units formed the building blocks of the QR code. SEM were taken before the deposition of the SiO<sub>2</sub> layer. Parts (b) and (c) from this figure are from Heydari, et.al. (2017) [6].

The dual state code in **Figure 5.7b** has outputs relating to the homepage URLs of Advanced Functional Materials (where this was published) and the University of Glasgow School of Engineering. The 16 μm x 16 μm codes (the smallest possible using the 2x2 pixel per QR-module limit with a periodicity of 250 nm between pixels) are clearly visible using a 100x

objective lens. Both information outputs can be easily decoded using a mobile phone QR-reader application. At this level, colour separation from immediately adjacent pixel groupings is maintained, as is the polarisation-switching capability (green boxes marked on **Figure 5.6b(i)** and **Figure 5.6b(ii)**). This visible-pixel density relates to an area of 370 nm x 370 nm for the smallest features demonstrated here (period and arm-length). At the time of its publication, this was believed to be the smallest, most information dense, optically resolvable QR codes demonstrated to date.

#### 5.4.5 Angle-Dependence of Nano-Pixel

As previously discussed in Chapter 1, EOT is highly dependent on the way the incident light couples with the nano-slitted, plasmon-supporting material. Changes to the angle of incident light alters the way light both couples with the structured surface and gives rise to the SPR. Therefore, an understanding of how the angle of incident light affects the transmission (and thus visible colour) is necessary in order to use these dual-state nano-pixels for any potential applications (such as anti-counterfeiting).

**Figure 5.8** and **Figure 5.9** shows the relationship between the angle of incident light with respect to the actively polarised ‘arm’ for the longest and shortest arm-lengths used in the colour palette, respectively. For long-arm nano-pixels, changes to the angle of incidence result in red-shifting of the transmission when the active arm is parallel to the axis of the angle of incidence and blue-shifting when the active arm is perpendicular to the axis of the angle of incidence. Comparing the shift caused by the same change in angle of incidence, the red-shift when the active arm is parallel to the axis of the angle of incidence is greater than the blue-shift when the active arm is perpendicular. For short-arm nano-pixels, changes to the angle of incidence when the axis is in parallel and perpendicular to the arm-length result in red-shifting of the transmission. The transmission shift that occurs is dependent on the orientation of the polarisation of light to the angle of incidence, with a greater shift occurring when the axis of the angle of incidence is parallel to the polarisation of light.

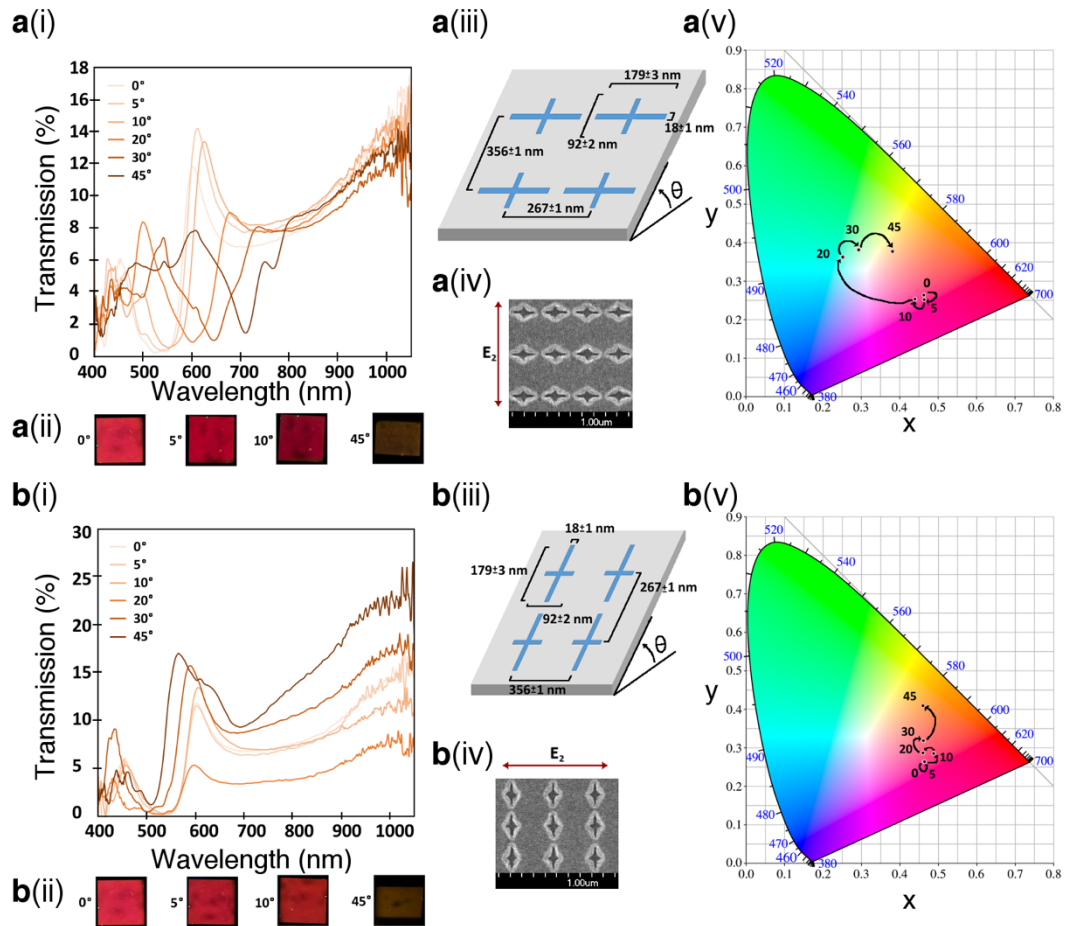


**Figure 5.8: Angle-dependence response for long-arm nano-pixels.** This figure shows how the angle of incident light ( $0^\circ$ ,  $5^\circ$ ,  $10^\circ$ ,  $20^\circ$ ,  $30^\circ$ , and  $45^\circ$ ) affects the transmission response of the active long-arm (measured by SEM as  $179 \pm 3$  nm by  $18 \pm 1$  nm [SD]) of a nano-pixel array when the angle of incident light is altered along the axis **(a)** parallel and **(b)** perpendicular to the active arm. For each sub-figure: **(i)** The transmission shift caused by increases in angle of incidence. **(ii)** Bright-field microscopy colour for  $0^\circ$ ,  $5^\circ$ ,  $10^\circ$ , and  $45^\circ$  incidence. **(iii)** Rendering of the nano-pixel array showing orientation of the pixels and the angle of incidence. **(iv)** SEM image of the nano-pixel array with orientation of the polarisation of incident light. **(v)** Plot for each angle of incidence of the nano-pixel array on the CIE XY chromaticity diagram. For long-arm nano-pixels, changes to the angle of incidence result in red-shifting of the transmission when the active arm is parallel to the angle of incidence axis and blue-shifting when the active arm is perpendicular to the angle of incidence axis. Comparing the shift caused by the same change in angle of incidence, the red-shift when the active arm parallel to the angle of incidence axis is greater than the blue-shift when the active arm is perpendicular.

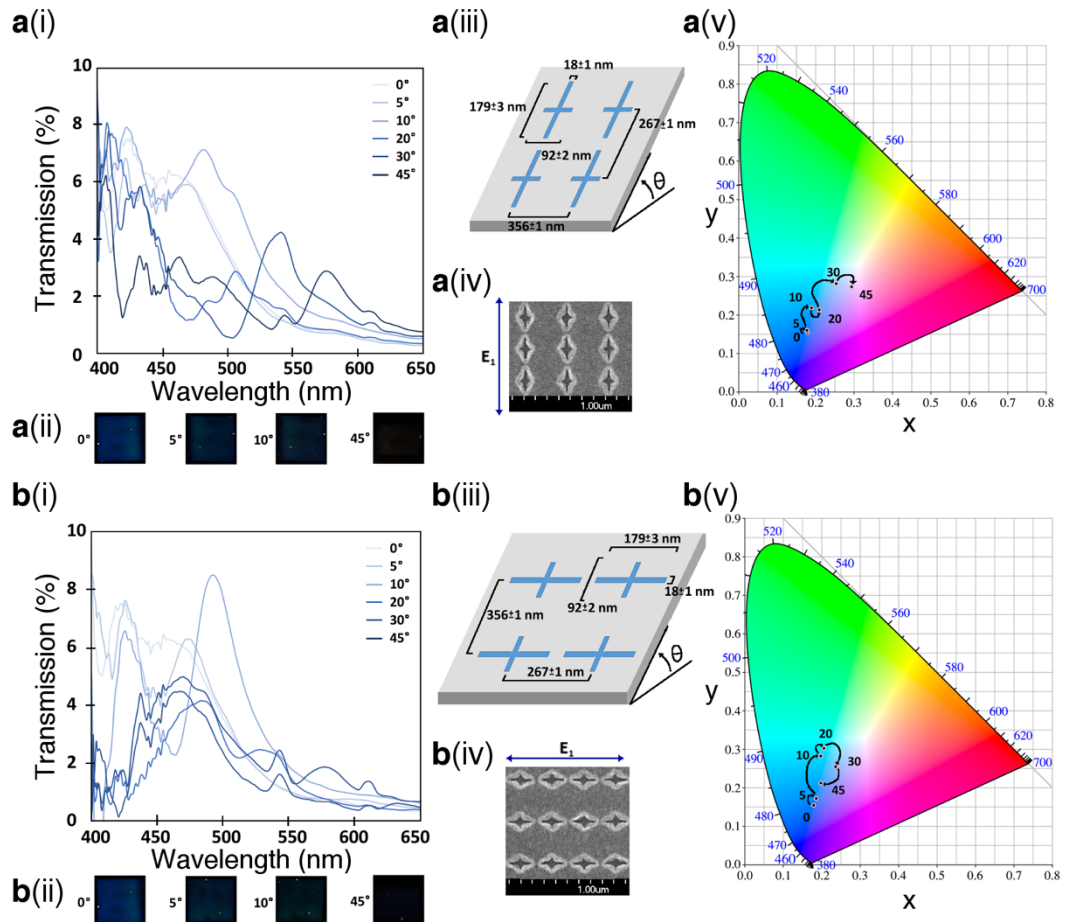


**Figure 5.9: Angle-dependence response for short-arm nano-pixels.** This figure shows how the angle of incident light ( $0^\circ$ ,  $5^\circ$ ,  $10^\circ$ ,  $20^\circ$ ,  $30^\circ$ , and  $45^\circ$ ) affects the transmission response of the active short-arm (measured by SEM as  $92 \pm 2$  nm by  $18 \pm 1$  nm [SD]) of a nano-pixel array when the angle of incident light is altered along the axis in **(a)** parallel and **(b)** perpendicular to the active arm. For each sub-figure: **(i)** The transmission shift caused by increases in angle of incidence. **(ii)** Bright-field microscopy colour for  $0^\circ$ ,  $5^\circ$ ,  $10^\circ$ , and  $45^\circ$  incidence. **(iii)** Rendering of the nanopixel array showing orientation of the pixels and the angle of incidence. **(iv)** SEM image of the nanopixel array with orientation of the polarisation of incident light. **(v)** Plot for each angle of incidence of the nanopixel array on the CIE XY chromaticity diagram. For short-arm nano-pixels, changes to the angle of incidence result in red-shifting of the transmission. The transmission shift that occurs is dependent on the orientation of the polarisation of light to the axis of the angle of incidence, with a greater shift occurring when the axis of the angle of incidence is parallel to the active arm.

**Figure 5.10** shows an example of the effect angle of incident light has on the dual-state encoded micro-images from **Figure 5.5**. When the polarisation of light is parallel to the axis of the angle of incidence (and thus perpendicular to the ‘active’ arm), increases from normal-to-the-surface to  $+45$  degrees results in red-shifting of the colours. When the polarisation of light is perpendicular to the axis of the angle of incidence (and thus parallel to the ‘active’

arm), increases from normal-to-the-surface to +45 degrees results in a ‘brightening’ of the colours.

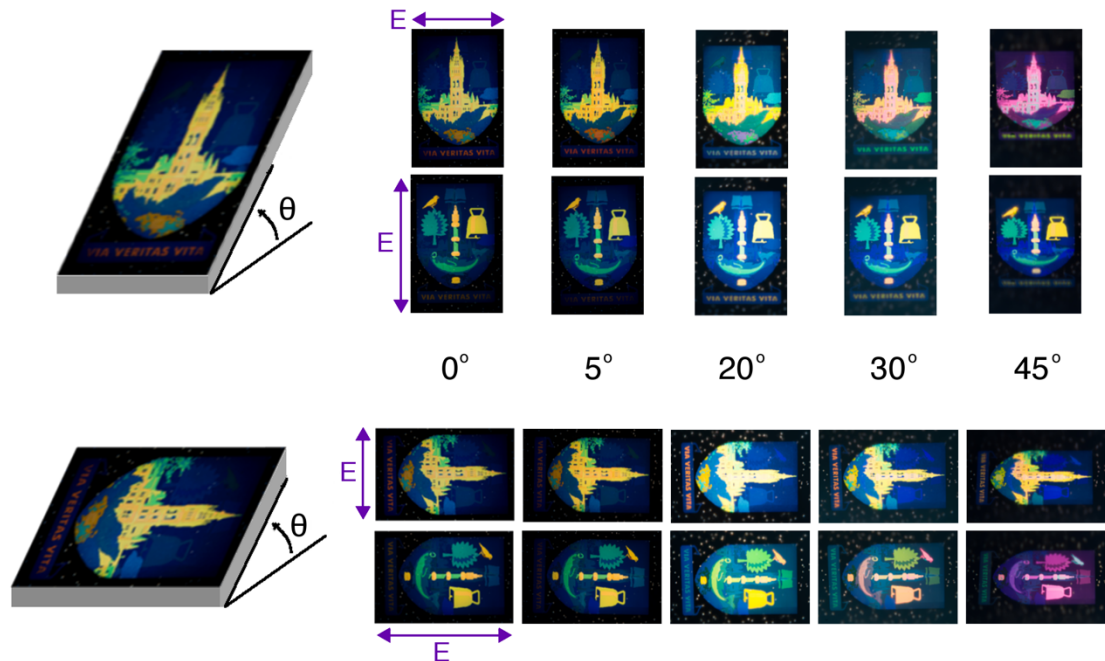


**Figure 5.10: Bright-field microscope images showing the incident light angle-dependence for switchable information displayed by a single set of nano-pixels. Bright-field transmission images showing changes in colour of the full-colour pictures from Figure 5.5 as a result of changes to the angle of incident light for each polarisation state of the pixels. The orientation of the picture to the polarisation and angle of incident light both affect the colour of the picture.**

As discussed in Chapter 1.2.4.2, the dimensions of the aperture in the array determine the coupling wavelength and the periodicity of the apertures determines the interference between the front and back SPR modes. When the angle of incident light is changed, the effective dimensions and periodicity of the aperture array, as interfaced with the light is altered. Thus, the shift in colour with change in angle of incident light observed in **Figure 5.8**, **Figure 5.9**, and **Figure 5.10** can all be attributed to the altered interference patterns of the EOT and frontside and backside SPR modes. The largest effect of angle-dependence occurs when the electric field is parallel to the plane of tilt, but images are still visible, and polarisation-dependence still remains.

## 5.5 Conclusion and Future Work

In this Chapter, nano-pixel apertures to encode two full-colour information states (both images and codes) in the same unit area were demonstrated. This technology shows promise

for future use in the micro-encoding and nano-imprinting industries. As dual-encoded pixels that exhibit virtually no cross-talk between information states, possesses a high PPI (>100,000), and are resistant to damage by heat, UV, and water, this technology may also be useful as an alternative to ink-based techniques used in high-resolution printing and anti-counterfeiting applications. When implemented for use as anti-counterfeiting measures in the printing of paper money, for example, the Al nano-pixel design will be subjected to the same day-to-day wear-and-tear of current bills in circulation. Transferring this technique to flexible surfaces is of particular interest, especially for this type of application. With this in mind, further research into the angle-dependence of the colour states and the effect of stress/strain/shear on nano-pixels built on a flexible surface is warranted.

## 5.6 References

- [1] Gu, Y.; Zhang, L.; Yang, J. K. W.; Yeo, S. P.; Qiu, C.-W. Color Generation Via Subwavelength Plasmonic Nanostructures. *Nanoscale* **2015**, *7* (15), 6409-6419, DOI: 10.1039/c5nr00578g.
- [2] Burgos, S. P.; Yokogawa, S.; Atwater, H. A. Color Imaging Via Nearest Neighbor Hole Coupling in Plasmonic Color Filters Integrated onto a Complementary Metal-Oxide Semiconductor Image Sensor. *Acs Nano* **2013**, *7* (11), 10038-10047, DOI: 10.1021/nn403991d.
- [3] Dean, N. Colouring at the Nanoscale. *Nature Nanotechnology* **2015**, *10* (1), 15-16, DOI: 10.1038/nnano.2014.316.
- [4] Miyata, M.; Hatada, H.; Takahara, J. Full-Color Subwavelength Printing with Gap-Plasmonic Optical Antennas. *Nano Lett.* **2016**, *16* (5), 3166-3172, DOI: 10.1021/acs.nanolett.6b00500.
- [5] Li, Z. B.; Clark, A. W.; Cooper, J. M. Dual Color Plasmonic Pixels Create a Polarization Controlled Nano Color Palette. *Acs Nano* **2016**, *10* (1), 492-498, DOI: 10.1021/acs.nano.5b05411.
- [6] Heydari, E.; Sperling, J. R.; Neale, S. L.; Clark, A. W. Plasmonic Color Filters as Dual-State Nanopixels for High-Density Microimage Encoding. *Adv. Funct. Mater.* **2017**, *27* (35), DOI: 10.1002/adfm.201701866.
- [7] Yokogawa, S.; Burgos, S. P.; Atwater, H. A. Plasmonic Color Filters for Cmos Image Sensor Applications. *Nano Lett.* **2012**, *12* (8), 4349-4354, DOI: 10.1021/nl302110z.
- [8] Tan, S. J.; Zhang, L.; Zhu, D.; Goh, X. M.; Wang, Y. M.; Kumar, K.; Qiu, C.-W.; Yang, J. K. W. Plasmonic Color Palettes for Photorealistic Printing with Aluminum Nanostructures. *Nano Lett.* **2014**, *14* (7), 4023-4029, DOI: 10.1021/nl501460x.
- [9] James, T. D.; Mulvaney, P.; Roberts, A. The Plasmonic Pixel: Large Area, Wide Gamut Color Reproduction Using Aluminum Nanostructures. *Nano Lett.* **2016**, *16* (6), 3817-3823.
- [10] Kumar, K.; Duan, H.; Hegde, R. S.; Koh, S. C. W.; Wei, J. N.; Yang, J. K. W. Printing Colour at the Optical Diffraction Limit. *Nature Nanotechnology* **2012**, *7* (9), 557-561, DOI: 10.1038/nnano.2012.128.
- [11] Cheng, F.; Gao, J.; Luk, T. S.; Yang, X. D. Structural Color Printing Based on Plasmonic Metasurfaces of Perfect Light Absorption. *Sci. Rep.* **2015**, *5*, 11045, DOI: 10.1038/srep11045.

- [12] Roberts, A. S.; Pors, A.; Albrektsen, O.; Bozhevolnyi, S. I. Subwavelength Plasmonic Color Printing Protected for Ambient Use. *Nano Lett.* **2014**, *14* (2), 783-787, DOI: 10.1021/nl404129n.
- [13] Olson, J.; Manjavacas, A.; Liu, L.; Chang, W.-S.; Foerster, B.; King, N. S.; Knight, M. W.; Nordlander, P.; Halas, N. J.; Link, S. Vivid, Full-Color Aluminum Plasmonic Pixels. *Proceedings of the National Academy of Sciences* **2014**, *111* (40), 14348-14353, DOI: 10.1073/pnas.1415970111.
- [14] Shao, L.; Zhuo, X.; Wang, J. Advanced Plasmonic Materials for Dynamic Color Display. *Advanced Materials* **2018**, *30* (16), DOI: 10.1002/adma.201704338.
- [15] Ahn, M.-S.; Chung, T.; Jeong, K.-H. Structural Coloration of Transmission Light through Self-Aligned and Complementary Plasmonic Nanostructures. *Nanoscale* **2018**, *10* (14), 6313-6317, DOI: 10.1039/c8nr01006d.
- [16] Lochbihler, H.; Ye, Y.; Xu, Y. Complementary Aluminum Nanopatch/Nanohole Arrays for Broad Palettes of Colors. *Plasmonics* **2018**, 1-7, DOI: 10.1007/s11468-018-0733-3.
- [17] Chen, T. H.; Reinhard, B. M. Assembling Color on the Nanoscale: Multichromatic Switchable Pixels from Plasmonic Atoms and Molecules. *Advanced Materials* **2016**, *28* (18), 3522+, DOI: 10.1002/adma.201506179.
- [18] Goh, X. M.; Zheng, Y.; Tan, S. J.; Zhang, L.; Kumar, K.; Qiu, C.-W.; Yang, J. K. W. Three-Dimensional Plasmonic Stereoscopic Prints in Full Colour. *Nature Communications* **2014**, *5*, DOI: 10.1038/ncomms6361.
- [19] Huang, Y. W.; Chen, W. T.; Tsai, W. Y.; Wu, P. C.; Wang, C. M.; Sun, G.; Tsai, D. P. Aluminum Plasmonic Multicolor Meta-Hologram. *Nano Lett.* **2015**, *15* (5), 3122-3127, DOI: 10.1021/acs.nanolett.5b00184.
- [20] Shrestha, V. R.; Lee, S.-S.; Kim, E.-S.; Choi, D.-Y. Aluminum Plasmonics Based Highly Transmissive Polarization-Independent Subtractive Color Filters Exploiting a Nanopatch Array. *Nano Lett.* **2014**, *14* (11), 6672-6678, DOI: 10.1021/nl503353z.
- [21] Zheng, B. Y.; Wang, Y. M.; Nordlander, P.; Halas, N. J. Color-Selective and Cmos-Compatible Photodetection Based on Aluminum Plasmonics. *Advanced Materials* **2014**, *26* (36), 6318-6323, DOI: 10.1002/adma.201401168.
- [22] Rajasekharan, R.; Balaur, E.; Minovich, A.; Collins, S.; James, T. D.; Djalalian-Assl, A.; Ganesan, K.; Tomljenovic-Hanic, S.; Kandasamy, S.; Skafidas, E.; Neshev, D. N.; Mulvaney, P.; Roberts, A.; Praver, S. Filling Schemes at Submicron Scale: Development of Submicron Sized Plasmonic Colour Filters. *Sci. Rep.* **2014**, *4*, DOI: 10.1038/srep06435.
- [23] Smith, A. F.; Patton, P.; Skrabalak, S. E. Plasmonic Nanoparticles as a Physically Unclonable Function for Responsive Anti-Counterfeit Nanofingerprints. *Adv. Funct. Mater.* **2016**, *26* (9), 1315-1321, DOI: 10.1002/adfm.201503989.
- [24] Zheng, Y. H.; Jiang, C.; Ng, S. H.; Lu, Y.; Han, F.; Bach, U.; Gooding, J. J. Unclonable Plasmonic Security Labels Achieved by Shadow-Mask-Lithography-Assisted Self-Assembly. *Advanced Materials* **2016**, *28* (12), 2330-2336, DOI: 10.1002/adma.201505022.
- [25] Chen, Q.; Das, D.; Chitnis, D.; Walls, K.; Drysdale, T. D.; Collins, S.; Cumming, D. R. S. A Cmos Image Sensor Integrated with Plasmonic Colour Filters. *Plasmonics* **2012**, *7* (4), 695-699, DOI: 10.1007/s11468-012-9360-6.
- [26] Frey, L.; Parrein, P.; Raby, J.; Pellé, C.; Hérault, D.; Marty, M.; Michailos, J. Color Filters Including Infrared Cut-Off Integrated on Cmos Image Sensor. *Optics Express* **2011**, *19* (14), 13073-13080, DOI: 10.1364/OE.19.013073.
- [27] Gu, M.; Zhang, Q.; Lamon, S. Nanomaterials for Optical Data Storage. *Nature Reviews Materials* **2016**, *1* (12), 16070, DOI: 10.1038/natrevmats.2016.70.

- [28] Gu, M.; Li, X. P.; Cao, Y. Y. Optical Storage Arrays: A Perspective for Future Big Data Storage. *Light-Science & Applications* **2014**, *3*, DOI: 10.1038/lsa.2014.58.
- [29] Chon, J. W. M.; Zijlstra, P.; Gu, M.; van Embden, J.; Mulvaney, P. Two-Photon-Induced Photoenhancement of Densely Packed Cdse/Znse/Zns Nanocrystal Solids and Its Application to Multilayer Optical Data Storage. *Applied Physics Letters* **2004**, *85* (23), 5514-5516, DOI: 10.1063/1.1829392.
- [30] Kimura, J.; Maenosono, S.; Yamaguchi, Y. Near-Field Optical Recording on a Cdse Nanocrystal Thin Film. *Nanotechnology* **2003**, *14* (1), 69-72, DOI: 10.1088/0957-4484/14/1/316.
- [31] Li, X. P.; Chon, J. W. M.; Evans, R. A.; Gu, M. Quantum-Rod Dispersed Photopolymers for Multi-Dimensional Photonic Applications. *Optics Express* **2009**, *17* (4), 2954-2961, DOI: 10.1364/oe.17.002954.
- [32] Li, X. P.; Zhang, Q. M.; Chen, X.; Gu, M. Giant Refractive-Index Modulation by Two-Photon Reduction of Fluorescent Graphene Oxides for Multimode Optical Recording. *Sci. Rep.* **2013**, *3*, 4, DOI: 10.1038/srep02819.
- [33] Li, L.; Gattass, R. R.; Gershgoren, E.; Hwang, H.; Fourkas, J. T. Achieving Lambda/20 Resolution by One-Color Initiation and Deactivation of Polymerization. *Science* **2009**, *324* (5929), 910-913, DOI: 10.1126/science.1168996.
- [34] Gan, Z.; Cao, Y.; Evans, R. A.; Gu, M. Three-Dimensional Deep Sub-Diffraction Optical Beam Lithography with 9 Nm Feature Size. *Nature Communications* **2013**, *4*, 2061, DOI: 10.1038/ncomms3061.
- [35] Cumpston, B. H.; Ananthavel, S. P.; Barlow, S.; Dyer, D. L.; Ehrlich, J. E.; Erskine, L. L.; Heikal, A. A.; Kuebler, S. M.; Lee, I. Y. S.; McCord-Maughon, D.; Qin, J. Q.; Rockel, H.; Rumi, M.; Wu, X. L.; Marder, S. R.; Perry, J. W. Two-Photon Polymerization Initiators for Three-Dimensional Optical Data Storage and Microfabrication. *Nature* **1999**, *398* (6722), 51-54.
- [36] Andrew, T. L.; Tsai, H.-Y.; Menon, R. Confining Light to Deep Subwavelength Dimensions to Enable Optical Nanopatterning. *Science* **2009**, *324* (5929), 917-921, DOI: 10.1126/science.1167704.
- [37] Harke, B.; Dallari, W.; Grancini, G.; Fazzi, D.; Brandi, F.; Petrozza, A.; Diaspro, A. Polymerization Inhibition by Triplet State Absorption for Nanoscale Lithography. *Advanced Materials* **2013**, *25* (6), 904-909, DOI: 10.1002/adma.201204141.
- [38] Stocker, M. P.; Li, L.; Gattass, R. R.; Fourkas, J. T. Multiphoton Photoresists Giving Nanoscale Resolution That Is Inversely Dependent on Exposure Time. *Nature Chemistry* **2011**, *3* (3), 223-227, DOI: 10.1038/nchem.965.
- [39] Zijlstra, P.; Chon, J. W. M.; Gu, M. Five-Dimensional Optical Recording Mediated by Surface Plasmons in Gold Nanorods. *Nature* **2009**, *459* (7245), 410-413, DOI: 10.1038/nature08053.
- [40] Ditlbacher, H.; Krenn, J. R.; Lamprecht, B.; Leitner, A.; Aussenegg, F. R. Spectrally Coded Optical Data Storage by Metal Nanoparticles. *Opt. Lett.* **2000**, *25* (8), 563-565, DOI: 10.1364/ol.25.000563.
- [41] Ren, H. R.; Li, X. P.; Zhang, Q. M.; Gu, M. On-Chip Noninterference Angular Momentum Multiplexing of Broadband Light. *Science* **2016**, *352* (6287), 805-809, DOI: 10.1126/science.aaf1112.
- [42] Knight, M. W.; King, N. S.; Liu, L.; Everitt, H. O.; Nordlander, P.; Halas, N. J. Aluminum for Plasmonics. *Acs Nano* **2014**, *8* (1), 834-840, DOI: 10.1021/nn405495q.
- [43] Palik, E. D. *Handbook of Optical Constants of Solids*, Academic Press: 1997; Vol. I-III.

- [44] Ellenbogen, T.; Seo, K.; Crozier, K. B. Chromatic Plasmonic Polarizers for Active Visible Color Filtering and Polarimetry. *Nano Lett.* **2012**, *12* (2), 1026-1031, DOI: 10.1021/nl204257g.

## Chapter 6: Preliminary Work: Dual-State SIBA/FRET Trap for the Study of Individual Proteins

### 6.1 Introduction

The study of biomolecule function within the human body is key to developing a better understanding of disease mechanisms, disease prevention, and drug discovery. Proteins, for instance, are significantly complex biomolecules that we know drive cellular function on the nano-scale. However, how each of these proteins operates remains unanswered, as we do not possess the technological tools to properly study and understand them on the nano-scale. For example, research has hypothesized that there is a link between Alzheimer's Disease and proteins [1-2], but the ability to fully investigate this link is limited by our understanding of how the proteins function. As a result, our ability to develop new pharmaceutical interventions, diagnostic tests, and therapeutic treatments is limited. The two major challenges with studying proteins arise from the difficulties in (1) trapping them and (2) observing how they function at the nano-scale [3].

While optical tweezing is a powerful tool capable of manipulating single microscopic objects by exerting forces resulting from the momentum carried by light [4], it does not work well for nanoscale objects. When decreasing the size of the object of interest down to the nanoscale, being able to develop a stable potential capable of overcoming environmental fluctuations becomes challenging as it would require a high optical power focused onto a very small (i.e. diffraction limited) spot [3-4]. For most dielectrics, these high optical intensities are far beyond their damage threshold [4]. In order to avoid using such high powers, the rapidly decaying evanescent fields of nanoplasmonic structures have been used to focus the light beyond the diffraction limit ( $L \ll \lambda$ ) [3-4]. However, due to photothermal effects, this could only be applied to nanoparticles higher than 100 nm. As a solution to the issues associated with photothermal effects in nanoplasmonic tweezing, devices based on "self-induced back action" (SIBA) effect were developed [3-10]. In these devices, the particle to be trapped plays an active role in the trapping mechanism by modifying the momentum of the plasmonic transmitted photons with which it interacts. Therefore, if the particle has been considered during the design of the trap, it can be used to promote an automatic back trapping by inducing a higher intensity when the particle is in the trap [3-10]. Therefore, the use of a SIBA device can resolve the first problem.

For proteins, conformational dynamics define function. A common way to understand the conformational dynamics of a protein is to use a Förster Resonant Energy Transfer (FRET) mechanism [11], which involves tagging the protein with two fluorescent labels. One tag is excited by a laser and the other tag experiences non-radiative energy transfer from the first tag, which is a distance-dependent effect. Measuring the photon response of the tags based on this distance-dependence provides vital information on the conformational dynamics of the protein [11]. However, the photons produced by single fluorescent tags using current trapping methods provide very little information before the tags bleach and switch off and there is low signal-to-noise. For example, using mNeonGreen as a donor, only 14 photons/ms can be detected above background noise and photo-bleaching occurs between 1-2 seconds [12]. Plasmonic enhancement has been demonstrated to improve signal-to-noise ratio and ‘enhance’ fluorescent molecules [13-17].

Combining the concept of plasmonic sensing presented in Chapter 3 and Chapter 4 with the dual-state capabilities of the nano-pixel design presented in Chapter 5 has the potential to allow for the development of multi-purpose plasmonic devices. In this chapter, the dual-state nature of the nano-aperture structures from Chapter 5 are proposed for the trapping of biomolecules with one arm while simultaneously, yet independently, sensing with the other. While only preliminary work is covered, once successfully developed, these novel devices will aid the understanding of proteins which define biological and chemical pathways and thus benefit the fields of biology, chemistry, medicine, and pharmacy. Additionally, they will allow for the testing and creation of new disease screenings and drug therapies.

Device design and characterisation were carried out at the University of Glasgow (UK). Single-photon measurements were carried out at University Hospital Jena (DE).

### 6.3 Materials

For the device setup, single-mode polarisation-maintaining fibre (PM-S405XP), half-wave plates, mirrors, filters, and lenses were all purchased from ThorLabs.

Additional materials used are available in Chapter 2.

## 6.4 Methods

### 6.4.1 Fabrication of Nano-Aperture Arrays

Devices were fabricated using electron-beam lithography, reactive ion etching, and inductively coupled plasma deposition as covered in Nano-Aperture Fabrication (Chapter 2.5.6). 100 nm of Al was deposited onto 500  $\mu\text{m}$  thick borosilicate substrate by electron-beam evaporation. A Vistec VB6 UHR EWF electron-beam lithography tool was used to pattern a ZEP520A etch mask. Nano-apertures were etched into the Al using  $\text{SiCl}_4$  gas in an Oxford Instruments System 100 reactive ion etch tool.

### 6.4.2 Optical Transmission Spectra

Transmission spectra were collected over the visible spectrum using a linear film polariser with a custom-built microspectrophotometer. A 10 x 0.5 NA objective was used to couple the transmitted light into an optical fibre attached to a StellarNet Microspectrophotometer (StellarNet Blue Wave).

### 6.4.3 Single-Photon Detection Setup

A custom inverted microscope optical setup was built for single-photon detection experiments. The optical diagram of the setup is shown in **Figure 6.1**. The device was inverted and placed on top of a polydimethylsiloxane (PDMS) reservoir filled with sample solution. Light from a 515 nm wavelength laser was coupled into a single-mode, polarisation-maintaining fibre (ThorLabs PM S405 XP) and a 20x objective was used to focus light (roughly 4 mW measured at the backside of the device) through the back-side of an inverted device, onto the nano-apertures. A half-waveplate was used to control the polarisation of laser light with reference to the device. The transmitted light was then focused onto single-photon detectors—one for detecting the SIBA trapping and the second for detecting the FRET mechanism. For the SIBA photon detector, the filter in front of it should allow only the wavelengths associated with the SIBA mechanism (in this case, 515 nm) to reach the photon detector. For the FRET photon detector, the filter in front of it should block wavelengths outside the emission curve of the second fluorophore in the FRET mechanism.

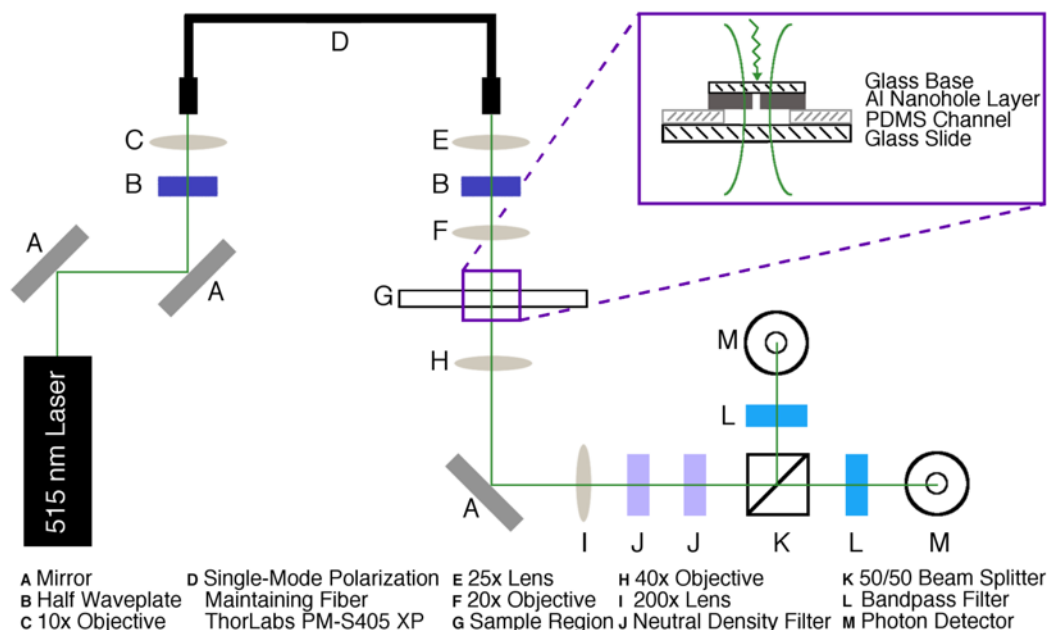


**Figure 6.1: Optical diagram of single-photon detection setup.** Light from a 515 nm wavelength laser was coupled to a single-mode, polarisation-maintaining fibre, focused on and transmitted through a sample, and then focused on single-photon detectors. One photon detector should be for detecting the SIBA trapping and the other should be for detecting the FRET mechanism. For the SIBA photon detector, the filter in front of it should allow only the 515 nm wavelength to reach the photon detector. For the FRET photon detector, the filter in front of it should allow only the emission wavelengths of the second fluorophore in the FRET mechanism. (**inset**) Sample region enlarged showing the back-side transmission of the laser light through the nanoholes on the sample. The device is placed onto a PDMS channel filled with molecules suspended in solution. Light passes through the glass base of the device and through the nano-apertures in Al, activating the device.

## 6.5 Results and Discussion

To build this dual-state device, each arm was planned to be design and tuned separately. The first arm chosen was that for SIBA-trapping. Only the preliminary work towards this end has been approached.

### 6.5.1 Design and Fabrication for the SIBA Arm

The colour pixels were designed as two nano-slit-apertures combined to form a nano-cross-aperture in a thin Al film. Similar to Chapter 5, Al was chosen for its wide spectral plasmonic band, which can be tuned from the UV to the NIR, and its low-cost. For SIBA with plasmonics, once a molecule gets trapped in the electric field of the nano-aperture, its presence will alter the local environment of structure and thus red-shift the resonance peak [4]. Therefore, the arm length of the SIBA-trapping arm will depend on the protein selected for study.

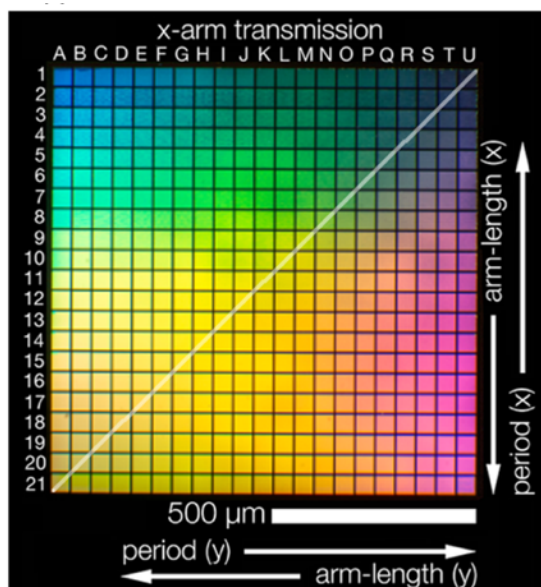


**Figure 6.2: Colour Palette from Chapter 5.** The green pixels of the colour palette from Chapter 5 are most likely to have a resonance around 515 nm, which is the wavelength of the laser used to activate the SIBA mechanism. Light is polarised along the Y-axis, therefore the dimensions of the X-arm and period in the Y-axis must be considered for device fabrication. For more details on the nano-pixels, see Chapter 5.

Given that a 515 nm wavelength laser was chosen for the SIBA trapping mechanism, structures with a resonance slightly blue-shifted from 515 nm are desired [4, 8]. The green pixels of the colour palette fabricated in **Chapter 5** and shown in **Figure 6.2** are most likely to have resonance peaks that meet this requirement. The polarisation of light in Figure 6.2 is parallel to the Y-axis; therefore, the dimensions of the X-arms and period in the Y-axis for the green regions are what to consider for designing the SIBA arm of the nano-aperture. With that in mind, regions F6 (145 nm length / 275 nm period), G7 (150 nm length / 280 nm period), H8 (155 nm length / 285 nm period), I9 (160 nm length / 290 nm period), and J10 (165 nm length / 295 nm period) from this palette were selected for the active arm for the initial set of devices. To maintain the shape integrity of the individual nano-pixels, the second ‘inactive’ arm using the parameters of region A1 (120 nm arm / 250 nm period) was chosen because it has very low transmission at 515 nm.

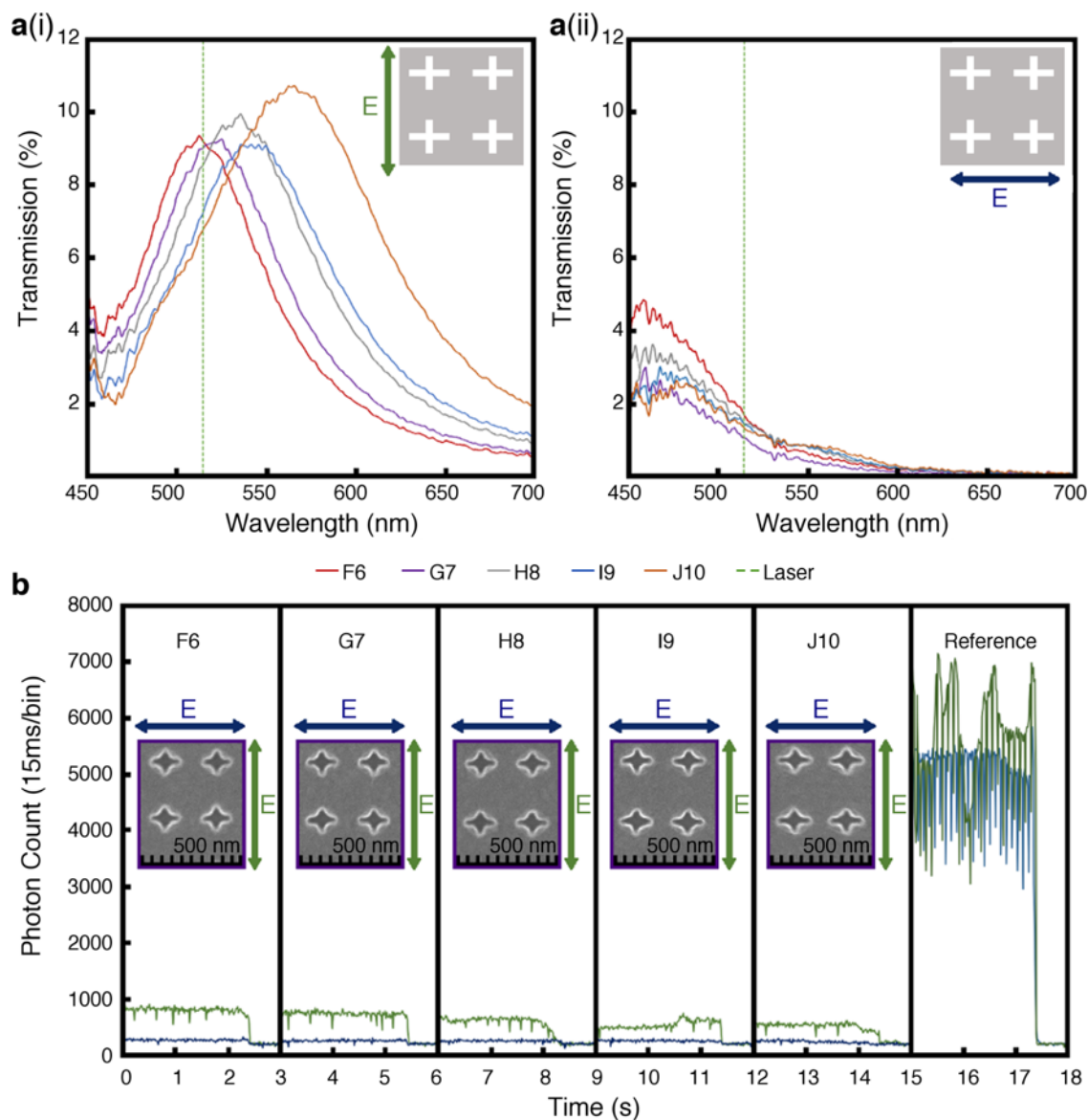


**Figure 6.3: Transmission and Single-Photon Detection of Preliminary Devices.** (a) Transmission spectra in water of the (i) horizontal, long arm and (ii) vertical, short arm of preliminary device regions. For all regions, the vertical, short arm was designed to be 120 nm length with a period of 250 nm. The horizontal, long arm was designed with the following parameters: F6 (145 nm length / 275 nm period), G7 (150 nm length / 280 nm period), H8 (155 nm length / 285 nm period), I9 (160 nm length / 290 nm period), and J10 (165 nm length / 295 nm period). The width of both arms was designed as 20 nm. The insets show a rendering of the device and indicate the polarisation of light used to activate the arms shown in the transmission spectra. The dotted green line indicates the wavelength of the laser used in the setup. (b) Preliminary results of photon count (15 ms/bucket) for F6, G7, H8, I9, and J10 in water when the (green) horizontal, long arm and (blue) vertical, short arm were activated by changing the polarisation of light. Moving from F6 to J10, the device becomes less-tuned for the laser wavelength and this is apparent in the decrease in photon count. For all devices, after 2.4 seconds, the sample was moved to a region where the laser light was blocked, which shows the baseline photon count of the detector. As can be seen by the photon counts, the vertical arms have a count almost as low as the background noise, as they are not tuned for the laser, whereas the horizontal arms have a much more noticeable count. Each panel also shows an SEM of the device. The far-right panel shows the photon count from a reference region for comparison.

**Figure 6.3a** shows the transmission spectra in water for the aforementioned regions from the colour palette. The light is polarised, as shown in the inset of each subfigure, along (i) the Y-axis (activating the longer X-arm) and (ii) the X-axis (activating the shorter Y-arm). As expected, the transmission peak in Figure 6.3a(i) red-shifts with increases to both the arm-length in X and period in Y; the transmission spectra shown in Figure 6.3a(ii) have the same peak resonance because the arm-length in Y and period in X are kept constant between each region. The X-arm from region F6 (red line in Figure 6.3a(i)) has its peak closest to the 515 nm laser (green dashed line) used in the SIBA setup.

SEM of each region is shown within each panel of **Figure 6.3b**. **Figure 6.3b** also shows the photon counts (15 ms/bucket) for F6, G7, H8, I9, J10, and a reference region in water for the 515 nm laser polarised along the Y-axis (green line) and X-axis (blue line). For all measurements, the photon count was taken starting on a particular region and, after 2.4 seconds, the sample was moved to a region where the laser light was blocked (which shows the baseline photon count of the detector). As can be seen by the photon counts, the count is the same for each region and almost as low as the background noise when the Y-arm is activated. This is because the Y-arm for each region is designed to be the same and has very low transmission at 515 nm. When the light is polarised to activate the long-arm, moving from F6 to J10, the photon count decreases because each subsequent region is less-tuned for the 515 nm laser. These results correspond well with the transmission spectra shown in Figure 6a(i) and Figure 6a(ii), respectively, and indicate that the designed setup is able to measure the photons transmitted through devices.

### 6.5.2 Fluorescent Marker Selection for FRET

While this work has yet to progress towards tuning the second arm of the nano-aperture for the FRET mechanism, there has been preliminary consideration of the fluorophores. As previously mentioned, the FRET mechanism requires two fluorescent markers where the emission of the first marker must be able to activate the second marker. Given that a 515 nm wavelength laser will be used to trap proteins, a fluorescent marker that can be activated by this wavelength must be chosen for the first fluorophore of the FRET mechanism. For example, one option for the first fluorophore would be to use Cy3B. As shown in **Figure 6.4a**, the 515 nm laser wavelength falls within the Cy3B excitation curve (max peak at 559 nm) and is below its emission curve (max peak at 570 nm) [18]. With Cy3B as the first fluorophore, an example second fluorophore to use could be Alexa Fluor 594. As shown in **Figure 6.4b**, the peak emission of Cy3B falls within the excitation curve of Alexa Fluor 594

(max peak at 590 nm) and is below Alexa Fluor 594 emission curve (max peak at 618 nm) [19]. **Figure 6.4c** shows the overlay of the emission spectra of Cy3B and excitation spectra of Alexa Fluor 594. If Alexa Fluor 594 is chosen as the acceptor fluorophore for this mechanism, control experiments to see how its excitation by the 515 nm laser affects its fluorescent output will be necessary. For example, a baseline control for this would be tagging the protein with only Alexa Fluor 594, trapping it in the system with the 515 nm laser, and observing the output signal of emission.

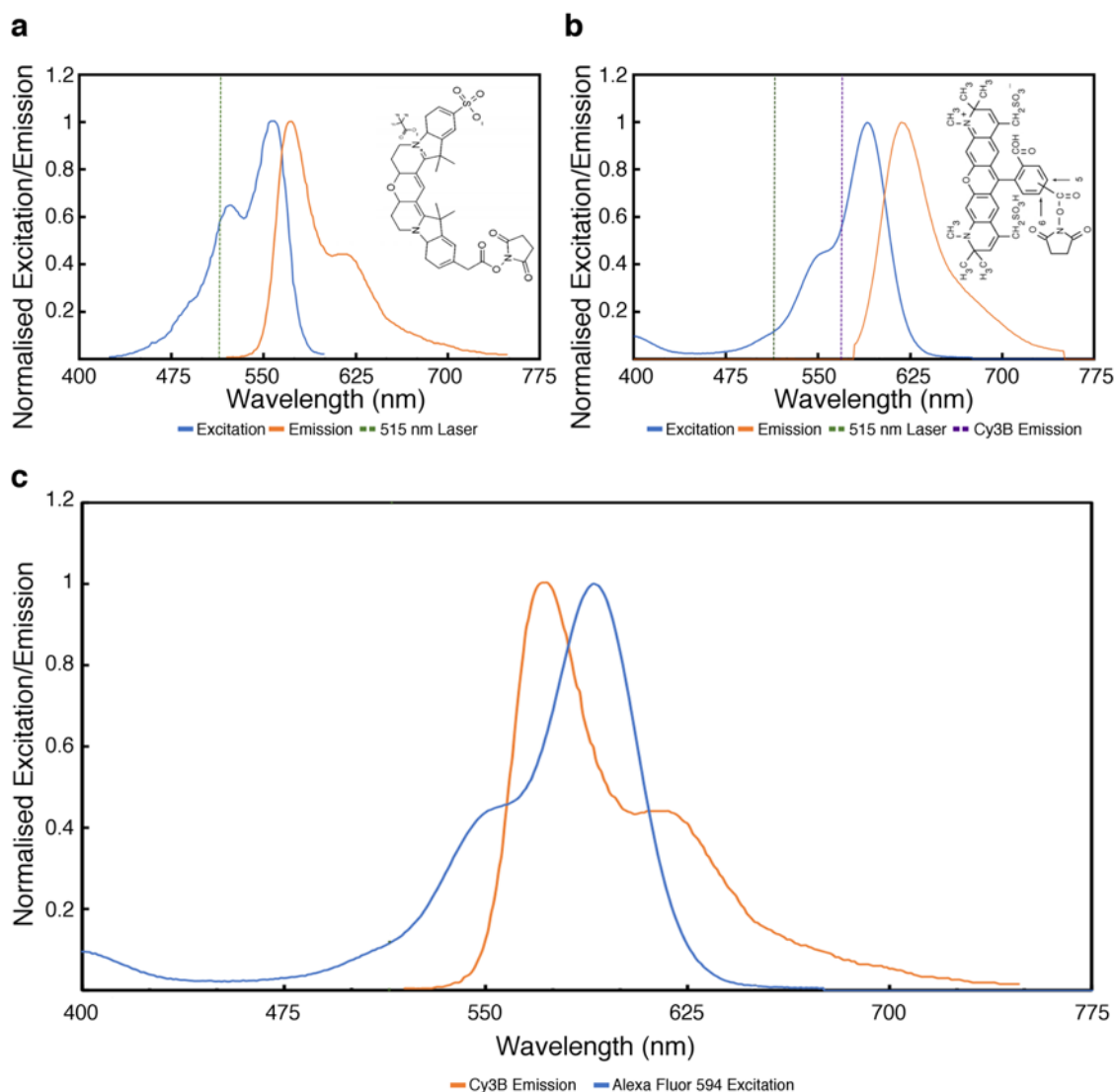


**Figure 6.4: Normalised excitation/emission for Cy3B and Alexa Fluor 594.** (a) The normalised extinction (blue) and emission (orange) for Cy3B. The wavelength of the 515 nm laser is indicated by the green dashed line. (inset) The Cy3B molecule [18]. (b) The normalised extinction (blue) and emission (orange) for Alexa Fluor 594. The wavelength of the 515 nm laser is indicated by the green dashed line and Cy3B emission is indicated by the dashed purple line. (inset) The Alexa Fluor 594 molecule [19]. (c) Overlay of Cy3B emission (orange) and Alexa Fluor 594 (blue) excitation curves.

### 6.5.3 Design for the FRET-Enhancing Arm

Continuing with this example, Alex Fluor 594 has an emission peak around 618 nm. Therefore, in consideration of the second arm for the nano-pixel structure, a resonance peak around 618 nm is ideal. From the colour palette in Figure 6.2, nano-aperture designs with resonance in this range can be found around S19 and T20 (see **Figure 6.5**). Since the trapping of a protein would result in a red-shift in the transmission spectra (compared to that without a particle trapped), S19 is a better choice between these two designs.

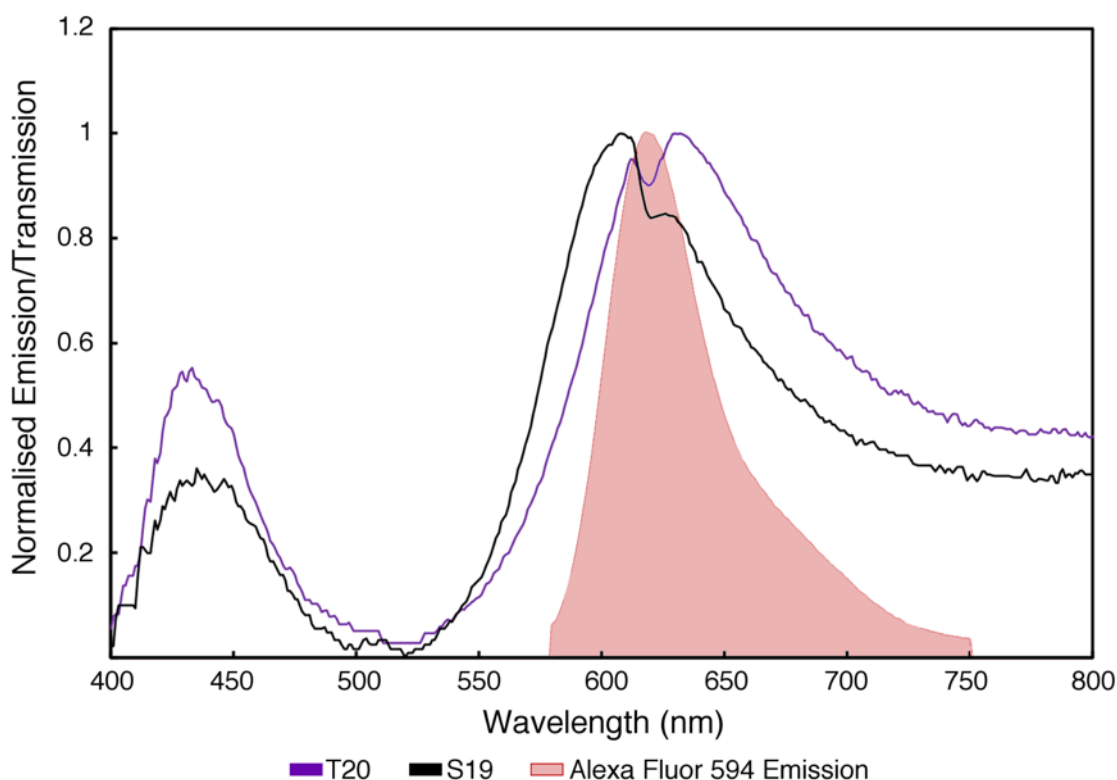


**Figure 6.5: Transmission of Selected Nano-Pixels for Alexa Fluor 594 Emission.** The normalised transmission of T20 (purple) and S19 (black) from the colour palette in Figure 6.2. T20 has dimensions of 215 nm arm-length in  $X$  with a 345 nm period in  $Y$ . S19 has dimensions of 210 nm arm-length in  $X$  with a 340 nm period in  $Y$ . The normalised emission spectrum of Alexa Fluor 594 is shaded in red. Since the trapping of a particle in the nano-aperture will result in a red-shift of the resonance peak, a structure with a transmission peak that is slightly blue-shifted (without a trapped particle) from the emission peak of the fluorophore is a better choice (i.e. S19).

## 6.6 Conclusion and Future Work

This chapter presented the initial ground-work for utilising the nano-apertures from Chapter 5 as a new device capable of simultaneously trapping and probing individual proteins.

Although the research has yet to progress to a fully working device, the preliminary results show great potential. Further exploration into the capabilities of this structure to support SIBA-trapping and enhancement of FRET is warranted. Once successfully developed, devices will be modified for different proteins, vastly increasing our understanding of the mechanisms behind many under-explored biological and chemical pathways and advancing the development of new disease screenings and drug therapies.

## 6.7 References

- [1] DeToma, A. S.; Salamekh, S.; Ramamoorthy, A.; Lim, M. H. Misfolded Proteins in Alzheimer's Disease and Type II Diabetes. *Chem. Soc. Rev.* **2012**, *41* (2), 608-621, DOI: 10.1039/c1cs15112f.
- [2] Nikolaev, A.; McLaughlin, T.; O'Leary, D. D. M.; Tessier-Lavigne, M. App Binds Dr6 to Trigger Axon Pruning and Neuron Death Via Distinct Caspases. *Nature* **2009**, *457* (7232), 981-U1, DOI: 10.1038/nature07767.
- [3] Juan, M. L.; Gordon, R.; Pang, Y.; Eftekhari, F.; Quidant, R. Self-Induced Back-Action Optical Trapping of Dielectric Nanoparticles. *Nature Physics* **2009**, *5* (12), 915-919, DOI: 10.1038/nphys1422.
- [4] Mestres, P.; Berthelot, J.; Acimovic, S. S.; Quidant, R. Unraveling the Optomechanical Nature of Plasmonic Trapping. *Light-Science & Applications* **2016**, *5*, DOI: 10.1038/lsa.2016.92.
- [5] Kotnala, A.; Gordon, R. Quantification of High-Efficiency Trapping of Nanoparticles in a Double Nanohole Optical Tweezer. *Nano Lett.* **2014**, *14* (2), 853-856, DOI: 10.1021/nl404233z.
- [6] Uddin, N.; Du, G.; Chen, F.; Lu, Y.; Yang, Q.; Bian, H.; Yong, J.; Hou, X. Fano Resonance-Assisted Plasmonic Trapping of Nanoparticles. *Plasmonics* **2017**, *12* (3), 627-630, DOI: 10.1007/s11468-016-0307-1.
- [7] Lu, Y.; Du, G.; Chen, F.; Yang, Q.; Bian, H.; Yong, J.; Hou, X. Tunable Potential Well for Plasmonic Trapping of Metallic Particles by Bowtie Nano-Apertures. *Sci. Rep.* **2016**, *6*, DOI: 10.1038/srep32675.
- [8] Pang, Y.; Gordon, R. Optical Trapping of a Single Protein. *Nano Lett.* **2012**, *12* (1), 402-406, DOI: 10.1021/nl203719v.
- [9] Zehtabi-Oskuie, A.; Zinck, A. A.; Gelfand, R. M.; Gordon, R. Template Stripped Double Nanohole in a Gold Film for Nano-Optical Tweezers. *Nanotechnology* **2014**, *25* (49), DOI: 10.1088/0957-4484/25/49/495301.
- [10] Al Balushi, A. A.; Gordon, R. A Label-Free Untethered Approach to Single-Molecule Protein Binding Kinetics. *Nano Lett.* **2014**, *14* (10), 5787-5791, DOI: 10.1021/nl502665n.
- [11] Giepmans, B. N. G.; Adams, S. R.; Ellisman, M. H.; Tsien, R. Y. Review - the Fluorescent Toolbox for Assessing Protein Location and Function. *Science* **2006**, *312* (5771), 217-224, DOI: 10.1126/science.1124618.
- [12] Dienerowitz, M.; Ilchenko, M.; Su, B.; Deckers-Hebestreit, G.; Mayer, G.; Henkel, T.; Heitkamp, T.; Boersch, M. In *Optimized Green Fluorescent Protein Fused to Fof1-Atp Synthase for Single-Molecule FRET Using a Fast Anti-Brownian Electrokinetic Trap*, Single Molecule Spectroscopy and Superresolution Imaging IX, San Francisco, CA, 2016 Feb 13-18; San Francisco, CA, 2016.

- [13] Faessler, V.; Hrelescu, C.; Lutich, A. A.; Osinkina, L.; Mayilo, S.; Jackel, F.; Feldmann, J. Accelerating Fluorescence Resonance Energy Transfer with Plasmonic Nanoresonators. *Chem. Phys. Lett.* **2011**, *508* (1-3), 67-70, DOI: 10.1016/j.cplett.2011.03.088.
- [14] Schuller, J. A.; Barnard, E. S.; Cai, W.; Jun, Y. C.; White, J. S.; Brongersma, M. L. Plasmonics for Extreme Light Concentration and Manipulation. *Nature Materials* **2010**, *9* (3), 193-204, DOI: 10.1038/nmat2630.
- [15] Chowdhury, M. H.; Ray, K.; Gray, S. K.; Pond, J.; Lakowicz, J. R. Aluminum Nanoparticles as Substrates for Metal-Enhanced Fluorescence in the Ultraviolet for the Label-Free Detection of Biomolecules. *Anal. Chem.* **2009**, *81* (4), 1397-1403, DOI: 10.1021/ac802118s.
- [16] Li, M.; Cushing, S. K.; Wu, N. Plasmon-Enhanced Optical Sensors: A Review. *Analyst* **2015**, *140* (2), 386-406, DOI: 10.1039/c4an01079e.
- [17] Zhang, J.; Fu, Y.; Lakowicz, J. R. Enhanced Forster Resonance Energy Transfer (FRET) on a Single Metal Particle. *J. Phys. Chem. C* **2007**, *111* (1), 50-56, DOI: 10.1021/jp062665e.
- [18] Cooper, M.; Ebner, A.; Briggs, M.; Burrows, M.; Gardner, N.; Richardson, R.; West, R. Cy3b: Improving the Performance of Cyanine Dyes. *Journal of Fluorescence* **2004**, *14* (2), 145-150.
- [19] Alexa Fluor™ 594 Antibody Labeling Kit. ThermoFisher Scientific.

## Chapter 7: Conclusion

The numerical simulations and experimental investigations of this thesis have demonstrated three novel nanoplasmonic devices and their applications in biological sensing, solvent differentiation, and polarisation-dependent high-resolution colour filtering and image encoding.

When it comes to molecular sensing, compared to standard assay-based techniques for detecting analytes, plasmonic-based devices are label-free, are highly-miniaturisable, can operate using simple optics, and are often reusable. This has led to their use in the continuous, real-time detection of molecules and binding kinetics using simple setups that are highly-portable. For applications where monitoring over extended periods of time is necessary, maintaining a stable baseline reference is necessary to verify that changes observed in the signal are due to analyte detection and not sensor drift. While the standard approach to account for this is to use a separate reference channel, a new approach was investigated in Chapter 3. Through simulation and multiple iterations of fabrication design, a technique was developed for building two nanoplasmonic arrays in the same X-Y space, offset in the Z-direction from one another. This multilayered nanoplasmonic device was then demonstrated capable of simultaneously obtaining sensing and referencing signals from one measurement without the need for either complex optics or multiple sensing regions. This design is especially useful for point-of-care applications because it accounts for potential problems with limitations in resources and sample quantities and can be incorporated into multiplexed microfluidic systems using a more-sensitive nanostructure design.

Plasmonic-based devices also hold promise for applications in mixture discrimination/identification, where only the identification of a mixture from a known set is desired (rather than analysis of all the individual components in the mixture). In these cases, the ‘gold-standard’ method of chromatography typically becomes limited by its cost, bulky equipment and time-consuming process. Instead, arrays of sensors, each contributing a partially-selective signal, can be used to generate an identification map based on pattern-recognition using multivariate techniques like PCA and LDA. In Chapter 4, a novel device made of sensing elements comprised of super-imposed, offset Al and Au nanoplasmonic arrays was demonstrated capable of differentiating between seven off-the-shelf whiskies with 99.7% accuracy (using LDA). Compared to their single-metal counterparts, the

bimetallic approach results in two (as opposed to one) partially-selective data points for pattern-based recognition from one measurement. Thus, the bimetallic approach uses half the number of sensing regions (halving device size) and has fewer elements to probe (reducing the time necessary to collect the data). This advance in device miniaturisation, functionalisation, and multiplexed readout makes bimetallic nanoplasmonic tongues ideal for chemical mixture identification in applications where exact identification of individual components in a mixture is not required and portability, reusability, and measurement speed are key.

In addition to their sensing capabilities, plasmonic devices can also serve as an alternative to standard pigments and dyes used in full-colour nano-imprinting and micro-encoding. In Chapter 5, polarisation-sensitive nano-aperture arrays in 100 nm thin sheets of Al were demonstrated to support two full-colour information states in the same physical space, independently, with virtually no cross-talk yielding ultra-high resolution (370 nm x 370 nm) images. At the time of its publication, this technology was used to produce the smallest optically-resolvable QR codes which were 16  $\mu\text{m}$  x 16  $\mu\text{m}$  in size. The high PPI (>100,000), resistance to damage (UV/heat/water), and ability to encode two full-colour information states in the same physical space make this technology a highly useful alternative to ink-based techniques in anti-counterfeiting and high-resolution printing applications. Transferring this technique to flexible surfaces, analysing stress/strain, and further analysing angle-dependence would be of particular interest, especially when it comes to anti-counterfeiting applications of this technology.

Combining the concept of plasmonic sensing presented in Chapter 3 and Chapter 4 with the dual-state nano-pixel design of Chapter 5, Chapter 6 presented preliminary development of a device where one arm of the aperture would serve to trap proteins via the SIBA effect while the second arm would independently be use for enhancing the signal-to-noise ratio of the FRET mechanism. While only preliminary work is covered, once successfully developed, these novel devices will aid the understanding of proteins which define biological and chemical pathways and thus benefit the fields of biology, chemistry, medicine, and pharmacy. Additionally, they will allow for the testing and creation of new disease screenings and drug therapies.

While all three applications explored in this work show promise as highly-miniaturisable devices for their given applications, the fabrication techniques required to produce them

have a fairly high-cost (i.e. electron-beam lithography) and involve multiple, time-consuming steps, all of which result in limitations when it comes to scalability and mass production of such devices. To overcome cost and increase production, electron-beam lithography can be replaced with techniques such as interference photolithography [1-3] or nanoimprint lithography [4]. Additionally, for the multilayered devices, switching from silicon nitride encapsulation / HSQ planarisation to using SU8 would reduce the number of steps in fabrication by one and remove two electron-beam lithography steps from the process.

In summary, the proof-of-concept work presented in this thesis holds promise in a number of fields related to plasmonic sensing and high-resolution colour printing. Further work improving the sensitivity of these devices and improving the fabrication techniques can yield a new generation of sensing devices with applications in point-of-care diagnostics, mixture discrimination/identification, anti-counterfeiting, and high-resolution colour printing.

## References

- [1] Levenson, M. D.; Viswanathan, N. S.; Simpson, R. A. Improving Resolution in Photolithography with a Phase-Shifting Mask. *IEEE Transactions on Electron Devices* **1982**, *29* (12), 1828-1836, DOI: 10.1109/T-ED.1982.21037.
- [2] Boto, A. N.; Kok, P.; Abrams, D. S.; Braunstein, S. L.; Williams, C. P.; Dowling, J. P. Quantum Interferometric Optical Lithography: Exploiting Entanglement to Beat the Diffraction Limit. *Physical Review Letters* **2000**, *85* (13), 2733-2736, DOI: 10.1103/PhysRevLett.85.2733.
- [3] Lu, C.; Lipson, R. H. Interference Lithography: A Powerful Tool for Fabricating Periodic Structures. *Laser & Photonics Reviews* **2010**, *4* (4), 568-580, DOI: 10.1002/lpor.200810061.
- [4] Shao, L.; Zhuo, X.; Wang, J. Advanced Plasmonic Materials for Dynamic Color Display. *Advanced Materials* **2018**, *30* (16), DOI: 10.1002/adma.201704338.

## Publications

Sperling, J.R.; Macias, G.; Neale, S.L.; Clark, A.W. Multilayered Nanoplasmonic Arrays for Self-Referenced Biosensing. *ACS Applied Materials & Interfaces* 2018, DOI: 10.1021/acsami.8b12604.

Sperling, J.R.; Neale, S.L.; Clark, A.W. Bridging the Gap: Rewritable Electronics Using Real-Time Light-Induced Dielectrophoresis on Lithium Niobate. *Sci. Rep.* 2017, 7, DOI: 10.1038/s41598-017-09877-9.

Heydari, E.; Sperling, J.R.; Neale, S.L.; Clark, A.W. Plasmonic Color Filters as Dual-State Nanopixels for High-Density Microimage Encoding. *Adv. Funct. Mater.* 2017, 27 (35), DOI: 10.1002/adfm.201701866.

Flynn, G.E.; Withers, J. M.; Macias, G.; Sperling, J.R.; Henry, S.L.; Cooper, J.M.; Burley, G.A.; Clark, A.W. Reversible DNA Micro-Patterning Using the Fluorous Effect. *Chem. Commun. (Cambridge)* 2017, 53 (21), 3094-3097, DOI: 10.1039/c7cc00288b.

## Conference Presentations/Proceedings

Sperling, J.R., Macias, G., Burley, G.A., Neale, S.L. and Clark, A.W. (2019) Nanoplasmonic discrimination of organic solvents using a bimetallic optical tongue. In: *SPIE BiOS 2019*, San Francisco, CA, USA, 2-7 Feb 2019, 108950G. DOI: [10.1117/12.2507275](https://doi.org/10.1117/12.2507275)

Sperling, J.R., Heydari, E. Neale, S.L., and Clark, A.W. (2018) High-density colour filtering and micro-image encoding using dual-state plasmonic nanopixels. In: *Glasgow Imaging Network 2018*, Glasgow, UK, 22 Aug 2018.